# A NOVEL HPGR ONLINE MODELING AND SIMULATION APPROACH COUPLED WITH REAL-TIME INFORMATION

Túlio Moreira Campos

Dissertação de Mestrado apresentado ao Programa de Pós-graduação em Engenharia Metalúrgica e de Materiais, COPPE, da Universidade Federal do Rio de Janeiro, como parte dos requisitos necessários à obtenção do título de Mestre em Engenharia Metalúrgica e de Materiais.

Orientadores: Luís Marcelo Marques Tavares

Horacio Andrés Petit

Rio de Janeiro

Janeiro de 2023

# A NOVEL HPGR ONLINE MODELING AND SIMULATION APPROACH COUPLED WITH REAL-TIME INFORMATION

Túlio Moreira Campos

DISSERTAÇÃO SUBMETIDO AO CORPO DOCENTE DO INSTITUTO ALBERTO LUIZ COIMBRA DE PÓS-GRADUAÇÃO E PESQUISA DE ENGENHARIA (COPPE) DA UNIVERSIDADE FEDERAL DO RIO DE JANEIRO COMO PARTE DOS REQUISITOS NECESSÁRIOS PARA A OBTENÇÃO DO GRAU DE MESTRE EM CIÊNCIAS EM ENGENHARIA METALÚRGICA E DE MATERIAIS.

Orientadores: Luís Marcelo Marques Tavares
Horacio Andrés Petit

Aprovada por: Prof. Luís Marcelo Marques Tavares, Ph.D.
Dr. Horacio Andrés Petit, D.Sc.
Prof. Rodrigo Magalhães de Carvalho, D.Sc.
Dr. Thiago Antonio Melo Euzébio, D.Sc.
Prof. Mohsen Yahyaei, Ph.D.

RIO DE JANEIRO, RJ – BRASIL
JANEIRO DE 2023

Campos, Túlio Moreira

A novel HPGR online modeling and simulation approach coupled with real-time information/ Túlio Moreira Campos. – Rio de Janeiro: UFRJ/COPPE, 2023.

XXXIII, p. 209: il., 29,7 cm.

Orientadores: Luís Marcelo Marques Tavares

Horacio Andrés Petit

Dissertação (mestrado) – UFRJ/ COPPE/ Programa de Engenharia Metalúrgica e Materiais, 2023.

Referências Bibliográficas: p. 190-209.

1. HPGR. 2. Online modeling. 3. Iron ore concentrates. I. Tavares, Luís Marcelo Marques *et al*. II. Universidade Federal do Rio de Janeiro, COPPE, Programa de Engenharia Metalúrgica e de Materiais. III. Título.

*To the memory of my grandfather Itamar*

Resumo da Dissertação apresentado à COPPE/UFRJ como parte dos requisitos necessários para obtenção do grau de Mestre em Ciências (M.Sc.)

# A NOVEL HPGR ONLINE MODELING AND SIMULATION APPROACH COUPLED WITH REAL-TIME INFORMATION

Túlio Moreira Campos

Janeiro/2023

Orientadores: Luís Marcelo Marques Tavares

Horacio Andrés Petit

Programa: Engenharia Metalúrgica e de Materiais

Paralelo às melhorias na tecnologia da prensa de rolos desde sua primeira aplicação na década de 1980, vários autores aplicaram modelagem empírica e fenomenológica para descrever o desempenho do equipamento. Embora importantes, nenhuma aplicação descrevendo a dinâmica do equipamento e a aplicação desses modelos respondendo a variabilidades em tempo real foi demonstrada. O presente trabalho propõe uma nova abordagem com um modelo fenomenológico aplicado como ferramenta *online* acoplada a informações em tempo real. O trabalho se baseia em recentes avanços na modelagem da prensa de rolos, além de selecionar uma usina de pelotização de minério de ferro como estudo de caso. Modificações no modelo para aplicação em escala industrial são feitas. A aplicação do modelo é demonstrada com a habilidade de capturar variações do processo em tempo real. Dados de escala de bancada são usados para calibrar o comportamento de quebra no modelo, enquanto um novo método é proposto para permitir a descrição do desempenho do equipamento com rolos desgastados. A aplicação do modelo como assistente digital *online* é demonstrada e um uso potencial de um modelo de *soft sensor* prevendo a alimentação da prensa de rolos acoplado com o modelo de prensagem é apresentado.

Abstract of Dissertation presented to COPPE/UFRJ as a partial fulfillment of the requirements for the degree of Master of Science (M.Sc.)

A NOVEL HPGR ONLINE MODELING AND SIMULATION APPROACH COUPLED WITH REAL-TIME INFORMATION

Túlio Moreira Campos

January/2023

Advisors: Luís Marcelo Marques Tavares

Horacio Andrés Petit

Department: Metallurgical and Materials Engineering

Parallel to improvements in the HPGR technology since its first applications in the 1980s, several authors have applied empirical and phenomenological modeling approaches to describe the machine performance. Despite the key advances provided by them, no proper description on the HPGR dynamics and application of these models responding to real-time variabilities has been demonstrated so far. The present work proposes a novel HPGR phenomenological modeling approach applied as an online simulation tool coupled with real-time information. The work takes advantage on recent advances in the HPGR mathematical modeling, beyond selecting an industrial-scale iron ore pelletizing plant as a case study for model application. Modifications for applying the model in industrial-scale are made, which partially required an investigation on particle breakage under confined conditions. Model application is demonstrated capturing variation in real-time. Bench-scale data is used to calibrate breakage behavior in the model, whereas a new method is proposed to allow the model describing HPGR performance when the rolls were worn. Model application as an online digital assistant tool is demonstrated and a potential use of a soft sensor model predicting the HPGR feed coupled with the HPGR model is presented.

**SUMMARY**

**LIST OF FIGURES**

Figure 8.13. Comparison between measure and predicted HPGR feed BSA in 1-month period for the year of 2018 using the soft sensor model built an Artificial Neural Network (ANN) and validated in Figure 8.12. Data is presented for every 5-min …. 171

Figure 8.14. Comparison between experimental and predicted values for the HPGR product BSA using the novel online HPGR modeling and accounting for the HPGR feed BSA predicted by the ANN soft sensor model as a model input. Data is presented for every 5-min ….……………………………………………………………........……... 172

Figure A1. Comparison between experimental and calculated values for the Blaine specific surface area (BSA) using Eqns. (A1) to (A3) ……………………….………….. 179

Figure B1. Relationship between the $t_{10}$ parameter and the specific input energy for particles tested in different narrow size ranges in the piston-and-die apparatus with Brucutu sample. Optimal parameters for Eq. (5.3) were $A$ as 35.5 and $b_{PD}$ as 0.38 …………………………………..…………………………………..………….. 180

Figure B2. Relationship between the $t_{10}$ parameter and the specific input energy for particles tested in different narrow size ranges in the piston-and-die apparatus with Timbopeba sample. Optimal parameters for Eq. (5.3) were $A$ as 37.6 and $b_{PD}$ as 0.39 ………………………………………………………………………………...….. 180

Figure B3. $t_n$-$t_{10}$ relationship considering all narrow size ranges tested in the piston-and-die apparatus with Brucutu sample ……………………………………..……..….. 181

Figure B4. $t_n$-$t_{10}$ relationship considering all narrow size ranges tested in the piston-and-die apparatus with Timbopeba sample ……………………………………..…….. 181

Figure B5. Proportion broken out of the original size Brucutu sample for different specific energies and feed particle sizes ……………………………….…………. 182

Figure B6. Proportion broken out of the original size Timbopeba sample for different specific energies and feed particle sizes …………………………..……………… 182

Figure C1. Probability distribution function for the fresh feed solids rate in the pelletizing circuit. Data used to plot the graphs was recorded every 5-min frequency ……………………………………………………………………………………….. 183

Figure C2. Probability distribution function for the ball mill specific energy. Data used to plot the graphs was recorded every 5-min frequency ………………..…..….......... 183

**LIST OF TABLES**

## LIST OF SYMBOLS

***Latin***

| | |
|---|---|
| $A_p$ | effective area of the pistons in the hydro-pneumatic system |
| $A$ | $t_{10}$ model parameter in Eq. (5.2) |
| $a_i$ | fraction of broken particles in the pre-crusher for size class *i* |
| $a_i'$ | fraction of broken particles after the interparticle breakage for size class *i* |
| $a_i^*$ | fraction of unbroken and broke particles at the extrusion zone for size class *i* |
| $A_{ij,k}$ | Reid's matrix |
| $b_a$ | specific compressive force model parameter in Eq. (3.14) |
| $b_{ij}$ | distributed breakage function |
| $b_{PD}$ | $t_{10}$ model parameter in Eq. (5.2) |
| $B_{ij}$ | cumulative breakage distribution function |
| c | model parameter in Eq. (3.33) |
| $c_f$ | particle bed compaction behavior parameter in Eq. (3.20) |
| $\varsigma$ | split energy factor in Eq. (3.35) |
| $d$ | model parameter in Eq. (3.33) |
| $D$ | roll diameter |
| $D_{bed}$ | particle bed diameter |
| $E$ | input energy |
| $E'$ | rescaled energy term in Eq. (3.29) |
| $E''$ | energy densification parameter in Eq. (6.1) |
| $E_{sp}$ | specific energy |
| $E_1$ | energy related to particle rearrangement in Figure 3.14 |
| $E_2$ | energy related to breakage and plastic deformation in Figure 3.14 |
| $E_3$ | energy related to elastic recovery in Figure 3.14 |

| | |
|---|---|
| $e$ | model parameter in Eq. (3.30) |
| $erfc^{-1}$ | inverse complementary error function |
| $f_1$ | model parameter in Eq. (7.1) |
| $f_2$ | model parameter in Eq. (7.2) |
| $f_j^{SP}$ | feed size distribution of the single particle breakage zone |
| $f_j^{IP}$ | feed size distribution of the interparticle breakage zone |
| $f'$ | fraction of roll surface area corresponding to the autogenous layer |
| $f_{\text{obj}}$ | objective function |
| $f_{obj}^{Setpoint}$ | objective function defined to achieve a given setpoint in HPGR performance |
| $f_{50}$ | feed 50% passing size |
| $F_{sp}$ | specific compressive force |
| $F_{max}$ | maximum force applied to the particle bed |
| $F_1$ | static force on the hydro-pneumatic system |
| $F_0$ | initial $N_2$ force |
| $F$ | compressive force |
| $F_m$ | hydraulic system force |
| G | model parameter in Eq. (5.1) |
| G | BSA model parameter in Eq. (A3) |
| $H_k$ | holdup for each block *k* |
| $h_{bed}$ | particle bed height |
| $J$ | BSA model parameter in Eq. (A3) |
| $j$ | model parameter in Eq. (3.30) |
| $k_D$ | model parameter in Eq. (3.45) |
| $k_g$ | amenability of the particle bed for compaction parameter in Eq. (3.10) |
| $k_p$ | power factor parameter in Eq. (3.24) |

| | |
|---|---|
| $k_a$ | specific compressive force model parameter in Eq. (3.14) |
| $L$ | roll length |
| $M$ | reference for median calculation |
| $\dot{m}$ | specific throughput |
| $m_p$ | compressive stress |
| $N$ | number of size classes |
| $n$ | number of nodes in the Fourier transform |
| $N_B$ | number of blocks |
| $p_1$ | set point of pressure in the hydro-pneumatic system |
| $p_0$ | initial nitrogen pressure at the hydro-pneumatic system |
| $p_{50}$ | product 50% passing size |
| $p_m$ | operating pressure |
| $p_i^{SP}$ | product of the single particle breakage zone |
| $p_{i,k}$ | fraction of the product size distribution in each class *i* of each block *k* |
| $P$ | power consumption |
| $P^*$ | fraction of broken particle after the HPGR |
| $P_k$ | calculated power consumption in each block *k* |
| $P_k'$ | axial roll profile |
| $P_{sp}$ | specific power draw |
| $P_{Dim}$ | dimensionless specific power factor |
| $Q$ | throughput |
| $r_D$ | breakage rate in Eq. (3.45) |
| $s_i^E$ | specific selection function |
| $s_1^E$ | specific selection function parameter in Eq. (3.39) |
| $S_{i,k}$ | breakage rate for each class *i* in each block *k* |
| $S_i$ | breakage rate for each class *i* |

$S'$ proportion broken out the original size

$S_\infty$ model parameter in Eq. (5.1)

$T$ Torque

$t_{10}$ percent passing in $1/10^{th}$ of the original size class

$t_n$ percent passing in $1/n^{th}$ of the original size class

$U$ roll peripheral velocity

$U_{max}$ maximum roll peripheral velocity of the HPGR used

$U_g$ material velocity in the compression zone

$var_i$ variable in index *i*

$var_{50}$ median for the variable $var$

$var_{norm}$ normalized variable

$var_{Pred}$ predicted variable

$var_{Meas}$ measured variable

$var_i'$ derivative of variable $var$

$\overline{var}$ historical mean value of variable $var$

$v_z$ constant velocity in the $z$ direction

$V_1$ initial volume of oil in the hydro-pneumatic system

$V_0$ initial volume of $N_2$ at the accumulator

$V_m$ final volume of oil for a given hydraulic pressure $p_m$

$var_{Pred,j}$ predicted variable *j*

$var_{SP,j}$ setpoint for variable *j*

$\chi_g$ operating gap

$\chi_{gsp}$ specific operating gap

$\chi_0$ zero or initial gap

$\hat{x}_i$ harmonic mean size

$\bar{x}_i$ representative size

$x_e$ particle size for $\Pi_i$=1 in Eq. (3.33)

$x_i$ particle size

$x^*$ 62.3% passing size parameter in Eq. (4.3)

$x_{max}$ maximum particle size

$w_{i,k}$ fraction retained in each size class *i* and section *k*

$w_i$ mass fraction retained in each size class in BSA model

$W_{Calc}^{HPGR}$ calculated fraction passing in size class *i*

$W_{Exp}^{HPGR}$ experimental fraction passing in size class *i*

$W_i$ calculated fraction passing in size class *i*

$y_k$ position of each block *k* related to the center of the roll

$\bar{y}_k$ normalized average position along the roll

$z^*$ distance between the interparticle breakage zone entrance and the HPGR extrusion zone

***Greek***

$\alpha_{ip}$ nip angle

$\alpha$ model parameter in Eq. (4.3)

$\alpha_D$ model parameter in Eq. (3.45)

$\alpha_n$ incomplete beta function parameter in Eq. (5.4)

$\beta'$ force-acting angle

$\beta_n$ incomplete beta function parameter in Eq. (5.4)

$\xi_1$ specific selection function parameter in Eq. (3.39)

$\xi_2$ specific selection function parameter in Eq. (3.39)

$\theta_c$ initial particle bed porosity

$\theta_g$ final particle bed porosity

$\theta$ adiabatic exponent

$\rho_g$ flake density

$\rho_a$ bulk density

$\rho_{sp}$ specific gravity

$\tau$ throughput model parameter in Eq. (3.16)

$\varphi$ throughput model parameter in Eq. (3.16)

$\upsilon$ throughput model parameter in Eq. (3.16)

$\delta$ percentage of material ejected by the edge of the rolls in Eq, (3.16)

$\vartheta_1$ hydro-pneumatic model parameter in Eq. (6.6)

$\vartheta_2$ hydro-pneumatic model parameter in Eq. (6.6)

$\gamma$ breakage function parameter in Eqns. (3.38) and (3.46)

$\phi$ breakage function parameter in Eqns. (3.38) and (3.46)

$\beta$ breakage function parameter in Eqns. (3.38) and (3.46)

$\chi'$ apparent relative bulk density

$\sigma_p$ compressive stress

$\kappa$ nip angle parameter in Eq. (3.27)

$\Omega$ energy dissipation parameter in Eq. (3.29)

$\Pi_i$ split factor for size *i*

$\Lambda$ proportion of material that should be broken in the edge region

$\omega$ breakage function parameter in Eq. (3.46)

$\eta$ breakage function parameter in Eq. (3.46)

$\chi_{gstud}$ operating gap measured from the distance between the top of the rolls studs

$\chi_p$ stud penetration in the particle bed

$\chi_c$ critical size

$\psi_{var,j}$ weights used for the setpoint in each variable *j*

$\Psi$ efficiency variable

$\Xi$ dimensionless fitting parameter in Eq. (6.1)

| | |
|---|---|
| $\mu$ | fitting parameter in Eq. (6.3) |
| $\exists$ | model parameter in Eq. (3.28) |
| $\varepsilon$ | absolute relative deviation from measurements |

**LIST OF ACRONYMS**

| | |
|---|---|
| $ANN$ | Artificial neural network |
| $BSA_{feed}$ | Blaine specific surface area of the feed |
| $BSA_{prod}$ | Blaine specific surface area of the product |
| $BM1$ | Ball milling line 1 |
| $BM2$ | Ball milling line 2 |
| $BSA$ | Blaine specific surface area |
| $DEM$ | Discrete element method |
| $DWT$ | Drop weight test |
| $HPGR$ | High-pressure grinding rolls |
| $HRC$ | Hydraulic roll crusher |
| $MAD$ | Median absolute deviation from median |
| $OCS$ | Optimizing control system |
| $PCA$ | Principal component analysis |
| $PCR$ | Principal component regression |
| $P\&D$ | Piston-and-die |
| $PLS$ | Partial least squares |
| $PIMS$ | Process information management system |
| $PSI$ | Particle size analyzer |
| $UFRJ$ | Universidade Federal do Rio de Janeiro |

**ACKNOWLEDGEMENTS**

I would like to express my gratitude to Prof. Luís Marcelo Tavares and Dr. Horacio Andrés Petit for their guidance and supervision of this work. The passion and strong dedication to research is inspiring for everyone working with you. I also thank the committee members for their time and interest in this work.

I would also like to express my gratitude to my parents Norton and Melba and to my sister Talita for the entire support along these years working and studying far away from home. I am glad to have you as family and you inspire me to go on every day.

Many thanks to my partner Brena for the support, patience, partnership and friendship during all these years. You were essential for me to complete this journey.

This work would not be possible without the support and friendship of all my colleagues from Laboratório de Tecnologia Mineral (LTM/COPPE/UFRJ). Thanks to Victor Rodriguez and Gabriel Barrios for several stimulating discussions in the course of the work. The assistance of Flavio and Marcio in the piston-and-die tests and Thiago Gutierrez in the Malvern size analysis is appreciated. Also, thanks to Prof. Malcolm Powell for many fruitful discussions in the last months of this work.

The research was fully supported by company Vale S.A. The assistance and contribution of Ricardo Olympio, Gilvandro Bueno and all technical team from Vale S.A. is much acknowledged.

The partial financial support of the Brazilian agency Conselho Nacional de Desenvolvimento Científico e Tecnológico (CNPq) is greatly appreciated.

## 1. INTRODUCTION

The high-pressure grinding rolls (HPGR) technology reached a significant position in the minerals industry in the last 30 years. Since its patent in the middle of 1980s, the HPGR application has reached an outstanding distinction in the minerals industry, being applied as a versatile equipment able to operate from ternary crushing stages to regrinding of fine materials prior to pelletizing (VAN DER MEER, 1997, MORLEY, 2006, MICHAELIS, 2009, MAZZINGHY *et al.*, 2017, ROCHA *et al.*, 2022a). The major purpose of the HPGR technology is to operate as an efficient comminution machine with its breakage response based on particle bed breakage behavior. SCHÖNERT (1988) was the pioneer to carry out studies to assess the HPGR breakage response in comparison to traditional comminution technologies. Results provided by him were key to ensure the growth in the HPGR application since then.

As such, in the last 30 years several applications of the HPGR technology were reported for different commodities, which a is presented in Figure 1.1 (updated from MORLEY, 2006). The first commercial application was in 1984, in the cement industry, with the HPGR replacing ball mills in clinker regrinding (KELLERWESSEL, 1990). Since then, the technology was applied in processing kimberlite diamond ores (DANIEL, 2002, MICHAELIS, 2009), iron ores in tertiary crushing stages (MORLEY, 2006, Mazzinghy *et al.*, 2017), iron ore concentrates (VAN DER MEER, 1997, CAMPOS *et al.*, 2019a) and hard rocks (MORLEY, 2006, MICHAELIS, 2009, GARDULA *et al.*, 2015, POWELL *et al.*, 2017, BURCHARD & MACKERT, 2019).

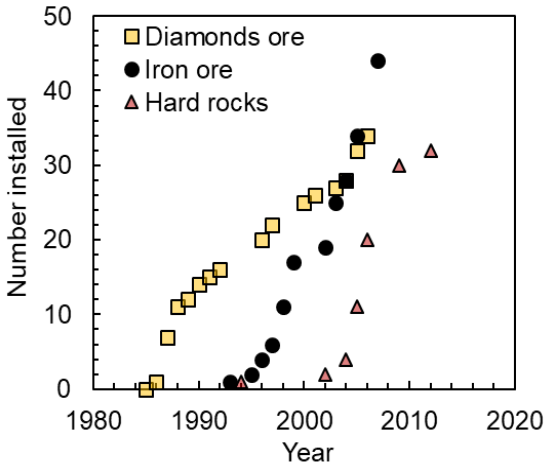


Figure 1.1. Number of installed HPGRs along the years for different commodities (updated from MORLEY (2006)).

Parallel to the HPGR application, important improvements have also been made to the technology (ALSMANN, 1996, FARAHMAND & EHRENTRAUT, 1997, LIM AND WELLER, 1999) and even in the machine performance under different conditions (SCHÖNERT, 1988, LIM *et al.*, 1997, FUERSTENAU & ABOUZEID, 1998, DANIEL, 2002, VAN DER MEER, 2015, CAMPOS *et al.*, 2019a, VAN DER ENDE et al, 2019, BURCHARD & MACKERT, 2019). Additionally, much attention has also been given to the development of proper mathematical relationships able to describe the HPGR performance (SCHÖNERT, 1988, FUERSTENAU *et al.*, 1991, MORRELL *et al.*, 1997, DANIEL & MORRELL, 2004, TORRES & CASALI, 2009, DUNDAR *et al.*, 2013, CAMPOS *et al.*, 2019b, RODRIGUEZ *et al.*, 2023).

Three of these mathematical models (MORRELL *et al.*, 1997, TORRES & CASALI, 2009, DUNDAR *et al.*, 2013) reached relative popularity in the industry in the last 25 years. Although they are robust and predictive models that have been validated for different applications and often relying on bench-scale testes (piston-and-die tests) to characterize the material breakage behavior (MORRELL *et al.*, 1997, DUNDAR *et al.*, 2013), recent investigations by the author (CAMPOS *et al.*, 2018, CAMPOS *et al.*, 2019b) showed limitations in their predictions. Among these modeling approaches, the Torres and Casali proposal (TORRES & CASALI, 2009), which proved to be most versatile of the three investigated, was modified by the authors to improve model accuracy (CAMPOS, 2018, CAMPOS *et al*, 2019b). The new model, now called Modified Torres and Casali model, was validated over a wider operating range for pressing iron ore concentrates in a pilot-scale HPGR (CAMPOS *et al.*, 2019b), demonstrating to be a more robust and predictive model for this application when compared to its original version. Besides that, recent works (BUENO, 2019) highlighted the application of the Modified Torres and Casali model assessing the HPGR performance for pressing iron ore pellet feed in industrial-scale for some of the pelletizing plants from Complexo de Tubarão from Vale S.A. (Vitória, Brazil). Promising results suggested the potential application of this model as a predictive tool that aims to assess different operational strategies from the point of view of the HPGR performance improvements.

Despite these important advances, this modeling approach has only been used so far offline and under steady-state conditions, thus not being assessed when dealing with real-time variations in operating conditions and feed size distribution of an industrial

HPGR. Indeed, the need to remain competitive in the minerals sector is compelling industries to adopt innovative mining practices with a great digital transformation and total process integration. From the point of view of an HPGR, which normally occupies the boundary between two different comminution stages in mostly of circuit configurations, there is a key requirement for a machine able to capture variabilities from the upstream process and deliver to the downstream operation a product with a high quality that follows the operational demand. These requirements are fully related to the need for improving understanding on how the machine should operate when dealing with variations in the process stability caused by real-time disturbances.

In this regard and taking advantage on recent developments in big data analytics and cloud database, applications of a phenomenological HPGR model receiving real-time information as an input to predict machine performance would be a good alternative to support this type of process integration with an ability to map the industrial operation and give a realistic representation of the process on the basis of variabilities in operating conditions and feed characteristics. Beyond that, this novel approach would allow avoiding applications that rely solely on back-fitted data that are limited to small ranges of operating conditions, thus not allowing its real use as a predictive and engineering tool.

Proper application of this modeling approach discussed above, which can be named as an online HPGR model, is still lacking in literature and in the minerals industry. In general, to investigate and apply a more robust phenomenological model with the ability to capture all features associated to an industrial HPGR operation in real-time might sound as an oxymoron. Nevertheless, it is the motivation of the present work.

## 2. RESEARCH OBJECTIVES AND DISSERTATION STRUCTURE

The main objective of this work is to propose a new HPGR modeling approach coupled with real-time information applied as an online tool in industrial-scale. The idea behind the HPGR online model is to describe the machine performance on the basis of real-time variabilities in operating conditions, feed characteristics and roll surface wear. The work will take advantage of recent improvements in HPGR mathematical modeling (TORRES & CASALI, 2009, CAMPOS *et al.*, 2019b) using a phenomenological approach, named Modified Torres and Casali model, capable to give rapid responses from several variations in operating conditions, design variables and feed characteristics.

A pellet feed preparation circuit from one of the pelletizing plants from Vale S.A., in Complexo de Tubarão (Vitória, Brazil), is used as the case study to apply the new modeling approach. The circuit relies on at least six different unit operation (Ball milling, hydrocyclones classification, thickening, homogenization, filtering and HPGR) and requires a proper understanding of all of them. The model is then used to describe and map the entire plant with the main investigation on the HPGR operation, which will cover the machine operating under different roll surface wear. The HPGR online model will be used to compose the structure of an online digital assistant able to determine the best set of HPGR operating conditions according to a give setpoint in the machine performance.

To make it possible to apply the HPGR model using the proposed structure, a set of requirements should be raised to give support to the main objective:

R#1 – An improvement in the HPGR mathematical model is required from some modifications in the Modified Torres and Casali model (TORRES & CASALI, 2009, CAMPOS *et al.*, 2019b):

R#1a – Improve understanding about particle bed breakage to build a model able to account for breakage saturation effect when predicting size reduction.

R#1b – Improve description of pressure profile along the roll length with ability of changing it according to design conditions.

R#1c – Use information from bench-scale tests (piston-and-die tests) to calibrate the energy-specific progeny size distribution in the description of particle breakage in an industrial HPGR.

R#1d – Apply and validate the model describing the HPGR pressing iron ore concentrates under steady-state conditions.

R#2 – Apply the phenomenological model as a pseudo-dynamic approach:

R#2a: Circumvent the effect of wear to increase model accuracy for a sufficient amount of time/equipment operation.

R#3 – Apply the HPGR online model as a digital assistant aiming to find an alternative set of conditions that satisfies a given setpoint in the HPGR performance:

R#3a – Define the main operational variables to be optimized based on a desired setpoint and all the operating conditions that should be manipulated to achieve this new target.

R#3b – Predict the operating gap, which should be a response variable, based on the operating pressure (main manipulated variable), material compressibility and HPGR hydro-pneumatic system.

R#4 – Propose a soft sensor model to predict the HPGR feed BSA based on real-time data from the upstream process. This goal is justified considering the poor reliability on the HPGR feed BSA measured in real-time:

R#4a – Point out the advantage of using a soft sensor based on process delay and giving heads up to the operator.

These requirements were addressed along the text to compose the structure of the work, being the dissertation divided in 9 Sections. Section 1 briefly introduces the work, Section 2 describes the main research objectives and Section 3 presents a review of the literature. Section 4 describes in great details the methodology used in the work, Section 5 partially assess the particle bed breakage behavior, Section 6 presents the

Modified Torres and Casali HPGR model shortcomings and new improvements and Section 7 describes the application of the entire online model structure with validations and applications as a digital assistant finding new alternative set of operating conditions to optimize HPGR performance. Section 8 finally investigates the design and application of a data driven soft sensor model predicting the HPGR feed BSA, whereas Section 9 presents the final discussions and conclusions.

# 3. REVIEW OF THE LITERATURE

## 3.1. Overview of HPGR technology

The high-pressure grinding rolls (HPGR), also called roller press (KLYMOWSKY & LIU, 1997), was developed and proposed as the result of a fundamental study about the “High Pressure Interparticle Comminution process” carried out by Prof. Klaus Schönert and his team (KLYMOWSKY & LIU, 1997).

The HPGR technology is able to break particles under confined conditions between two counter-rotating rolls, being one mounted in a fixed bearing, whereas the other is mounted in a movable bearing. The movable roll, also called floating roll, has a hydro-pneumatic pressurizing system coupled to it that aims to increase or decrease the applied pressure on the particle bed. As such, the particle breakage behavior in the HPGR occurs normally in an autogenous way, unlike other widely used comminution devices such as ball mills, rod mills and conventional roll crusher. In general, the applied grinding force is transferred between each particle in the confined bed with only a small proportion of particles into direct contact with the rolls (DANIEL, 2002).

Among the different comminution equipment used in the minerals industry, the HPGR stands out for its versatility in the operational circuit. Indeed, this equipment is able to increase the throughput (KELLERWESSEL, 1990, DUNDAR *et al.*, 2013), reduce the specific energy consumption during grinding (MCIVOR, 1997, BENZER *et al.*, 2001, DANIEL, 2002, AYDOĞAN, 2006), besides allowing to improve the operational stability and even simplifying the comminution circuit (MAZZINGHY *et al.*, 2017). A brief comparison between the HPGR and a double roll crusher, for instance, shows that the HPGR allows significant changes in the operating gap during grinding according to the set of operating pressure or even the material response. These features have provided a high reduction ratio coupled to a low specific energy consumption into the HPGR, beyond being able to give a better response for some variations in the feed size distribution in comparison to the double roll crusher (OTTE, 1988).

Therefore, the roller press technology was first implemented in the cement industry in the middle of the 1980s, reaching some popularity in the minerals industry for soft ores in the 1990 decade (VAN DER MEER, 1997, MORLEY, 2006) and for hard ores after 2006 (MORLEY, 2006, MICHAELIS, 2009, BANINI *et al.*, 2011,

GARDULA *et al.*, 2015, POWELL *et al.*, 2017, BURCHARDT & MACKERT, 2019). In addition to the wider range of applications in the minerals industry, which is briefly discussed in Section 3.2, the manufacture of the roller press was restricted for a long time to three main companies: Thyssenkrupp Polysius (current owned by FLSmidth), KHD/WEIR and Köppern. Nowadays, the company Metso has also produced the hydraulic roll crusher (HRC) as a new approach considering the flanged rolls with the aim of improving the throughput and reducing the specific energy consumption (KNORR *et al.*, 2013, ZERVAS, 2019). Moreover, a German company called ArgoIPS is also developing a new approach for the HPGR named Argo Mill, which basically operates coupled to a hydro-pneumatic pressurizing system and with both rollers sloped 30º (Argo IPS, 2020).

## 3.2. HPGR applications

### *3.2.1. Industrial-scale applications*

Since its introduction in the cement industry in 1984, the industrial-scale application of the HPGRs has reached a significant position in the minerals industry. The first commercial industrial-scale application was performed in order to increase the plant throughput in the cement industry (KELLERWESSEL, 1990), being the HPGR applied for grinding cement clinker in the Dykerhoff Lengerich cement plant in Wiesbaden, Germany (MCIVOR, 1997). Given its success in this application, around 500 HPGRs were installed in the cement industry up to 2009, being those machines able to operate with an installed throughput from 200 to 1200 t/h (KÖPPERN, 2009). DUNDAR *et al.* (2013) highlighted that the cement industry was important to consolidate the HPGR technology as an efficiency alternative to fine grinding and also increase the plant capacity. Studies carried out by the group from the Hacettepe Üniversitesi, in Turkey, showed that the application of the HPGR can demand about 10 to 50% less energy consumption when compared to ball milling, being this feature one of the main reasons for the its outstanding successful application in the cement industries (AYDOĞAN, 2006, BENZER *et al.*, 2001).

After reaching popularity in the cement industry, the HPGR was also applied for grinding kimberlite diamond ores (DANIEL, 2002, MICHAELIS, 2009) aiming to improve the recovery of valuable particles and to reduce the damage to the gems.

Nevertheless, only in the middle of 1990s the HPGR reached the status of great acceptance of the technology in different applications in industry (KELLERWESSEL, 1990).

In this regard, the first successful application was in the iron ore industry, with the HPGR operating in the tertiary and quaternary crushing stages in the Los Colorados mine/plant (Chile) in 1990. The replacement of the traditional crushing stages was a success, allowing significant reductions in operational cost (MORLEY, 2006). VAN DER MEER (1997) also reported some applications of the HPGR for pressing iron ore concentrates in the pellet feed preparation steps prior to pelletization (VAN DER MEER, 1997). Current applications with this material can be seen in the Brazilian companies Vale S.A. and Samarco S.A. for pressing fine iron ore concentrates and in the Minas-Rio operation from Anglo American pressing itabirite iron ore in the tertiary crushing stages.

Parallel to the iron ore applications, the HPGR technology experienced an appreciable learning and development curve along the 1990s. The unsuccessful application in hard rock carried out as an initial study in the Cyprus Sierrita copper mine (Arizona, USA) warned about the need for improving the knowledge related to the behavior of the surface wear (MORLEY, 2006). Indeed, many valuable lessons were learnt from these operations, and it was only in 2006 that the first commercial application for hard rocks took place in the Cerro Verde mine (Peru). According to MICHALIS (2009), the HPGR allowed reaching higher throughput and lower specific energy consumption when replacing SAG milling for grinding copper ore.

Considering the appreciable improvements in the HPGR roll surface wear and the outstanding success provided in its application in Cerro Verde, nowadays the roller press is widely used for grinding copper, molybdenum and gold ore (MICHAELIS, 2009, BANINI *et al.*, 2011, GARDULA *et al.*, 2015, BURCHARDT & MACKERT, 2019) as well as platinum ores (POWELL *et al.*, 2017), limestone (MORLEY, 2006) and even smelter slags (MICHAELIS, 2009). Figure 3.1 presents a summary of the timeline application of the HPGR technology since its introduction in the cement industry in 1984.

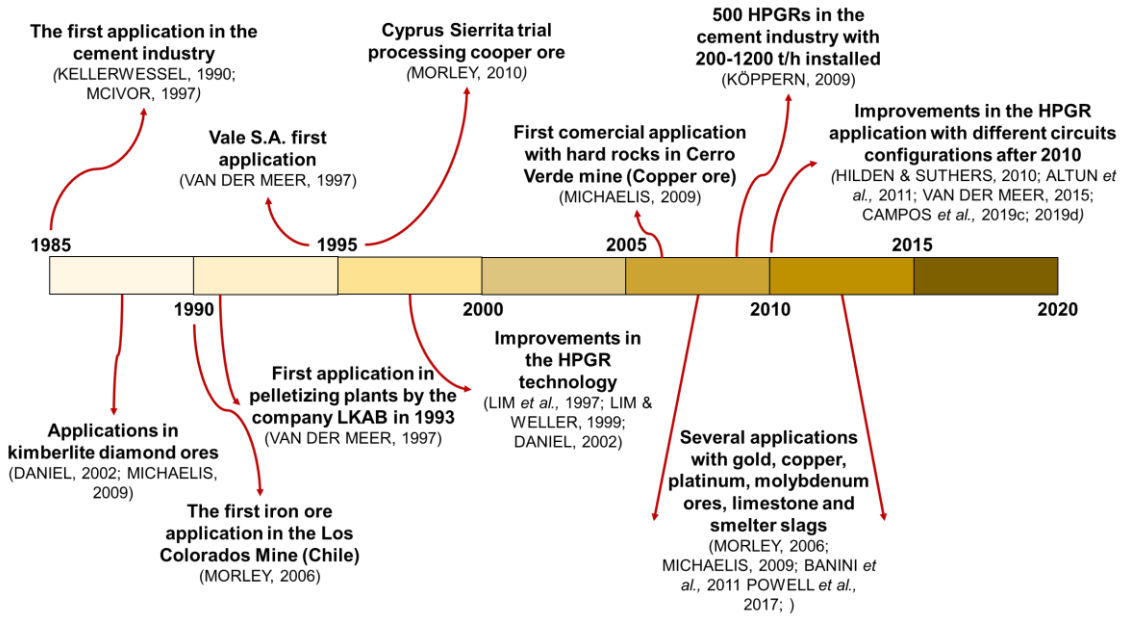


Figure 3.1. Summary of the timeline application for the HPGR technology since its first commercial application in 1984.

### *3.2.2. Iron ore concentrates applications*

The first industrial application for pressing iron ore concentrates was carried out by the Swedish company LKAB in the Malmberget plant in 1993 with a small HPGR operating with blended concentrates and with an installed capacity of 50 t/h (VAN DER MEER, 1997). Two years later, the Kiruna plant, also from LKAB, installed an HPGR with a 750 t/h throughput pressing filter cakes from apatite flotation (VAN DER MEER, 1997).

Taking into account these successful applications, the company Vale S.A., then called Companhia Vale do Rio Doce (CVRD), introduced the HPGR in some of the pelletizing plants of the Complexo de Tubarão in the city of Vitória (Espírito Santo state, Brazil). This application was one of the pioneering applications of the HPGR in an integrated circuit with ball milling in the pellet feed preparation stage, with the roller press operating either in pre-grinding or regrinding prior to pellet formation (VAN DER MEER, 1997, CAMPOS *et al.*, 2019a). According to VAN DER MEER (1997) the aim of the HPGR application in Vale's pelletizing plants was the improvement in quality of the final product and the reduction in the energy consumption. Figure 3.2 illustrates a typical flowsheet from the pelletizing plants of Complexo de Tubarão, with the HPGR

operating in regrinding prior to pellet formation (CAMPOS *et al.*, 2019a). Nowadays, the HPGR is applied in seven of the eight pelletizing plants that make up the Complexo de Tubarão.

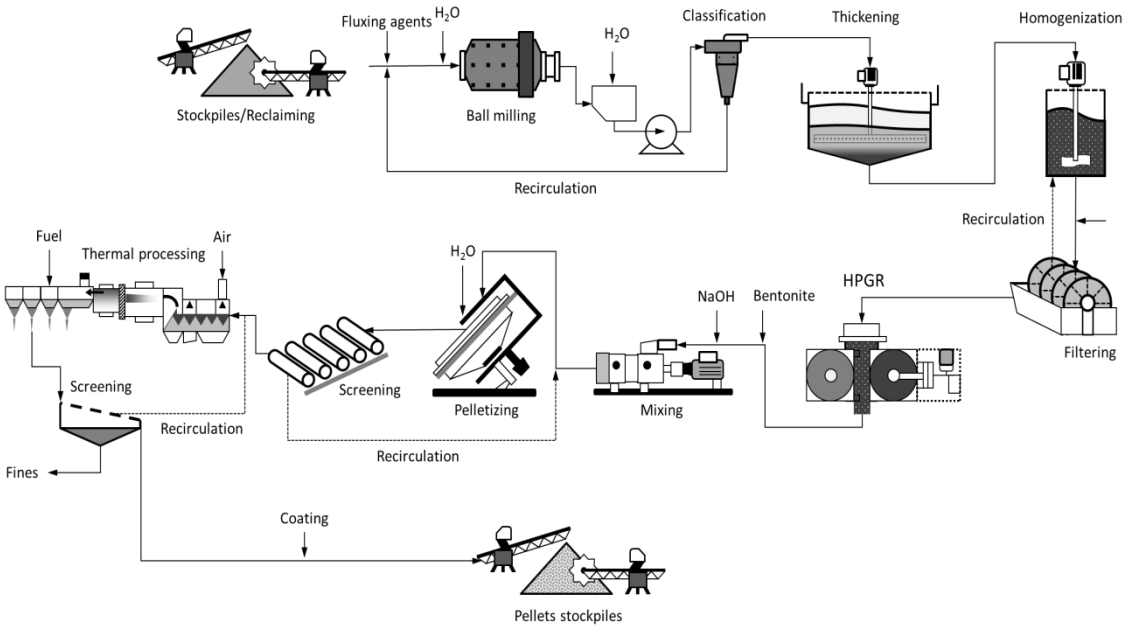


Figure 3.2. Schematic flowsheet of the pelletizing plants of Complexo de Tubarão (Vale) with the HPGR operating in regrinding pre-pelletizing (CAMPOS *et al.*, 2019a).

Indeed, the HPGR application for pressing iron ore concentrates prior to pellet formation achieved an outstanding success due to several important advantages of this process. The main advantages in the application are the reduction in the energy consumption through the introduction of microcracks in the material (ENRENRAUT & RAO, 2001, VAN DER MEER, 2015), the generation of large proportion of ultrafine particles (VAN DER MEER, 2015), the ability to operate with moisture contents up to 8-12% (VAN DER MEER, 2015), the improvement in the product surface area (ABAZARPOOR *et al.*, 2017) and the lower consumption of additives and higher strength in the iron ore pellet (VAN DER MEER, 1997).

*3.2.3. Different circuit configurations for pressing iron ore concentrates*

Defining the optimal circuit configuration is always key to achieve the best performance in mineral processing. For the HPGR operation, choosing the best circuit configuration remains a key question for a particular task (CAMPOS *et al.*, 2019b) and should be investigated in detail case-by-case. Indeed, experimental evidence has demonstrated the feasibility to operate the HPGR in closed circuit with classification using a V separator (ALTUN *et al.* 2011) or an air classification (JANKOVIC *et al.*, 2014) and also recycling a fraction of the product (AYODOĞAN *et al.*, 2006, OZCAN *et al.*, 2015). HILDEN & SUTHERS (2010) has demonstrated for pressing hard rocks that a single stage with product edge recycle is able to improve the size reduction energy efficiency. In addition, RASHIDI *et al.* (2014) demonstrated that multi-stage pressing has demonstrated to be an alternative for pressing soft materials, whereas closed circuit with classification would be the most suitable choice for hard rocks.

In the case of pressing iron ore concentrates, 25 years ago VAN DER MEER (1997) discussed about a near-future application in the Iron Dynamics Inc. (USA) using product edge recycle configuration and having about 300% of circulating load with a circuit throughput of 100 t/h (VAN DER MEER, 1997). Currently, several opportunities have proven to be attractive from an industrial point of view, where the HPGR would be used as the main equipment within the production of pellet feed fines. This type of circuit configuration could allow a drastic reduction in the operational cost since it would potentially allow moving forward from traditional circuit (Figure 3.2) with ball milling, hydrocyclone classification, thickening, filtering and homogenization (CAMPOS *et al.*, 2019a, THOMAZINI *et al.*, 2020).

VAN DER MEER (2015) showed through experimental results, whereas CAMPOS *et al.* (2019b) demonstrated through process simulation in a pilot-scale HPGR, the feasibility of pressing at multiple stage and product edge recycling, thus demonstrating capability to reach a high increment in the BSA associated to a high energy efficiency. Indeed, it would be extremely attractive to replace the work carried out by ball milling or, at least in part, transfer it to the pressing process. CAMPOS *et al.* (2019c) presents several results from process simulations indicating that it is feasible to reduce the specific surface area of the HPGR feed from 1770 $cm^2/g$ to 1570 $cm^2/g$, allowing to produce a pellet feed of the same quality in its product (1911 $cm^2/g$) and therefore reduce the work done by upstream ball milling (CAMPOS *et al.*, 2019c).

CAMPOS *et al.* (2019d) also showed using process simulations that operating with 40% of product edge recycle in an industrial-scale HPGR would allow achieving an increment in the BSA of the iron ore concentrate of 400 cm²/g. More recently, THOMAZINI *et al.* (2020) showed the feasibility to use multi-stage pressing process to produce qualified pellet feed fines for pelletizing process, thus demonstrating the validity of the whole novel approach.

### 3.3. HPGR machine settings

Although celebrating around 35 years of application in the minerals industry in a period with some great improvements in technologies, in general, the HPGR still remains mainly with its original design proposed by Prof. Klaus Schönert in the middle of the 1980s. The equipment can break particles under confined conditions between two counter-rotating rolls, being one mounted on a fixed bearing, whereas the other is mounted on a movable bearing. The movable roll has a hydro-pneumatic pressurizing system coupled to it that aims to increase or decrease the applied pressure on the particle bed. Figure 3.3 summarizes the main components of an HPGR.

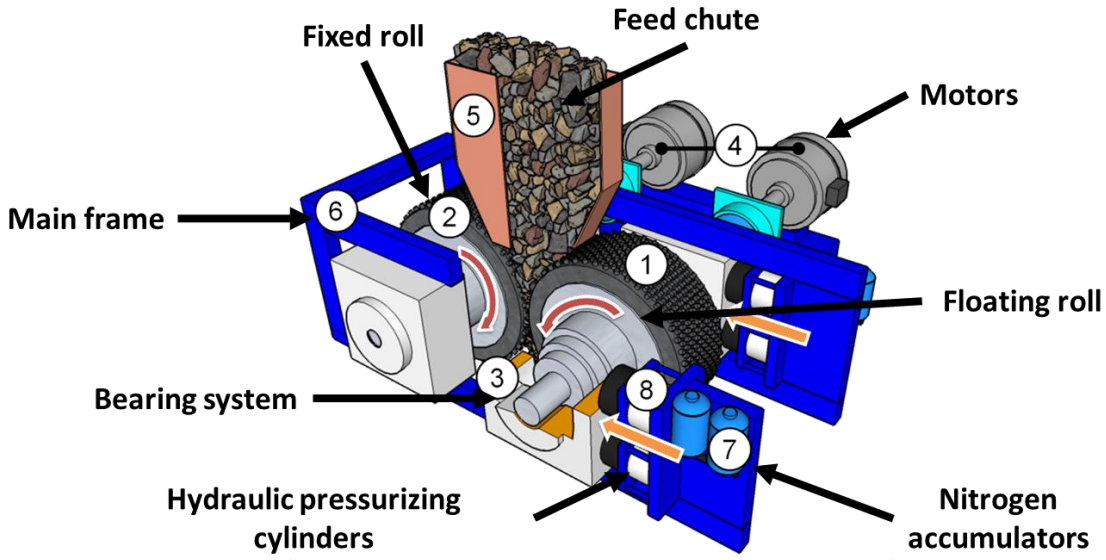


Figure 3.3. The main components in an HPGR (CAMPOS *et al*. 2019b).

Basically, the high-energy input provides a relatively high torque between rollers allowing to pass the material until the extrusion zone. As the packed material passes through the rolls the pressure increases in the particle bed and breakage occurs under a high specific compressive force (OTTE, 1988). In general, the main HPGR machine settings can be summarized in the features of the hydro-pneumatic suspension system, type of confinement system, surface wear and machine dimensions.

### *3.3.1. Roll dimensions*

MORLEY (2006) stated that there was no fundamental difference between the HPGR manufactures at the time, although some variations in the rolls designs have been proposed to take into account the aspect ratio between the roll diameter and the roll length. A high aspect ratio design is inherently more expensive, although offers a longer wear lifetime for some particular applications. MORLEY (2006) also highlighted that a low aspect ratio is associated to a uniform pressure profile along the axial roll position, being thus capable of generating a finer product size distribution. According to him (MORLEY, 2006), this effect is relatively modest. Nevertheless, a recent work using DEM simulations showed significant variations in the shape and magnitude of the pressure profile varying the roll aspect ratio from 0.83 to 3.13 in a pilot-scale HPGR (RODRIGUEZ *et al.*, 2021).

### *3.3.2. Hydro-pneumatic suspension system*

The hydro-pneumatic suspension system consists of mainly three components: a hydraulic cylinder, a hydro-pneumatic accumulator coupled to the hydraulic cylinder and the hydraulic fluid (BAUER, 2011). The system works with a set of oil pressure in the cylinders followed by a fixed nitrogen pressure in the accumulator volume. When the material passes through the rolls the nitrogen is compressed, thus defining the system stiffness and, consequently, the floating roll behavior during operation. Figure 3.4 presents a schematic diagram with the main characteristics of the hydro-pneumatic suspension system (a) and the main components of the system in a pilot-scale HPGR (b).

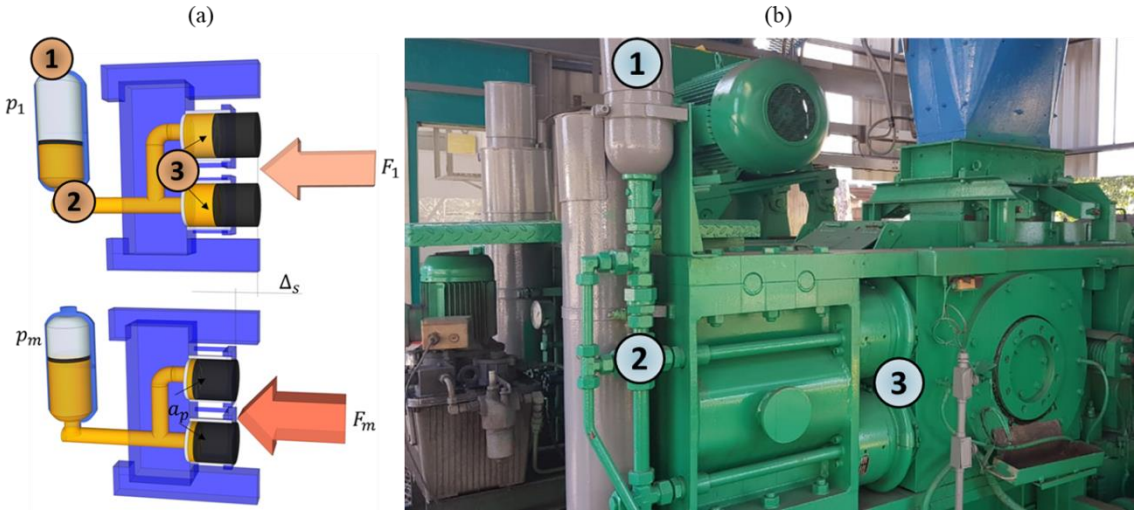


Figure 3.4. Scheme of the main characteristics of the hydro-pneumatic suspension system (a) and the main components of the system in a pilot-scale HPGR (b). Highlight of the accumulator volume (1), the hydraulic fluid (2) and the hydraulic cylinders (3) (b).

The nitrogen gas in the accumulator volume originally works as a linear spring within the system. VAN DER MEER & DICKE (2008) stated that the nitrogen gas (pneumatic system) is able to control the operating gap against the hydraulic pressure applied. According to them, the absence of significant pressure peaks results in a lower roll surface wear, although it would result in coarser product size distribution (VAN DER MEER & DICKE, 2008). Some other authors have also showed through experimental results in a lab-scale HPGR (DANIEL, 2002, BARRIOS, 2015) that the response of the hydraulic spring is directly related to the initial nitrogen pressure. Indeed, for hydro-pneumatic systems such as the ones used for lab-scale HPGRs, low nitrogen pressures would restrict the motion of the floating roll, thus limiting changes in the operating gap even when significant variations in the operating pressure are applied (DANIEL, 2002, BARRIOS & TAVARES, 2016).

On the other hand, JOHANSSON & EVERTSSON (2018) warned that dynamics of the HPGR movable roll cannot be associated only to the nitrogen pressure in the hydraulic system. This statement is endorsed by BAUER (2011) arguing that one of the main features of the hydro-pneumatic suspension system is the capability of readjust the suspension position after a change of the suspended load, simply by adding or removing hydraulic fluid. This key feature provides a more elaborate pressurizing

system that potentially can give different responses than the previous results found elsewhere in lab-scale HPGRs (DANIEL, 2002, BARRIOS, 2015). Nevertheless, no experimental evidence has been presented to support it so far.

### *3.3.3. Roll surface wear*

According to MORLEY (2006) the majority of lost operating time in the HPGR operation is associated to the rolls surface wear. Indeed, since the unsuccessful application in the Cyprus Sierrita trial in 1995 for a copper ore operation, the rolls surface wear characteristics have become one of the main focus areas in the HPGR operation aiming to improve the lifetime of the rollers.

As such, in the second half of the 1990s some studies were carried out (ALSMANN, 1996, FARAHMAND & EHRENTRAUT, 1997, LIM & WELLER, 1999) to investigate the effect of different rolls surface characteristics in the HPGR operation. Several variants were proposed to replace the smooth rolls, which included welded rolls, profiled rolls and studded rolls (DANIEL, 2002). Currently, the studded rolls are the most common configuration used in the minerals industry. Parallel to that, LIM & WELLER (1999) also showed through experimental measurements that the changes in the pressure profile along the roll length are able to provide much higher wear in this region of the rollers, which was also demonstrated recently (SÖNMEZ *et al.*, 2015, NEJAD & SAM, 2017, BURCHARDT & MACKERT, 2019, RASHIDI AND RAJAMANI, 2020). Lifetime of HPGR rolls is often close to 8,000 for hard rock processing, reaching up to 15,000 hours for pressing iron ore pellet feed (BURCHARDT & MACKERT, 2019).

However, even with the development of new technologies, there is still great challenge in terms of reducing wear on the rolls for HPGR operation. The development of new materials, including new metallic alloys with tungsten carbide and ceramic materials, is recognized to be the key for increasing the lifetime of this equipment. However, nowadays the studded roll is still the most appreciated design in order to minimizes the risk of roll damage, especially for applications that operate at specific forces higher than 3 N/mm² (VAN DER MEER & DICKE, 2008). Figure 3.5 shows two rotating rolls (studs made of tungsten carbide) at the beginning (a) and at the end (b) of

their life when processing iron ore concentrates, highlighting the severe wear on the center region (Figure 3.5b).


Figure 3.5. Difference between two rotating rolls in a lab-scale HPGR used to process iron ore concentrates with different wear patterns. Figure 3.5a shows the roll at the beginning of roll lifetime, whereas Figure 3.5b shows the intense surface wear after several hours of testing. Studs on both rolls are made of tungsten carbide.

Additionally, recent works (QUIST & EVERTSSON, 2012, RODRIGUEZ *et al.*, 2021) have showed through DEM simulations that different roll wear patterns can change the axial roll profile in the HPGR operation and, therefore, the machine performance. RODRIGUEZ *et al.* (2021) carried out a detailed study of a pilot-scale HPGR pressing iron ore concentrates and emulating a trapezoidal wear profile along the roll length. In that case, they found a pressure profile following the called "bathtub" shape, which is associated to a significant drop in the pressure in the center of the roll. Results demonstrated potential application to describe and investigate the roll wear effect in the HPGR performance.

### *3.3.4. Confinement system and edge effect*

One of the great challenges in the HPGR operation is to avoid, or at least to reduce, the edge effect during size reduction. As already found by LUBJUHN & SCHÖNERT (1993) and previously observed by several other authors (MORRELL *et al.*, 1997, DANIEL, 2002, CAMPOS *et al.*, 2019b, RODRIGUEZ *et al.*, 2021), the

material passes through the rolls in two different regions, being the center and the edge zones along the axial roll position. Indeed, a reduction in the applied pressure close to the edge region is possible to occur during grinding, which provides an ejection of part of the feed material by the edge of the roll.

The most common way to avoid this material ejection by the edge of the rolls is a confinement system proposed more than 75 years ago (TAGGART, 1945), which was named “cheek plates”. Figure 3.6 presents a bearing of the cheek plate used in an industry HPGR (a), with a highlight to the wear pattern in the same cheek plate (b).


Figure 3.6. Cheek plate used in an industrial-scale HPGR (a) and the highlighted wear pattern of the same cheek plate (b). Cheek plate at the end of lifetime presented was registered for an HPGR pressing fine iron ore concentrates.

The first cheek plates were widely used in double roll crushers and, more recently, have also been used to hold the material between the rolls in the HPGR. However, in analogy to roll surface, the cheek plates were also found to be a source of significant downtime due to high wear (DUNNE, 2006). As such, it is key to bear in mind that lifetime of the cheek plates has experienced a significant improvement owing to the use of materials such as tungsten carbide incorporated into it (WATSON & BROOKS, 1994), thus achieving a significant position in the HPGR operation in the last 25 years. Besides that, recent developments have been carried out in order to improve the lifetime of the cheek plates by using a new approach called the spring-loaded cheek plates (VAN DER ENDE *et al.*, 2019). According to VAN DER ENDE *et al.* (2019),

this new approach is able to hold the material between rolls in the presence of skewing (discussed in Section 3.3.5). As such, besides being important to reduce the extrusion of material along the edge of the roll, the spring-loaded cheek plates may also assist in prevent material slippage and thereby improving size reduction (VAN DER ENDE *et al.*, 2019).

Moreover, a new approach proposed as a confinement system for HPGRs is presented by the flanged rolls. The HRC (HERNAN *et al.*, 2013, SÖNMEZ *et al.*, 2015) from Metso® was the first design of the HPGR incorporating flanged rolls, which are bolted on the side of the roll, as shown in Figure 3.7.

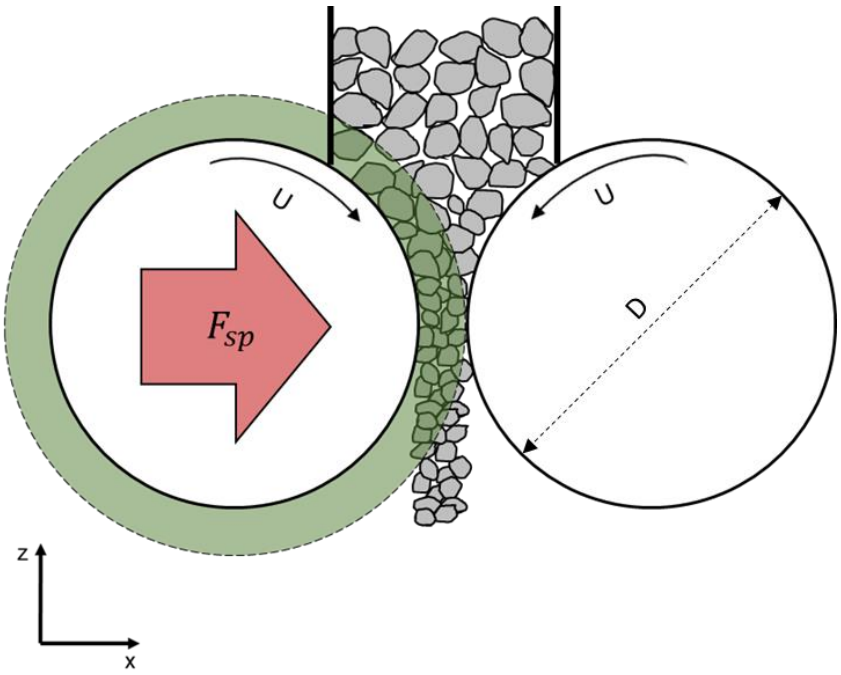


Figure 3.7. Schematic diagram of the HPGR (or HRC) highlighting the flanges (in green color) used to hold the material between rolls during grinding.

In contrast to the traditional cheek plates, the flanges move in the same direction and speed of the roll, thus pulling the material to the compression zone. Using preliminary results from DEM simulations, BUENO *et al.* (2017) showed that flanged rolls are able to reduce the feed material ejected by the edge of the rolls (BUENO *et al.*, 2017). More recently, RODRIGUEZ *et al.* (2021), with a more detailed study also using DEM simulations in compared with experimental tests in a pilot-scale HPGR, provided several insights about the improvement of the specific throughput and more uniform

pressure profile and breakage profile when using flanged rolls. Nevertheless, a more uniform pressure profile, thus coupled to a reduction in the pressure at the center region, was demonstrated by them to reach coarser product size distribution when compared to the traditional HPGR using cheek plates (RODRIGUEZ *et al.*, 2021).

### *3.3.5. Skewing*

Uniform pressure distribution along the axial roll position would be necessary to achieve optimal size reduction. However, several reasons in the HPGR operation that includes extrusion of material by the edge of the roll (edge effect) and uneven feed size or material hardness distribution, may be responsible for creating a non-uniform pressure distribution (KNAPP *et al.*, 2019). Therefore, skewing technology is reported as the ability of only one of the HPGR rolls to move in order to achieve the optimal pressure distribution along the axial roll position. Figure 3.8 presents a schematic diagram which highlights the effect of skewing in the HPGR operation.

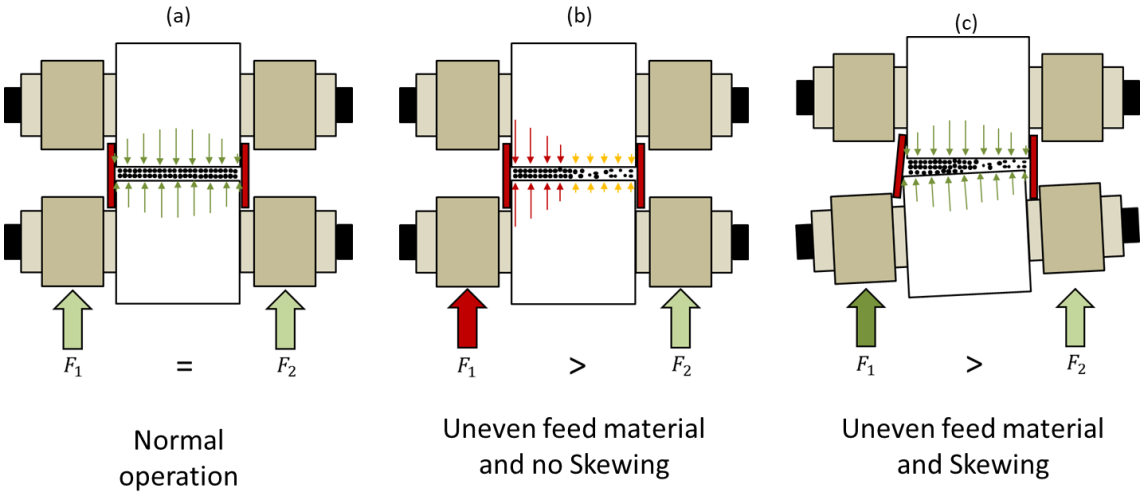


Figure 3.8. Schematic diagram of an HPGR presenting normal operation (a), an operation with uneven feed material and no skewing (b) and an operation with uneven feed material and skewing applied (c). (Adapted from VAN DER ENDE *et al.*, 2019)

KNAPP *et al.* (2019) showed that skewing results in some variation in the operating gap, besides being reasonably important to change the local peaks in the pressure profile. More recently, RODRIGUEZ *et al.* (2022b) using DEM simulations

investigated the skewing in the system when dealing with variation in particle size in the feed, throughput and material resistance to breakage. They showed that increasing uneven feed effect generates a non-uniform pressure profile, being the skewing strategy able to contribute generating a more uniform compression of the particle bed. BURCHARDT & MACKERT (2019) also pointed out potential future challenges for HPGR control when dealing with skewing and surface wear (Section 3.3.3) when describing the dynamics of the process.

### 3.4. HPGR operating parameters

The HPGR operation can be defined by different operating parameters. Usually, these parameters are associated to the operating conditions, material characteristics, machine settings and performance variables. Therefore, the main operating parameters can be summarized as: specific compressive force, roll velocity, operating gap, specific energy consumption, specific throughput, feed moisture, material extrusion and slippage, and nip angle. Figure 3.9 presents a schematic diagram of the HPGR illustrating some of its main operating parameters.

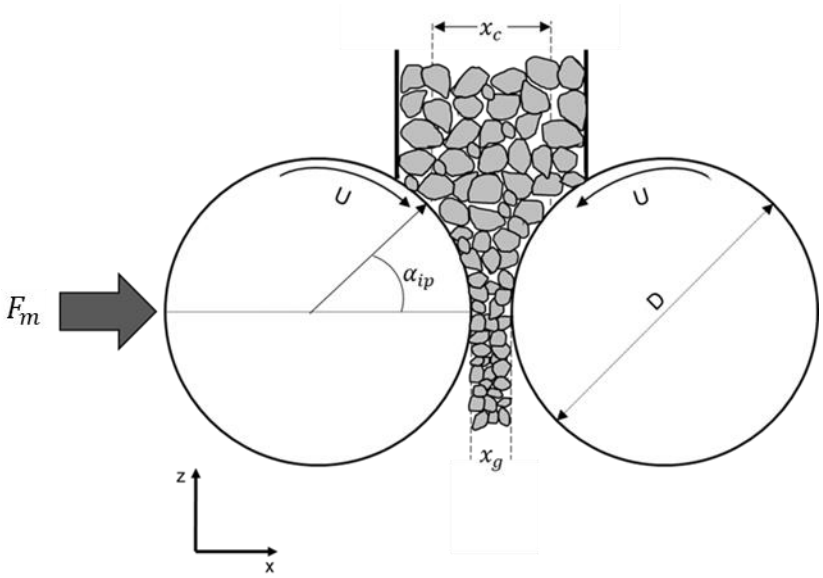


Figure 3.9. Schematic diagram of the HPGR highlighting the some of its main operating parameters. *D* is the roll diameter, *U* is the roll peripheral velocity, $F_m$ is the compressive force, $\chi_g$ is the operating gap, $\chi_c$ is the critical size and $\alpha_{ip}$ is the nip angle.

In addition, it is key to bear in mind that nowadays the HPGRs are widely used for several applications and in different scales of operation. Table 3.1, updated from KLYMOWSKY *et al.* (2002), summarizes the main common range of values observed for the HPGR operating parameters. The wider range of roll dimensions as well as throughputs and power consumptions demonstrate how the machine can be fitted for a wide range of applications in the minerals industry.

Table 3.1. Summary of the main design and operating parameters for HPGRs

| Parameter | Value |
|---|---|
| Roll diameter – $D$ (m) | 0.5 – 3.0 |
| Roll length – $L$ (m) | 0.2 – 2.0 |
| Operating gap – $\chi_g$ (mm) | 2 – 50 |
| Specific compressive force – $F_{sp}$ (N/mm$^2$) | 0.5 – 5.0 |
| Roll velocity – $U$ (m/s) | 0.2 – 3.0 |
| Throughput – $Q$ (t/h) | 50 – 5,400 |
| Power consumption – $P$ (kW) | 2 × 100 – 2 × 5,700 |
| Specific energy consumption - $E_{sp}$ (kWh/t) | 0.5 – 3.5 |

### *3.4.1. Specific compressive force*

TAGGART (1954) was one of the pioneers assessing the specific compressive force in conventional roll crusher. However, only after the middle of the 1980s, with the patent of the HPGR by Prof. Schönert that a more detailed analysis was carried out in order to properly understand this parameter in compressive crushing operation. Indeed, the specific compressive force is the main parameter that influences the product finesses in the HPGR (KLYMOWSKY *et al.*, 2006). SCHÖNERT (1988) defined the specific compressive force as the total hydraulic compressive force applied to the particle bed divided by the projected area of the roll as follows:

$$F_{sp} = \frac{F_m}{DL} \tag{3.1}$$

where $F_{sp}$ is the specific compressive force given, $F_m$ is the hydraulic compressive force and $D$ and $L$ are the roll diameter and the roll length, respectively.

Moreover, besides Schönert´s original work, other authors (LUBJUHN, 1992, MORRELL *et al.*, 1997, KLYMOWSKY *et al.*, 2006, VAN DER MEER & LEITE, 2018, CAMPOS *et al.*, 2019a) have also contributed to the understanding of the specific compressive force effect on the HPGR performance.

### *3.4.2. Roll velocity*

The rolls velocity during pressing is one of the most important machine settings that have a high impact on power consumption and throughput of the machine. LIM *et al.* (1997) showed for gold and diamond ores, while VAN DER MEER (2010) showed for iron ore concentrates and ZHANG *et al.* (2022) for cement clinker, that increments in roll velocity tends to increase the specific energy consumption besides providing a drop in the specific throughput. Recent work (CAMPOS *et al.*, 2019a) also showed a relative drop in the specific throughput for high roll velocities for pellet feed pressing. In addition, high roll velocities tend to increase the slippage and the extrusion of material by the roll side during the machine operation (SCHÖNERT & LUBJUHN, 1990).

On the other hand, some authors argue that the roll velocity does not contribute to the reduction ratio and even the finesses of the HPGR product, so that operating at higher velocities may lead to an increase in process inefficiency (MÜTZE & HUSSEMANN, 2007, DUNDAR *et al.*, 2011). Unlike discussed by LIM *et al.* (1997), for pressing iron ore concentrates operation with high roll velocities should be avoided in order to increase the BSA (ABAZARPOOR & HALAI, 2017). Indeed, VAN DER MEER & LEITE (2018) showed for multi-stage pressing process that low roll velocities are able to reach higher increments in the BSA of the iron ore concentrate. Moreover, CAMPOS *et al.* (2019a) showed an unaltered BSA profile along the axial roll position for different roll velocities, besides indicating a reasonably lower energy utilization for operations with high roll velocities. ZHANG *et al.* (2022), for cement clinker, also found no significant improvement in size reduction with an increment in roll velocity.

*3.4.3. Operating gap*

The operating gap, also called working gap, is commonly set as consolidated HPGR manipulated variable during grinding (KLYMOWSKY, 2003). This operating parameter often relies on a consequence of the hydro-pneumatic system parameters, pressure applied, besides the particle bed behavior (DANIEL, 2002, BARRIOS & TAVARES, 2016, JOHANSSOM & EVERTSSON, 2018). Several authors have dedicated time to improve understanding about the operating gap from the point of view of machine performance (CAMPOS *et al.*, 2019a, PAMPARANA *et al.*, 2022) to scale-up methodologies (SCHÖNERT, 1988, MORRELL *et al.*, 1997, DANIEL & MORRELL, 2004, CAMPOS *et al.*, 2020). In that regard, SCHÖNERT (1988) proposed the definition of a dimensionless operating gap, which is accepted worldwide as a scale-up variable, being described as:

$$\chi_{gsp} = \frac{\chi_g}{D} \tag{3.2}$$

where $\chi_{gsp}$ is the operating specific gap and $\chi_g$ is the operating gap.

Finally, is it key to bear in mind that the measured operating gap in an industrial-scale or even in pilot-scale and lab-scale machines is given by the distance between the top of the roll's studs, since they define the autogenous layer depth. LIM & WELLER (1999) proposed an equation that enables to calculate the real operating gap considering the penetration of the studs in the particle bed as follows:

$$\chi_g = \chi_{gstud} + 2(f')\chi_p \tag{3.3}$$

where $\chi_g$ is the operating gap, $\chi_{gstud}$ the distance between the rollers measured from the top of the studs, $\chi_p$ is the stud penetration in the particle bed and $f'$ is the fraction of the roll surface area corresponding to the autogenous layer.

*3.4.4. Specific energy consumption*

The specific energy consumption is defined as the ratio between the net power consumption ($P$) and the throughput ($Q$) (Eq. (3.4)). This variable has an almost linear relationship with the specific compressive force as already discussed by other authors (FUERSTENAU & ABOUZEID, 1998, LIM *et al.*, 1997, MORRELL *et al.*, 1997, KLYMOWSKY *et al.*, 2006, DUNDAR *et al.*, 2011, CAMPOS *et al.*, 2019a).

$$E_{sp} = \frac{P}{Q} \tag{3.4}$$

Figure 3.10 shows the variation of the specific energy consumption with the increment of specific compressive force in a pilot-scale HPGR pressing iron ore pellet feed (CAMPOS *et al.*, 2019a).

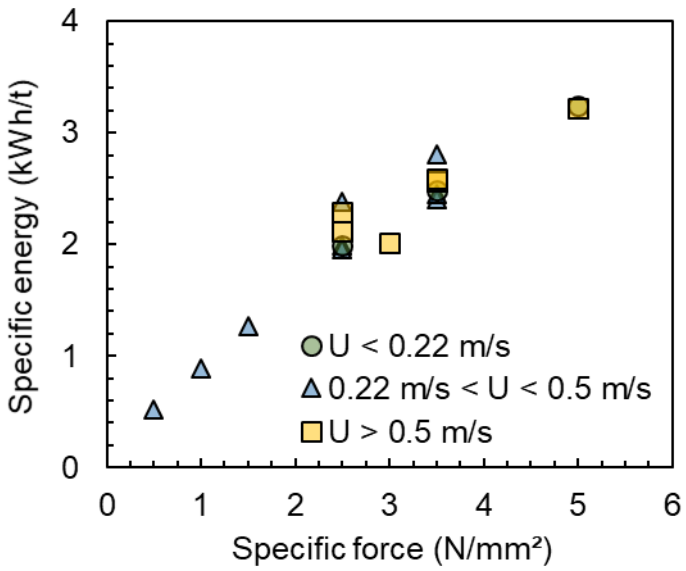


Figure 3.10. Variation of the specific energy consumption with the increment in the specific force in a pilot-scale HPGR pressing iron ore pellet feed. Results are discriminated by roll velocity (CAMPOS *et al.*, 2019a).

Moreover, a lesser-known term for HPGR operation, called volumetric specific power draw (KLYMOWSKY *et al.*, 2006), was also proposed as follows:

$$P_{sp} = \frac{P}{DLU} \tag{3.5}$$

where $P_{sp}$ is the specific power draw and $U$ is the roll velocity. According to KLYMOWSKY *et al.* (2006), Eq. (3.5) can be used in scale-up procedures in order to estimate the power requirement of a larger-scale machines on the basis of lab-scale HPGR data.

### *3.4.5. Specific throughput*

The specific throughput is one of the most important scale-up variables of the HPGR and has been used widely for sizing the machine capacity in larger scales. Schönert (SCHÖNERT, 1988) previously discussed the first concept of the volumetric capacity and specific throughput. Nevertheless, in the years that followed Schönert's pioneer work, some authors (SCHÖNERT & LUBJUHN, 1990, LUBJUHN & SCHÖNERT, 1992, AUSTIN *et al.*, 1993, LIM *et al.*, 1997, MORRELL *et al.*, 1997, KLYMOWSKY *et al.*, 2002) were responsible for important advances in knowledge related to this variable.

AUSTIN *et al.* (1993) proposed a relationship to calculate the specific throughput as follows:

$$\dot{m} = \frac{Q}{DLU\rho_g} \tag{3.6}$$

where $\rho_g$ is the flake density. On the other hand, KLYMOWSKY *et al.* (2002) proposed the same approach with a minor modification (Eq. (3.7)) and considering that the specific throughput will be affected mainly by the physical properties of the material, type of roll surface and grinding pressure. However, some authors (VAN DER MEER & LEITE, 2018, CAMPOS *et al.*, 2019a) have observed for pressing iron ore concentrates that the roll velocity is also able to change the specific throughput. This approach defines the specific throughput as the throughput of an HPGR with a roll

diameter and roll length of 1 m and a roll velocity of 1 m/s (KLYMOWSKY *et al.*, 2002).

$$\dot{m} = \frac{Q}{DLU} \tag{3.7}$$

*3.4.6. Feed moisture content*

The moisture content is one of the most critical operating variables, although little controlled in HPGR operation. KAPUR *et al.* (1990) and FUERSTENAU & ABOUZEID (1998) were the pioneers assessing the variations in the HPGR performance due to change in the feed moisture. The feed moisture is able to reduce the operating gap and increase the specific energy (FUERSTENAU & ABOUZEID, 1998, SARAMAK & KLEIV, 2013, VAN DER MEER & LEITE, 2018, CAMPOS *et al.*, 2019a), besides reducing the specific throughput (VAN DER MEER & LEITE, 2018, CAMPOS *et al.*, 2019a).

Recent works (SARAMAK & KLEIV, 2013) showed, for pressing olivine sand, an optimal value of the feed moisture content around 4% to increase the reduction ratio. On the other hand, for pressing iron ore concentrates, some authors (VAN DER MEER & LEITE, 2018, THOMAZINI *et al.*, 2020) showed that at moisture contents above 8% the Blaine specific surface area of the product was lower than the value reached with moisture content below that target. MÜTZE (2015) also commented that pressing moist feeds could cause energy losses by material ejection by the edge of the rolls. CAMPOS *et al.* (2019a) presented some results assessing the size reduction characteristics of an iron ore concentrate with different feed moisture content in a pilot-scale HPGR, which demonstrated a higher amenability for breakage using a feed moisture content around 7.5% when compared to a moisture content of 1.5%. Further results presented by them were able to conclude that a feed moisture content of 7.5% was able to ensure a homogeneous pressure profile along the roll length and a lower edge effect (CAMPOS *et al.*, 2019a). Figure 3.11 presents some these results to illustrate this outstanding difference in the axial roll profile (CAMPOS *et al.*, 2019a).

Nevertheless, even though recent advances seem to show the right way to improve understand this, it is worth mentioning that this variable is still poorly understood in the HPGR operation as all.

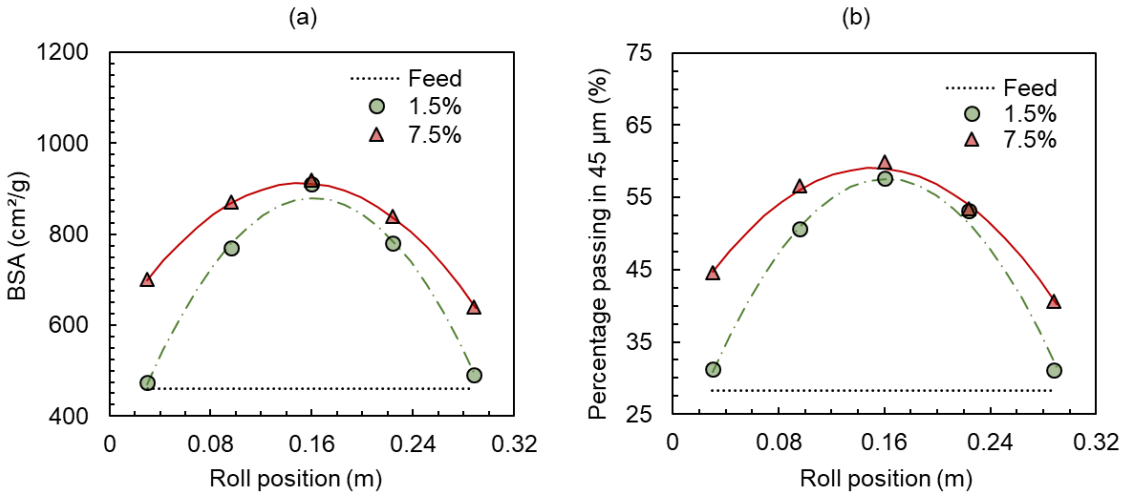


Figure 3.11. Comparison between the Blaine specific surface area (a) and percentage passing 0.045 mm (b) profiles along the roll for tests at 1.5% moisture and 7.5% moisture from tests conducted at 2.5 N/mm² and 0.2 m/s (CAMPOS *et al.*, 2019a).

### *3.4.7. Material ejection and slippage*

As discussed previously in the text (Section 3.4.5), the HPGR throughput is mainly affected by the operating conditions, roll dimensions and material properties. In addition to that, some well-known features of the HPGR operation as the proportion of material ejected by the edge of the rolls and the material slippage and acceleration in the compression zone, although not always considered, are key to understand and determine the equipment throughput. These phenomena have been observed widely for different operations (LIM *et al.*, 1997, LIM & WELLER, 1998, SCHÖNERT & SANDER, 2001, CAMPOS *et al.*, 2019b, VAN DER ENDE *et al.*, 2019, ROCHA *et al.*, 2022a), although the way on how the operating variables will affect them is still poorly understood. Nowadays, a common way to avoid the material ejection by the edge of the rolls is using different confinement systems and edge protections (Section 3.3.4) in order to hold the material between the rolls. Figure 3.12 illustrates a schematic diagram

of the HPGR showing the region where the feed material is ejected along the sides of the rolls during size reduction (CAMPOS *et al.*, 2019b).

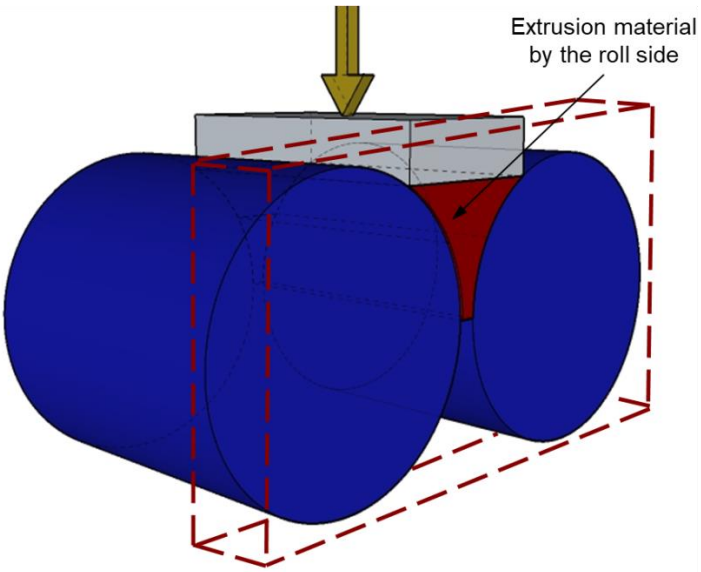


Figure 3.12. Schematic diagram of the HPGR showing the region where the feed material is ejected along the edges of the rolls during grinding (CAMPOS *et al.*, 2019b).

LIM *et al.* (1997) estimated that an industrial-scale operation could achieve around 30% of feed material ejected by the edge of the rolls, thus reducing the fineness of the final product (coarser product size distribution). They found that the high specific compressive forces and high roll velocities are able to improve the percentage of material ejected, beyond using this evidence to propose a relationship as:

$$\chi' = \dot{m}\left(\frac{D}{\chi_g}\right) = \left(\frac{U_g}{U}\right)\left(\frac{\rho_g}{\rho_{sp}}\right) \tag{3.8}$$

where $\chi'$ is the apparent relative bulk density, $\dot{m}$ is the specific throughput (Eq. (3.6)), $U_g$ is the material velocity and $\rho_{sp}$ is the specific gravity. According to them, value of $\chi'$ above one indicates the presence of an extrusion effect, besides indicating a relatively higher material velocity than the roll velocity. Assessing an extended database of bauxite ore, gold ore and diamond ore, they showed that specific compressive forces

higher than 3 N/mm² are responsible to increase the extent of this extrusion and acceleration of the material in the compression zone (LIM *et al.*, 1997).

VAN DER ENDE *et al.* (2019) showed from experimental results using different materials (including a fine iron ore concentrate) in a pilot-scale HPGR that the percentage of material ejected by the edge of the rolls reaches values around 60% of the feed material in the case of absence of confinement system. On the other hand, they found values of material ejection close to 20% for all materials when the HPGR operation was carried out with the cheek plates positioned as close as possible to the rolls. For the pressing fine iron ore concentrate, which is the object of the case study in the present work, they found a proportion of the feed material ejected of 23.2% using as specific compressive for of 4.2 N/mm², a roll velocity of 0.41 m/s and an operating gap of 12 mm. Also, for pressing fine iron ore concentrates (CAMPOS *et al*., 2019b) showed, using an empirical relationship, that the feed material ejected by the edge of the roll varies from 15 to 35%, which is lined up with results found elsewhere (LIM *et al.*, 1997, VAN DER ENDE *et al.*, 2019). More recently, RODRIGUEZ *et al.* (2022a) presented a more detailed investigation of a pilot-scale HPGR operation using DEM simulations providing some insights about the mechanisms that control this phenomenon. Results found by them were also close to the ones discussed in this Section.

### *3.4.8. Nip angle*

The nip angle is an HPGR parameter required to determine the real specific pressure force applied and even to determine the region between rollers responsible for the inter particle breakage behavior. The main relationship proposed in order to describe this operating parameter ($\alpha_{ip}$) was first formulated by AUSTIN *et al.* (1993), being given by:

$$\cos\alpha_{ip} = \frac{1}{2D}\left[\left(\chi_g + D\right) + \sqrt{\left(\chi_g + D\right)^2 - \frac{4\chi_g\rho_g D}{\rho_a}}\right] \tag{3.9}$$

where $\rho_a$ is the bulk density.

DANIEL (2002) and KELLERWESSEL (1996) reported that the nip angle is often in the range from 7º to 14º and may be affected by several operating parameters. SARAMAK & NAZIEMIEC (2013) showed that the chamber volume as well as the roll dimensions are some of the main input variables able to change the nip angle. On the other hand, CAMPOS *et al.* (2019b) also suggested that the feeder silo dimensions, feed size distributions and even the rheological properties of the material may be responsible for changes in the nip angle, although these parameters do not explicitly appear in Eq. (3.9) (CAMPOS *et al.*, 2019b).

### *3.4.9. Process control and operational strategies*

Usually, the control strategies for comminution operations aim to ensure reduction ratio during breakage, energy efficiency and solids production as high as possible. For HPGRs, JONES (2012) reviewed different control strategies adopted in industry stating independent speed regulators and torque regulation as the two main approaches used. The main point about torque regulation is to ensure that HPGRs will be working closer to the maximum allowed torque, thus being able to provide the finest possible product size distribution. In general, hydraulic pressure is the main manipulated variable used to achieve the required target for size reduction (Section 3.4.1), whereas roll peripheral velocity is more related to keep or improve the machine throughput (Sections 3.4.2 and 3.4.5). For some particular operations the operating gap can be also used as the main manipulated variable, being the operating pressure defined according to the target set for the gap and some feed characteristics.

GARDULA *et al*. (2015) processing gold ore reported several key challenges when dealing with uneven feed material and requirement of skewing (Section 3.3.5), beyond correlating it to roll surface wear (Section 3.3.3). According to them, limitation in torque regulation were presented given the excessive skew after 8,000 hours of operation when the HPGR achieved important roll surface wear patterns. Despite the challenges presented above, recent works using DEM simulations started providing some evidence on how the operation can deal with these types of variabilities for pressing fine iron ore concentrates (RODRIGUEZ *et al.*, 2021, RODRIGUEZ *et al.*, 2022b).

More recently, ARAÚJO *et al*. (2019) also reported an implementation for working gap auto control for a HPGR processing iron ore concentrates. Their system allows to control the hydro-pneumatic system stiffness in order to ensure good responses to variations in the feed moisture content. Results by them also showed feasibility applying the approach with good industrial survey information.

For the particular case of HPGRs operating for pressing iron ore concentrates in some pelletizing plants from Vale S.A. (Brazil), the machine is controlled by an Optimizing Control System (OCS) that relies on fuzzy logic to optimize the process (OCS PLANT 3, 2019). The system usually has the torque and operating gap as two main control variables, whereas pressure is the main manipulated variable. The aim in the fuzzy logic is to define a setpoint of pressure to maximize the torque and to keep it in given operational range, which is supposed to provide a high reduction ratio during breakage. Basically, the OCS will increase the setpoint of pressure when torque is below the bottom limit in the operational range and the operating gap is above the upper limit. On the other hand, when the torque is above the upper limit and the operating gap below the bottom limit according to their operational ranges, the setpoint of pressure will decrease (OCS PLANT 3, 2019). Other process variables as electric current, hopper level, roll velocity and temperature in the bearing system would work establishing the OCS limits (OCS PLANT 3, 2019). Information presented up to this point allows to conclude that HPGRs pressing iron ore concentrates are controlled solely based on torque variabilities, which is probably limited to changes in the operational strategy when dealing with important variabilities in the feed size distribution and/or material hardness. Potentially, operating under these set of conditions that are current used in the OCS, the machine would not be operating under optimal performance.

Beyond the main strategies and works discussed in this Section, model predictive control algorithms (MPC) applied to HPGRs, which are also important, are better discussed in Section 3.6.6.

## 3.5. Size reduction characteristics

Research carried out by Prof. Klaus Schönert and his team from the 1960s onwards was critical for improving the understanding about particle breakage behavior under different conditions and applied stresses. The mechanism of the interparticle

breakage behavior studied by them, which resulted in a breakthrough about this subject and thus leading to the patent of the “high-pressure interparticle comminution process”, was very important to validate the application of the HPGR in comminution circuits.

### *3.5.1. Interparticle breakage behavior*

Comminution in the roller press is a result of a high stress intensity in a confined particle bed between two counter rotating rolls. When the particle bed is compressed under these conditions, each particle is responsible to convey the stress intensity and the energy between its neighborhoods, thus improving the breakage response. Tavares (2005) pointed out that these factors are responsible for the large proportion of fines in comparison to conventional crushing systems. As such, in the last 40 years the breakage response of particle bed under confined conditions, also named interparticle breakage behavior, was extensively investigated by different authors (SCHÖNERT, 1979, SCHÖNERT & FLÜGEL, 1980, SCHÖNERT, 1990, FUERSTENAU *et al.*, 1996, SCHÖNERT, 1996, LIU & SCHÖNERT, 1996, BARRIOS *et al.*, 2011, MÜTZE, 2015).

SCHÖNERT & FLÜGEL (1980) published one of the first works assessing the interparticle breakage behavior under confined conditions in order to evaluate the differences between single particle breakage and a particle bed breakage behavior. In the years that followed some other works were responsible to contribute significantly to the understanding of particle bed behavior, thus presenting the classification of the type of stress application (SCHÖNERT, 1988) and even assessing the breakage response of fine particles (SCHÖNERT, 1990). Afterwards, SCHÖNERT (1996) made an important contribution highlighting the influence of the particle rearrangement in the breakage response. Moreover, based on this, SCHÖNERT (1996) pointed out that an ideal cylindrical particle bed should take into account several relationships between bed diameter, bed height and particle size distribution in order to ensure the absence of the wall effect in size reduction. These particle bed characteristics were later adopted by several authors using a piston-and-die apparatus (DANIEL, 2002, BARRIOS *et al.*, 2011) and DEM simulations (ANDRÉ, 2019, BARRIOS *et al.*, 2020, RODRIGUEZ *et al.*, 2022a), although some other authors have tried to use a different approach on this (DAVAANYAM, 2015, PAMPARANA *et al.*, 2022). Figure 3.13 presents the main

particle bed configurations presented by Schönert according to the particle bed shape and the size distribution used (SCHÖNERT, 1996).

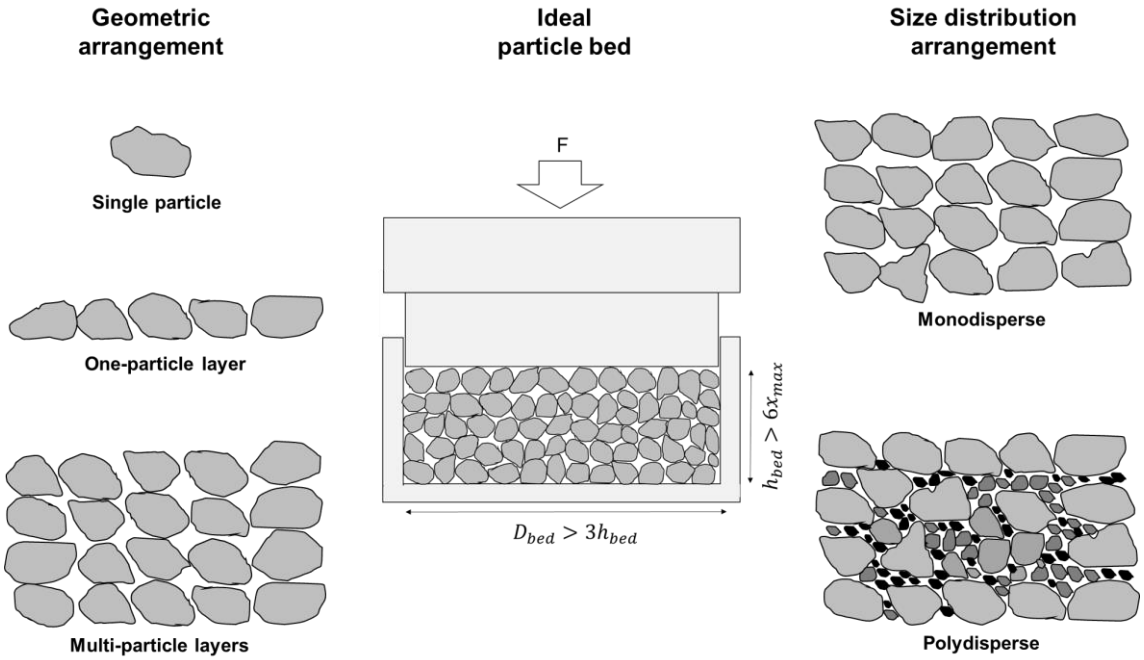


Figure 3.13. Classification of the different types of particle arrangements according to geometric shape and size distribution. Piston-and-die apparatus at the center of the figure highlights the ideal particle bed suggested by SCHÖNERT (1996). $D_{bed}$ is the bed diameter, $h_{bed}$ is the bed height and $x_{max}$ is the maximum particle size.

Taking into account the outstanding contributions from Shönert's works, some mathematical models (MORRELL *et al.*, 1997, DUNDAR *et al.*, 2013) that describe size reduction in the HPGR started to use the piston-and-die apparatus from the ideal particle bed (Figure 3.13) to calibrate the parameters describing breakage response. Although these models are currently available in commercial software's and have been widely used for industrial-scale operations, some works have showed a great limitation of these models in correlating the information provided from the bench-scale test to predict the HPGR size reduction in industrial-scale (DANIEL & MORRELL, 2004, YAHYAEI *et al.*, 2020).

Furthermore, some other authors have made important contributions to the understanding of the particle bed breakage behavior (FUERSTENAU *et al.*, 1996,

KALALA *et al.*, 2011, BARRIOS *et al.*, 2011) and even modeling the breakage response under confined conditions (LIU & SCHÖNERT, 1996, MÜTZE, 2015).

### *3.5.2. Particle bed breakage saturation effect*

As already reported by other authors (SCHUBERT, 1967, RUMPF, 1973, TAVARES, 1999) the particle breakage behavior as well as the mechanical properties of each material are extremely important to elucidate the energy utilization in the comminution process, besides being used for assessing the material deformation response under applied stress (SCHÖNERT, 1990).

For particle bed breakage behavior, the piston-and-die apparatus has provided important insights about the confined bed breakage (SCHÖNERT, 1996, KALALA *et al.*, 2011) besides being used to fit the main breakage model parameters that describe the HPGR performance (HAWKINS, 2007). Through these tests it is possible to analyse how the energy is dissipated in a particle bed and used to break the particles. Figure 3.14 shows how the spent energy is dissipated according to the force-deformation profile in a particle bed.

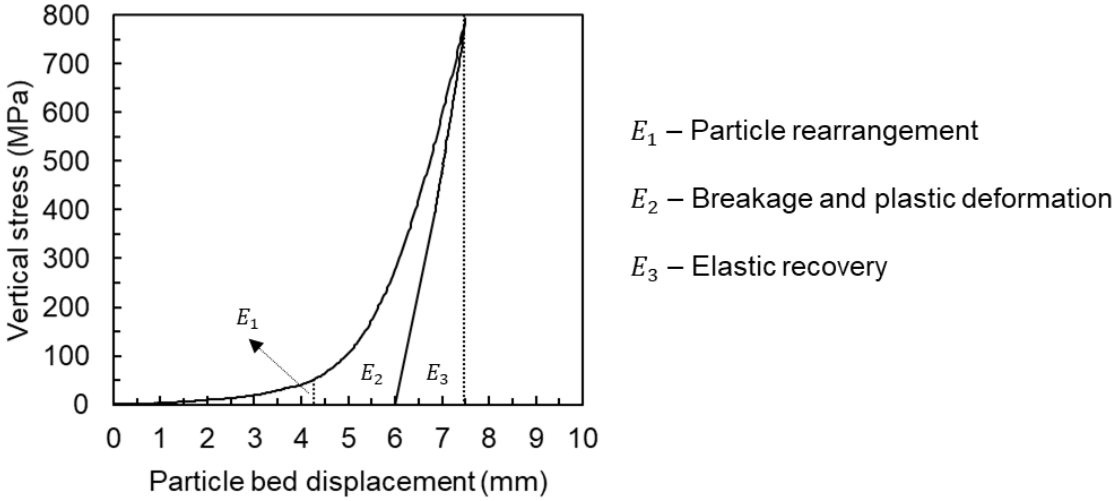


Figure 3.14. Schematic stress-deformation curve in a piston-and-die test showing the different mechanisms responsible for storing energy during the pressing process.

Indeed, great attention has been dedicated to the several microprocesses involved in this breakage response as presented in Figure 3.14, which includes friction

losses, plastic deformation work, elastic recovery, energy dissipated during breakage and compaction (SCHUBERT, 1967, MÜTZE, 2015). Briefly, all microprocesses through which the input energy can be dissipated are summarized in three mainly effects: breakage energy, elastic energy and plastic energy (Figure 3.14).

LIU & SCHÖNERT (1996) showed from piston-and-die tests that the energy dissipated in breakage in a particle bed depends on the particle size and the amount of energy spent. The results presented by them showed that a part of spent energy is not dissipated for breakage. Indeed, energy loss due to irreversible structural changes in particles must be related to the plastic deformation work existent in the compaction behavior. Afterwards, several other authors (MÜTZE & HUSSEMANN, 2007, KALALA *et al.*, 2011, DUNDAR *et al.*, 2013, DAVAANYAM, 2015, MÜTZE, 2015, MÜTZE, 2016, BENZER *et al.*, 2017) have dedicated great attention to understanding how the spent energy is dissipated on the particle bed.

Using force-displacement curves and size reduction results from piston-and-die tests, MÜTZE (2016) showed that the energy dissipated in breakage strongly depends on the compaction behavior of the particle bed. Based in previous works carried out by him and co-workers (MÜTZE & HUSSEMANN, 2007, MÜTZE, 2015), a model was proposed to take into account the mechanisms that describe, beyond the breakage energy, the energy stored in the elastic and plastic deformation behaviors. Assessing the breakage behavior for iron ores using 12 mm particles, KALALA *et al.* (2011) showed that around 40% of the spent energy could be transformed in elastic recovery in a piston-and-die test with compressive force of 1700 kN. These results demonstrate the need to ensure that the compaction behavior must be better described in the particle bed breakage operation.

Studies have been dedicated to understand the compaction behavior of particulate materials under confined conditions. Such compaction occurs during processes that include metal powder smelting, as well as tableting and pelletizing in the pharmaceutical, ceramic and food industries. In general, compaction has been studied and modelled for inorganic powders (TRAIN, 1956), metal powders (HECKEL, 1961), ceramic powders (COOPER & EATON, 1962), fine grinding processes (MÜTZE, 2015, WÜNSCH *et al.*, 2019, CABISCOL *et al.*, 2020) and organic powders in the manufacture of the pharmaceutical tablets (KAWAKITA & LÜDDE, 1971, ARMSTRONG & HAINES-NUTT , 1974, VACHON & CHULIA, 1999, PATEL *et al.*,

2007). The particle-bed compaction behavior can be influenced by different parameters, such as the deformation or stress-strain behavior (TYE *et al.*, 2005, DAVID & AUGSBUERGER, 1977) and particle size and shape (PODCZECK & SHARMA, 1996, PATEL *et al.*, 2007). On the other hand, recent works have attempted to assess the particle bed behavior under confined conditions from computational simulations using the discrete element method (GARNER *et al.*, 2018, ZHOU *et al.*, 2020). The complexity of this process is the main reason for the poor predictability and the limited understanding yet available for this feature in particle bed breakage.

### *3.5.3. Particle weakening in confined particle bed*

As discussed in this Section, several authors tried to understand the interparticle breakage mechanism and the well-known feature of breakage saturation effect. As decoupled by some of them (LIU & SCHÖNERT, 1996, DUNDAR *et al.*, 2013), there is a significant proportion of coarser material that remains in the original size class after compression. They showed that beyond a certain level of specific energy or vertical stress applied to the particle bed, the proportion of material broken becomes nearly constant. TAVARES (2005) observed that, whereas little or no additional breakage occurred at these higher energy inputs in HPGR experiments, particles may become progressively weaker. A recent work (AMINALROAYA & POURGHAHRAMANI, 2022) presented very similar conclusions to the ones discussed elsewhere (TAVARES, 2005), but now accounting for binary mixtures in a lab-scale HPGR. Analyzing cement clinker, ZHANG *et al.* (2022) also demonstrated a very significant effect on the particle specific fracture energy before and after passing through a lab-scale HPGR.

## 3.6. Modeling overview

Defining the optimal operating conditions as well as the best circuit configuration in the HPGR operation requires a detailed study about the HPGR performance under different conditions. Given the unfeasibility of applying this analysis in practice, the HPGR mathematical modeling coupled to process simulation have demonstrated to be an excellent alternative in order to assess the equipment performance.

Mathematical models of the HPGR have evolved in parallel to the development and application of the technology (RASHIDI *et al.*, 2017). These models were primarily proposed to estimate throughput, power consumption, product size distribution and even to describe some scale-up factors for sizing the HPGR (Section 3.6). The models correlate operating conditions, material characteristics and machine settings to predict the machine performance as presented in Figure 3.15 (CAMPOS *et al.*, 2019b).

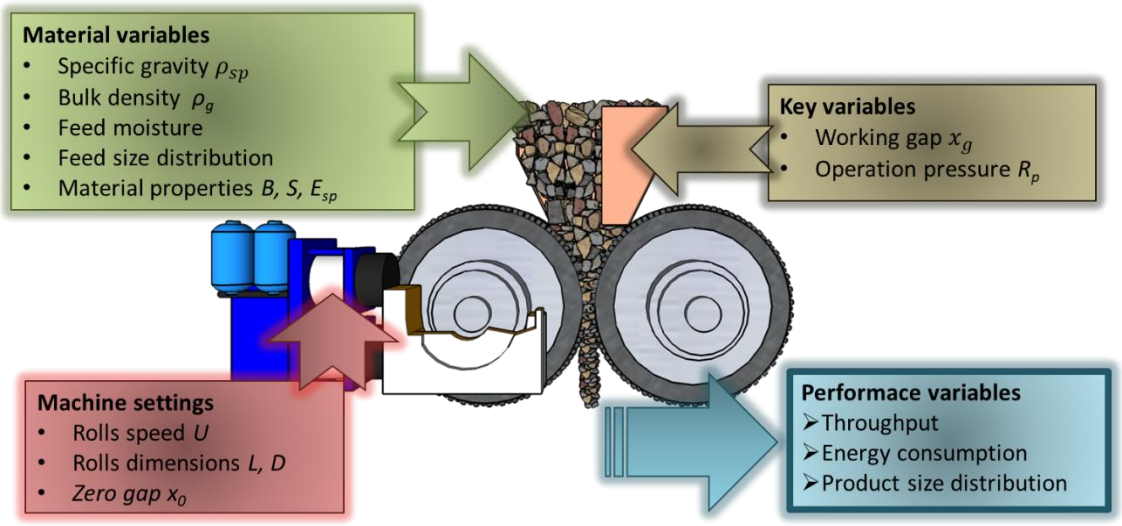


Figure 3.15. Interrelationships between material variables, machine settings and key parameters in HPGR performance models (CAMPOS *et al.*, 2019b).

Indeed, since its introduction in the minerals industry, mathematical modeling of the HPGR has experienced an appreciable learning curve with the improvement in the understanding of the phenomenology that is involved in its operation. SCHÖNERT (1988) was the pioneer proposing mathematical relationships to calculate the throughput and power consumption of the HPGR. Since him, some authors (FUERSTENAU *et al.*, 1991, AUSTIN *et al.*, 1993, 1995, LIM & WELLER, 1999, MORRELL *et al.*, 1997, LIU & SCHÖNERT, 1996, TORRES AND CASALI, 2009, SCHNEIDER *et al.*, 2009, DUNDAR *et al.*, 2013, VYHMEISTER *et al.*, 2019, CAMPOS *et al.*, 2019b, RODRIGUEZ *et al.*, 2022a, RODRIGUEZ *et al.*, 2023, THIVIERGE *et al.*, 2022, PAMPARANA *et al.*, 2022) have investigated the HPGR operation from the point of view of mathematical modeling and simulation. Some of these models reached

popularity in the minerals industry and are currently available in commercial software (MORRELL *et al.,* 1997, DUNDAR *et al.,* 2013), some have been applied in industrial-scale operations (AUSTIN, 1993, 1995, MORRELL *et al.,* 1997, TORRES & CASALI, 2009, DUNDAR *et al.,* 2013, CAMPOS *et al.,* 2019b) whereas others in a model predictive control (NUMBI & XIA, 2015, VYHMEISTER *et al.,* 2019, JOHANSSOM & EVERTSSON, 2019). Since these models were developed on the basis of different sub models (throughput, power consumption and particle breakage equations), it is worth mentioning the possibility of building new models based on specific pieces of selected equations available in literature, which was recently done elsewhere (THIVIERGE *et al.,* 2022).

### *3.6.1. Throughput model*

All models used to predict throughput rely on the equations proposed originally by Schönert (SCHÖNERT, 1988) correlating roll dimension, operating gap, particle bed porosity, roll velocity and nip angle. Eq. (3.10) presents the relationship proposed by him in order to calculate the HPGR throughput (SCHÖNERT, 1985, SCHÖNERT & LUBJUHN, 1990):

$$Q = k_g DLU \tag{3.10}$$

where $k_g$ is the amenability of the particle bed for compaction given by:

$$k_g = \rho_g \left(\frac{x_g}{D}\right) \tag{3.11}$$

Following the initial study carried out by Schönert, other authors (AUSTIN *et al.,* 1993, AUSTIN & TRUBELJA, 1994) also made important contributions to improving the description of the HPGR throughput. AUSTIN *et al.* (1993, 1995) proposed a phenomenological mathematical model that is able to predict throughput from:

$$Q = \dot{m}\rho_g ULD \tag{3.12}$$

where $\dot{m}$ is defined as the specific throughput and calculated from:

$$\dot{m} = \frac{\left(1 - \cos\alpha_{ip}\right)}{\left(\frac{1}{\left(1-\theta_c \cos\alpha_{ip}\right)} - \frac{1}{\left(1-\theta_g\right)}\right)} \tag{3.13}$$

where $\theta_c$ e $\theta_g$ are initial particle bed porosity and the final particle bed porosity, respectively, and $\alpha_{ip}$ the calculated nip angle (AUSTIN *et al.*, 1993, 1995).

AUSTIN *et al.* (1995) relied on a detailed experimental campaign using a lab-scale HPGR to assess the phenomena behind the HPGR performance, especially the throughput. Among the extended database provided by them, the significant influence of the material grindability and grinding pressure in the specific throughput (Eq. (3.6)) can be summarized as the main important results (Figure 3.16).

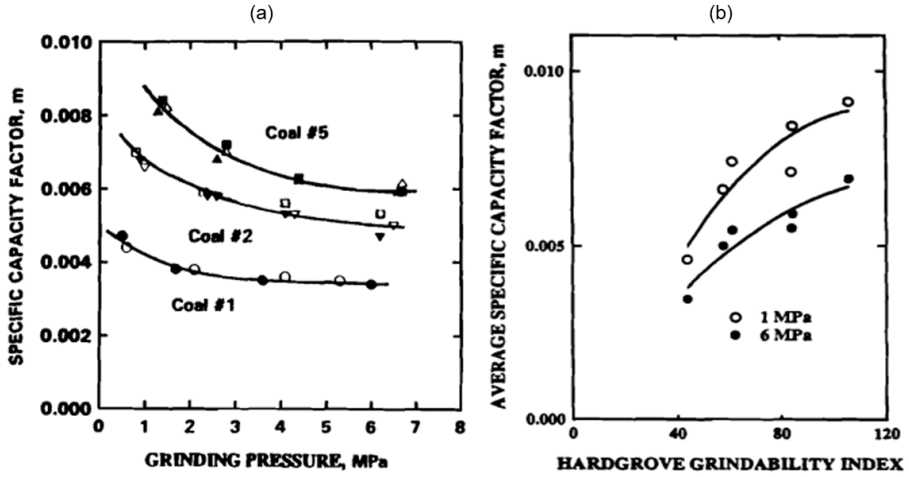


Figure 3.16. Variation of the specific throughput with the grinding pressure (a) and with the Hardgrove grindability index (b) (AUSTIN *et al.*, 1995).

AUSTIN *et al*. (1995) also proposed an empirical equation able to describe the relationship between the specific compressive force and the particle bed porosity:

$$\left(1-\theta_g\right)-\left(1-\theta_c\right)=k_a{F_{sp}}^{b_A} \tag{3.14}$$

where $k_a$ and $b_A$ are model parameters and $F_{sp}$ is the specific compressive force (Eq. (3.1)). Moreover, these results from Figure 3.16 can also indicate a reasonable dependence of the throughput with the particle bed compaction behavior and thus the particle bed porosity.

More recently, based on the advances achieved by SCHÖNERT (1988) and AUSTIN *et al.* (1993, 1995), DANIEL & MORRELL (2004) proposed that the piston flow model may describe the capacity of the HPGR. These authors also take into account several advances about the HPGR performance under different conditions analyzed and presented in detail by other authors (MORRELL *et al.*, 1997), thereby proposing the HPGR throughput as:

$$Q=\rho_g\chi_g UL \tag{3.15}$$

DANIEL & MORRELL (2004) suggested a fitting parameter multiplying the result from Eq. (3.15) in order to increase the throughput and account for the material ejection and slippage when the HPGR is operating with high roll velocities ($U$ > 3 m/s). The relationship presented in Eq. (3.15) is accepted worldwide both by both roller press manufacturers and researchers for predicting the HPGR performance and even used for sizing large-scale equipment. As such, mathematical models developed in the last years have relied on this relationship to predict the HPGR throughput (TORRES & CASALI, 2009).

CAMPOS *et al.* (2019b), using the Torres and Casali model approach, showed that the piston flow model underestimate the HPGR throughput for pressing iron ores concentrates in a pilot-scale HPGR for a wider range of operating conditions (CAMPOS *et al.*, 2019b). The authors recognized the underestimation of the working gap measured from the top of the studs in operation, then using Eq. (3.3) to account for the stud penetration in the particle bed (LIM & WELLER, 1999). Also, it is recognized that the Torres and Casali model does not account for several important effects, including the acceleration of the material in the compression zone and the feed material ejected by the

edged of rolls, both effects already discussed in Section 3.4.7. As such, CAMPOS *et al.* (2019b), in order to predict the percentage of material ejected by the edge of the rolls, proposed Eq. (3.16) as follow, being the relationship predicted by the equation illustrated in Figure 3.17 for a pilot-scale HPGR (CAMPOS *et al*., 2019b):

$$\ln\frac{\delta}{\varphi} = -\upsilon\frac{\chi_g}{D}\left(\frac{U}{U_{max}}\right)^{\tau} \tag{3.16}$$

where $\delta$ is the percentage of material ejected by the roll side, $U_{max}$ is the maximum roll velocity in operation for the HPGR and φ, υ and $\tau$ are fitting parameters.

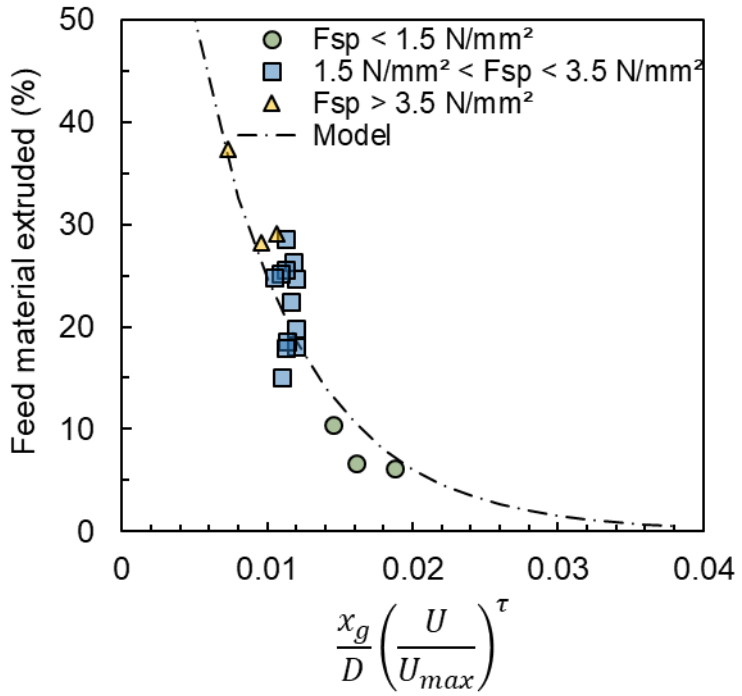


Figure 3.17. Relationship between the product of the dimensionless gap and the dimensionless rolls speed raised to parameter $\tau$ and the proportion of material ejected from the edge of the rolls. Experiments identified by their specific compressive forces (CAMPOS *et al.*, 2019b).

Figure 3.17 presents the percentage of material ejected by the edge of rolls according to the specific operating gap multiplied by the ratio between the roll velocity

and the maximum roll velocity in operation for each HPGR and raised to the parameter $\tau$ (CAMPOS *et al.*, 2019b). Parameters calibrated on the basis of data presented in Figure 3.17 were given by φ equal to 100, υ equal to 140, $\tau$ equal to 0.1. Parameter $f'$ from Eq. (3.3) was measured and given as 0.65. This approach considers the fact that high compressive forces are able to increase the feed material ejected by the edge of the rolls due to the reduction of the operating gap. Besides that, the model is also able to capture the effect of high roll velocities in operation and how this operating variable affects the extrusion effect.

CAMPOS *et al.* (2019b) also validated this modification in a wide operating range and in a pilot-scale HPGR for pressing iron ore pellet feed in a pre-grinding process. Moreover, CAMPOS (2018) proposed a relationship in order to calculate the material velocity in the compression zone. The relationship was based on the mass balance of a lamination process (DIETER & BACON, 1984) and is presented as follows with a minor modification:

$$U_g = \frac{U \chi_c \rho_a}{\chi_g \rho_g} \tag{3.17}$$

where $U_g$ is the material velocity and $\chi_c$ is the critical size given by (TORRES & CASALI, 2009):

$$\chi_c = \chi_g + D\left(1 - \cos \alpha_{ip}\right) \tag{3.18}$$

where $\alpha_{ip}$ is the nip angle given by Eq. (3.9). This modification was also validated in a wide range of operating conditions and for different HPGRs in industrial scale, demonstrating the reasonable model agreement with measured values and even showed the availability of the model for these applications (CAMPOS, 2018). The new way to calculate the HPGR throughput proposed is then presented as follow as:

$$Q = U_g L \rho_g x_g \left(\frac{100}{100 - \delta}\right) \tag{3.19}$$

Recent works revisited some of those previous modeling approaches discussed above to propose minor modifications and calibrations aiming to improve their predictions (THIVIERGE *et al.*, 2022), whereas other authors proposed new methods based on piston-and-die tests to estimate the HPGR throughput (PAMPARANA *et al.*, 2022).

### *3.6.2. Power consumption model*

Besides the first relationship proposed in order to describe the specific compressive force (SCHÖNERT, 1988), one of the first works, and still one of the most relevant assessing the HPGR operation, was also carried out by Prof. Schönert (SCHÖNERT, 1988) analyzing the HPGR power consumption. Eq. (3.20) presents the linear relationship between the specific compressive force (Eq. 3.1) and maximum force applied to the particle bed ($F_{max}$), besides suggesting that the nip angle ($\alpha_{ip}$) and the particle bed compaction behavior parameter ($c_f$) can reduce the power consumption from their increment. Indeed, CAMPOS *et al.* (2019a) showed for pressing iron ore concentrates in a pilot-scale HPGR that the increment in feed moisture is able to increase the particle bed compactness owing to the reduction of the operating gap, being this fact directly related to the increment in the specific energy consumption (CAMPOS *et al.*, 2019a):

$$F_{max} = \left(\frac{1}{\alpha_{ip} c_f}\right) F_{sp} \tag{3.20}$$

As such, the torque needed to move both rolls could be described as (SCHÖNERT, 1988):

$$T = 2\left(\frac{D}{2}\right) F \sin\beta \tag{3.21}$$

where $T$ is the torque and $\beta$ is the force-acting angle. Considering that $\sin\beta$ can be approximated by its own value for small angles, SCHÖNERT (1988) proposed Eq.

(3.22) to calculate the power consumption from the torque provided in Eq. (3.21) multiplied by the roll angular velocity:

$$P = 2UF\beta \tag{3.22}$$

where $P$ is the power consumption. In addition, RASHIDI *et al*. (2017) stated that the force acting angle should be always less than the nip angle (Eq. (3.9)) in order to efficiently apply the grinding force on the particle bed.

GUEVARA & MENACHO (1993) proposed that the power consumption in a roller press may be described as follows:

$$P = P_{Dim}ULD\sigma_p \tag{3.23}$$

where $\sigma_p$ is the compressive stress and $P_{Dim}$ is defined as the dimensionless specific power factor that must be fit to experimental data. This model was also presented and discussed by AUSTIN *et al.* (1993) besides being validated for predicting the power consumption in a lab-scale HPGR for copper ore (AUSTIN *et al.*, 1993). However, results presented by AUSTIN *et al.* (1993) also highlighted several model limitations as the requirement to calibrate the parameter $P_{Dim}$ for different materials.

MORRELL *et al.* (1997) proposed one of the main mathematical models that describe the HPGR performance (MORRELL *et al.*, 1997). Aiming to predict the power consumption by the HPGR they proposed, as well as previously presented by SCHÖNERT (1988), that the power draw may be calculated by the torque applied to both rolls multiplied by the angular velocity. Furthermore, taking into account several advances achieved by LUBJUHN (1992) describing the force-acting angle at the particle bed, they showed an almost linear relationship between the force-acting angle and the power consumption in the HPGR. However, in order to predict the power consumption, they proposed that the power must be calculated multiplying the predicted throughput (Eq. (3.15)) by the measured specific energy in a lab-scale test:

$$P = k_p E_{sp} Q \tag{3.24}$$

where $k_p$ is a fitting parameter that relates the measured power consumption in a lab-scale test to the power consumption predicted by the model. DANIEL (2002) presents some results with reasonable agreement between experimental and predicted values for the power consumption in a lab-scale HPGR, whereas SALAZAR (2014) showed for pressing itabirite iron ore in an industrial-scale that the Eq. (3.24) underestimates the measured values.

TORRES & CASALI (2009) showed that the power consumption in the HPGR operation can be summarized and predicted based in four main operating parameters: hydraulic pressure, nip angle, roll dimension and angular velocity. These authors take into account a similar relationship presented by AUSTIN *et al.* (1997) in order to predict the compressive force that acts on the particle bed as follows:

$$F = p_m \frac{D}{2} L \tag{3.25}$$

where $p_m$ is the hydraulic pressure. As previously discussed by other authors (SCHÖNERT, 1988, LUBJUHN, 1992, KLYMOWSKY *et al.*, 2006) the force-acting angle should be smaller than the nip angle. KLYMOWSKY *et al.* (2006) also warned that half of the nip angle gives the force-acting angle. As such, TORRES & CASALI (2009) proposed that HPGR power consumption is given by twice the torque required to move the roll multiplied by the angular velocity:

$$P = 2F \sin\left(\frac{\alpha_{ip}}{2}\right) U \tag{3.26}$$

where $F$ is the compressive force given from Eq. (3.25) and $\alpha_{ip}$ is the nip angle given by Eq. (3.9).

Although all the presented equations were very important and even responsible for achieving and improving the knowledge about the HPGR power consumption under

different operating conditions, there are a few models that have reached some popularity in the minerals industry. Nevertheless, researchers from UFRJ (CAMPOS *et al.*, 2016, CAMPOS *et al.*, 2017, CAMPOS, 2018, CAMPOS *et al.*, 2019b) showed that these models still have limitations in predicting the HPGR power consumption. Indeed, as previously discussed in Section 3.4.8, the nip angle is also affected by several important operating parameters, although they do not appear explicitly in these models. According to CAMPOS *et al.* (2019b), the poor understanding about this phenomenon is the main responsible factor for the poor prediction of the presented power consumption models. As such, CAMPOS *et al.* (2019b) proposed a minor modification of Torres and Casali model aiming to increase the calculated nip angle by introducing a fitting parameter. The procedure proposed by them uses an experimental test as a base case to fit an optimal parameter able to increase the nip angle, being the Eq. (3.26) rewritten as:

$$P = 2F \sin\left(\frac{\kappa\alpha_{ip}}{2}\right) U \tag{3.27}$$

where $\kappa$ is fitting parameter. This was validated in a wide operating range for pressing iron ore concentrates in a pilot-scale HPGR (CAMPOS *et al.*, 2019b) with $\kappa$ equal to 2.8.

### *3.6.3. Particle breakage model*

Size reduction–energy relationships in particle breakage provide important information in comminution process (TAVARES, 2007) and have been widely used for modeling crushers, tumbling mills, stirred media mills and HPGRs in the minerals industry. In the past decades several authors (AUSTIN & LUCKIE, 1972, WHITEN, 1972, HERBST & FUERSTENAU, 1980, AUSTIN *et al.*, 1984) were responsible for important advances in the field and for consolidating some mathematical modeling approaches used to describe particle breakage behavior in some of these equipment. However, the HPGR mathematical modeling requires a more detailed description, since what makes this equipment unique is the process representing a distinctive interparticle comminution process, as previously discussed in Section 3.5. Indeed, it is key to bear in mind that the particle breakage behavior in a confined particle bed cannot be associated

only to a perfect mixing model to predict the breakage response, since some other effects should be accounted for with the aim of a more realistic description of the breakage response.

Nevertheless, although there is a lack of detailed description for the most part of the models, some of them have reached popularity and showed further potential for development. FUERSTENAU *et al.* (1991) was one of the first trying to apply the population balance model approach to describe the breakage response in HPGRs. Basically, they modified the ball mill grinding kinetics equation (AUSTIN *et al.*, 1984) replacing the grinding time by the energy dissipated in the grinding process, using the energy-normalized selection function (Eq. (3.28)).

$$S_i = s_i^E \frac{P}{E_{sp}^{\exists}} \tag{3.28}$$

Where ∃ is a fitting parameter and $s_i^E$ is the specific selection function (HERBST & FUERSTENAU, 1980). In addition, they also proposed that the rescaled energy term used in the modified grinding kinetics equation is given by (FUERSTENAU *et al.*, 1991):

$$E' = \frac{1}{1-\Omega} E^{1-\Omega} \tag{3.29}$$

where $E$ is the input energy and Ω is a fitting parameter that varies from 0 (all spent energy is not dissipated in the breakage process) and 1 (all spent energy is dissipated in the breakage process). FUERSTENAU *et al.* (1991) also assumed that the breakage rate is independent of the particle size for this model approach since the same amount of energy is transmitted to the particle bed equally for all size classes. They also proposed that the reduction ratio in size reduction in the HPGR could be assumed as a simplified equation presenting a linear relationship with the input specific energy:

$$\frac{f_{50}}{p_{50}} = jE_{sp} + e \tag{3.30}$$

where $f_{50}$ is the is the feed 50% passing size, $p_{50}$ is the product 50% passing size and $j$ and $e$ are fitting parameters. However, although this model approach presented from Eq. (3.28) to (3.30) were previously validated and verified elsewhere (FUERSTENAU *et al.*, 1991), the assumption of a linear size reduction energy relationship may not be valid for high specific energy inputs.

AUSTIN & TRUBELJA (1994) proposed a particle breakage model for the HPGR designed by them as a multicomponent model. This approach, strongly based in the double roll crusher model proposed previously by the senior author and his co-workers (AUSTIN *et al.*, 1980, AUSTIN *et al.*, 1981), uses a sequential discrete size model to predict the product size distribution considering that a fraction of the particle that passes through the rollers are kept intact after the process ($P_i$), whereas a fraction of particles are broken ($P^*_i$). The model equations are presented as follows (AUSTIN & TRUBELJA, 1994):

$$P_i = \begin{cases} (1 - a_i)(1 - a_i') & \text{for } i = 1 \\ (1 - a_i)(1 - a_i')P_i^* & \text{for } 1 < i \leq n \end{cases} \tag{3.31}$$

$$P_i^* = \begin{cases} 0 & \text{for } i = 1 \\ -a_i^* b_{i,1} + \sum_{j=1}^{i-1} b_{i,j} a_j^* P_j^* & \text{for } 1 < i \leq n \end{cases} \tag{3.32}$$

where $a_i^* = a_i + a_i'(1 - a_i)$ is the fraction of unbroken and broken particles at the extrusion zone, represented by $(1 - a_i)$ e $(1 - a_i')$, respectively. The model assumption of unbroken particles during grinding allows, at least in part, describing the presence of remaining coarser particles in the product. However, it is important to bear in mind that this approach does not account physically for the breakage kinetics in the particle bed. Recently, SCHNEIDER *et al.* (2009) proposed a minor modification to

Austin's model aiming to incorporate the compression-grinding selection function (SCHNEIDER *et al.*, 2009).

Besides that, some other authors (SCHÖNERT, 1996, LIU & SCHÖNERT, 1996, LIM *et al.*, 1996) carried out very relevant works assessing the breakage response in the HPGR operation. Unlike presented by FUERSTENAU *et al.* (1991), LIU & SCHÖNERT (1996) showed through experimental results in a piston-and-die apparatus that the breakage response for different size classes is quite different, besides being related to the input energy. Their main contribution was the importance of how the spent energy is dissipated on the particle bed, proposing the so-called energy split function (LIU & SCHÖNERT, 1996):

$$\ln \Pi_i = -c \ln\left(\frac{x_i}{x_e}\right) - d\left(\ln \frac{x_i}{x_e}\right)^2 \tag{3.33}$$

where $\Pi_i$ is the split factor for each particle size $x_i$, $x_e$ is the particle size for $\Pi_i$=1 and $c$ and $d$ are fitting parameters. Briefly, the term proposed by them is associated to the size reduction energy efficiency. The results presented by Eq. (3.33) are extremely important to show the variation of the split factor (efficiency parameter) according to the particle size and the input energy (LIU & SCHÖNERT, 1996), as presented in Figure 3.18.

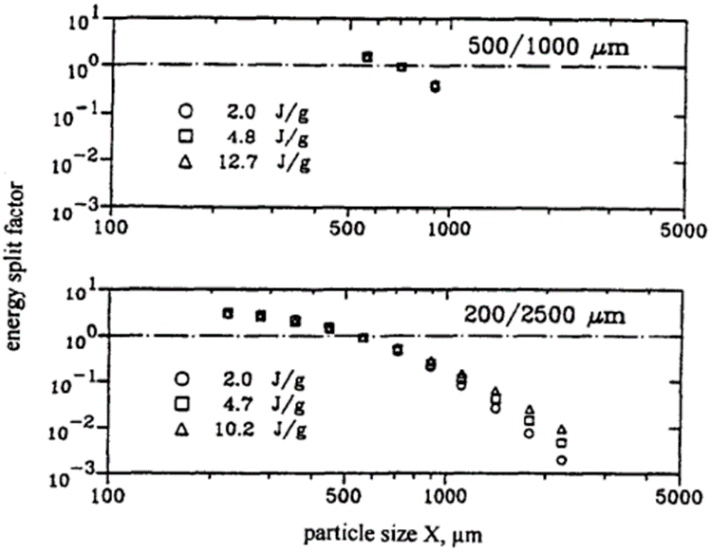


Figure 3.18. Variation of the energy split factor according to the particle size and specific input energy (LIU & SCHÖNERT, 1996).

However, it was only after 1997 when a new mathematical modeling proposition was able to improve the applicability of this approach to describe the breakage response in the roller press. MORRELL *et al.* (1997) proposed a more detailed description of the particle bed, considering different breakage zones along the roll length. The model is strongly based on the Whiten crusher model (WHITEN, 1972) and takes into account that the breakage in the HPGR may be divided in three sub-processes named (MORRELL, *et al.*, 1997): single particle breakage in the pre-crushing zone, interparticle breakage in the edge zone, interparticle breakage in the center zone.

The pre-crushing zone is defined as the region where particles are going to break if they are coarser than the critical size ($\chi_c$), which is given by Eq. (3.34). The fragments of the pre-crushing zone and the particles initially smaller than the critical size are then fed to the interparticle breakage zone.

$$\chi_c = 0{,}5\left(\left(D + \chi_g\right) - \left(\left(D + \chi_g\right)^2 - \frac{4\rho_g D x_g}{\rho_{sp}}\right)^{0{,}5}\right) \tag{3.34}$$

MORRELL *et al.* (1997), based on a previous work (LUBJUHN & SCHÖNERT, 1993), considered the so-called edge effect within the interparticle breakage behavior (Figure 3.19) with a drop in the pressure at the edge of the rolls.

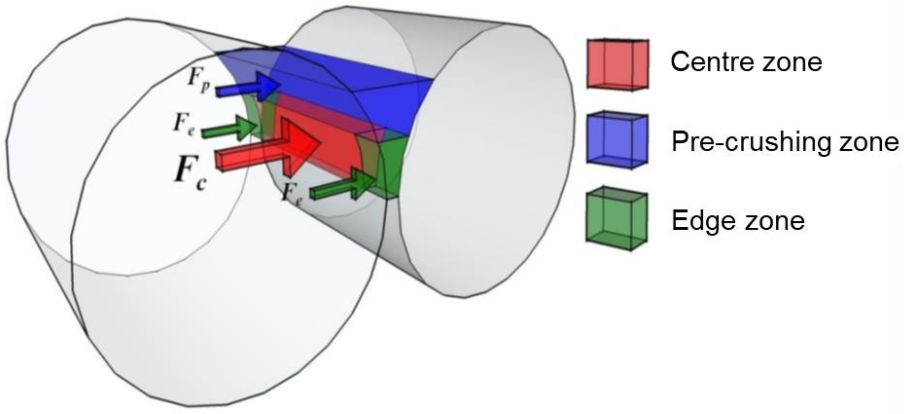


Figure 3.19. Schematic diagram showing Morrell's model approach defining the different breakage zones along the vertical position (pre-crushing zone and interparticle breakage zone) and along the axial roll position (center zone and edge zone).

Eq. (3.35) presents the proportion of material that should be broken in the edge region (MORRELL *et al*., 1997):

$$\Lambda = \varsigma \frac{\chi_g}{L} \tag{3.35}$$

where $\varsigma$ is the split edge factor. In order to calculate the selection function this model uses the classification function from Whiten's model (WHITEN, 1972) and also some results from a drop weight test (DWT) or piston-and-die tests to fit the $t_{10}$ model (NARAYANAN & WHITEN, 1988) aiming to predict the progeny size distribution. Moreover, DANIEL & MORRELL (2004) presented reasonable agreement between experimental and simulated size distributions using this model approach in a lab-scale HPGR, whereas highlighting a relatively difficulty of the model when describing the size reduction in industrial scale. Furthermore, SALAZAR (2014) presented results that demonstrated some deviations in the predicted product size distribution for pressing itabirite iron ore in an industrial scale. Indeed, the model requirements for calibration on the basis of lab-scale HPGR tests to simulate industrial-scale operations (which is not yet a clear topic), can be one of the reasons of this poor model prediction is some particular cases as reported elsewhere (DANIEL & MORRELL, 2004, SALAZAR, 2014).

The model proposed by TORRES & CASALI (2009) is also based on the population balance model following the hypothesis of relative independence of breakage rates on operating conditions (CAMPOS *et al.*, 2019b). As also proposed by MORRELL *et al.* (1997), this model considers that particle coarser than the critical size (Eq. (3.18)) should be broken individually in the same breakage rate as follows:

$$p_i^{SP} = \sum_{j=1}^{N} b_{ij} f_j^{SP} \tag{3.36}$$

where $p_i^{SP}$ is the fraction retained in the product of single-particle breakage, $f_j^{SP}$ is the fraction retained in the feed of single particle breakage region and $b_{ij}$ is the breakage function.

This model also allows discriminating between center and edge products, since it discretizes the roll in $N_b$ blocks along the axial roll position (TORRES & CASALI, 2009). The pressure profile along the roll's length is assumed to have parabolic shape, as previously discussed by other authors (LUBJUHN & SCHÖNERT, 1993, MORRELL *et al.*, 1997). Figure 3.20 presents the main parameters of the Torres and Casali model (a) beyond the parabolic power profile along the axial roll position (b) (CAMPOS *et al.*, 2019b).

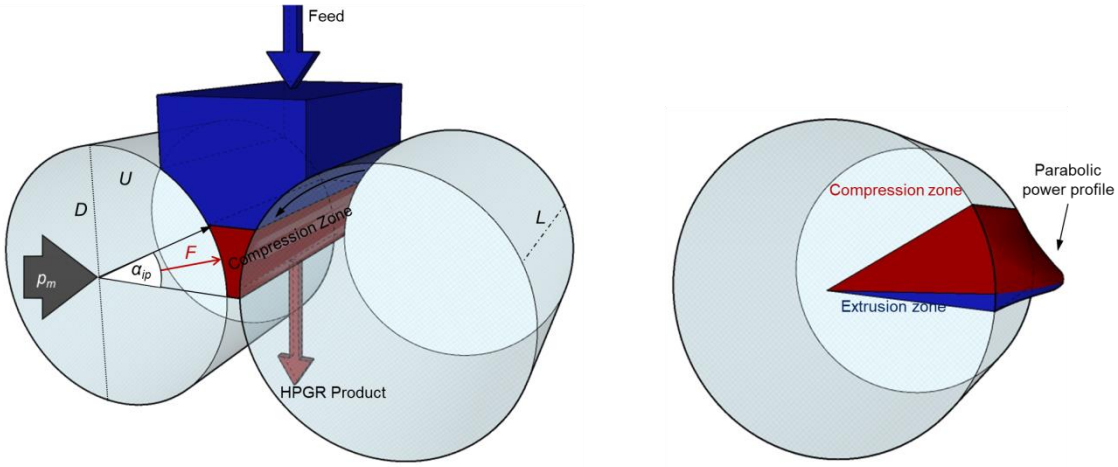


Figure 3.20. HPGR Schematic diagram with the main variables in Torres and Casali model (left) and the assumed parabolic profile along the rolls length (right) (CAMPOS *et al.*, 2019b).

As such, the authors used the population balance model (Eq. (3.37)) assuming steady-state and plug flow conditions with a constant velocity ($v_z$) in the vertical position *z*, assumed by them as the roll peripheral velocity. This approach considers a variation of the breakage rates ($S_{i,k}$) for each defined block along the axial roll position.

$$v_z \frac{d}{dz} w_{i,k}(z) = \sum_{j=1}^{i-1} S_{j,k} b_{ij} w_{j,k}(z) - S_{i,k} w_{i,k}(z) \tag{3.37}$$

In order to solve the system of equations the authors used the cumulative breakage function (AUSTIN & LUCKIE, 1972) and the specific selection function (HERBST & FUERSTENAU, 1980), represented by Eq. (3.38) and Eq. (3.39), respectively:

$$B_{ij} = \phi\left(\frac{x_i}{x_j}\right)^{\gamma} + (1-\phi)\left(\frac{x_i}{x_j}\right)^{\beta} \tag{3.38}$$

$$\ln(s_i^E/s_1^E) = \xi_1 \ln(\bar{x}_i/\bar{x}_1) + \xi_2 \ln(\bar{x}_i/\bar{x}_1)^2 \tag{3.39}$$

where $\phi$, $\gamma$, $\beta$, $s_1^E$, $\xi_1$and $\xi_2$ are fitting parameters, $\bar{x}_i$ is the representative size give by $\bar{x}_i = \sqrt{x_i x_{i-1}}$ and $b_{ij}$ is the distributed breakage function given by $b_{ij} = B_{i-1,j} - B_{i,j}$. Moreover, the breakage rate is given by a minor modification of the relationship proposed by HERBST & FUERSTENAU (1980) for ball milling:

$$S_{i,k} = \frac{P_k}{H_k} s_i^E \tag{3.40}$$

where $S_{i,k}$ is the breakage rate for each block and each size class, $P_k$ is the parabolic power profile given from Eq. (3.41) and $H_k$ is the holdup of each block given from Eq. (3.42) (TORRES & CASALI, 2009):

$$P_k = 2F \sin\left(\frac{\alpha_{ip}}{2}\right) U \frac{(L^2 - 4y_k^2)}{\sum_{j=1}^{N_B}(L^2 - 4y_j^2)} \tag{3.41}$$

where $y_k$ is the position of each block *k* related to the center of the roll.

$$H_k = \frac{1}{N_B} Q \frac{z^*}{3600U} \tag{3.42}$$

where $z^*$ is the distance between the extrusion zone pressing and the beginning of the interparticle compression zone.

As such, using an analytic solution for Eq. (3.37) and taking into account Reid's matrix $A_{ij,k}$ (REID, 1965), the authors proposed that the product size distribution for each block and each size class could be determined as:

$$p_{i,k} = \sum_{j=1}^{i} A_{ij,k} exp\left(-\frac{S_{j,k}}{v_z} z^*\right) \tag{3.43}$$

The HPGR product at the extrusion zone is predicted as the average of all products in each block (TORRES & CASALI, 2009):

$$p_i^{HPGR} = \frac{1}{N_B} \sum_{k=1}^{N_B} p_{i,k} \tag{3.44}$$

Although the Torres and Casali model is a robust model and known for allowing detailed predictions of the axial roll profile, there are still limitations of this model in describing physically the size reduction within the equipment. Given the absence of evidence and knowledge on the behavior of pressure profile and mass distribution profile along the axial roll position, this model relies on the simplifying assumption of a constant parabolic pressure profile (3.41) and an even partition of the solids rate along the roll length (Eq. (3.42)). Recent works using an industrial-scale HPGR (CLEARY & SINNOTT, 2021) and using a pilot-scale HPGR (RODRIGUEZ *et al.*, 2021, RODRIGUEZ *et al.*, 2022a) showed, through DEM simulations, how the pressure and mass flow rate profiles are affected by operating conditions, design variables and surface wear patterns. RODRIGUEZ *et al.* (2021) highlighted a great challenge to describe the "bathtub" effect in the pressure profile with the HPGR operating with worn rolls. They also found significant insights about a peak of pressure above the extrusion zone, which was also recently demonstrated mathematically by other authors (THIVIERGE *et al.*, 2021).

More recently, researchers from Hacettepe Universitesi (DUNDAR *et al.*, 2013) proposed an approach considering the perfect mixing model and ensuring that the breakage function and the breakage rate distribution should be calibrated from experimental results in a piston-and-die apparatus. Eq. (3.45) represent the breakage rates in the top particle size that should be fitted to experimental results.

$$r_D = k_D x^{\alpha_D} \tag{3.45}$$

where $r_D$ is the breakage rate and $k_D$ and $\alpha_D$ are fitting parameters. Although trying to correlate information from bench-scale tests to characterize the breakage response in industrial scale, the model still lacks proper description of the size reduction. Simulations carried out using the Integrated Extraction Simulator (IES) software with this model and using different materials (YAHYAEI *et al.*, 2020) showed poor predictability of the model in several cases.

To assess the particle breakage behavior of an iron ore concentrate in a pilot-scale HPGR, CAMPOS *et al.* (2019b) showed that the Torres and Casali model (TORRES & CASALI, 2009) does not provide good prediction for the product size distribution. According to them, the challenge experienced by TORRES & CASALI (2009) in predicting the fine end of the size distribution can be associated to the assumption that the progeny size distribution is normalizable below the grain-size, which is a feature not normally observed for Brazilian iron ores (FARIA *et al.*, 2019, ROCHA *et al.*, 2022b) and even for other types of ores and rocks (TAVARES, 2000, TAVARES & NEVES, 2008). Therefore, CAMPOS *et al.* (2019b) suggested a non-normalizable breakage function (KING, 2001) in order to improve the particle breakage prediction for iron ore concentrates. Eq. (3.46) presents the non-normalizable breakage function (KING, 2001):

$$\begin{aligned} B_{ij} &= \phi\left(\frac{x_i}{x_j}\right)^{\gamma} + (1-\phi)\left(\frac{x_i}{x_j}\right)^{\beta} \text{ for } x_i \geq \omega \\ B_{ij} &= \phi\left(\frac{x_i}{\omega}\right)^{\eta}\left(\frac{x_i}{x_j}\right)^{\gamma} + (1-\phi)\left(\frac{x_i}{x_j}\right)^{\beta} \text{ for } x_i < \omega \end{aligned} \tag{3.46}$$

where $\omega$ and $\eta$ are additional fitting parameters.

Additionally, one phenomenon that occurs in both confined bed breakage and HPGRs, that was discussed in detail in Section 3.5.2, is saturation. As pressures increase beyond a certain level, the bed of particles becomes progressively less able to dissipate the strain energy in breakage of the particles. In addition, a larger fraction of the strain energy of the bed is stored as elastic energy and even plastic energy, which results in reduction in energy efficiency under these conditions. Unfortunately, no HPGR model in the literature has been capable to incorporate this effect.

Finally, it is important to point out that, even though these models have been widely used in the minerals industry and literature, the assumptions of a simplest crusher model (MORRELL *et al.*, 1997), piston flow conditions (TORRES & CASALI, 2009, CAMPOS *et al.*, 2019b) or a perfect mixing model (DUNDAR *et al.*, 2013) are just a simplification of the real and complex size reduction within the HPGR. As the main applications of the population balance model for different size reduction operations, these approaches can give reliable and accurate predictions for the average of the population of particles. Nevertheless, several limitations can be found using them in extreme conditions when the HPGR operates with high compressive forces, high roll velocities, high moisture content and some important variations in the design conditions. Indeed, the remaining lack of proper understanding about the fine details of the interparticle breakage (Section 3.5) and how the HPGR operating conditions can really affect size reduction are one of the main reasons for handicapping these model applications in several cases.

### *3.6.4. HPGR working gap model*

The HPGR working gap model is based on the description of the hydro-pneumatic suspension system as depicted in Section 3.3.2. The model presented briefly as follows should be able to calculate the working gap on the basis of the operating conditions and the hydro-pneumatic pressurizing system (BAUER, 2011). The mathematical relationship accounts for a thermodynamic description that allows to calculate the hydraulic piston displacement according to the variation of the hydraulic pressure and some other variables.

As such, before calculating the HPGR working gap $\chi_g$ as a function of the pressure at the piston or working pressure $p_m$ it is necessary to identify the various possible states of the system (BAUER, 2011):

- State #0: Hydraulic system force $F_0 = 0$. The nitrogen pressure in the accumulator is the preload pressure $p_0$, which is defined at the beginning of the HPGR operation. The gas fills out the complete internal volume $V_0$ of the accumulator. The relationship between the hydraulic system force $F_m$ and the working pressure $p_m$ is:

$$F_m = \frac{p_m}{A_p} \tag{3.47}$$

  where $A_p$ is the effective area of the pistons.

- State #1: The static force $F_1$ is loading the system ($F_1 > F_0$). The force is sufficiently high to compress the gas volume in the accumulator isothermally to the volume $V_1$, which corresponds to a new pressure $p_1$. On the basis of the isothermal change of state from 0 to 1 it is stated:

$$p_1 V_1 = p_0 V_0 \tag{3.48}$$

- State #2: $F_m$ is the dynamic force and oscillates around $F_1$. Therefore, the gas volume is compressed (compression) and expanded (restitution) by a polytropic change of state to the volume $V_m$ and the operating pressure $p_m$:

$$p_1 V_1^{\theta} = p_m V_m^{\theta} \tag{3.49}$$

In Eq. (3.49) $\theta$ is the adiabatic exponent, which is the ratio of the specific heat capacity at constant pressure and the specific heat capacity at constant volume for a particular gas. In the literature values are quoted that refer to the properties at low pressures and room temperature. For instance, it is approximately 1.66 for monoatomic gases (e.g. He), 1.40 for diatomic gases (e.g. $N_2$, $O_2$ and therefore also air) and 1.30 for triatomic gases (e.g. $CO_2$) (BAUER, 2011). For HPGR operations the most common gas used is the nitrogen, thus accounting for the polytropic exponent ($\theta$) equal to 1.4.

The HPGR working gap measured from the top of the studs $\chi_g$ may be calculated as a function of the difference in volumes, the effective piston area $A_p$ and the zero gap $\chi_0$ as presented in Eq. (3.50).

$$\chi_g = \frac{V_1 - V_m}{A_p} + \chi_0 \tag{3.50}$$

The model presented (BAUER, 2011) and previously validated by predicting the operating gap for lab-scale HPGRs (BARRIOS & TAVARES, 2016), relies in describing a closed-circuit suspension system, very common for lab-scale HPGRs (DANIEL, 2002, BARRIOS & TAVARES, 2016), and, therefore, not accounting for the capability for adding or removing the hydraulic fluid from the system during operation.

Although presenting an elegant thermodynamic modeling approach to describe the hydro-pneumatic pressurizing system, BAUER (2011) admitted that most of the systems already seen for industrial applications have the capability to readjust the suspension position after any change in the hydraulic pressure, simply by adding or removing the hydraulic fluid (BAUER, 2011). According to him, this is one of the main reasons for applying the hydro-pneumatic pressurizing system coupled with a level control. These so-called self-pumping systems are particularly used for some pilot-scale and industrial-scale HPGRs and were not yet properly investigated until now.

*3.6.5. DEM modeling approach*

The HPGR was widely studied in this decade by several authors using DEM (HERBST *et al.*, 2011, QUIST & EVERTSSON, 2012, BARRIOS & TAVARES, 2016, NAGATA *et al.,* 2020, CLEARY & SINNOTT, 2021, RODRIGUEZ *et al.,* 2021, RODRIGUEZ *et al.,* 2022a, RODRIGUEZ *et al.,* 2022b). HERBST *et al.* (2011) presented a promising approach working with DEM coupled to the population balance model. QUIST & EVERTSSON (2012) also showed in pilot-scale HPGR DEM simulations assessing the pressure distribution along the roll's length, although using unbroken particles. To assess the dynamic of the roll during grinding, BARRIOS & TAVARES (2016) proposed a model able to describe the rolls movement using the Multi Body Dynamics (MBP) coupled with DEM. RODRIGUEZ *et al.* (2022a) used a successful approach combining DEM, MBP and a Particle Replacement Model to describe a pilot-scale HPGR. They showed promising results to quantify the throughput and power consumption, although only describing the size reduction qualitatively (RODRIGUEZ *et al.,* 2022a). Additionally, recent investigations were also made through DEM to understand the real effect of roll wear pattern (RODRIGUEZ *et al.,* 2021) and skewing strategy (RODRIGUEZ *et al.,* 2022b). These two features were already discussed previously in Section 3.3.3 and Section 3.3.5, respectively.

Indeed, there is still a challenge in applying DEM simulations to describe breakage in HPGRs since a large number of particles should be used and a good description of the finesses of the size distribution is not easy to reach. On the other hand, discussions made on Sections 3.6.1 to 3.6.3, made it clear that phenomenological approaches are not able to create a more realistic and mechanistic description of HPGR operations. Therefore, a new modeling approach has become focus of discussion, which was first proposed by HERBST *et al,* (2011), and is named as hybrid modeling. This approach combines reliable and physical information from DEM simulations with traditional population balance model in order to predict the HPGR size reduction. RODRIGUEZ *et al.* (2023) used DEM simulations to get the pressure and throughput profiles along the roll length, besides calculating the total throughput and power consumption in a pilot-scale HPGR. This information was then used in the traditional population balance model solution used by TORRES & CASALI (2009) to describe size reduction and, in turn, circumvent issues with the model depicted in Section 3.6.3. The approach showed a potential application to simulate different design and operating

conditions, which is not possible when using the simpler purely phenomenological approach (RODRIGUEZ *et al.*, 2023). Evidence presented by them up to this point suggested that, at least considering the overall HPGR product, results were not so different when compared to predictions using the purely phenomenological model (CAMPOS *et al.*, 2019b).

### *3.6.6. Model predictive control*

Model predictive control (MPC) is an advanced method of process control that allows controlling the process while subjected to set of constraints. In the minerals industry, the MPC has reached some popularity and several applications can be found for flotation plants (SUICHIES *et al.*, 2000), granulation systems (GATZKE & DOYLE, 2001), ball milling (RAMASAMY, *et al.* 2005), crushing (JOHANSSON & EVERSTSSON, 2018) and even for HPGR operation (NUMBI & XIA, 2015, JOHANSSON & EVERTSSON, 2018, VYHMEISTER *et al.*, 2019).

In the case of the HPGR operation a key task that remains a great challenge is the detailed description of the process dynamics and thus the application of an effective control technique. JOHANSSON & EVERTSSON (2018) proposed to use a sequence of steady-state process conditions to describe the time dynamic operation of the HPGR. Among the main equations used by them, some empirical relationships were presented to predict the roll dynamic and the particle bed compaction behavior. The model was validated in a small range of operating conditions and showed a relatively good description of the HPGR performance in an industrial scale.

On the other hand, VYHMEISTER *et al.* (2019) proposed a model predictive control based on the previously discussed Torres and Casali model (TORRES & CASALI, 2009). They designed and implemented a multivariable controller in an HPGR dynamic model where the MPC considered the specific energy consumption and the product size distribution as the two main controlled variables, whereas the roll peripheral velocity and operating pressure as the only manipulated variables. They partially validated the model for a pilot-scale HPGR. Nevertheless, although the authors recognized the well-known relationship between operating pressure and operating gap (Section 3.3.2), they did not consider the latter as a manipulated variable and set its value to 24 mm. This simplified assumption when dealing with the significant changes

in the operating pressure creates a bias in the results achieved. NUMBI & XIA (2015) proposed a model similar to the Torres and Casali model (TORRES & CASALI, 2009) with a detailed analysis on the applications of an HPGR saving up to 4.5% of energy for a particular set of operating conditions. This was also the case of the approach proposed by VHMEISTER *et al.* (2019), which assumed no clear relationship between operating pressure and gap, which limited the application of the model for this purpose.

Using a hybrid model with the population balance equation and information provided by DEM simulations (Section 3.6.5), HERBST *et al.* (2011) implemented a control loop for tunning the hopper level in an HPGR operation in which the roll peripheral velocity was the only manipulated variable. The simplicity of control loop limited the model application and did not make validation possible (HERBST *et al.*, 2011). POWELL *et al.* (2012) carried out pseudo-dynamic simulations of an industrial-scale HPGR with the model applied to control HPGR throughput but without taking into account variations or disturbances in the feed size distribution. Despite the several applications, a more realistic description of the HPGR dynamics is still missing and limiting the applications of those models.

### 3.7. Online modeling background

With the current advances in Industry 4.0, smart factories and smart productions have been widely required. Industrial processes are increasingly shifting towards the traditional operation to new approaches able to correlate the multi-scale dynamic modeling and simulation with the main industrial demands to make decisions in order to rise the production capabilities (DAVIS *et al.,* 2012). Nowadays, extended database information and data transmissions, also called “Big Data” analytics, provide much information throughout different stages in the operation.

Industry 4.0 is strongly related to the digitalization of the process. This approach requires a vertical or a horizontal networking integration, real-time information and good connections between digital technologies. Furthermore, several authors (FETTKE, 2013, LASI *et al.,* 2014) suggested that this new trend requires multifaceted areas of application concerning the operation that include: integration between physical and digital aspects and data models and exchange formats. RÜBMANN *et al.* (2015) pointed out that several technologies are changing the industrial production nowadays.

According to them, a brief vision of the industrial production of the future is entirely linked to big data and analytics, system integrations, simulations, cloud computing and the industrial or internet of things (IoT) (RÜBMANN *et al.* 2015).

All these characteristics are totally related to the purposes of increasing the efficiency, productivity of resources and even the ability to adapt to new demands. Different concepts have been proposed and adopted to increase digitalization and to apply an online modeling approach able to correlate extended database in real time to describe operations. Online modeling approaches are better for predicting variations within the process and can be used in a robust model predictive control. New approaches dealing with the application of an online integration of physical and digital process through extended database, soft sensor models, real time information, model predictive control have showed a huge potential to provide a significant industrial paradigm change.

### *3.7.1. State of the art*

The application of online models coupled with real-time information become a trend in the last ten years or so with the improvement of digitalization. According to TAO *et al*. (2018), the advancement and rapid development provided by the growth of new technologies was key to transform this in a very popular research field. Among several approaches adopted and designed, two of them attracted great attention from the industry and are named Digital Shadow and Digital Twin.

KRITZINGER *et al.* (2018) defined both terms from the point of view of the level of data integration, besides comparing those with a simpler third approach. Following an order of complexity, the first of them, named “Digital Model”, is associated to digital representation of an operation or industrial process without real connection to the physical model, being the information provided by both physical and digital components connected manually. The second one can be defined as an upgrade of the “Digital Model”, where connections are established from the physical object to the digital object. This term is called “Digital Shadow”, where the digital component can change its own state from information provided by the physical operation. A Digital Shadow approach is normally more substantial than the Digital Model approach, being a distinguished and robust tool capable to aid the operator in the decision making by

describing, in real-time, the performance of industrial operations. Finally, the Digital Twin (DT) can be stated as a complete integration between both digital and physical components. A DT allows to control the operation in real-time as a result of any change in the physical model condition and vice versa (KRITZINGER *et al.*, 2018). Basically, both Digital Shadow and Digital Twin are entirely based in a realistic replica of the physical operations in the digital mode but differing from how the connections between these two main parts is performed (TAO *et al.*, 2018). Figure 3.21 presents a comparison between the data flow in the three different approaches of digital components.

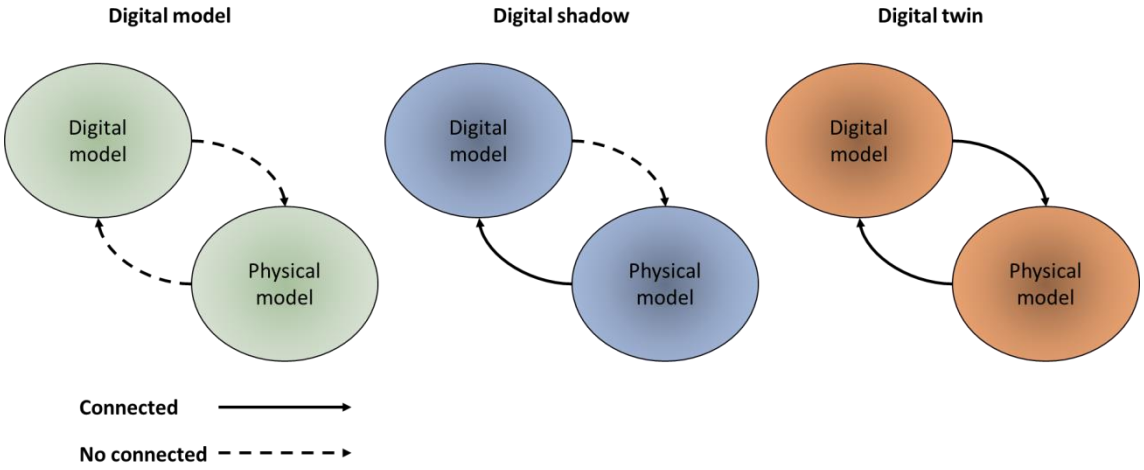


Figure 3.21. Schematic diagram presenting the differences between different digital components from the standpoint of data flow.

In general, considering the recent development of the technologies, many changes and alternative definitions are used in industry to characterize the main features and capabilities of them (GRIEVES, 2014, STARK *et al.*, 2017, ZHUANG *et al.*, 2018, XU *et al.*, 2019). Following the first definition proposed by Grieves in 2003 (GRIEVES, 2014) and then revised and updated in 2012 by the National Aeronautics and Spatial Administration (NASA), these online devices are defined by three main pillars as: digital asset, physical asset and connections. Additionally, the device should be considered based on simulations that reflect, with an outstanding agreement and in real-time, the operation of a physical asset (GLAESSGEN & STARGEL, 2012). Besides that, the device must be able to consider the historical data, real time sensor

data, physical model operation and even the multiscale and probabilistic simulations (GLAESSGEN & STARGEL, 2012).

Taking advantage of the recent improvements in technology, IoT incorporation, extend database analytics, cloud database and data fusion, online models coupled with real-time information can be stated as the new trend. Some authors (GABOR *et al.*, 2016, MAURER, 2017) argued that the approach allows linking the physical asset through mapping the process and improving the physical performance. Also, considering a realistic representation of the operation in a digital mode, it is possible to reach optimal performances, reduce process disturbances and even find more attractive operational strategies to auxiliary the making decision.

Following this new trend, it is easy to find in the literature some reports about digital twin applications and online models in process industry, even though some of them using different definitions than presented in Figure 3.21. These alternative definitions are more related to the desire of application of technology and not to the real application in its state of the art. TAO *et al.* (2018) argued that the DTs application, for instance, is at a growing stage and an optimist perspective for the next years suggests that this device system tends to change drastically the industrial operation coupled to the IoT, big data analytics and cloud computing technologies. However, the reality is not so simple as suggested by him and proper applications of the technology are still missing.

Indeed, great attention has been devoted to the industrial operation, but there are still challenges in using the technological devices. LU *et al.* (2020) pointed out three main limitations of its application in industry, being summarized as: the lack of references in online models, superficial knowledge of research challenges and only preliminary applications as example (LU *et al.*, 2020). Also, it is important to bear in mind that implementation of these devices in process industry represent a disruptive technology able to change completely the operation, especially when considering a more complex design as a digital twin. As such, care should be taken in applying the technology, besides a significant expert knowledge coupled to a detailed study about the impacts should be considered to ensure a smooth transformation.

*3.7.2. Architecture, capabilities, and features*

The main architecture for an online model approach can be summarized in three main dimensions: physical, virtual and connection parts (GRIEVES, 2014). TAO *et al.* (2018), based in the three-dimensional architecture of Grives, pointed out a new and more detailed architecture just dividing the connection in data and service parts.

A key point in the application of these devices is entirely related to the clear understanding about the physical entity and its main properties that could affect the process, besides a detailed modeling in the digital component. NATIS *et al.* (2017) pointed out that the digital component is characterized by several elements as model data structure and critical and elementary variables in the system. As suggested by them, it is possible to extend the model aiming to improve the digital component description from enriching it by adding extra model elements and data (NATIS *et al.*, 2017). Additionally, the model can be expanded to integrate the digital and physical assets to provide a more complex and composite tool. This approach could be applied to evaluate upstream and downstream variables in the operation in detail, although it requires a more complex model assembly.

CANEDO (2016) taking as an example the digital twin, highlighted the technology with a great potential to provide notable improvement by adding the data feedback from the digital part. Indeed, the connection between both physical and digital components is very important to reinforce the DT capabilities such as structure monitoring, lifetime predicting, in-time maintenance and real-time performance (TAO *et al.,* 2018). The connections in these approaches are summarized in sensors and actuators. Such sensors are able to provide to the digital component, in real-time, information about physical parameters and properties, variations in the operational performance and the main demands in the physical asset. The actuators are the components responsible to pass the information from the digital part to the physical part. This last tool might be associated to the process control in an advanced DT approach. On the other hand, sensor is more related to any database from the system or even any estimations made by data driven soft sensors (depicted in detail in Section 3.7.4).

Coupled to the sensors and actuators, the data flow is also associated to a constant and real time connection between physical and digital components in a system.

This feature is the main difference that can be observed between digital shadow and digital twins with the simpler digital model (Figure 3.21). In addition, the data flow must be always filtered and analyzed aiming to provide a proper description of the operation and avoiding any disturbance and data outliers, which, in other words, tries to avoid the well-known issue of “garbage in, garbage out”.

TAO *et al.* (2018) pointed out some requirements of this application related to a detailed approach in the model environment with the aim of providing an effective representation of the physical component. As such, an online modeling approach characteristics can be summarized, as well as their functionalities, as:

- Model: Digital representation of the equipment in the process that should be realistic and sufficiently detailed to ensure an optimal description of the operation in real-time (TAO *et al.*, 2018).

- Model synchronization: Data model synchronization with the real-time data operation using data cloud, big data analytics and IoT (KRITZINGER *et al.*, 2018, IBRAHIM, 2019). This part is entirely related to the development of data driven soft sensor models to support the prediction of any critical or unmeasured variable.

- Connect analytics: Algorithms, operational parameters and computational results provided by a real description and knowledge about the physical component.

- Simulation: It should be carried out aiming to describe with fidelity the behavior of a physical model and must be able to give a rapid response for changes observed in the physical model and provided by the connection between both digital and physical components (TAO *et al.*, 2018, BARRICELLI *et al.*, 2019).

- Trust: This feature suggests that it might be able to handle critical tasks in the operation, being also responsible for some type of process control based on the prediction made by the digital component (IBRAHIM, 2019).

### *3.7.3. Modeling, simulation and data fusion*

Modeling and simulation are the basis of the online modeling optimization. Defining the physical properties and a good description of the process is required in order to ensure that the digital part will be a mirror of the physical part. SCHROEDER *et al*. (2016) proposed that the digital part could be discretized in five layers: device layer, user interface layer, web service layer, query layer, and data repository layer. Such layers are entirely coupled to data connection and data transmission.

Indeed, the data transmission is mainly linked to data format conversion, data storage and data source protection (TAO *et al.*, 2018). This idea considers three stages defined as data mining, data processing and data optimization. Indeed, most industrial processes have an extended database provided by a varied number of channels in the process as physical properties and performance and historical database. As such, several authors (RICKS *et al.*, 2015, TAO *et al.*, 2018, XIANG *et al.*, 2018) have suggested some technologies in order to enable the data fusion, allowing better manipulation of the data source, data generation, data cleaning and data evolution. Data fusion is still important for aiming at the reduction of a massive database using order reduction techniques. Nevertheless, although the data fusion has proven to be a promising alternative allowing to improve the online modeling approach performance, there is not much application of this technique in these devices (TAO *et al.*, 2018).

### *3.7.4. Soft sensor models*

Among all features reported above for online model applications, an industrial process instrumented with many sensors is usually the best way to start the implementation. However, there are a few and available accurate sensors for online measurements in some of critical variables within the process. This failure to accurately estimate some of the process outputs may limit the application of such technology and provide unreliable description of the physical asset. A common way to overcome this

issue is the development and application of soft sensor models. The term is mainly derived from the term's "software" and "sensor" and a very large number of applications have been reported elsewhere (KADLEC *et al.,* 2009, PANI & MOHANTA, 2011, LIU *et al.,* 2016).

The heart of a soft-sensor model deals with a model using easily measured process variables to estimate a critical/unmeasured variable as an output. The soft sensor models can be divided in two main groups. The first one, called model-driven soft sensor, is a white-box model, which is a full phenomenological model built on the basis of the knowledge about the process. The second one is the data driven soft sensor, which relies on a black-box model developed based in statistical techniques and empirical observations of the process. Hybrid soft sensors (Gray-box models) are also a possible design in the process industry, which allows to achieve, sometimes, a more robust approach (KADLEC, 2009, PANI & MOHANTA, 2011). Nevertheless, given the lack of physical understanding about the entire operation, data-driven soft sensors have become more popular in the industry.

Indeed, the large number of variables stored in the process industry stimulate the development of a data-driven soft sensor. However, it is important to bear in mind that there are a lot of different issues that must be dealt with while developing data-driven soft sensors, as the availability of plant historical data and the quality of the measured variables in the database. Usually, a soft sensor design relies on a set of steps to be taken in order to develop a suitable model, which can be summarized as (FORTUNA *et al.,* 2005, KADLEC *et al.,* 2009, PANI & MOHANTA, 2011): data collection, data pre-processing, data segmentation, variable selection, model training and model validation. Additionally, a huge number of statistical inference techniques can be raised and employed in the data-driven soft sensor design as the partial least squares (PLS), principal component regression (PCR), principal component analysis (PCA) and artificial neural network (ANNs) (SHANG *et al.,* 2015).

An alternative way for developing a soft sensor model that has attracted great attention in recent years is the application of Artificial Neural Networks (ANNs) as a data-driven method with potential use to model high-complexity processes. ANNs are usually described on the basis of three main groups with the aim to computationally emulate the signal transfer and data processing in a biological neural network. The first group is a single layer that relies on the input data and the last group is a single layer

responsible for computing the output data. The middle group, where the hidden layers can be found, is the main point to properly model the data according to the type of algorithm and ANN method adopted. Applications of this model approach for soft sensor models were adopted to predict selected process parameters when combining available measurement (FORTUNA *et al.*, 2005) or as an alternative to predict hard-to-measure values from the operation (FERNANDEZ DE CANETE *et al.*, 2016).

Despite the large number of applications in different fields as reported above, soft sensor models in mineral processing have faced important challenges to become consolidated as new substantial technology. Although the digitalization has presented success in mining and optimizing haulage fleet (briefly discussed in Section 3.7.6), mineral processing technology finds some difficulty to use data-driven soft sensor models to describe comminution, classification and concentration operations, even using extended databases from supervisory system. Recent works showed important advances dealing with process monitoring and control of comminution circuits (YAHYAEI *et al.*, 2021, HILDEN *et al.*, 2022), but the number of publications available in the literature is still small. The reason for that is the often-significant variability of the ore that feeds the plants, whose properties cannot be measured online and that vary significantly with time. Regarding the ANNs, criticisms can also be raised about the extended database required for model training when applying it to real world operations, which several times can lead to overfitting.

In general, the methodology adopted in the development of data-driven soft sensor models can be questioned since usually no physical understanding about the operating is taken into account. Alternative ways using hybrid soft sensor models with a mixture of data driven and mechanistic information can be raised to overcome this issue. Nevertheless, using phenomenological (or mechanistic) models integrated with soft sensors have great potential to provide on-line control systems with a modeling architecture that runs significantly faster than real time.

### *3.7.5. Applications in mining and mineral processing*

Within the mining and mineral processing, online modeling has also reached some popularity, but not yet applied in its full version (digital twin technology). Nowadays companies are widely using digitalization of the plants aiming to improve

the equipment and production performance, reduce the environment impact, etc. Different to the past, where the simulation approach was disconnected from the entire operation, currently the data flow between different process, equipment and operations have allowed to raise important improvements in this area (NAZARI & CRISTONFFANI, 2019).

Several mining companies are proposing to apply solutions with digitalization. GE Mining has been using data mine solution in order to increase the equipment uptime, stabilize the operation, increase productivity (GE, 2017). According to them, the main benefits are summarized in the increment of the plant´s throughput and recovery, besides reducing its energy consumption (GE, 2017). Vale is also one of the pioneers applying the mining digitalization from using autonomous trucks in their Brazilian iron ore mines (FLEET, 2019, BARBOSA *et al.,* 2019). This application allows optimizing the throughput and even improve the life cycle of the haulage fleet (FLEET, 2019, BARBOSA *et al.,* 2019). LEONIDA (2018) also presented several cases of digital twin application in a large number of companies. Besides pointing out GE Mining as the main application and currently the most advanced in the sector, the researcher stated that a Rio Tinto mine is using data science bandwagon and even Anglo American, into Los Bronces Mine, improving the haulage since 2016 (LEONIDA, 2018). In addition, some other companies have dedicated extended resources to the digitalization of its mining and mineral processing operations. Included in this is the CRC ORE and the development of cloud-based simulation and optimization platform called IES (Integrated Extraction Simulator).

Specifically in the field of mineral processing, NAZARI & CRISTONFFANI (2019) presented virtual instrumentation of hydrocylones aiming to measure the slurry density and percentage of solids in the slurry. The results were sufficiently promising to encourage the Oceana Gold Hale mine (SCHUG *et al.,* 2019) to apply a virtual instrumentation in its plant operation. Figure 3.22 presents results provided by them highlighting the very good agreement between virtual and physical measurements.

According to the authors (SCHUG *et al*., 2019) their preliminary digital twin device will be expected to work more properly when it takes into account other important parameters in the process model, which can explain the relative difference observed between virtual and physical measurements in Figure 3.22. OLIVER and TOOHER (2018) also used a preliminary online model device to optimize operation of

a flotation plant. Their results showed that this application suggested some perspectives for optimizing the flotation plant, besides still requiring improvements in the digital model description. In addition to that, several years back, HULTHÉN & EVERTSSON (2011) also presented a real-time algorithm to control two variables in crushing stages.

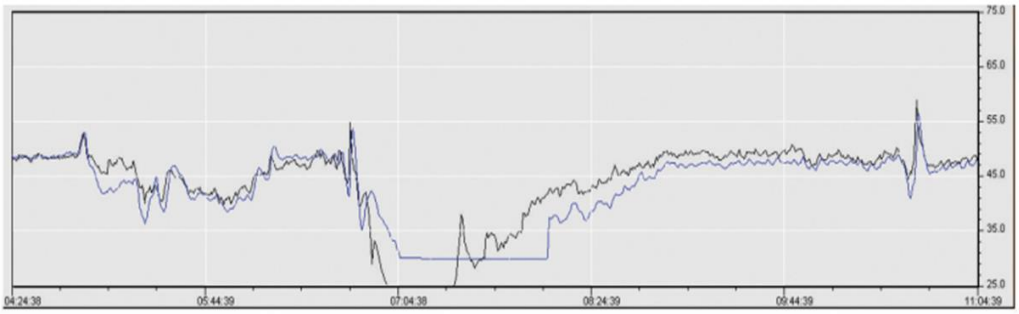


Figure 3.22. Comparison between physical (blue line) and virtual/predicted (black line) percentage of solids in the hydrocyclone slurry in the Oceana Gold Hale mine (SCHUG *et al.*, 2019).

From the point of view of HPGR operation, recent works (TOHRY *et al*., 2020, CHELGANI *et al.,* 2021) applied fully back-calculated models based on extended database to predict HPGR power and 80% passing size in the product. Results showed potential, but still missing validation for a large range of operating conditions.

# 4. METHODOLOGY

The work relies on proposing a novel HPGR online modeling approach. An industrial-scale application will be used as a case study, which relies on pressing iron ore concentrates in one of Vale's pelletizing plants at Complexo de Tubarão (Vitória, Brazil). This Section presents the experimental work and industrial surveys that were carried out, all the HPGR model implementation and all the main features that will compose the online modeling approach architecture.

The Section is divided in 4 subsections. Sections 4.1 and 4.2 will describe the material used and the set of experiments performed to assess the main ore characteristics and particle breakage behavior under confined conditions. Section 4.3 presents the industrial surveys carried out and all data collected from the process in order to investigate the online modeling approach, beyond discussing the pelletizing plant from Vale S.A. selected as a case study to apply the online model. Section 4.4 describes all modeling and simulation work, including the main model equations and online approach adopted.

## 4.1. Materials

Samples of four iron ore concentrates that are fed to Vale´s pelletizing plants at Complexo de Tubarão (Vitória, Brazil) have been collected. Three of these concentrates (Itabira, Brucutu and Timbopeba) are produced by flotation of ores from the Iron Quadrangle in the state of Minas Gerais (Brazil), having a top particle size of, approximately, 1 mm. The fourth consists of the result of preparation of ore from the Carajás mineral province (Pará, Brazil), being the top particle size about 10 mm. The blend feeding the pelletizing plant is composed by a mixture of these iron ore concentrates. For each iron ore concentrate, the specific gravity was measured using Helium pycnometry and the apparent (bulk) density was obtained from the ratio between the sample mass and a known volume. Particle size distribution was measured by laser scattering using Malvern Mastersizer 2000 (Malvern Instruments Inc) and Blaine specific surface area (BSA) was measured in a PCBlaine-Star (Zünderwerke Ernst Brün GmbH). A summary of the main physical characteristics for each iron ore concentrate analyzed is presented in Table 4.1.

Table 4.1. Summary of the main physical characteristics of the samples investigated.

| Sample | Specific gravity ($g/cm^3$) | Apparent density ($g/cm^3$) | 80% passing size (μm) | BSA ($cm^2/g$) |
|---|---|---|---|---|
| Brucutu | 5.03 | 3.02 | 234 | 480 |
| Itabira | 5.07 | 3.01 | 122 | 550 |
| Timbopeba | 4.80 | 2.85 | 152 | 380 |
| Carajás | 4.55 | 2.70 | 3197 | 544 |

### 4.2. Piston-and-die tests

Piston-and-die (P&D) tests are widely used to characterize high-pressure interparticle comminution process under confined conditions and to estimate the breakage parameters of different mathematical models that describe the HPGR performance (HAWKINS, 2007). Particles contained in three size ranges were tested, named 150-125 μm, 106-75 μm and 53-45 μm, which were prepared by careful wet sieving. The piston has a diameter of 40 mm and the resulting initial bed height was 13 mm. As such, these tests were conducted under ideal confined particle bed conditions (Section 3.5.1), as preluded by SCHÖNERT (1990, 1996), as $h_{bed} > 6x_{max}$ and $D_{bed} > 3h_{bed}$, where $h_{bed}$ is the bed height, $D_{bed}$ is the bed diameter and $x_{max}$ is the top size particle. Each test demanded about 30 g of sample.

The compressive forces were applied in the range of 50-1000 kN (40-795 MPa), and the deformation rate was maintained constant at 5 mm/min, which is equivalent to a strain rate of 0.0064 $s^{-1}$. The output of the test was the force–displacement curve. In addition, the bed of particles was removed from the die, dispersed and the size distribution measured. Size analyzes using Malvern Mastersizer (wet) were conducted directly of the material from the test, as well as of the material passing the screen used for the bottom size interval containing the narrow feed size.

To investigate the differences between breakage efficiency in a narrow size range and using a complete size distribution, a set of tests was carried out with Itabira sample covering all compressive forces depicted above.

An additional set of tests consisted of conducting multiple pressings of material contained in the 106–75 µm size range. The test considered that the initial bed pressed up to 200 kN (159 MPa), the load removed, the material dispersed and analyzed, then it was reloaded to the die and the same procedure repeated.

Force-displacement profiles were recorded for all tests to check the particle bed compaction behavior. From numerical integration it was possible to estimate the energy dissipated in the particle bed for each test. Specific energies were then calculated dividing the energy by the mass of the lot tested.

Figure 4.1 illustrates the servohydraulic press (Shimadzu Inc.) used, as well as details of the piston-and-die, showing the linear variable differential transformer (LVDT) used to measure the particle bed displacement. Elastic deformations of the system were subtracted from the deformations measured using the LVDT when considering a steel Young´s Modulus of 210 GPa.

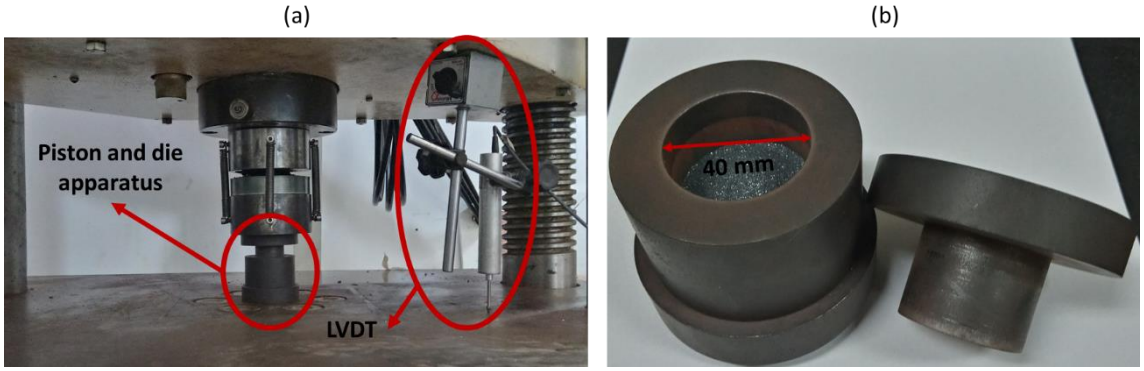


Figure 4.1. Experimental device from Shimadzu used in the piston-and-die tests highlighting the piston and die apparatus and the LVDT used to measure the particle bed displacement.

Tests carried out in this section would allow giving support to better describe the material breakage behavior in the modeling approach, which was pointed out in R#1a and R#1c as a key objective of the present work (Section 2).

## 4.3. Industrial surveys

### *4.3.1. HPGR performance investigation*

High-pressure grinding rolls operating in different pelletizing plants at the Complexo de Tubarão from company Vale (Vitória, Brazil) were investigated. The pelletizing plants are fed with a blend of iron ore concentrates from different mines, being composed predominantly by iron oxides, mainly hematite, with minor amounts of quartz, as already depicted in Section 4.1. A total of four experimental campaigns were conducted in four different industrial-scale machines (#1 to #4) to assess the performance of HPGRs in pellet feed pressing. Two different circuit design configurations were surveyed: roller presses #1 to #3 operated after ball milling, in regrinding prior to pellet formation (Figure 3.2) whereas roller press #4 corresponded to an HPGR in a pre-grinding operation, that is, prior to ball milling. Moreover, campaigns were conducted with a moisture content of 8 ± 0.5%, which is recognized to be close to the maximum value that is tolerated in HPGR operation involving iron ore pellet feed (VAN DER MEER, 1997).

Among the HPGRs, three of them (#1 to #3) were manufactured by Thyssenkrupp Polysius (current owned by FLSmidth) and the remaining one (#4) was manufactured by KHD/WEIR. All machines were connected to a supervisory system, which allowed capturing information on roll peripheral velocity, operating gap, operating pressure, power consumption and throughput. Care was taken to guarantee that the cheek plates were closely adjusted, with a gap smaller than 1.5 mm in respect to the rolls, and the autogenous main frame and wear parts were in very good condition, with no noticeable signs of wear. Process information from each survey was gathered when the supervisory system indicated that the HPGR was operating under steady-state conditions.

Table 4.2 summarizes the main operating conditions as well as the main material characteristics for the experimental campaigns on each of the HPGRs, while Figure 4.2 compares the mean size distributions of each feed.

Table 4.2. Summary of the main characteristics of the HPGR as well as of the feed material in the various surveys.

| | HPGR* | | | |
|---|---|---|---|---|
| | #1 | #2 | #3 | #4 |
| Roll diameter (m) | 1.7 | 2.25 | 2.0 | 1.4 |
| Roll length (m) | 1.4 | 1.55 | 1.5 | 1.6 |
| Aspect ratio (-) | 1.21 | 1.45 | 1.33 | 0.88 |
| Specific force (N/mm²) | 0.5 – 2.1 | 0.5 – 1.5 | 1.5 – 1.7 | 2.0 – 2.5 |
| Operating pressure (bar) | 40 – 100 | 25 – 75 | 60 – 80 | 50 – 65 |
| Roll peripheral velocity (m/s) | 0.5 – 1.7 | 0.8 – 1.0 | 1.5 – 1.9 | 1.3 |
| Operating gap (mm) | 9 – 22 | 9 – 12 | 9 – 12 | 6 |
| Maximum roll velocity (m/s) | 1.83 | 2.01 | 2.19 | 1.95 |
| Feed 80% passing size (µm) | 70 | 52 | 84 | 143 |
| Feed % passing 45 µm | 62 | 73 | 55 | 26 |
| Feed BSA (cm²/g) | 1750 ± 10 | 1700 ± 10 | 1650 ± 10 | 470 ± 10 |

**Each HPGR corresponds to one of the pelletizing plants from Vale S.A: HPGR #1 from Plant 6, HPGR #2 from Plant 3, HPGR #3 from Plant 8 and HPGR #4 from Plant 1*

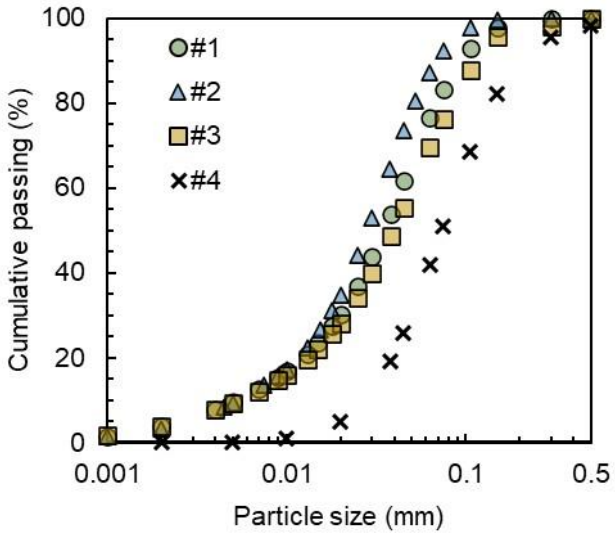


Figure 4.2. Mean size distributions of the feed to the various HPGRs studied in the present work.

The coarser feed size corresponding to HPGR #4 is consistent with its pre-grinding role in the circuit. The feed size distributions of the feed to HPGRs #1 and #2

are finer and consistent with the regrinding pre-pelletizing role of the machines downstream from ball mills operating in closed-circuit. Although with the same regrinding role, HPGR #3 is fed with material with slightly coarser top size, since upstream ball mills operate in open circuit.

The specific gravity of the feed for the different campaigns was measured using a Helium pycnometer and is average value is given as 4.9 t/m$^3$. The bulk density was obtained from the ratio between the sample mass and a known volume and is given by 3.0 t/m$^3$, whereas the flake density was measured using Archimedes principle with preserved flakes from one operation, being its average value around 3.5 t/m$^3$. Both bulk and flake densities were kept constant for simulations purposes. For all industrial surveys carried out the blend feed the plants was estimated in 54% Brucutu and 46% Itabira.

For each survey, samples were collected along the axial roll position during the HPGR discharge in order to assess the variation in size reduction along the roll length. Samples were collected in seven different points using a manual sample cutter introduced underneath the rolls. Right after that the HPGR operation was interrupted and samples from the feed and product conveyors were also collected from belt cuts.

All samples were quartered, dried, and subjected to wet size analysis by laser scattering in a Malvern Mastersizer 2000 (Malvern Instruments Inc) and Blaine specific surface area (BSA) in a PCBlaine-Star (Zünderwerke Ernst Brün GmbH).

All analysis carried out in the industrial survey would provide the necessary information to calibrate, validate and modify the phenomenological model used in the present work, which was depicted as one of the research objectives (R#1b and R#1d) in the present work (Section 2).

### *4.3.2. Case study in Plant 3*

One of the pelletizing plants from Complexo de Tubarão from Vale S.A. (Vitória, Brazil), which relies on the plant operating with HPGR #2 (Table 4.2), was selected as case study for the online model application. This plant relies in a circuit configuration with the HPGR operating in regrinding prior to pellet formation (Figure 3.2) and is composed of at least six main unit operations in the pellet feed preparation

circuit, named ball milling, hydrocyclone classification, thickening, homogenization, filtering and HPGR.

The ball milling is divided in two different and independent lines using two ball mills with 5.2 m (17.1 ft) of internal diameter and 10.6 m (34.8 ft) of effective length, besides being equipped with two 2.25 MW drivers. The mill operates with overflow discharge and the mill liners are made of rubber. Each ball mill has a nominal fresh feed capacity of 200 t/h. Both ball mills operate in closed circuit with a cluster containing six hydrocyclones with 500 mm diameter and an average inlet pressure around 0.95 ± 0.15 kgf/cm². Detailed descriptions and investigations of a similar operation for iron ore concentrates can be found elsewhere (FARIA *et al.,* 2019). The overflow from the hydrocyclone cluster is used to feed a single Dorr thickener with 50 m of diameter, 2.95 m effective length, and a nominal capacity 2200 m³/h. The thickener underflow is divided in two slurry tanks with an effective volume of 1600 m³ and a nominal capacity of 3000 t/h each that are used to compose the homogenization stage. At the end of the HPGR upstream operation, the slurry from the homogenization tanks feeds nine Simpson® disk filters with a total area of 75 m².

Finally, the HPGR #2 from Plant 3, which was already presented in Section 4.3.1 (HPGR #2), is the focus of investigation in the present work. Figure 4.3 presents a shot of the HPGR #2 (Plant 3) highlighting some of the main machine settings.

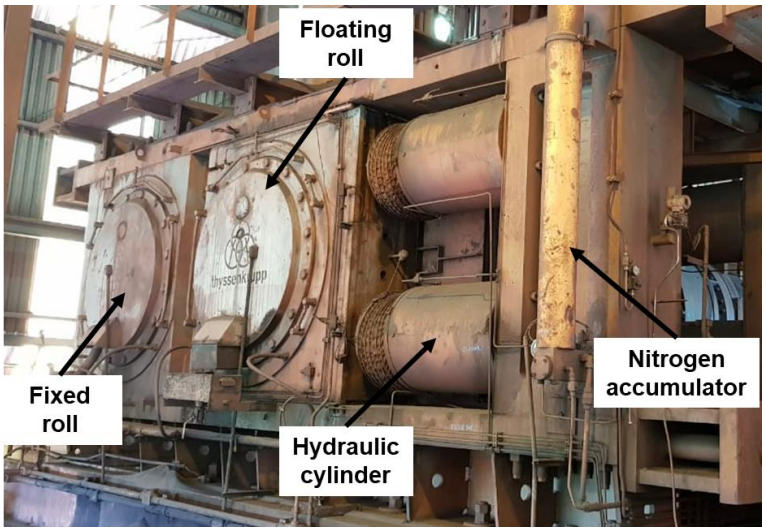


Figure 4.3. HPGR #2 (Plant 3) in operation.

Given its large roll dimensions (Table 4.2), the machine faces a particular challenge by operating below the designed capacity since the feed hopper does not allow to keep the HPGR operating in choke fed condition, thus driving the machine to operate with roll peripheral velocities below the recommended value. As already presented in Section 3.4.9, the machine is controlled by torque regulation following the OCS based in fuzzy logic (OCS PLANT 3, 2019).

In addition to information presented in Table 4.2, Table 4.3 summarizes the main range of operating conditions and performance variables of the machine, beyond including characteristics from the hydro-pneumatic pressurizing system.

Table 4.3. Operational ranges and hydro-pneumatic settings from HPGR #2 (Plant 3)

| Operational ranges | | Hydro-pneumatic system | |
|---|---|---|---|
| Operating pressure (bar) | 20 – 180 | Piston diameter (mm) | 600 |
| Roll velocity (m/s) | 0.2 – 2.01 | Number of piston (-) | 4 |
| Operating gap* (mm) | 5 – 15 | Initial oil pressure (bar) | 20 – 180 |
| Nominal throughput (t/h) | 400 – 1200 | Initial $N_2$ pressure (bar) | 41.5 |
| Total power consumption (kW) | 500 – 3600 | Zero gap* (mm) | 5 |

**Measured by the edge of the rolls*

To investigate the wear profile along the roll length a method was adopted as described in Figure 4.4. The method relies on simply measuring the distance between the top of the studs and a metal strip placed in front of the rolls along their axial position (Figure 4.4). A digital caliper was used to measure the distance between the roll surface and the metal strip periodically in sixty-three studs selected in both rolls, which allowed an assessment of the rolls from the beginning of the roll lifetime up to 15,000 hours of operation. It is worth mentioning that measurements made using this methodology allow to have an idea about the wear shape profile along the roll length. Nevertheless, recent works analyzing the same HPGR operation demonstrated that the method adopted would overestimate a bit the real roll surface wear (BUENO, 2019).

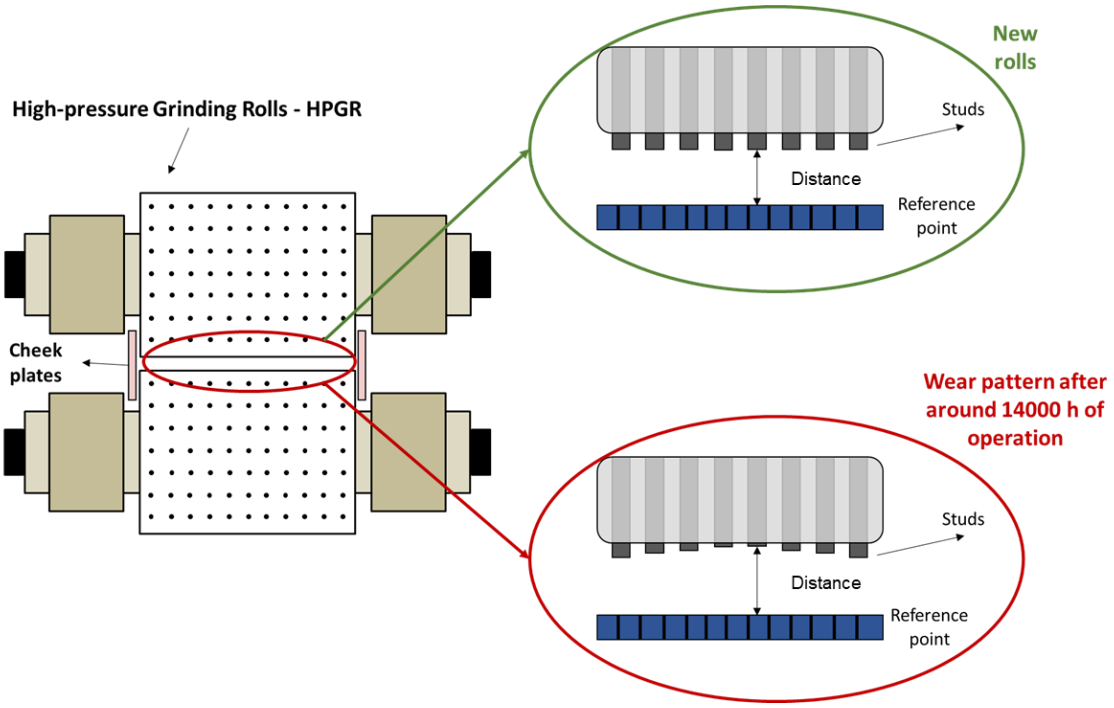


Figure 4.4. Scheme showing the experimental device used to measure the distance between a reference point and the top of different studs along the roll length. The green insert presents the rolls at the beginning of the wear lifetime, whereas the red insert presents a qualitative wear profile after 15,000 hours of operation, which is usually the entire wear lifetime for HPGRs pressing iron ore concentrates.

### *4.3.3. Data collection*

All the pelletizing plant is equipped with a supervisory system that allows capturing information in real time about several operational variables, which is called Process Information Management System (PIMS). For the present work a period of 24 months was selected with information being gathered in a frequency of 5 min, which corresponded to 210,240 for each process variable analyzed. Data points for a total of 42 process variables among all unit operations depicted above were selected for investigation. For the particular case of the HPGR operation, data collected relies on roll peripheral velocity, operating pressure, operating gap, throughput and power consumption.

The supervisory system also allows capturing real-time information of the size distribution and Blaine specific surface area (BSA) from an estimation using the Metso Outotec PSI 300i Particle Size Analyzer (PSI). The information is recorded in the

hydrocyclone overflow (which is associated to the size distribution of the HPGR feed as showed in Figure 4.5) and corresponds to six index measurements of size distribution, named: percent passing in 8 µm, percent passing in 13 µm, percent passing 38 µm, percent passing in 45 µm, percent passing in 75 µm and Blaine specific surface area. Recent analysis made the operational team from Vale S.A. (BUENO & OLYMPIO, 2021) indicated that no reliability existed on the BSA estimations made by the PSI.

Therefore, to ensure a proper analysis of the BSA of the HPGR feed and product, data from samples that are routinely collected using an automatic sample cutting system for offline laboratory analyzes every 4 hours in the entire period were used. These samples were subjected to BSA measurements using a PCBlaine-Star (Zünderwerke Ernst Brün GmbH). A total of 4,380 points were collected in this second dataset, which is related to BSA of the HPGR feed, HPGR product and pelletizing plant fresh feed. An additional dataset with information about the proportion of each iron ore concentrate composing the blend (Section 4.1) used to feed the pelletizing plant was also recorded every day in the entire period. For this dataset, a total of 730 points were collected. The proportion of each iron ore concentrates used to compose the blend feeding the pelletizing plant was collected at the fresh feed of the pelletizing plant. It is worth mentioning that information collected at this point corresponds to average estimation of all different stockpiles used for operation in the pelletizing plant used as a case study in the present work, which allowed to ensure a more reliable estimation of this blend composition. Blend composition relied on the iron ore concentrates presented in Section 4.1.

Figure 4.5 then presents a schematic diagram with a vision of the entire pellet feed preparation circuit and the main operational variables from the supervisory system and laboratory analyzes. Green squares represent data points collected every 4-hours in the fresh feed and HPGR feed and product (Blaine specific surface area), red circles represent the particle size distribution indexes and blaine specific surface area measured in the PSI for both ball milling lines, while blue triangles represent all the process variables recorded in real-time in the supervisory system (PIMS). Green squares in the fresh feed also represent the blend of iron ore concentrates used to feed the plant and estimated every day frequency.

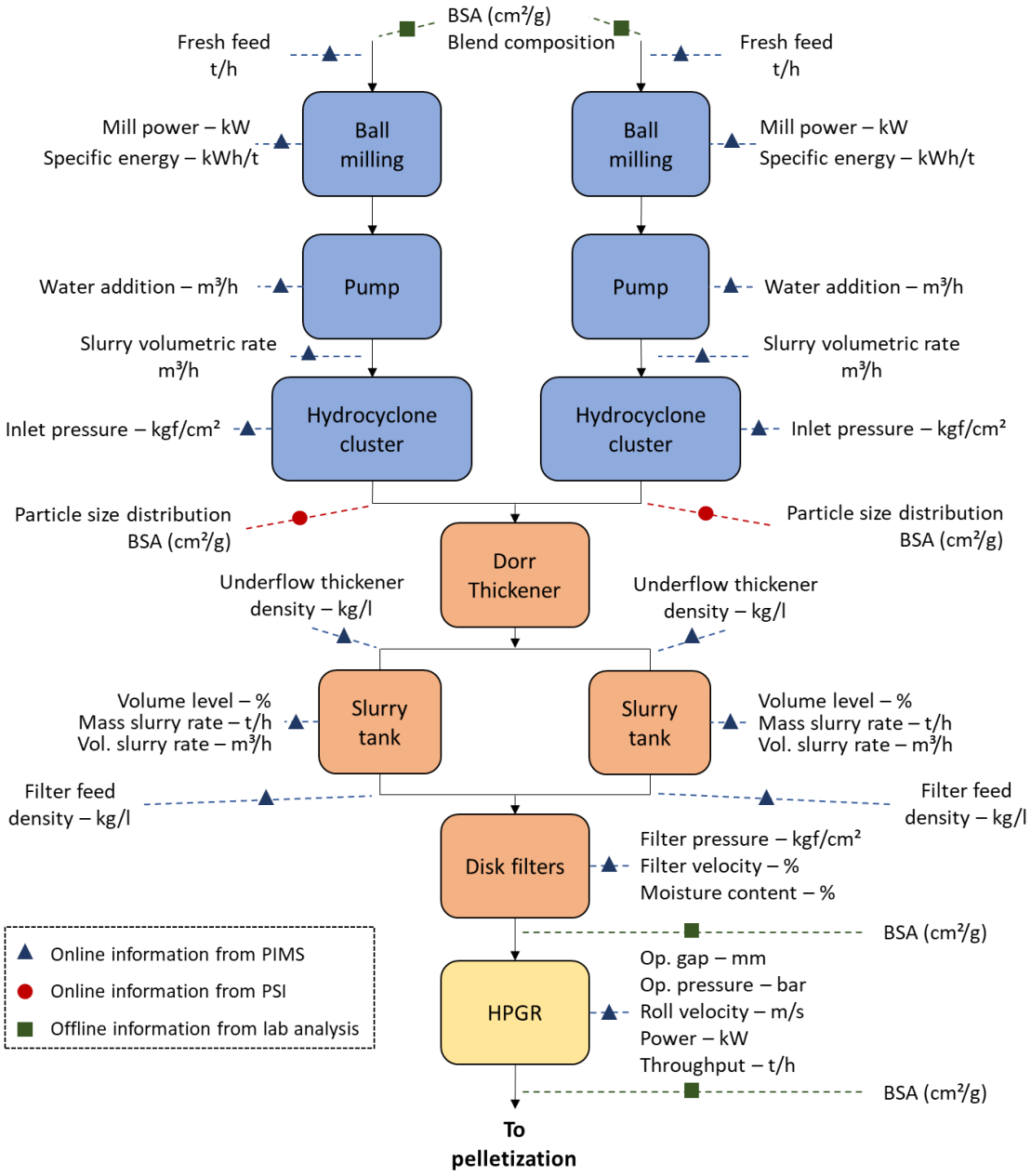


Figure 4.5. Schematic diagram highlighting all the operational variables gathered from the supervisory system for the circuit. Red circles represent the point in which information from the PSI is recorded, whereas green squares represent the sampling point in which sample is collected for BSA measurements in laboratory analysis. Blue triangles are online information recorded from the supervisory system (PIMS).

Aiming a reliable data quality assessment using the information collected from the process, two steps were used in the present work. First, considering the mismatch in frequency of data from PIMS and the laboratory, reconciliation between both became

necessary. As such, the value of the BSA for the HPGR feed and product measured every 4h frequency was assumed as being representative of the average of the last four hours within the process and, therefore, its value was replicated for these previous four hours considering the frequency of 5 min adopted in the PIMS dataset.

Considering the new data reconciled, the second step consisted of cleaning the data to avoid missing values, data outliers, measurement disturbances and low accuracy in all process variables. Data deletion strategy was adopted to deal with missing values, which is considered acceptable when the amount of missing data is only a negligible fraction of the entire dataset (QIN *et al.,* 2007). To remove data outliers, a preliminary stage consisted of censoring data when they do not satisfy physical conditions and usual operating ranges, as presented in Tables 4.2 and 4.3. Outliers were also identified and removed when their individual value exceeded three scaled median absolute deviation from median (MAD), being the scaled MAD given as (ROUSSEEUW & CROUX, 1993):

$$MAD = -\frac{M|var_i - var_{50}|}{2^{0.5} erfc^{-1}(3/2)} \tag{4.1}$$

where *M* is the reference for median calculation, $var_i$ is the variable in index $i$, $var_{50}$ is the median for the variable *var* and $erfc^{-1}$ is the inverse complementary error function. After data reconciliation and data cleaning a total of 130,385 data points served as the basis for modeling and simulation, which is related to the entire 24-month period.

## 4.4. Modeling and simulation

### *4.4.1. HPGR model implementation and calibration*

The Modified Torres and Casali model (TORRES & CASALI, 2009; CAMPOS *et al.,* 2019b) was selected to be used in the present work. Considering the detailed HPGR modeling overview presented in Section 3.6, it is possible to conclude that models from MORRELL *et al*. (1997) and DUNDAR *et al.* (2013) are unable to predict the product size distribution along the rolls length, being unable to discriminate between center and edge products. Moreover, the model proposed by DUNDAR *et al.* (2013)

does not contain an expression to predict the HPGR power consumption and throughput (YAHYAEI *et al.*, 2020). On the other hand, the model proposed by Torres and Casali (TORRES & CASALI, 2009) has the advantage of allowing a detailed description of the particle breakage along the roll's length, besides providing physical description of all HPGR performance variables. In addition to that, the Modified Torres and Casali model proposed by the authors (CAMPOS *et al.*, 2019b) has being validated under a wider range of conditions pressing iron ore concentrates in a pilot-scale HPGR and demonstrated to be the most versatile model among the ones analyzed.

The model was then implemented in Matlab® (version R2022a, Mathworks Inc.) to perform all the simulations. The main equations for the Modified Torres and Casali model, detailed discussed in Section 3.6, are summarized in Table 4.4.

Table 4.4. Summary of the main equations in the Modified Torres and Casali model

| | | |
|---|---|---|
| Throughput | $\boldsymbol{Q = LU_g\rho_g\chi_g\left(\frac{100}{100-\delta}\right)}$ (TORRES & CASALI, 2009, CAMPOS *et al.*, 2019b) | $\boldsymbol{\ln\left(\frac{\delta}{\varphi}\right) = -v\frac{\chi_g}{D}\left(\frac{U}{U_{max}}\right)^{\tau}}$ (CAMPOS *et al.*, 2019b)<br>$\boldsymbol{U_g = \frac{U\chi_c}{\chi_g}\frac{\rho_a}{\rho_g}}$ (CAMPOS, 2018) |
| Compressive force | $F_m = p_m\frac{D}{2}L$ (TORRES & CASALI, 2009) | |
| Power consumption | $P = 2F_m\sin\left(\frac{\kappa\alpha_{ip}}{2}\right)U$ (TORRES & CASALI, 2009, CAMPOS *et al.*, 2019b) | $\cos\alpha_{ip} = \frac{1}{2D}\left[\left(\chi_g + D\right) + \sqrt{\left(\chi_g + D\right)^2 - \frac{4\chi_g\rho_g D}{\rho_a}}\right]$ (TORRES & CASALI, 2009) |
| Product size distribution | $w_{i,k} = \sum_{j=1}^{i} A_{ij,k}exp\left(-\frac{S_{j,k}}{v_z}z^*\right)$ (TORRES & CASALI, 2009) | $P_k = 2F_m\sin\left(\frac{\kappa\alpha_{ip}}{2}\right)U\frac{L^2-4y_k^2}{\sum_{j=1}^{N_B}(L^2-4y_k^2)}$ (TORRES & CASALI, 2009, CAMPOS *et al.*, 2019b) |
| Breakage function | $B_{i,j} = \phi\left(\frac{x_i}{x_j}\right)^{\gamma} + (1-\phi)\left(\frac{x_i}{x_j}\right)^{\beta}$ $x_i \geq \omega$<br>$B_{i,j} = \phi\left(\frac{x_i}{\omega}\right)^{\eta}\left(\frac{x_i}{x_j}\right)^{\gamma} + (1-\phi)\left(\frac{x_i}{x_j}\right)^{\beta}$ $x_i < \omega$ (KING, 2001) | |
| Selection function | $\ln(s_i^E/s_1^E) = \xi_1\ln(\bar{x}_i/\bar{x}_1) + \xi_2\ln(\bar{x}_i/\bar{x}_1)^2$ (HERBST & FUERSTENAU, 1980) | $S_{i,k} = \frac{P_k}{H_k}s_i^E$ (HERBST & FUERSTENAU, 1980) |

A non-linear optimization method was used to calibrate the breakage parameters (Eqns. (3.39) and (3.46)), which basically relies in a function available in Matlab®, called *fminsearch*, able to find the minimum of a multivariable scalar function using a derivative-free method from an initial estimation (LAGARIAS *et al.*, 1998). The objective function consisted of the sum of the differences in the logarithms of the experimental and the fitted values of the particle size distribution of a reference test in cumulative form using the least squares method:

$$f_{obj} = \sum_{i=1}^{N} \left[ \log\left(W_{Calc}^{HPGR}(i)\right) - \log\left(W_{Exp}^{HPGR}(i)\right) \right]^2 \qquad (4.2)$$

where $N$ is the number of size classes, $W_{Calc}^{HPGR}$ and $W_{Exp}^{HPGR}$ are, respectively, the calculated and experimental fraction passing in size $i$. The objective function was proposed in the logarithmic form in order to ensure a more reliable description of the fine part of the size distribution. Figure 4.6 shows a schematic diagram highlighting the optimization method adopted.

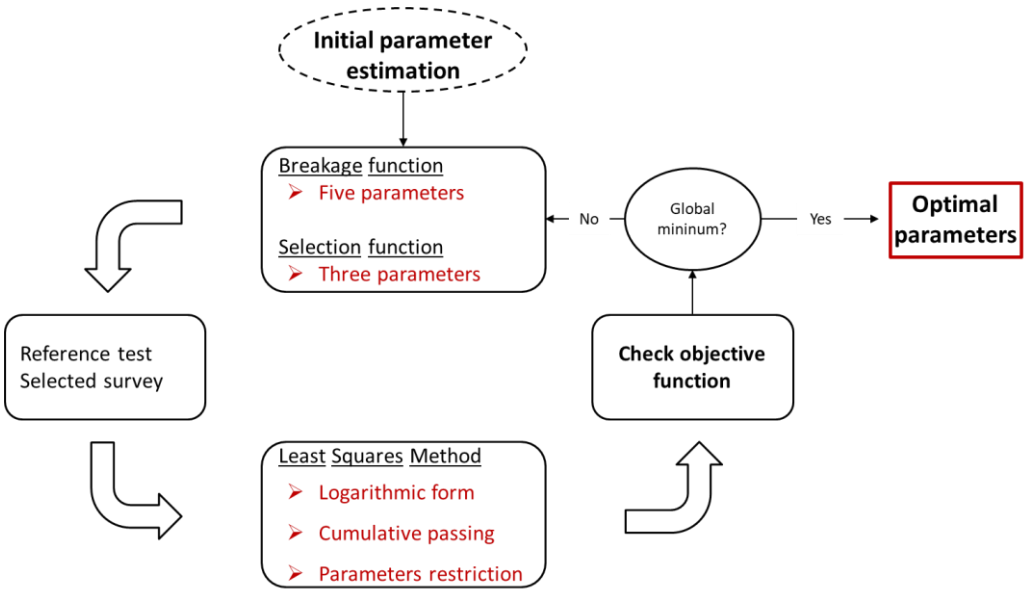


Figure 4.6. Schematic diagram showing the method used to estimate the optimal parameters able to describe the material breakage response. Parameters were fitted from Eq. (3.39) and (3.46).

Parameters restrictions assumed: $\beta > \gamma$; $\gamma > 0$; $0 < \phi < 1$; $0 < \omega < x_{max}$; $0 < \eta < 1$; $s_1^E > 0$; $\xi_2 < 0$. Model application will be analyzed on the basis of comparisons between measured and predicted values and using the absolute relative deviation from measurements ($\varepsilon$), which is defined as $\varepsilon = 100|var_{Meas} - var_{Pred}|/var_{Meas}$. Where $var_{Meas}$ and $var_{Pred}$ are the measured and predicted variables, respectively.

*4.4.2. Online model structure*

Sources of variability that influence the performance of the HPGR in the application in question vary according to type and to their scale of time. Important variations are related to the feed ore characteristics in terms of the sources and proportions of concentrates that make up the feed to the plant. This influences the fresh feed to the comminution circuit and, therefore, its size distribution, besides the actual susceptibility of the material to size reduction in the first ball milling stage and the downstream HPGR. Such variations exhibit mid- and long-term variations, since they are associated to the planning of the make-up of the feed to the pelletizing plant. Variability in the feed to the HPGR is, therefore, influenced by operation and control strategies adopted in the ball milling circuit upstream, besides conditions of individual units. In this regard, variations in the filling and liner condition of the ball mill, besides wear of hydrocyclone parts are some of the most significant. In addition, operation and control strategies of the ball mill circuit can induce significant short-term fluctuations, although its role would be to reduce them. On the other hand, variations in machine condition are more in the mid- and long-term scales, since they are associated to wear, which is a gradual variation, including resulting from the rolls.

The online model structure will be analyzed in the present work following two modules. The first one relies on the assumption that no reliable estimation of the HPGR feed BSA can be made, thus imposing the use of the reconciled dataset with the measured HPGR feed BSA every 4 hours frequency as previously discussed in Section 4.3.3. The second module will assess the potential application of a data driven soft sensor model to estimate the HPGR feed BSA on the basis of online data from the ball milling and classification step. That information will then be used as an input to the HPGR model in order to predict the machine performance. Figure 4.7 presents an overview of the online model structure and its main components.

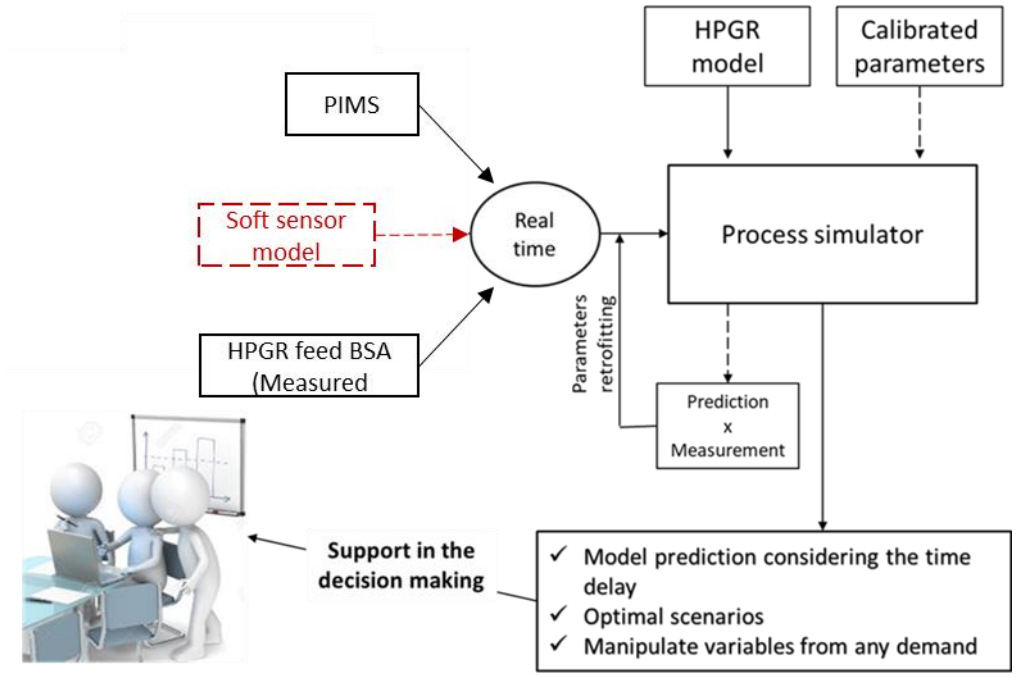


Figure 4.7. Schematic diagram of the online model structure and its main components. Soft sensor model highlighted in red color should be used in the second module of the online approach.

For both cases, the online model relied on the application of the Modified Torres and Casali model coupled with real-time information about HPGR operating conditions and feed characteristics. Model predictions are assessed on the basis of the absolute relative deviation from measurements and from time series comparisons. The basis of the online modeling approach can be summarized on the three following main points:

- Operational system: The supervisory system from the pellet feed preparation circuit should work properly to ensure reliable information feeding the model structure. Use of Information about online measurements as the operating conditions and solids rate of the process are required in real-time.

- HPGR feed: Information measured every 4-hours are used as model input in a reconciled dataset as depicted in Section 4.3.3. Information about the blend of different iron ore concentrates feeding the pelletizing plant is also used in the modeling approach. A second module based on a data-driven soft sensor model used to predict the HPGR feed BSA is investigated.

- Process simulator: Simulations will be carried out based on the Modified Torres and Casali model with the main equations presented in Table 4.4 (CAMPOS *et al.*, 2019b), which provides a real-time rapid response based on operating conditions, feed characteristics and machine settings. For this purpose, the model will be applied following a pseudo-dynamic approach.

*4.4.3. Particle size distribution to BSA*

Taking into account the key model requirement of using the complete feed size distribution as an input, it is key to bear in mind that measurements from the HPGR feed BSA should be converted in a feed size distribution. As such, the present work proposes that the feed sizes follow a Rosin-Rammler distribution function, given by:

$$W_i = 1 - exp\left[-\left(\frac{x_i}{x^*}\right)^{\alpha}\right] \tag{4.3}$$

where $x_i$ is particle size (mm) and $x^*$ is the 62.3% passing size (mm). Based on a database containing 162 measurements of BSA and size distributions from the process, a relationship was then proposed to calculate the size parameter $x^*$ as a function of the Blaine specific surface area. Figure 4.8 presents the relationship between these two variables for 80% of the database, which was randomly selected as calibration dataset.

The clear linear relationship between this parameter and BSA suggests a simple linear equation to describe it, represented by:

$$x^* = 126.5 - 0.0412 BSA_{Feed} \tag{4.4}$$

where $x^*$ is given in µm and $BSA_{Feed}$ is the Blaine specific surface area (cm²/g) of the HPGR feed gathered from laboratory measurements. The parameter $\alpha$ in Eq. (4.3) was set to the optimal constant value of 0.97. Predictions made using Eq. (4.3) were then compared to the respective experimental size distributions for both calibration datasets

(80% used for training) and validation data set (the remaining 20% of the original dataset) using Eq. (4.2). Results demonstrate the good predictive capabilities of the model with average values for the objective function for calibration and validation data sets of 0.04 and 0.06, respectively. Figure 4.8 also exhibits the 10% bounds for the relative deviations between model (black line) and fitted sizes (green circles).

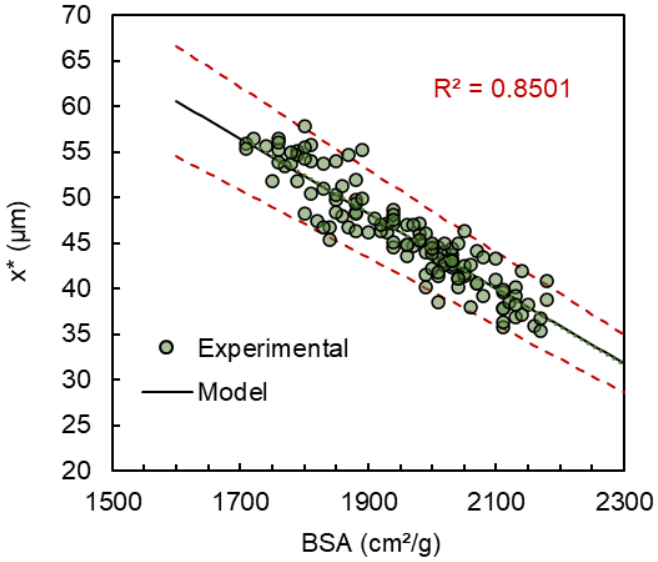


Figure 4.8. Relationship between BSA for several measurements carried from industrial surveys and the critical size fitted in Eq. (4.3). Green circles are values fitted from Eq. (4.3) and black line is the model prediction by Eq. (4.4). The red dotted lines bound the region with relative deviations between black line and experiments up to 10%.

Predicted product size distribution will be used to calculate the product BSA from a method proposed elsewhere (ZHANG & NAPIER-MUNN, 1995) and already used for pressing iron ore concentrates (CAMPOS *et al.*, 2019a). Calibration of this model with data from industrial-scale HPGR pressing iron ore concentrates is presented in Appendix A.

### *4.4.4. HPGR online digital assistant architecture*

The online model structure will be used as a digital assistant aiming to find the best set of conditions that should be used in the industrial HPGR when dealing with

real-time variabilities in the feed BSA. The main idea behind the algorithm is to define a desired setpoint for a given HPGR performance variable and then find a reasonable set of operating conditions to achieve this target value.

Unlike the torque regulation control strategy originally used by the Plant 3 (OCS PLANT 3, 2019), which was previously discussed in Section 3.4.9, the present work applies the online model to regulate the HPGR product BSA and the throughput using setpoints that will keep the quality of the final product and to keep the machine production rate. As such, to achieve this setpoint, the algorithm proposed will be able to change operating conditions following the operational ranges presented in Tables 4.2 and 4.3, which are also lined-up with limits on the control system used by industrial HPGR (OCS PLANT 3, 2019).

For the particular case investigated in the present work (HPGR from Plant 3), the algorithm states the operating pressure as the main manipulated variable, being the operating gap reached as a consequence of the hydro-pneumatic system and the particle bed stiffness. As such, to ensure operating gap being correctly predicted after setting up the operating pressure, the present work considers a relationship between both variables on the basis of the hydro-pneumatic model depicted in Section 3.6.4 and further investigated in Section 6.6. Additional secondary operational variable as the roll peripheral velocity is also considered as manipulated variable, which is well-known recognized to achieve a given setpoint for power consumption and throughput (DANIEL, 2022). Eq. (4.5) then presents the objective function used to find the optimal set of operating conditions that satisfies the setpoint for selected performance variables:

$$f_{obj}^{Setpoint} = \sum_{j=1}^{N_{var}} \psi_{var,j} \left( \frac{var_{Pred,j} - var_{SP,j}}{var_{SP,j}} \right)^2 \tag{4.5}$$

where $var_{Pred,j}$ is the predicted variable $j$, $var_{SP,j}$ is the setpoint for variable $j$ and $\psi_{var,j}$ is the weights used for the setpoint in each variable $j$. As a default, $\psi_{var,j}$ is equal to 1.

Two simulation case studies will be carried out in order to assess the potential application of the online model finding optimal routes based on real-time variabilities in

the HPGR feed BSA. Simulations considered HPGR operating in January 2017 when the rolls were relatively new.

- **Case study 1:** Reducing the variability of the HPGR product

This case study applies the online model structure aiming to reduce the HPGR product BSA variability. As the HPGR is situated in the boundary between the end of the pellet feed preparation step and the beginning of the pellet formation process (Figure 3.2), the equipment occupies a critical position aiming to increase the BSA of the iron ore concentrate and potentially allowing to deliver a more homogenous product to the downstream operation. Nevertheless, current analysis from the process (Figures 7.7 and 7.8) showed how the HPGR product BSA is mainly governed by the trend imposed by the feed BSA coming from the upstream operation. Assuming that no changes would be possible in the upstream operation to reduce the variability of the HPGR feed BSA, this simulation case study proposes to define a desired setpoint of 1850 cm²/g for the HPGR product BSA and 600 t/h for the throughput. Target values were defined as the average value in the entire period assessed for each operational variable optimized. Figure 4.9 shows a comparison between the base case and the desired setpoint for both HPGR product BSA (a) and throughput (b), showing that target values selected are in position to keep the quality of the final product and the HPGR solids production in the plant.

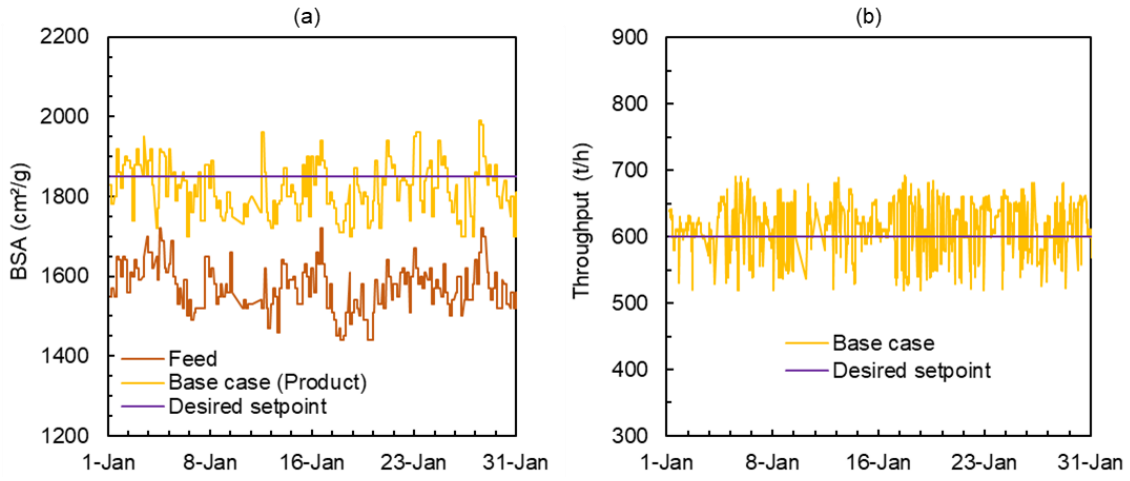


Figure 4.9. Comparison between data from the base case and the target value selected as a desired setpoint for the HPGR product BSA (a) and throughput (b) in the entire period assessed in January 2017. Data is presented every 5 min frequency.

- **Case study 2:** Reducing the ball milling work

Case study 2 relies on transferring work carried out by the ball milling (upstream) to the HPGR. As the ball milling steps are recognized for the higher inefficiency during grinding with an average energy utilization around 90 cm²/g/kWh/t (VIANNA *et al.*, 2019), an interesting scenario would be to reduce the work carried out by the ball milling stage and transfer it to the HPGR operation, which has an average energy utilization around 120 cm²/g/kW/t (CAMPOS *et al.*, 2019a). Therefore, a scenario will be analyzed with a reduction in the HPGR feed BSA of 100 cm²/g in the entire period investigated. The desired setpoint for the HPGR product BSA and throughput are again defined as 1850 cm²/g and 600 t/h, respectively. Figure 4.10 presents a comparison between the feed in the base case and the proposed coarser feed used in this case study.

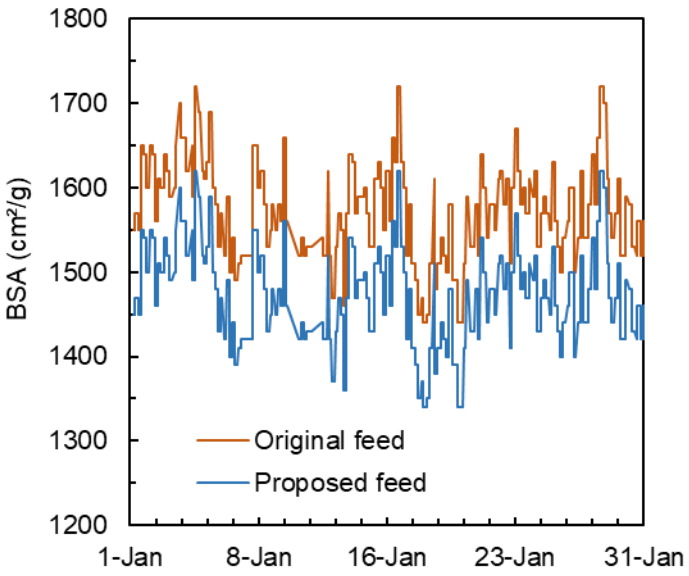


Figure 4.10. Comparison between HPGR feed BSA used in the base case (original feed) and the proposed HPGR feed BSA used in case study 2 (proposed feed) for the entire period assessed in January 2017. Data is presented for 5 min frequency.

## 5. PARTICLE BREAKAGE UNDER CONFINED CONDITIONS

### 5.1. Force deformation profiles

Extensive piston-and-die tests were carried out with the aim of investigating the breakage behavior under confined conditions with the four different iron ore concentrates.

One of the key results provided by piston-and-tests is the force-deformation profile achieved after compression, which can be presented on the basis of the vertical stress applied instead of compressive forces. Figure 5.1 then presents the stress–deformation curves for different forces for the Itabira sample, highlighting the load and unload (relief) curves.

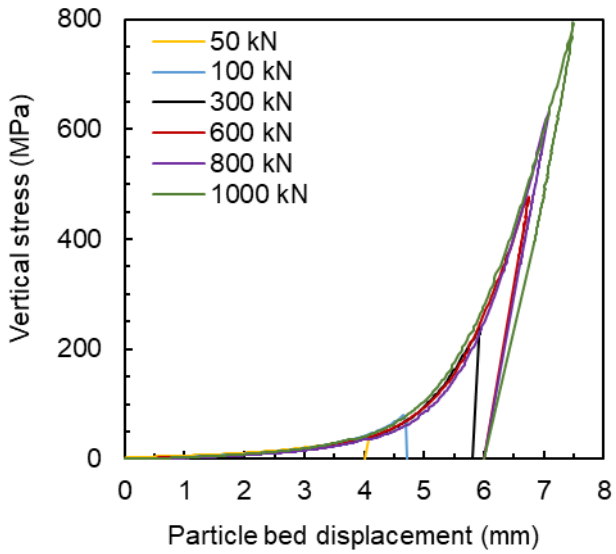


Figure 5.1. Load and unload stress–deformation curves in piston-and-die tests up to different applied compressive forces for the Itabira sample contained in the size range of 150–125 µm.

It is evident that, when the bed is compressed up to relatively small loads, named below 80 MPa (100 kN), no elastic recovery appears, with no recoil of the bed. MÜTZE (2015) observed that, in this case, all energy applied to the bed is either dissipated in rearranging the particles or in producing particle breakage. Under such conditions, the thickness of the bed after unloading progressively reduces as loads increase. Beyond this point, as loads increase, the force–displacement curves become steeper. In this case,

unloading exhibits progressively more elastic response, with the bed presenting ever more elastic recovery, which becomes evident from the lower slopes of the unloading curves.

Stress–deformation curves such as those in Figure 5.1 may also be presented more suitably as a function of the packing density (ratio between apparent density of the bed and specific gravity) according to different levels of vertical stress applied. Results are presented in Figure 5.2 for the Itabira and Carajás samples contained in the narrow particle size range of 150–125 µm. For a vertical stress of 800 MPa (1000 kN), the Itabira sample presented a maximum packing density of around 0.88, whereas a maximum of 0.95 was reached for the Carajás sample. The reasonable difference in the curves indicates a softer response for the Carajás sample under compressive loads. In addition, both results can show that, even though different vertical stresses were applied, the final packing density after total relief was nearly constant for each material, being equal to around 0.70 for the Itabira and 0.75 for the Carajás samples.

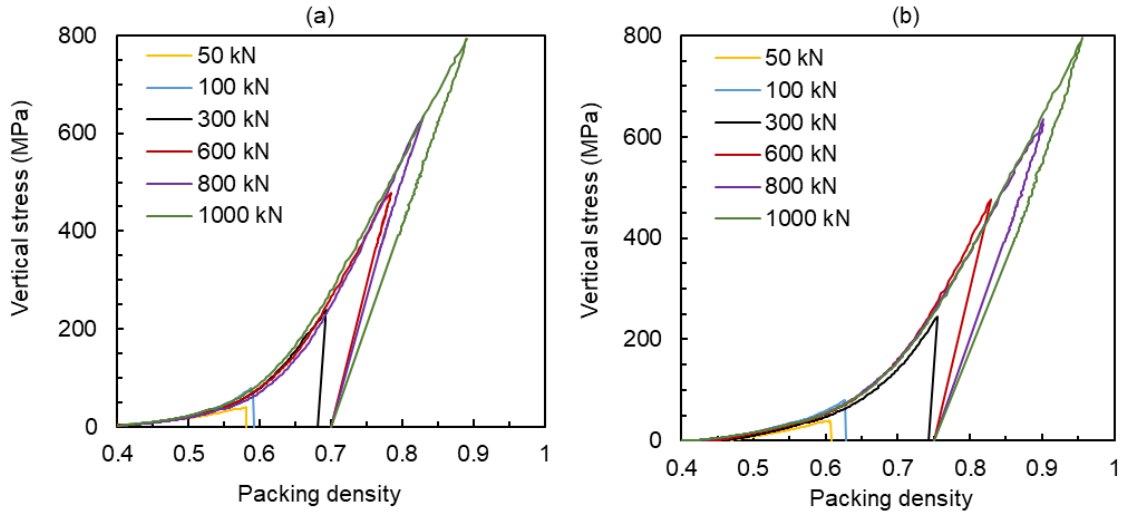


Figure 5.2. Relationship between the vertical stress and the packing density for different compressive forces applied for the (a) Itabira and (b) Carajás samples in the narrow size range of 150–125 µm in the piston-and-die system.

Relationship between vertical stress and packing density were also analyzed in different size classes for Itabira and Carajás sample (Figure 5.3). Results indicated variations in the compaction behavior for Itabira sample according to the different initial

particle sizes. Similar to results presented elsewhere for pharmaceutic powders (CABISCOL *et al.*, 2020), the larger initial size classes were softer than the small ones. Carajás sample, on the other hand, showed an almost ever constant profile for different initial size classes (Figure 5.3b).

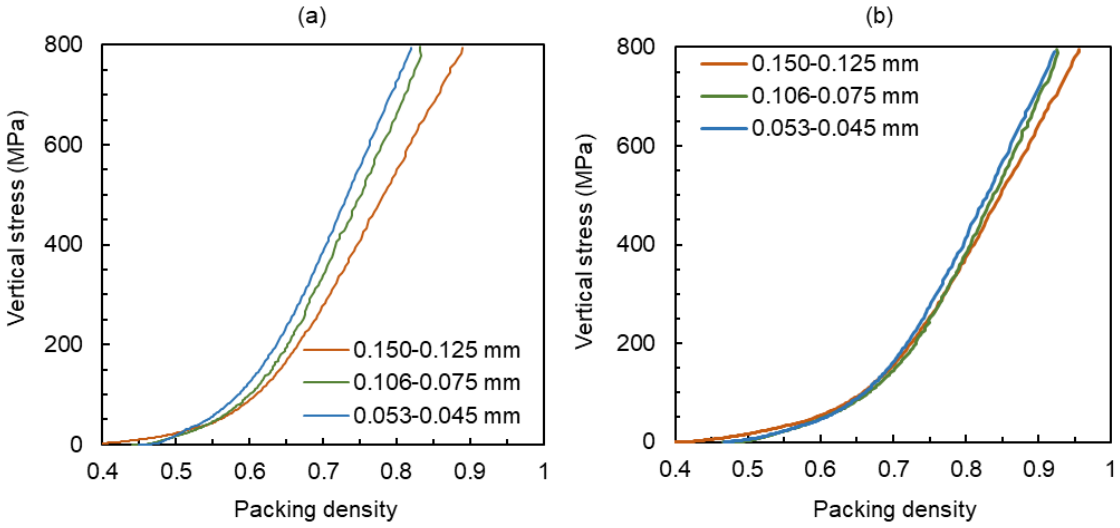


Figure 5.3. Relationship between vertical stress and packing density for Itabira (a) and Carajás (b) according to different initial size classes for the piston-and-die system. Vertical stress is presented up to the maximum compressive force used (1,000 kN).

A more detailed examination of the results is possible by calculating the areas below the curves. The input energy is given by numerical integration of the curves up to the maximum compressive force, whereas the elastic energy is given by the area corresponding to the unloading of the piston. The inelastic or dissipated energy is simply given by the difference between the two. Results are presented in Figure 5.4, which shows the rapid increase in elastic energy with the increment in vertical stress. The results also show that for low compressive forces the elastic energy is almost negligible, whereas it corresponds to around 60% of the input energy for the highest compressive force. Results from Figure 5.4 are lined up with analysis carried out by KALALA *et al.* (2011) using piston-and-die tests with platinum, gold and iron ores with top particle size of 12 mm.

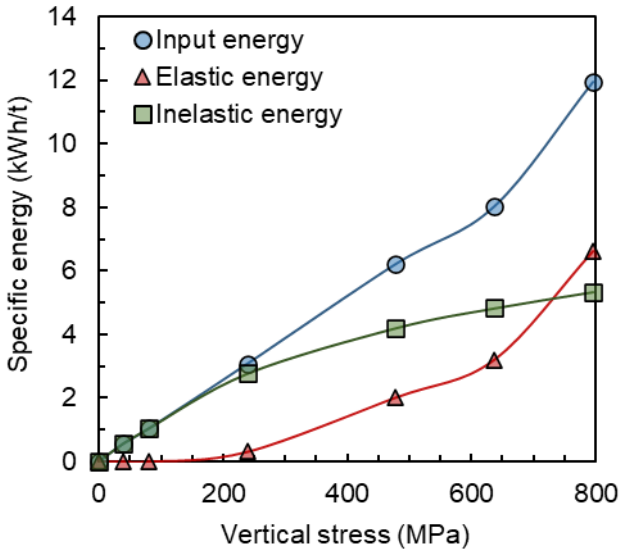


Figure 5.4. Variation of the input, elastic, and inelastic energy in the particle bed as a function of vertical stress for the Itabira sample in the narrow size range of 150–125 µm.

To assess the particle bed behavior under multiple pressing cycles, Figure 5.5 shows the relationship between the packing density with the vertical stress applied in seven repeated pressing stages. For a vertical stress of up to 160 MPa (200 kN), the different pressing stages showed a great distinction in the initial bed configuration with the packing density reaching a maximum value of around 0.7 for the last stage. This result is consistent with the maximum packing density found after the single stage pressing process presented in Figure 5.2a for the Itabira sample. Indeed, there is a marked relationship between the initial feed size distribution and the progressive change in packing density of the material. The results from Figure 5.5 indicate that, for the fine feed size distributions used, there is an increment in packing density caused by the reduction in the voids fraction within the particle bed. As the multiple stages of pressing were applied, the stress–deformation profile started to superimpose, with this effect being potentially associated with the high particle bed packing. This effect is also related to an increment in the particle bed stiffness, which was recently observed dealing with multiple stages of pressing in a pilot-scale HPGR processing fine iron ore concentrates (CAMPOS *et al.*, 2019a). The dispersion of the material following each pressing cycle, coupled with the application of a relatively low vertical stress in each cycle, allowed to prevent particle bed saturation.

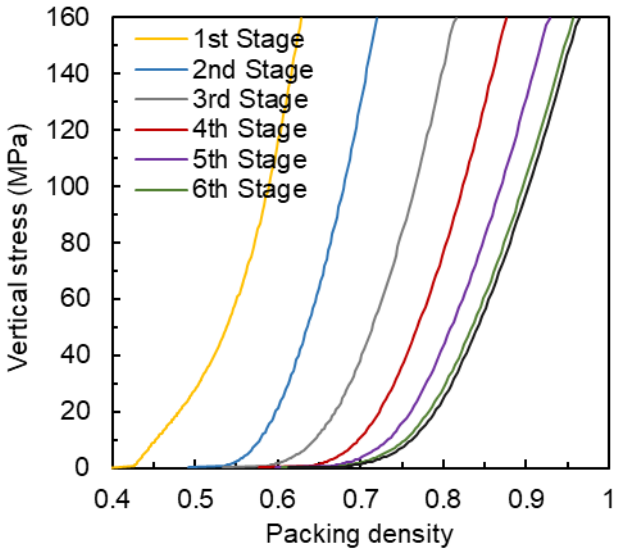


Figure 5.5. Relationship between vertical stress and packing density for different stages of pressing for the Itabira sample in a narrow size range of 106–75 µm in the piston-and-die system.

## 5.2. Breakage behavior

A proper investigation about the size reduction is also required in the piston-and-die tests. Figure 5.6 presents the product size distributions for the Itabira and Carajás samples at different stressing conditions.

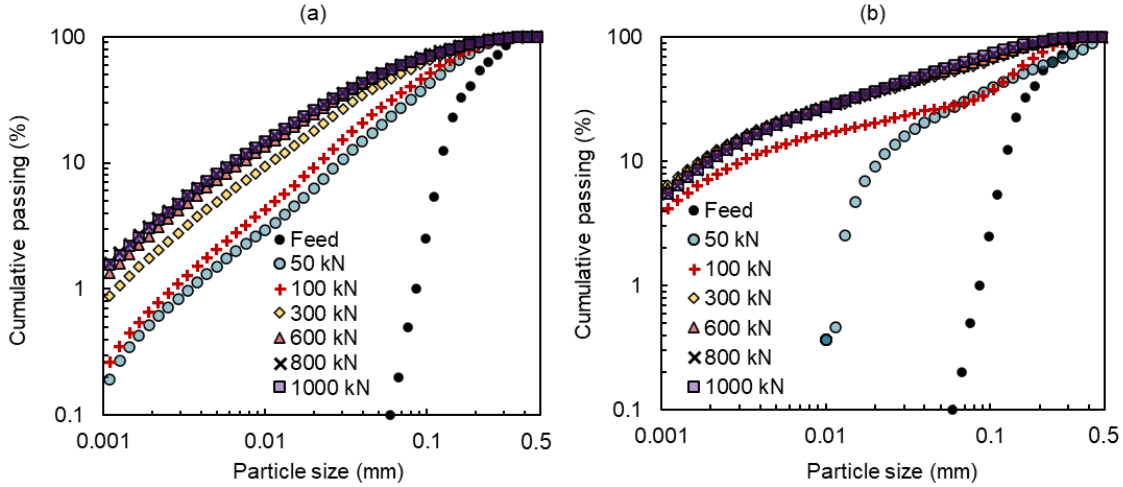


Figure 5.6. Product size distributions for different maximum compressive forces for the (a) Itabira and (b) Carajás samples contained in the size range of 150–125 µm in piston-and-die tests.

They demonstrate the increase in fineness as compressive force increases, as well as the onset of the breakage saturation associated with the application of compressive forces higher than about 300 kN (240 MPa). Beyond that, it is also important to highlight the higher amenability for breakage for the Carajás sample when compared to Itabira sample when looking to the full particle size distribution.

A detailed investigation about the particle breakage under confined conditions made it necessary to understand the breakage of coarse particles and fine particles separately. As such, after each piston-and-die test, the proportion passing the original narrow size range was recorded by sieving. The proportion broken was then plotted as a function of specific energy in Figure 5.7, following the approach used by LIU & SCHÖNERT (1996) and DUNDAR *et al.* (2013).

The figure shows that the proportion of particles broken increases significantly at low specific input energies, but reaches a maximum value, which becomes nearly constant with increasing input energies. Beyond this point, increasing the input energy does not lead to more breakage of particles contained in the original size range. AMINALROAYA & POURGHAHRAMANI (2022) suggested that, after reaching the saturation point, the coarser particles can work just as a point able to transfer the energy for one to particle to another, since they are protected and become stabilized by neighboring particles. Furthermore, as observed by LIU & SCHÖNERT (1996), it is evident that this maximum proportion broken varies with size, reducing significantly for the finer size range studied.

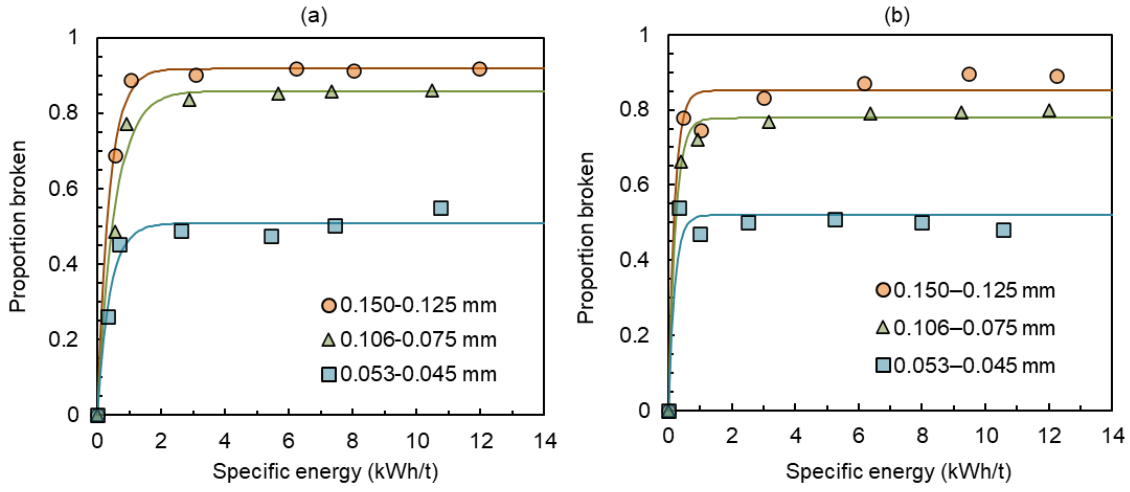


Figure 5.7. Proportion broken out of the original size for (a) Itabira and (b) Carajás samples for different specific energies and feed particle sizes.

Indeed, in the finest size range studied (53–45 μm), less than half of the particles broke for the Itabira sample (Figure 5.7a), despite the energy applied, showing the significant size effect on particle stabilization in confined bed breakage. The figure also shows that, at specific energies in the order of 2 kWh/t, saturation is reached on the maximum proportion of particles broken. This specific energy corresponds to a maximum load in the order of 200 kN (159 MPa), coinciding with the conditions in which the bed starts to recoil partially elastically (Figure 5.2) and also the condition under which the multiple stage pressings (Figure 5.5) were carried out.

To describe the trend in Figure 5.7, results have been fitted using the expression:

$$S' = S_\infty\left[1 - exp\left(-gE_{sp}\right)\right] \tag{5.1}$$

where $S'$ is the proportion broken out of the original size range and $S_\infty$ and $g$ (t/kWh) are fitting parameters. Figure 5.7 then compares the data to the fit to Eq. (5.1).

The derivative of Eq. (5.1) at the origin ($E_{sp}$ = 0) gives an idea of amenability of each sample to breakage under confined conditions. The reciprocal of this value, given by $1/(S_\infty g)$ and representing a resistance of the material to breakage, is then plotted as a function of mean particle size in Figure 5.8.

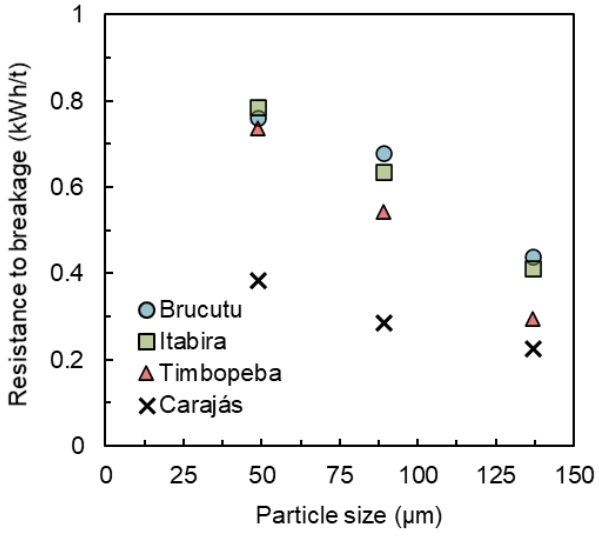


Figure 5.8. Variation of resistance to breakage ($1/S_\infty g$) in piston-and-die tests as a function of particle size for all samples analyzed.

Figure 5.8 shows the well-known trend of higher energy demand for breakage of fine particles. Beyond that, it is evident that Carajás sample proved to have comparatively lower specific energy demand, being almost 1.6 times lower than the second concentrate more amenable for breakage (Timbopeba). These results show that Itabira and Brucutu samples have very similar particle breakage behavior when assembled in particle beds.

Additionally, Figure 5.9 presents the variation of the maximum proportion broken ($S_\infty$) fitted using Eq. (5.1) according to particle size for all samples. As observed by LIU & SCHÖNERT (1996), the maximum proportion broken varies with size. In the finest size range studied (53-45 µm) less than half of the particles broke, despite the energy applied. This shows that finer particles more readily become stabilized by neighbouring particles, preventing their further breakage at higher stressing energies.

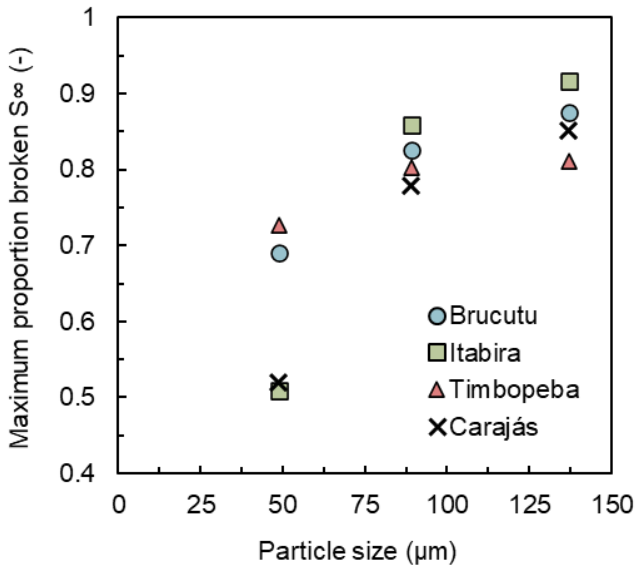


Figure 5.9. Variation of $S_\infty$ in piston-and-die tests as a function of particle size for all samples analyzed.

Results from Figures 5.8 and 5.9 also allow to conclude that Itabira and Brucutu samples presented a very similar breakage behavior for the coarse particles within the bed. Timbopeba sample, although relatively more amenable to breakage, was in the same order of magnitude of them.

Finally, Figure 5.10 compares results on the proportion broken for the Itabira sample as a function of input energy in individual pressings at progressively higher vertical stresses and results from multistage pressings. It shows that the sequential pressing and dispersion of the material prior to another pressing stage allowed the additional breakage of particles contained in the top size fraction, thus preventing saturation. Results from Figure 5.10 give technical support for applications of multiple stages of pressing in HPGR operation, whose feasibility was also demonstrated previously through experiments in a pilot-scale HPGR (THOMAZINI *et al.*, 2020), process simulations in a pilot-scale HPGR (CAMPOS *et al.*, 2019b) and through industrial tests using iron ore concentrates (BUENO, 2019).

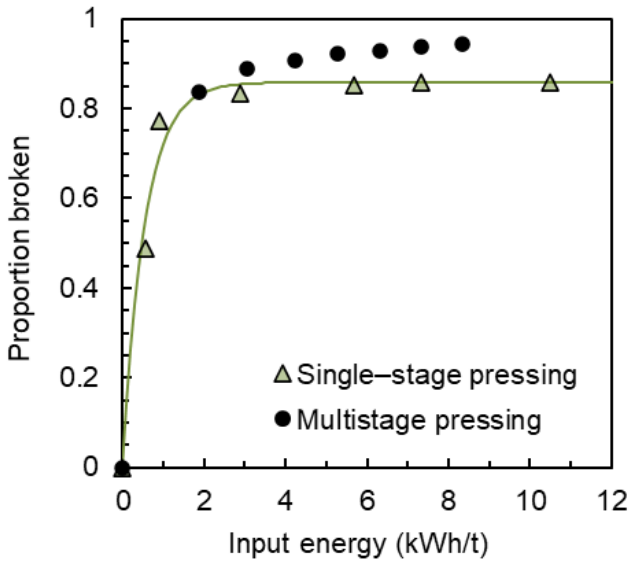


Figure 5.10. Proportion broken out of the original size for the Itabira sample in the narrow particle size range of 106–75 µm for single-stage pressing and multistage pressing in a piston-and-die system. Line fits data from single-stage pressing.

### 5.3. Surface area analyzes

Beyond the investigation of the coarser particles, the fineness of the size distribution was assessed according to the surface area generation after compression. Indeed, for pressing fine iron ore concentrates, it is common to analyze the particle breakage from the point of view of surface area generation (MEYER, 1980). Figure 5.11 shows the relationship between the BSA increase, which is simply calculated by the product BSA minus the feed BSA, and the specific energy applied for all samples in

piston-and-die tests and lab-scale HPGRs tests carried out elsewhere (BUENO, 2019). Lab-scale HPGR tests considered the complete feed size distribution (BUENO, 2019). It is evident that the BSA increase is nearly proportional to the input specific energy up to a point, beyond which the slope of the line reduces. As such, in analogy to Figure 5.7, the data approach a maximum value, but in this case only at specific energy inputs above about 6 kWh/t. Such a value corresponds to maximum vertical loads in the order of 600 kN (480 MPa). Results are still able to highlight the higher amenability for breakage of Carajás sample, whereas Brucutu and Itabira showed a BSA increase in the order of magnitude. Timbopeba sample, as depicted in the previous Sections, presented an intermediate behavior between the others.

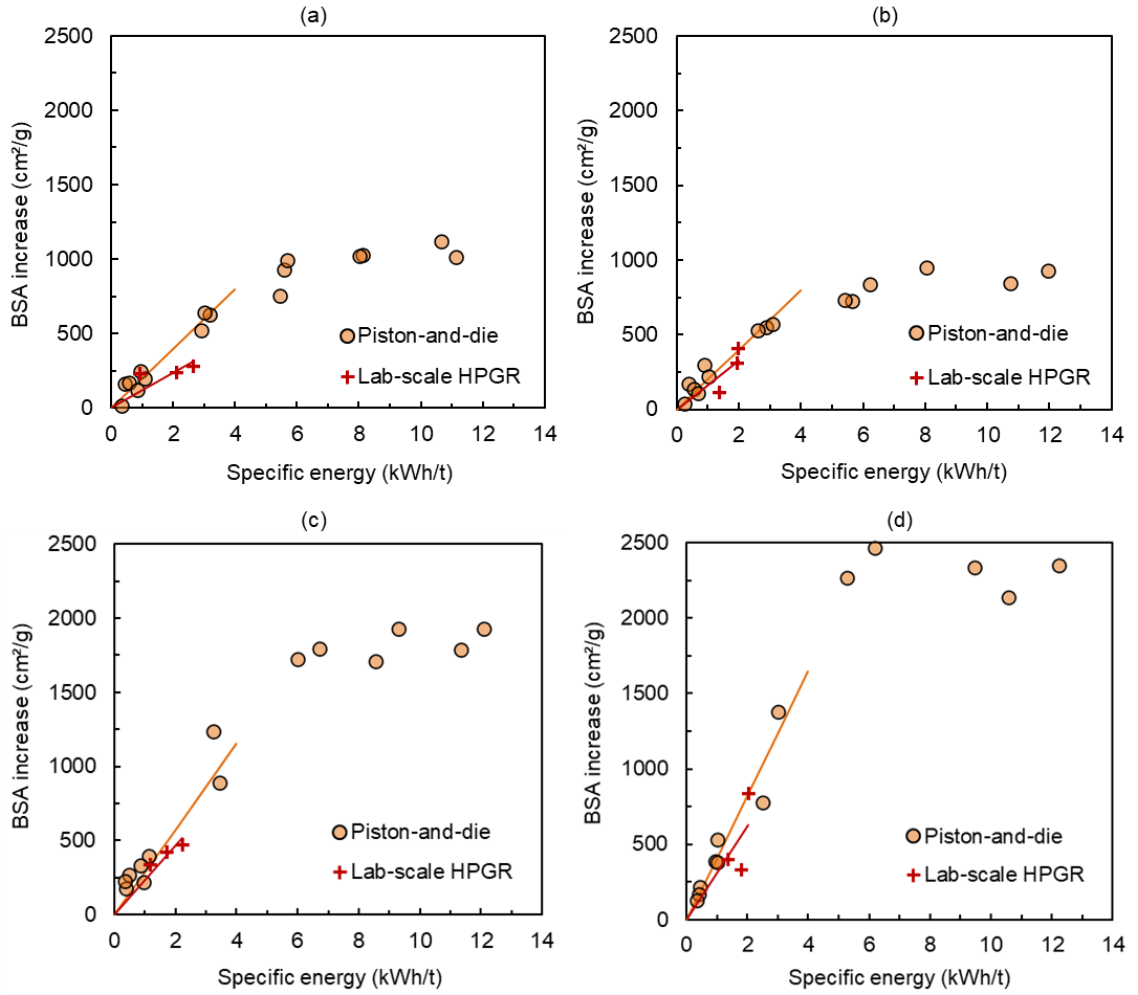


Figure 5.11. Relationship between BSA increase and specific input energy for (a) Brucutu, (b) Itabira, (c) Timbopeba, and (d) Carajás samples. Lab-scale HPGR data relies on tests carried out elsewhere with the same iron ore concentrates but using the complete feed size distribution (BUENO, 2019).

As already reported by SCHÖNERT (1996) and recently observed by ZHOU *et al*. (2020) using DEM simulations, the main cause for the drop in energy efficiency in particle bed breakage is the reduction in the voids that are caused by fine debris relocating themselves as a result of the application of high normal applied stresses. Such a drop in energy efficiency in compressed bed breakage is also evident in Figure 5.11 for specific energies higher than about 6 kWh/t. Besides that, results also showed a relatively similar BSA increase against the input energy for piston-and-die tests and lab-scale HPGR.

Results from multiple stages of pressing were also analyzed based on the surface area generation. Figure 5.12 showed that the dispersion of the material after each pressing cycle allowed reaching significantly higher BSA values than those obtained in a single pass at higher pressures. This effect becomes noticeable at specific energies above about 3 kWh/t. These results showed the potential application of multiple stages of pressing to increase the BSA of the product, instead using a single stage pressing with high values of pressure, which is in good agreement with other works (THOMAZINI *et al.*, 2020).

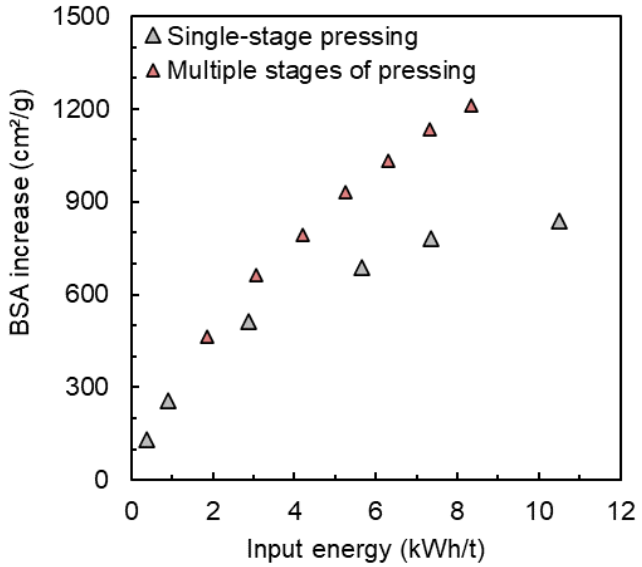


Figure 5.12. Comparison between the BSA increase against the specific energy applied in a single and multiple stages of pressing in a piston-and-die apparatus with particles in a narrow size range of 106-75 µm.

Another way to evaluate particle breakage from the point of view of size reduction energy efficiency, is using the so-called term energy utilization. The term was first proposed by RUMPF (1973) assessing breakage of fine materials and basically correlates the surface are increase with the spent energy in the process. With a minor modification, this equation can be rewritten as the ratio between the increase in the specific surface area from the product over the specific energy spent in the process as:

$$Energy\ utilization = \frac{BSA_{prod} - BSA_{feed}}{Specific\ energy} \tag{5.2}$$

where $BSA_{feed}$ (cm²/g) is the Blaine specific surface area of the feed and $BSA_{prod}$ (cm²/g) is the Blaine specific surface area of the product, whereas the energy utilization is given in cm²/g/kWh/t. This ratio provides a valid description of how effectively energy is being used to create new surfaces within the scope of iron ore pellet feed preparation (CAMPOS *et al.*, 2019a).

Table 5.1 then summarizes the values of energy utilization for the experimental tests shown in Figure 5.11 for all concentrates in both lab-scale HPGR tests (BUENO, 2019) and piston-and-die tests. In all cases the energy utilization is given by the slope of the trendlines that started in the origin of the graph. In the case of the piston-and-die tests these values correspond to the trendlines that are representative of the average response for the different initial particle sizes but limited to a maximum specific energy of 5 kWh/t. Compared to the lab-scale HPGR, piston-and-die presented the highest energy efficiency as already reported by other authors (SCHÖNERT & FLÜGEL, 1980, SCHÖNERT, 1996). Nevertheless, no statistical difference existed between the piston-and-die tests and the results for the lab-scale HPGR tests (BUENO, 2019) for Timbopeba, Carajás and Itabira, with the only exception of Brucutu.

When compared to the energy utilization of 90 cm²/g/kWh/t reported for ball milling stages dealing with the same iron ore concentrates investigated in the present work (VIANNA *et al.*, 2019), these results endorse the well-known high energy efficiency for piston-and-die tests and lab-scale HPGRs.

Table 5.1. Summary of energy utilization ($\times 10^3$ $m^2$/kWh) values for each iron ore concentrate for the different testing devices. Values obtained by fitting data from the different tests, including the 90% confidence interval.

| | Piston-and-die test | Lab-scale HPGR (BUENO, 2019) |
|---|---|---|
| Brucutu | 19.9 ± 1.5 | 11.9 ± 3.3 |
| Itabira | 19.9 ± 1.3 | 16.2 ± 4.3 |
| Timbopeba | 28.8 ± 1.8 | 23.4 ± 2.6 |
| Carajás | 41.1 ± 1.7 | 30.8 ± 2.0 |

A comparison of the data for the different concentrates shows that Brucutu and Itabira have equivalent and the lowest amenability to breakage in the piston-and-die apparatus, followed closely by Timbopeba, with Carajás being responsible for the highest energy utilization for this mode of breakage.

An additional analysis of efficiency in creating new surfaces is also possible through Figure 5.13, which presents the energy utilization calculated on the basis of both input specific energy and inelastic specific energy (gathered from force-deformation profiles as depicted in Figure 5.1). Results indicated a maximum energy utilization when the bed was subjected to the lowest pressure. Such high energy utilization can be explained by the fact that almost all the stressing energy dissipated in the particle bed is predominantly used to break particles. As pressure increases, there is sharp reduction of the energy utilization, in particular for pressures above 150 MPa. Also, it is key to recognize the great difference between both energy utilizations in Figure 5.13. This demonstrated how a large amount of energy has been dissipated in elastic deformation (Figure 5.4), thus not providing any addition improvement in the surface area of the product. On the other hand, when considering only the inelastic energy, a nearly average constant value for the energy utilization can be stated around 200 $cm^2$/g/kWh/t.

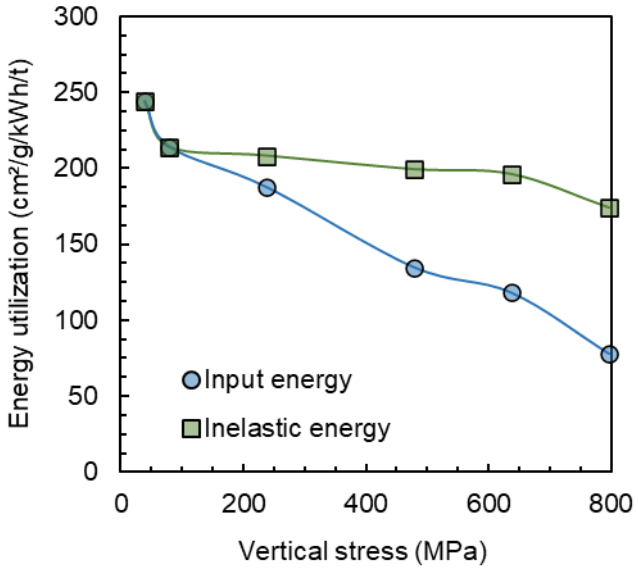


Figure 5.13. Comparison of energy utilization for different applied vertical stresses for Itabira sample for the narrow size range of 150-125 µm, considering both the input and the inelastic energy.

### 5.4. Energy-specific progeny size distribution

Another common way to analyze the amenability for breakage of narrow size ranges is from the $t_{10}$ parameter. Figure 5.14 presents the $t_{10}$-energy relationship for Itabira (a) and Carajás (b) for tests carried out with all narrow size ranges, which highlights the higher amenability for breakage for Carajás sample. Figure 5.14 also presents a comparison between the experimental and calculated $t_{10}$, being the model defined as:

$$t_{10} = A\left[1 - exp\left(-b_{PD}E_{sp}\right)\right] \tag{5.3}$$

where $A$ and $b_{PD}$ are fitting parameters. Optimal parameters for $A$ and $b_{PD}$ were 39.4 and 0.54 for Itabira sample and 40.5 and 0.85 for Carajás sample. Following the same approach adopted in Eq. (5.1), the derivative of Eq. (5.3) at the origin ($E_{sp} = 0$) gives an idea on the amenability for breakage. That parameter, known as $A \times b_{PD}$, was given as 34.4 t/kWh for Carajás sample and equal to 21.3 t/kWh for Itabira sample, which is lined-up with results presented in Sections 5.2 and 5.3.

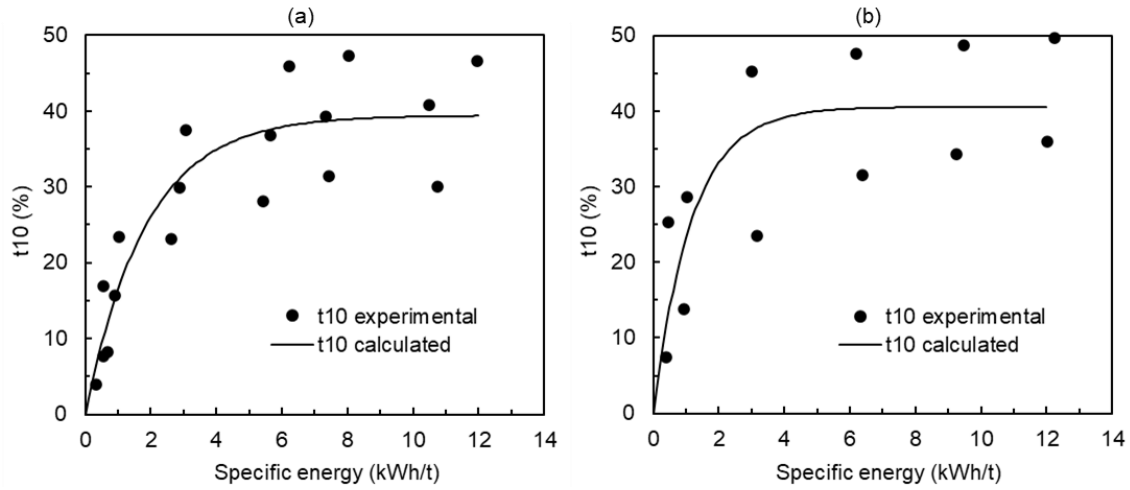


Figure 5.14. Comparison between $t_{10}$ parameter and specific energy consumption for Itabira (a) and Carajás (b) samples in all narrow size ranges investigated. Black circles are experimental measurements and black line is the model from Eq. (5.3) fitted on the basis of experimental results.

Taking into account the well-known $t_{10}$-$t_n$ method to describe the appearance-function (NARAYANAN & WHITEN, 1988), Figure 5.15 presents the $t_{10}$-$t_n$ for Itabira (a) and Carajás (b) samples for all narrow size ranges tested.

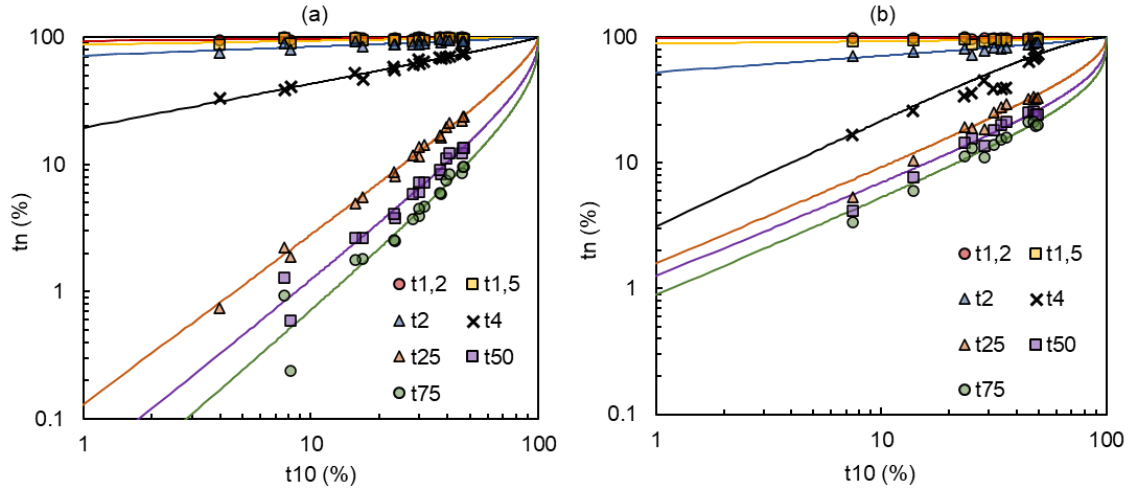


Figure 5.15. $t_{10}$-$t_n$ relationship (appearance function) for Itabira sample (a) and Carajás sample (b) considering all narrow size ranges tested. Markers are experimental values whereas lines are fitted values using the incomplete beta function.

Results demonstrated good behavior with all narrow size ranges, being them well grouped when analyzed together. Figure 5.15 still presents a comparison between experimental and fitted values for the appearance function made by the incomplete beta function (Eq. (5.4)), being the optimal parameters presented in Table 5.2.

$$t_n(t_{10}) = \frac{100}{\int_0^1 x^{\alpha_n-1}(1-x)^{\beta_n-1}dx}\int_0^{t_{10}} x^{\alpha_n-1}(1-x)^{\beta_n-1}dx \qquad (5.4)$$

where $\alpha_n$ and $\beta_n$ are fitting parameters and the $t_{10}$ is given in fraction.

Table 5.2. Summary of the incomplete beta function parameters (Eq. (5.4)) fitted to describe the $t_{10}$-$t_n$ relationship from for all samples analyzed.

| | Itabira | | Brucutu | | Timbopeba | | Carajás | |
|---|---|---|---|---|---|---|---|---|
| $t_{ns}$ | $\alpha_n$ | $\beta_n$ | $\alpha_n$ | $\beta_n$ | $\alpha_n$ | $\beta_n$ | $\alpha_n$ | $\beta_n$ |
| $t_{1,2}$ | 0.02 | 1.75 | 0.02 | 2.39 | 0.01 | 0.65 | 0.001 | 0.10 |
| $t_{1,5}$ | 0.03 | 1.22 | 0.05 | 1.36 | 0.02 | 0.56 | 0.02 | 0.38 |
| $t_2$ | 0.07 | 0.92 | 0.12 | 1.12 | 0.11 | 0.75 | 0.13 | 0.78 |
| $t_4$ | 0.34 | 0.89 | 0.53 | 1.18 | 0.70 | 1.29 | 0.85 | 1.67 |
| $t_{25}$ | 1.32 | 0.63 | 1.21 | 0.61 | 1.06 | 0.60 | 0.75 | 0.46 |
| $t_{50}$ | 1.44 | 0.39 | 1.27 | 0.38 | 1.10 | 0.41 | 0.73 | 0.30 |
| $t_{75}$ | 1.54 | 0.31 | 1.34 | 0.29 | 1.21 | 0.35 | 0.76 | 0.25 |

. Assuming a specific energy of approximately 1 kWh/t to ensure no saturation effect (Sections 5.2 and 5.3), it is possible to estimate the energy-specific progeny size distribution from the appearance function calculated for each iron ore concentrate. Except for Carajás, high similarity was observed between the other concentrates, with Timbopeba presenting a slightly finer progeny size distribution (Figure 5.16). As already demonstrated in the previous discussions, Carajás presented the highest

amenability for breakage with the most aggressive progeny size distribution among the different iron ore concentrates investigated.

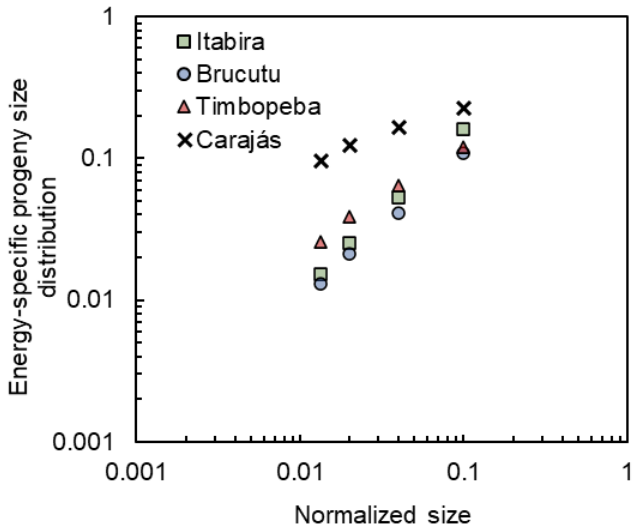


Figure 5.16. Energy-specific progeny size distribution for all iron ore concentrates analyzed from piston-and-die tests at 1 kWh/t. Results are presented for $t_{ns}$ lower or equal to the $t_{10}$ value.

### 5.5. Final discussions

Results presented in this Section allowed a deep analysis about the particle breakage behavior under confined conditions of the different iron ore concentrates used to compose the HPGR feed analyzed in the present work. From the various analyzes it becomes possible to improve understanding about the well-known saturation effect on the particle bed, which was quantified on the basis of surface area generation and energy spent during compression.

For pressing fine iron ore particles, Figure 5.17 summarizes the main feature of the particle bed when submitted to compressive stress up to 800 MPa. Particle rearrangement below 40 MPa is the predominant phenomenon in the particle bed, which is fully related to low energies applied to the particle bed (MÜTZE, 2016) and marked as point A in Figure 5.17. As detailed demonstrated in Section 5.2, an earlier saturation of top size particle is clear around 180 MPa (point B). Beyond this point, a proportion of particles contained in the top size, which varied from about 10% for the coarsest sizes

tested to about 50% for the finest, remained unbroken, even as stressing energies increased. This is associated with the well-known phenomenon in confined particle bed breakage in which the finer debris from breakage of the coarser particles are able to prevent the remaining coarser particles from further breaking (LIU & SCHÖNERT, 1996, DUNDAR *et al.*, 2013). For the last part of the force-deformation profile (Figure 5.17) it is also possible to identify further breakage for the very fine particles, being the complete breakage saturation achieved beyond 500 MPa as discussed in Section 5.3. Analysis on the breakage saturation will be used as the basis for an improvement in the particle bed breakage description in the modified Torres and Casali model (Table 4.4) used in the present work, which is lined up with R#1a (Section 2).

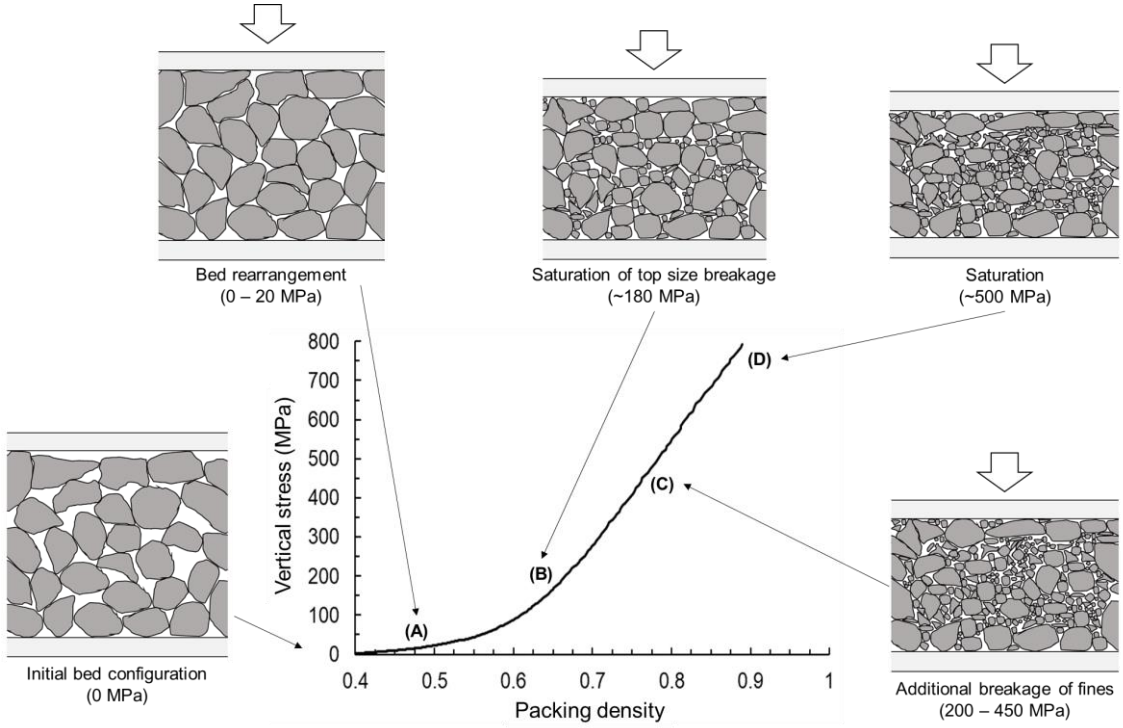


Figure 5.17. Scheme summarizing the main features of the particle bed pressing behavior for fine iron ore particles.

Analysis on the appearance function following the $t_{10}$-$t_n$ approach (NARAYANAN & WHITEN, 1988) allowed estimating the energy-specific progeny size distribution for each iron ore concentrate investigated. Results will then be used in the Section 7 to improve description of the model predicting the particle breakage behavior of different blends feeding the pelletizing plant.

## 6. HPGR MODEL VALIDATION AND IMPROVEMENTS

Section 6 relies on the application of the Modified Torres and Casali model (Table 4.4) describing industrial-scale HPGRs pressing iron ore concentrates under steady state and controlled conditions (Section 4.3.1). Specific modifications on model equations were then proposed in order to improve model prediction.

### 6.1. Power consumption

Figure 6.1 presents a comparison between measured and predicted power consumptions using the original Torres and Casali model (a) as well as the modified Torres and Casali model (b) for all HPGR experiments (Section 4.3.1). As shown in the previous study that dealt with pressing iron ore concentrate in a pilot-scale HPGR (CAMPOS *et al.*, 2019b), the original Torres and Casali model underestimated the power consumption with an average absolute relative deviation from measurements of 54.4% in industrial-scale HPGRs (Figure 6.1a). On the other hand, Figure 6.1b showed that the modified Torres and Casali model (Table 4.4) was able to provide predictions which agreed very well to experiments, being now the average absolute relative deviation from measurements of 5.9%. This resulted in fitting the machine-specific constant $\kappa$ in Eq. (3.27) to each individual HPGR.

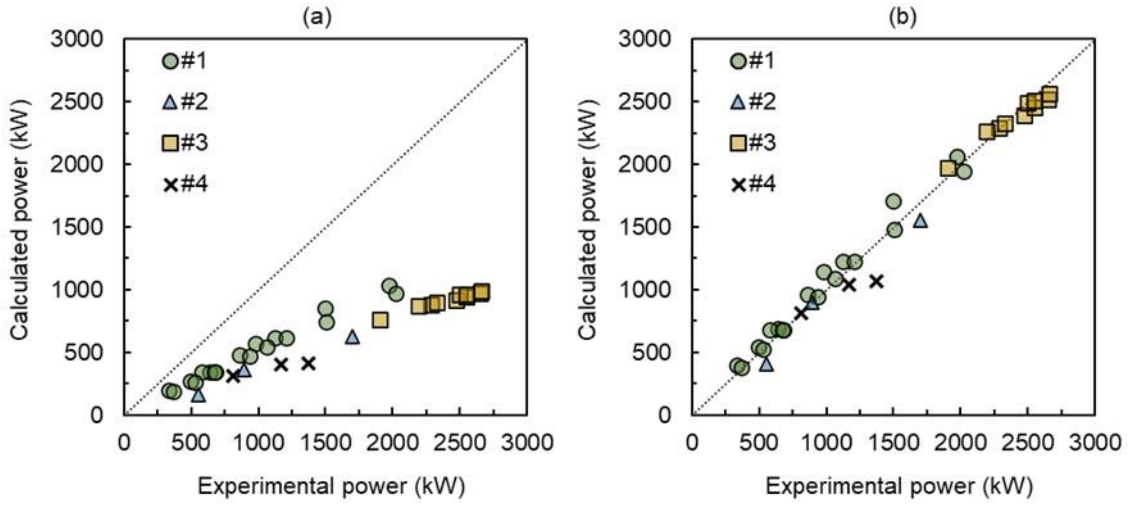


Figure 6.1. Comparison between experimental and predicted powers calculated with the Torres and Casali model (a) and the modified Torres and Casali model (b) for all experimental surveys described in Section 4.3.1. Data is discriminated by machine.

Table 6.1 then presents the selected test used as a base case for the industrial surveys investigating each HPGR (Section 4.3.1). Tests used for calibration were selected based on operating conditions close to the average values for each HPGR, in which each parameter $\kappa$ varied from 2.00 to 2.75. Optimal value for HPGR #2, which is the focus of investigation in the online modeling approach (Section 7) was close to the optimal values found in the previous work ($\kappa$ = 2.80) by the authors (CAMPOS *et al.*, 2019b).

Table 6.1. Summary of the base case conditions selected to fit parameter $\kappa$, as well as its optimal value (Eq. 3.27) for each HPGR.

| | HPGR | | | |
|---|---|---|---|---|
| | #1 | #2 | #3 | #4 |
| Operating pressure (bar) | 41 | 75 | 82 | 48 |
| Roll peripheral velocity (m/s) | 0.78 | 1.00 | 1.54 | 1.30 |
| Measured power (kW) | 525 | 1702 | 2325 | 814 |
| $\kappa$ (-) | 2.00 | 2.75 | 2.60 | 2.60 |

## 6.2. Throughput

Experimental results are shown in Figure 6.2 that illustrate the relationship between the specific throughput and the specific operating force for all surveys in the different HPGRs. As already observed by VAN DER MEER & LEITE (2018) and confirmed by CAMPOS *et al*. (2019a), an inverse relationship appears between the specific throughput and the specific force. CAMPOS *et al.* (2019a) suggested that such variation is a consequence of the variation in operating gap. However, different from the results presented there (CAMPOS *et al.*, 2019a), Figure 6.2 shows that no single and simple relationship exists that is valid for the different industrial-scale HPGRs surveyed. Such variability would be explained by changes in the blend and grindability of ores composing the feed of the HPGR, beyond important effects as feed moisture content, material ejected by the edge of the roll and acceleration on the compression zone.

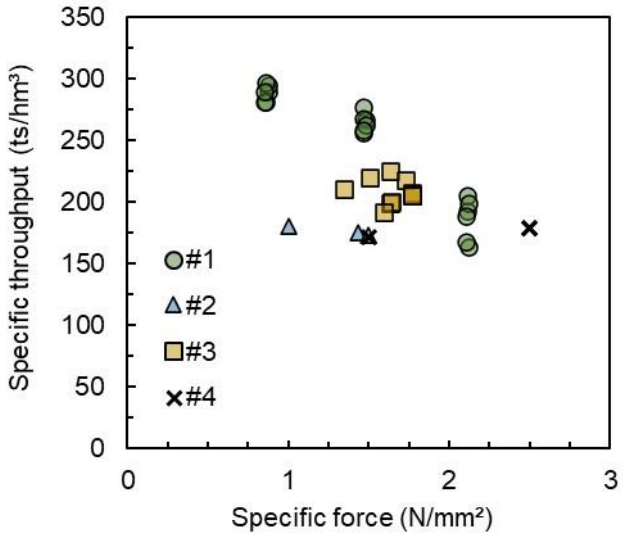


Figure 6.2. Relationship between specific throughput and specific force for tests in all industrial-scale HPGRs. Results are discriminated by machine.

To assess the applicability of the Torres and Casali (TORRES & CASALI, 2009) model to the industrial survey data, predictions from Eq. (3.15) are compared to experiments in Figure 6.3a, showing poor agreement between model and experiments and an average absolute relative deviation from measurements of 53%. Results were like a previous study involving a pilot-scale HPGR (CAMPOS *et al.*, 2019b).

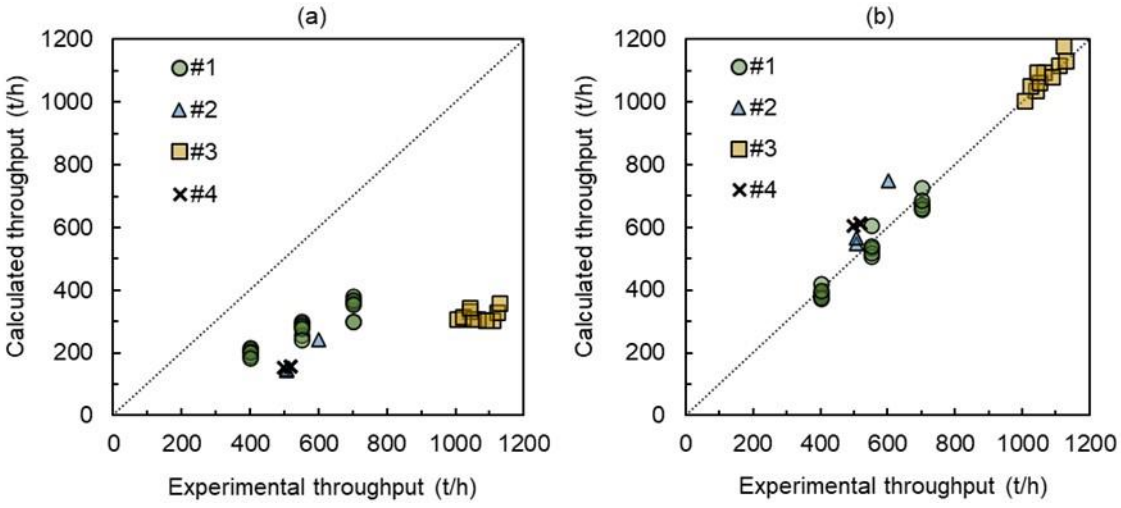


Figure 6.3. Comparison between experimental and calculated throughputs using the original Torres and Casali model (a) and the model modified in the present work (b) for all industrial-scale HPGRs.

Incorporating the modifications associated to the increase in material velocity along the extrusion zone, besides the ejection of material between the edge of the rolls and the cheek plates (Table 4.4), parameters of Eq. (3.16) were fitted to data. Figure 6.4 shows the reasonable agreement between model fit (line) and measured values for the different HPGRs over the entire range of operation conditions surveyed. As such, the model suggests that between about 10 and 35% of material would have been ejected from the edge of the rolls in operation, which is in good agreement with estimations made by other authors (LIM *et al.*, 1997) measured in a pilot-scale HPGR (VAN DER ENDE *et al.*, 2019) and reported from DEM simulations (RODRIGUEZ *et al.*, 2022a). The optimal values of the parameters, valid for all industrial-scale HPGRs, were τ equal to 0.1, υ equal to 190, φ equal to 100 and $f'$ equal to 0.65, being only the parameter υ recalibrated from a previous work with pilot-scale HPGR (CAMPOS *et al.*, 2019b) and presented in Section 3.6.1.

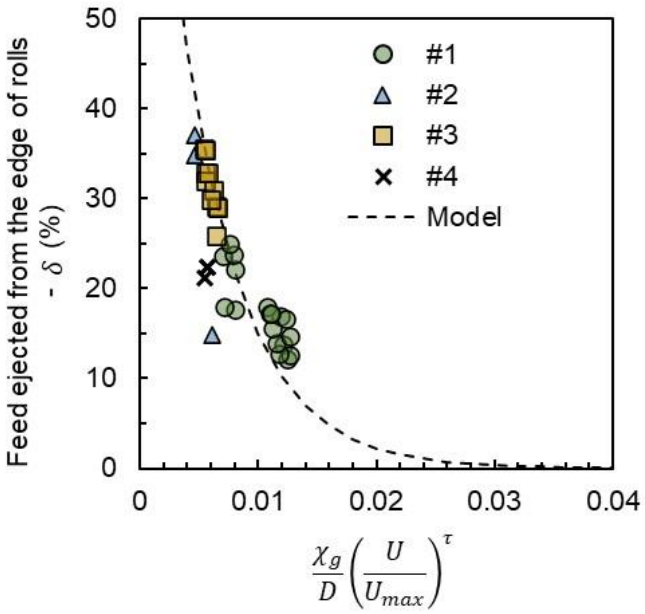


Figure 6.4. Relationship between the product of the dimensionless gap and the dimensionless rolls speed raised to parameter $\tau$ and the estimate of the proportion of material ejected from the edges of the rolls and the cheek plates. Data identified by machine.

A comparison between the survey results and the improved model fit is presented in Figure 6.3b which demonstrates the very good agreement between them

with an average absolute relative deviation from measurements of 6.4%. As such, although Figure 6.2 did not show a straightforward relationship between the operating conditions and the measured specific throughput, the model was able to incorporate these effects. Comparison between model and experiments in Figure 6.3b were made with Eq. (3.19) when considering the proportion of material ejected by the edge of the roll (Eq. (3.16)) and the material acceleration on the compression zone (Eq. (3.17)).

Analyzing HPGR #2 (Plant 3) separately allows calibrating parameter υ equal to 550 to better describe the proportion of material ejected for this particular equipment. Challenges faced by HPGR #2 operating under the designed throughput pushes the machine to a more restricted range of operating conditions (Section 4.3.2), which can, at least in part, justify the new calibration of this single parameter in Eq. (3.16). Figure 6.5 presents a comparison between measured and fitted throughput for two datapoints collected for HPGR #2 (Plant 3) under steady-state conditions when using parameter υ equal to 550, which allowed to achieve an average absolute relative deviation from measurements of 2.1%.

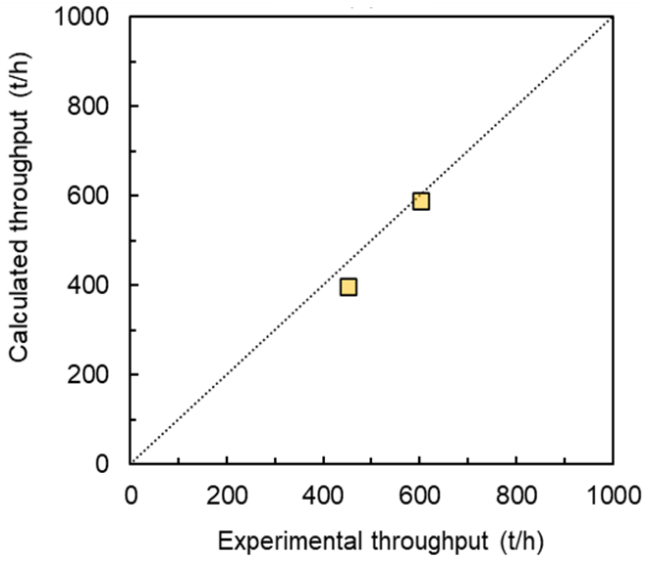


Figure 6.5. Comparison between measured and fitted values for the throughput (a) and power consumption (b) for two tests carried out under controlled conditions and in steady-state for the industrial-scale HPGR investigated in the present work.

### 6.3. Product size distribution

Typical size reduction results from the industrial surveys are presented in Figure 6.6, which shows the significant effect of specific compressive force on the product size distribution, demonstrating the importance of this variable in HPGR performance.

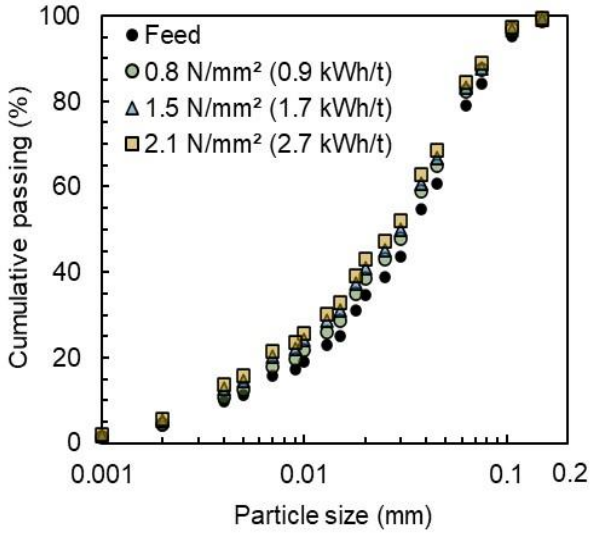


Figure 6.6. Feed and product size distributions from surveys with HPGR #1 discriminated by specific force (and energy) at a constant throughput of 400 t/h.

To use the modified Torres and Casali model for describing the breakage response from the surveys (Table 4.2), the present work assumes validity of the non-normalizable breakage function (Eq. (3.46)) parameters fitted by CAMPOS *et al.* (2019b) from pressing iron ore concentrates in a pilot HPGR. Besides these, two of the parameters in the selection function (Eq. (3.39)) were also assumed to be constant for all industrial HPGRs, whereas the remaining parameter $s_1^E$ in Eq. (3.39) has been fitted on the basis of a base case for each HPGR.

Table 6.2 summarizes all model parameters, while Figure 6.7 presents the fitted breakage function (CAMPOS *et al.*, 2019b) and the specific selection functions fitted for each HPGR (b). Parameter $s_1^E$ for the specific selection function (Eq. (3.39)) was fitted and given as $s_1^E$ = 0.20 t/kWh for HPGR #1, 0.16 t/kWh for HPGR #2, 0.15 t/kWh for HPGR #3 and 0.40 t/kWh for HPGR #4.

Table 6.2. Summary of the fitted parameters for all HPGRs

| | Parameter | Value |
|---|---|---|
| Selection function | $\xi_1$ | -0.60 |
| | $\xi_2$ | -0.16 |
| Breakage function | $\gamma$ | 0.89 |
| | $\beta$ | 5.46 |
| | $\phi$ | 0.86 |
| | $\eta$ | 0.46 |
| | $\omega$ | 0.0133 |

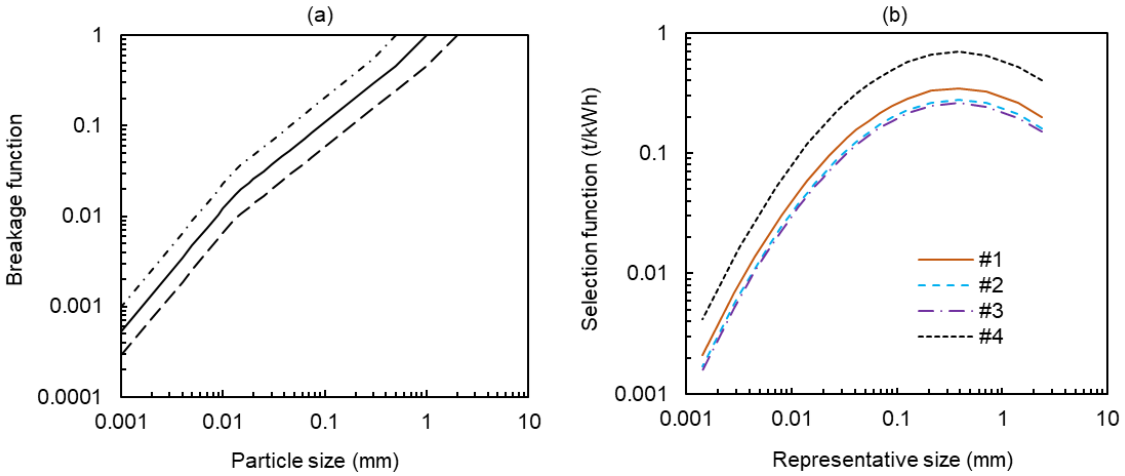


Figure 6.7. Cumulative breakage function for selected parent particle size classes (a) and specific selection functions (b) fitted for all HPGRs using $s_1^E$ = 0.20 t/kWh (#1), 0.16 t/kWh (#2), 0.15 t/kWh (#3) and 0.40 t/kWh (#4).

Results from Figure 6.7 are able to highlight the relatively higher specific breakage rates for tests performed in the HPGR #4 (Pre-grinding), showing smaller variations among the other surveys. Specific selection function for HPGR #2 (Plant 3) was fitted considering the throughput model calibrated on the basis of data provided only by Plant 3, which consists in parameter $v$ from Eq. (3.16) equal to 550 (Section 6.2). For all simulations the breakage model relied on 100 sections divided along the roll length ($N_B$ in Eqns. (3.40) to (3.41)).

In order to assess the model predictive capabilities to deal with different operating conditions, Figure 6.8 compares experimental and simulated product size distributions from surveys with HPGRs #1 and #4. These results demonstrate the very good ability of the model in predicting the product size distribution both when the HPGR is fed with a coarser feed size distribution, such as in a pre-grinding operation (Figure 6.8b), and a finer feed size distribution in the regrinding pre-pelletizing process (Figure 6.8a) in HPGR #2. Objective function (Eq. (4.5)) calculated for both model predictions was up to 0.035.

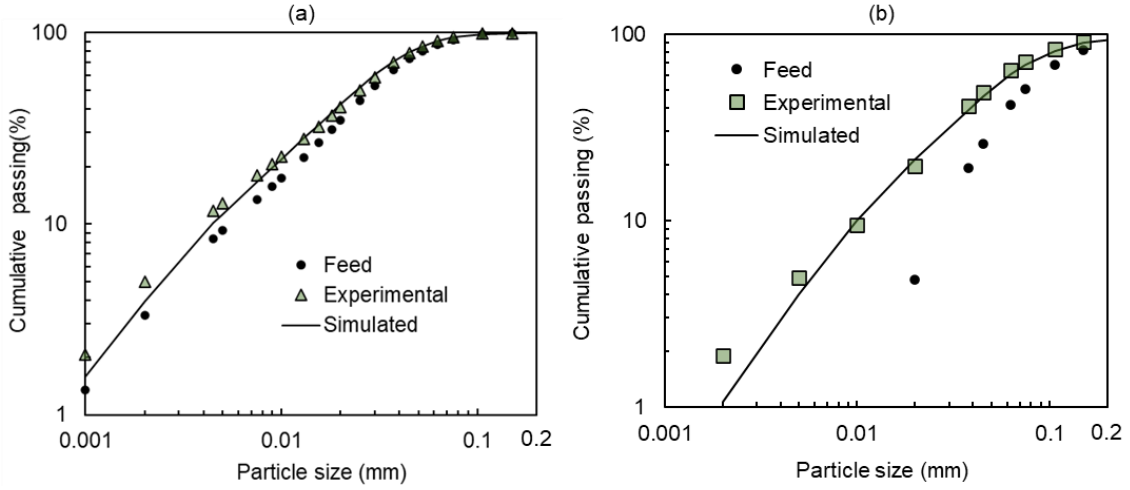


Figure 6.8. Comparison of experimental and predicted product size distributions in regrinding pre-pelletizing at 600 t/h and specific force of 1.5 N/mm$^2$ (HPGR #2) (a) and pre-grinding at 500 t/h and specific force of 2.5 N/mm² (HPGR #4) (b).

Very good agreement in both the coarser and the finer parts of the size distribution are required in pelletizing, since both extremes have a significant impact on iron ore pellet characteristics (MEYER, 1980). A well-known way to capture these features of the size distribution in the iron ore pelletizing industry is through measurement of the amount of material passing the 45 µm sieve and the Blaine specific surface area (MEYER, 1980). A model, presented in Appendix A, has been used to estimate the BSA from the predicted size distributions (ZHANG & NAPIER-MUNN, 1995, CAMPOS *et al.,* 2019b). As such, Figure 6.9 compares measured and predicted values of the BSA (a) and of the percent passing the 45 µm sieve (b) in the product for all surveys with HPGRs #1 to #3. Average absolute relative deviation from

measurements for the percent passing in 45 µm sieve in the product was 6.4%, whereas the HPGR product BSA presented 3.4%. The results demonstrate good agreement for surveys carried out with specific compressive forces below about 2 N/mm². Indeed, when higher specific forces and specific energies were used, the model tended to overestimate the product fineness.

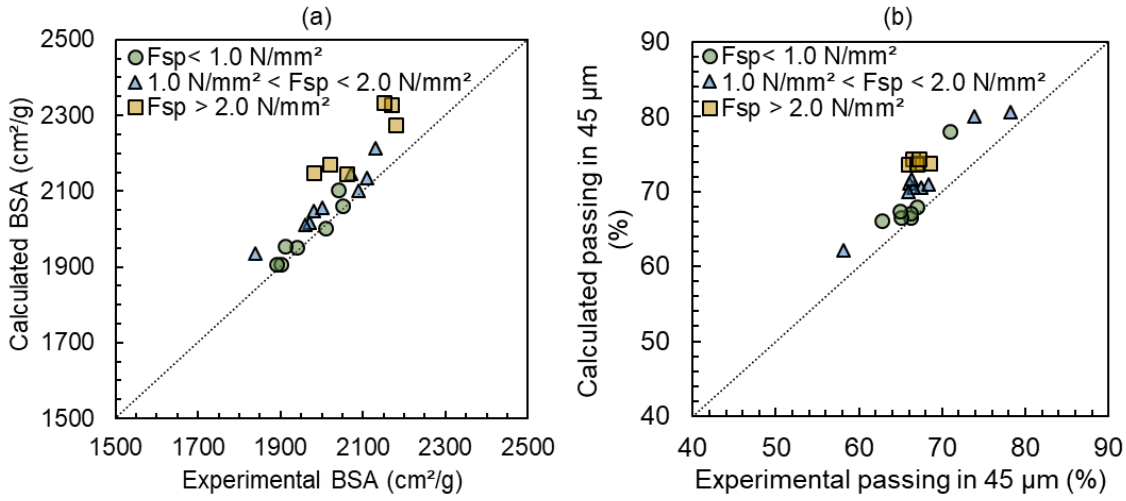


Figure 6.9. Comparison between measured and predicted BSA (a) and percent passing the 45 µm sieve (b) in the product from surveys with HPGRs #1 to #3 using the modified Torres and Casali model presented in Section 3.6.3.

These results suggest the appearance of a well-known phenomenon in confined breakage that is associated to high compressive forces, in which the energy input to the bed is no longer effectively used in generating new surfaces (LIU & SCHÖNERT, 1996, KALALA *et al.*, 2011, MÜTZE, 2015). Indeed, such saturation is influenced by several variables, but can be carefully studied under controlled conditions in a piston-and-die apparatus, as discussed in Section 5.

### 6.4. Breakage saturation description

Section 3.5.2 described in detail the large number of operational variables and feed characteristics able to influence the breakage saturation effect. As expected, no HPGR model in the literature has been capable to incorporate this effect (Section 3.6.3), fact which limits the HPGR model application to describe breakage of very fine

materials. The present work takes advantage of an important alternative way to assess this phenomenon, which relies on performing experimental tests under controlled conditions in a piston-and-die apparatus.

Section 5 provided some insights about how the energy spent in the particle bed is dissipated in different microprocesses, as breakage and elastic recovery. In order to illustrate such saturation, the concept of energy utilization (Eq. (5.2)) has been used. Results from testing particles, contained both in narrow size ranges and as complete size distributions in a piston-and-die apparatus are presented in Figure 6.10, following the same approach from Figure 5.13 but now as a function of the input specific energy. The energy utilization was calculated on the basis of the input specific energy and shows a significant reduction in the efficiency in creating new surfaces.

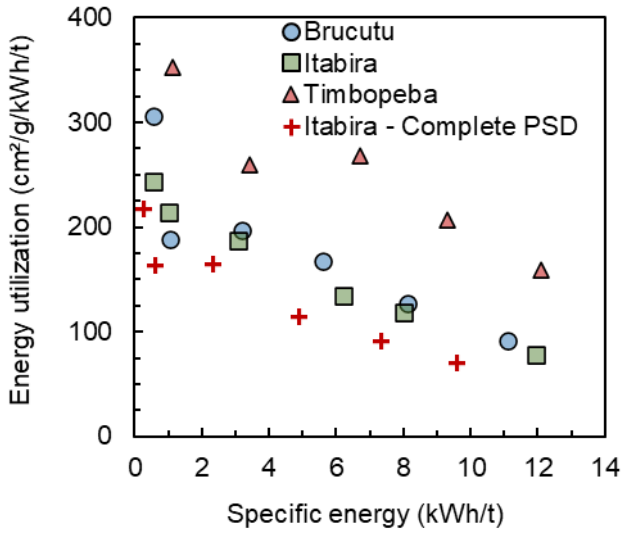


Figure 6.10. Variation of the energy utilization as a function of specific input energy for pressing different iron ore concentrates from a narrow feed size range of 150–125 μm (Itabira, Brucutu and Timbopeba) and complete feed size distribution (Itabira – Complete PSD) in a piston-and-die apparatus.

Defining an efficiency variable as the ratio between the actual energy utilization reached at a given input specific energy and the maximum energy utilization from the smallest vertical stress applied, results are given in Figure 6.11, which have been fit to the empirical equation:

$$\Psi(E_i) = exp\left[-\left(\frac{E_{sp}}{E'}\right)^{\Xi}\right] \tag{6.1}$$

where $\Psi$ is the proposed efficiency variable, $E_i$ is the input energy, $E''$ is the energy densification parameter, given in kWh/t, and $\Xi$ is a dimensionless fitting parameter.

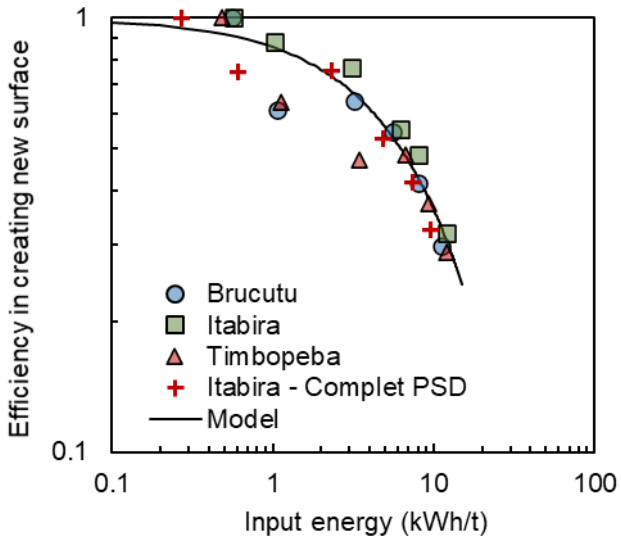


Figure 6.11. Comparison between experimental and fitted values for the efficiency in creating new surface for different iron ore concentrates from a narrow feed size range of 150–125 μm (Itabira, Brucutu and Timbopeba) and complete feed size distribution (Itabira – Complete PSD) in a piston-and-die apparatus.

Results from Figure 6.11 show Eq. (6.1) can describe the data reasonably well for pressing iron ore concentrates in a piston-and-die test. As previously discussed in Section 5.5, low input energies are related to vertical stresses up to 40 MPa, which usually relies on particle rearrangement in the particle bed (Figure 5.17). These results can, at least partially, explain some of the outliers presented in Figure 6.11 when dealing with low input energies.

Considering Eq. (6.1), it is hereby proposed that Eq. (3.40) of the Torres and Casali model is modified to account for the breakage saturation, by applying the constant $\Psi$ to reduce the breakage rates at each block and size class, giving:

$$S_{i,k} = s_i^E \frac{P_k}{H_k} \Psi \left(\frac{P}{Q}\right) \tag{6.2}$$

Indeed, questions can be raised about using results from a piston-and-die apparatus to calibrate a model describing an industrial-scale HPGR machine, since understanding about this scale relationship is not yet complete. However, it is important to recognize that, for this particular case of application for pressing iron ore concentrates, experimental results demonstrated a very similar surface area generation (Figure 5.11) and energy utilization (Table 5.1) when comparing lab-scale HPGR tests (BUENO, 2019) and piston-and-die tests, which, at least in part, justify the application of these results to calibrate the model for industrial-scale HPGR operations. Nevertheless, results from Section 5 indicated that the energy utilization varies with particle size and size distribution, thus suggesting that caution should be exercised in the use of Eq. (6.1) to simulate very large changes in feed size distribution. Finally, Figure 6.12 then compares experimental and predicted values of BSA (a) and percentage passing in 45 µm sieve in the product of tests carried out with HPGRs #1 to #3 after applying Eq. (6.2).

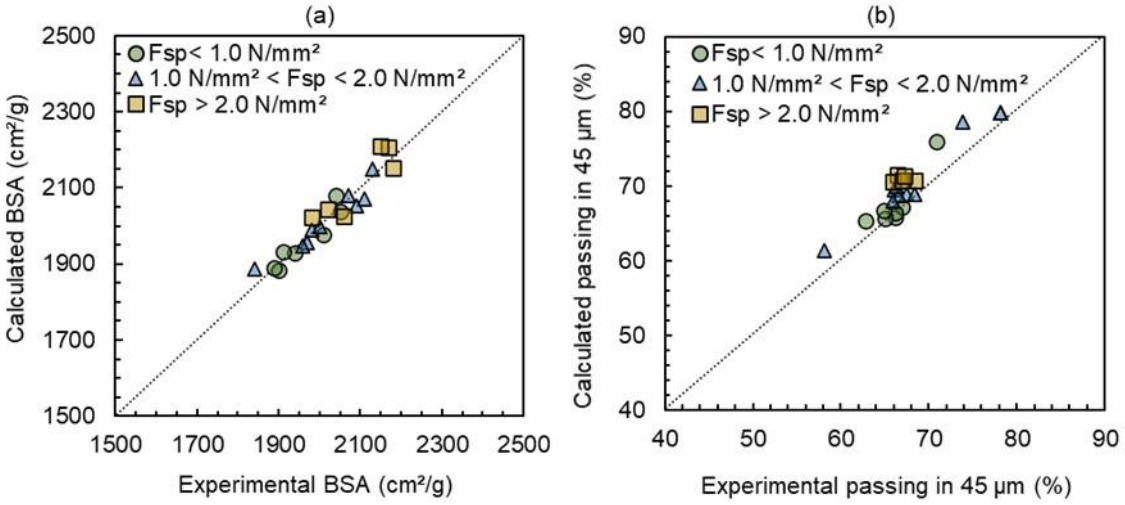


Figure 6.12. Comparison between measured and predicted BSA (a) and percentage passing the 45 µm sieve (b) in the product from surveys on HPGRs #1 to #3 with different specific compressive forces using the modified Torres and Casali model with the description of the breakage saturation effect given by Eq. 6.1.

Results demonstrate the good description of both variables when using the proposed model modification in contrast with Figure 6.9, being now the average absolute relative deviation from measurements estimated in 3.9% for the percentage passing in 45 µm sieve in the product and 1.2% for the HPGR product BSA. Results from this Section give support to answer R#1a (Section 2).

### 6.5. Axial variation of product size distribution along the rolls´ length

In selected surveys, samples from underneath the rolls were collected, so as to map the axial variation of the product along the roll's length. Results are presented in Figure 6.13, showing the significant variation of both BSA (Figure 6.13a) and percent passing the 45 µm sieve (Figure 6.13b) along the length of the rolls.

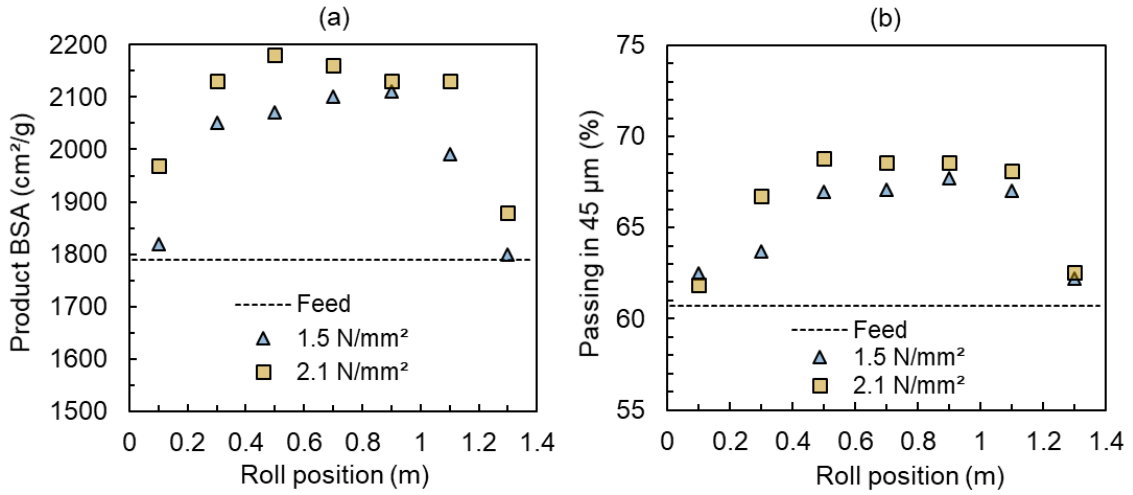


Figure 6.13. Variation of BSA (a) and percentage passing the 45 µm sieve (b) along the axial roll position for surveys in HPGR #1 with a constant throughput of 400 t/h at different specific forces.

As already reported by CAMPOS *et al.* (2019b) for pressing iron ore pellet feed in a pilot-scale HPGR and suggested by other authors (LUBJUHN & SCHÖNERT, 1992, MORRELL *et al.,* 1997), it shows the edge effect with a coarser product formed close to the edges of the rollers and a finer product being generated in the central zone. However, Figure 6.13 does not show the parabolic profile suggested in Eq. (3.41) as preluded by the Torres and Casali model, since a region of approximately constant

fineness appears in the central part of the rolls. The figure also shows that in the edges nearly no size reduction occurs, since both BSA and the proportion passing the 45 μm sieve in the product are only marginally higher than in the feed.

As such, an alternative expression to Eq. (3.41) has been sought to describe such observed profile. It is proposed that the axial roll profile ($P'_k$) can be described as a periodic function based on the Fourier Transform:

$$P'_k = \frac{4}{\pi}\sum_{n=1}^{100}\frac{1-\cos n\pi}{2n}e^{-\mu(n^2\pi^2)}\sin n\pi\bar{y}_k \tag{6.3}$$

where $\mu$ is a single fitting parameter that can be selected to match the profile shape, varying in the range of 0.001 to 0.1, $\bar{y}_k$ is the normalizable average position along the roll length given by $\bar{y}_k = \frac{y_{k-1}+y_k}{2}$, in which $y_k$ is given by:

$$y_k = \frac{k}{N_B} \tag{6.4}$$

where $N_b$ is the number of blocks. Therefore, the power profile along the axial roll position, previously described in Eq. (3.41), would be replaced by:

$$P_k = 2F_m \sin\left(\frac{\kappa\alpha_{ip}}{2}\right) U \frac{P'_k}{\sum_{j=1}^{N_B} P'_j} \tag{6.5}$$

Figure 6.14 compares experimental and predicted values of BSA (a) and percentage passing the 45 μm sieve in the product using Eq. (6.5), comparing to results obtained using the parabolic relationship proposed by Torres and Casali (Eq. 3.41). It clearly shows that the new proposed expression is able to more closely describe the shape of the profile observed in the plant survey. Minor deviations were found in Figure 6.14b with Eq. (6.5) overestimating the measured percent passing in 45 μm, even

though still showing a relatively good agreement. These results showed that the value of μ of about 0.01 is able to describe the approximately trapezoidal profile observed in Figure 6.14. It is important to emphasize that when $\mu$ is approximately equal to 0.1, Eq. (6.3) approaches the parabolic profile given by Eq. (3.41), thus demonstrating its wide applicability. Results from this Section give support to answer the R#1b (Section 2).

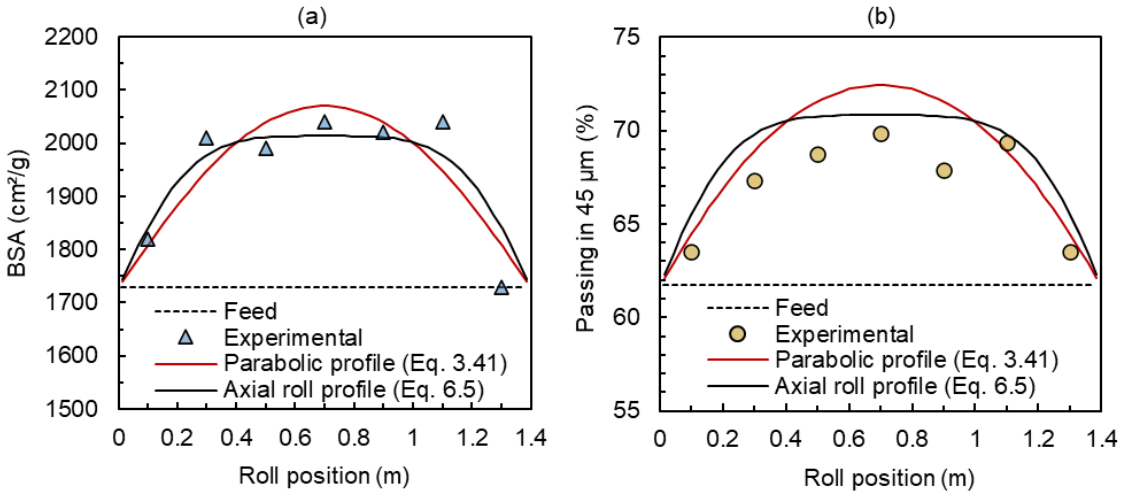


Figure 6.14. Comparison between experimental and predicted BSA (a) and percentage passing the 45 µm sieve (b) in the product along the roll axial position using Eq. (6.5) with $\mu$ = 0.01 (Eq. 6.3) and the parabolic profile (Eq. 3.41). Survey with HPGR #1 with a specific force of 1.5 N/mm$^2$ and a constant throughput of 700 t/h.

Indeed, recent works using DEM simulations (RODRIGUEZ *et al.*, 2021) showed how the pressure profile and, consequently, the breakage profile can change with operating conditions and machine settings. They found both parabolic and trapezoidal profiles for different simulated conditions, besides presenting, in some cases, a shape of the breakage profile not totally equal to the shape of the pressure profile (RODRIGUEZ *et al.*, 2021). Additionally, even though the model presented a distinguished ability to describe from a parabolic to a trapezoidal profile with great accuracy, RODRIGUEZ *et al.* (2021) also showed a more complicated axial roll profile when the HPGR operates with different wear patterns, called the “bathtub” profile. These profile, unfortunately, cannot be predicted by Eq. (6.3).

### 6.6. Working gap prediction

HPGR working gap depicted in Section 3.6.4 presents a clear relationship between setting in the hydro-pneumatic system and hydraulic pressure to predict the working gap when HPGR is under operation. Even though it is recognized as a reliable description (DANIEL, 2002, BARRIOS & TAVARES, 2016, JOHANSSON & EVERTSSON, 2019), the model does not allow capturing changes in the hydraulic pressure of the system from when the equipment is under load. This corresponds to a change in the initial hydraulic pressure of the system from $p_1$ to $p_m$. Assuming that information coming from the process relies solely on the hydraulic pressure ($p_m$), the present work suggests a simple relationship between a new operating pressure $p_m$ and the set point pressure $p_1$ as:

$$\log(p_1) = \frac{\log(p_m) - \vartheta_2}{\vartheta_1} \tag{6.6}$$

where $\vartheta_1$ and $\vartheta_2$ are fitting parameters related to the compaction behavior of the material within the particle bed and can vary according to feed BSA and blend composition feeding the pelletizing plant. As such, using Eq. (3.47) to Eq. (3.50) and the proposed relationship in Eq, (6.6) it is possible to calculate the working gap $\chi_g$ at working pressure $p_m$.

Figure 6.15 presents a comparison between experimental and fitted values for 30 selected tests performed when the HPGR was operating under good roll wear conditions. Results demonstrate good agreement and an ability for capturing the trend between those operational variables, being optimal parameters given as $\vartheta_1$ equal to 1.058 and $\vartheta_2$ equal to 0.011.

Model validation can be seen in Figure 6.16 for HPGR #2 (Plant 3) operating in different periods when the rolls were relatively new. Predictions made by the model demonstrate excellent agreement with measured data when the HPGR is operating up to 6,480 hours, being the average absolute relative deviation from measurements estimated in 4.8%. Assuming that working gap is measured by the edge of the rolls, no relationship between measured and predicted gap should be considered when the HPGR

is under significant roll surface wear. Further discussions on this are presented in Section 7.1.

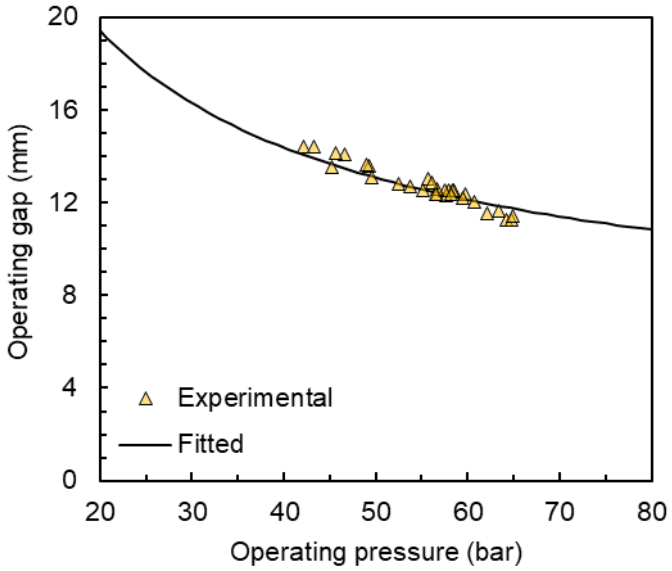


Figure. 6.15. Comparison between experimental and fitted values for the relationship between operating pressure and working gap for selected tests carried in HPGR #2 (Plant 3) investigated in the present work when the rolls were under good wear conditions. Optimal parameters were $\vartheta_1$ equal to 1.058 and $\vartheta_2$ equal to 0.011.

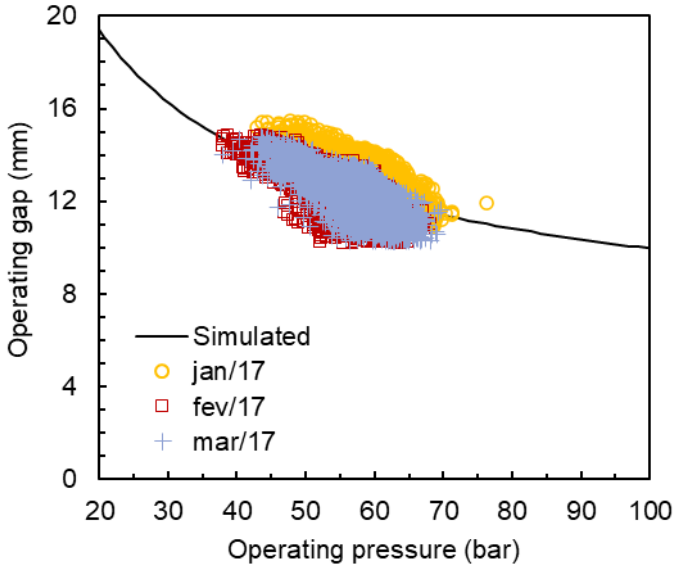


Figure 6.16. Comparison between the relationship between working gap and operating pressure for experimental measurements (markers) and predictions (black line) made by the model calibrated on the basis data presented in Figure 6.15.

An additional result can be found in Figure 6.17 with model prediction showing the relationship between operating pressure and operating gap when changing the nitrogen pressure on the accumulator. An increment in the hydro-pneumatic system stiffness is noticed with a small variation in the working gap for the same range of pressure when nitrogen pressure is low. Up to this point, experimental evidence supporting model prediction in Figure 6.17 were presented elsewhere for tests carried out in a lab-scale HPGR (DANIEL, 2002, BARRIOS, 2015).

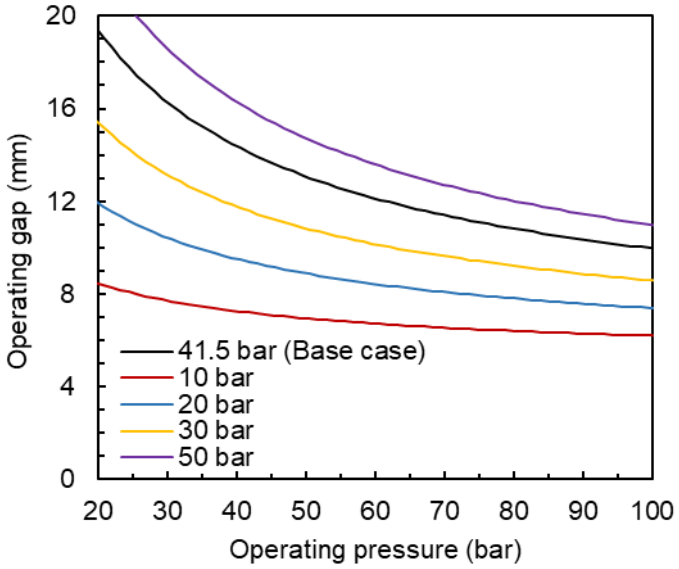


Figure 6.17. Relationship between operating pressure and operating gap predicted by the model when changing the nitrogen pressure in the accumulator. Black line represents the base case calibrated in Figure 6.15.

## 6.7. Final discussions

Improvements on model prediction presented in the present Section were key to set the Modified Torres and Casali model as robust tool describing an industrial-scale HPGR pressing iron ore concentrates. The versatility of the model was demonstrated with the model capturing a wider range of operating conditions and different feed size distributions (Figure 4.2). Modifications proposed allowed the model to capture different pressure profiles along the roll length, which provided a better prediction of the trapezoidal profile presented in the industrial-scale machine. Breakage saturation model was important to partially capture this well-known effect on the particle bed and

improve the prediction of specific surface area generation. Application of a thermodynamic model describing the response of the operating gap based on the operating pressure, material compressibility and hydro-pneumatic system demonstrated potential use to simulate new set of operating conditions in a more realistic approach, which was pointed out as a key limitation is several other models (Section 3.6.6). Results presented in this Section set the Modified Torres and Casali model in a good position to be applied as simulation tool describing variabilities in the operating conditions, feed size distribution and feed characteristics (R#1b and R#1d in Section 2). Additionally, results are also able to support model application when looking to new set of conditions to optimize machine performance (R#3b in Section 2).

# 7. ONLINE MODELING APPROACH

## 7.1. Operational data

Data collected from PIMS (Section 4.3.3) and related to the case study adopted (Section 4.3.2) was analyzed in the entire period. Statistical analysis provided detailed information about operating conditions and performance variables, which were analyzed in the light of global variation in the entire period and local variations when dealing with each specific month.

### *7.1.1. Rolls' surface wear*

Figure 7.1 shows the wear profile in the beginning, middle and end of rolls lifetime.

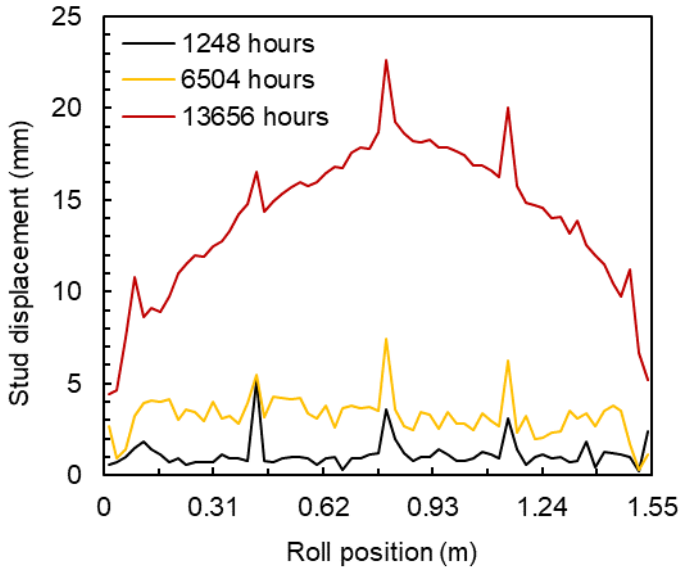


Figure 7.1. Roll wear patterns registered from the beginning of operation up to the end of roll wear lifetime with nearly 15,000 hours of operation.

A trapezoidal profile already discussed and investigated elsewhere (GARDULA *et al.*, 2015, BURCHARDT & MACKERT, 2019, RODRIGUEZ *et al.*, 2021) is evident in the beginning, whereas a parabolic profile is reached when the HPGR is closer to 15,000 hours of operation, which is typically the maximum lifetime for the rolls in operation. Wear profiles were concave and more intensive wear occurred in the middle

of the rolls, besides presenting modest wear on the edge region up to the middle lifetime and a significant edge effect when the parabolic wear profile was achieved in the end of its lifetime. Results are lined up with previous industrial-scale measurements for pressing iron ores (NEJAD & SAM, 2017).

### *7.1.2. Process variables*

Figure 7.2 presents the average variation of roll peripheral velocity (a) and operating pressure (b) in the twenty-four months investigated, whereas vertical lines represent the standard deviation for each month. Figure 7.2a shows the minor global variation of the roll peripheral velocity, in which average values varied from 1.00 to 1.04 m/s for almost the entire period but dropping to around 0.8 m/s for the last months. The very small standard deviation for each month (up to 0.04 m/s) also confirms that this process variable varies within a very narrow range of operating conditions. As discussed in Section 4.3.2, the HPGR investigated does not allow to ensure a choke fed condition when dealing with high throughputs (higher than 600 t/h), thus imposing nearly constant roll velocities throughout its operation.

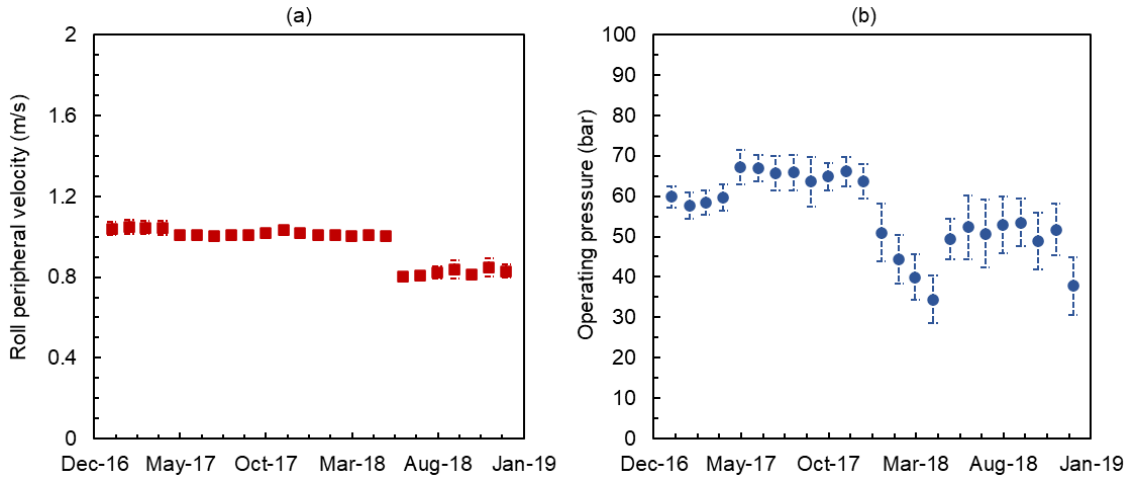


Figure 7.2. Monthly variation of operating pressure (a) and roll peripheral velocity (b) over a period of 24-months. Markers are the average values for each month and vertical lines present the standard deviations in each month.

Additionally, operating pressure, which is the key variable used to improve size reduction, presented monthly averages from 56.7 to 66.9 bar and standard deviations for each month up to 7.1 bar from January 2017 to December 2017, which indicates a small variation of this process variable at that time (Figure 7.2b). The significant reduction of operating pressure after December 2017 demonstrates a clear change in the operational strategy, with average values for each month dropping to values close to 45 bar. This significant global variation justify itself once a reduction in the operating pressure is required when the HPGR is operating under significant roll wear patterns (Figure 7.1), thus trying to avoid the rolls touching themselves. Local variations in the operating pressure in each month can be related to the control strategy adopted in order to maintain constant the torque in both rollers, besides potentially absorbing variation in the feed.

Variation of the average value for the measured operating gap in each month is presented in Figure 7.3.

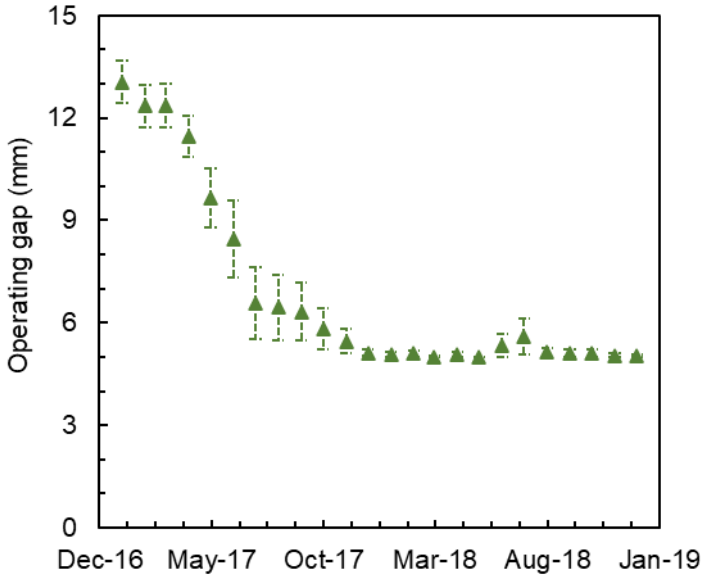


Figure 7.3. Monthly variation of operating gap over the entire 24-month period. Green triangles represent the average values and vertical lines present the standard deviations for each month.

Results showed significant changes in the entire period with average values ranging from 13.0 to 5.1 mm. Unlike the well-known trend between operating pressure

and operating gap (DANIEL, 2002, BARRIOS & TAVARES, 2016), changes in operating pressure depicted Figure 7.2b do not have a clear relationship with the significant reduction in operating gap. In association to Figures 7.1 and 7.2b, the reduction of the operating gap and the poor relationship with operating pressure can be again explained on the basis of roll wear (Figure 7.1). Indeed, taking into account the approach used to determine the operating gap (Section 4.3) and the usual concave profile of the rolls (Figure 7.1), it is worth mentioning that measurements of operating gap are only associated to the distance between rollers in the edge, thus not accounting for the parabolic profile in the center region. Results from Figure 7.3 allow to state that operating gap is not a reliable variable in the process when dealing with worn rollers, although it remains valid as an indicator of roll condition.

Month-to-month variation of throughput and power consumption in the period investigated are shown in Figure 7.4. Minor global variations can be seen in the throughput with average values from 531 to 623 t/h. Standard deviations for each month (vertical lines) up to 52 t/h also show the HPGR throughput varying within a narrow range of operating conditions. Results from Figure 7.4a are mainly governed by the roll peripheral velocity (Figure 7.2a), thus explaining its small changes.

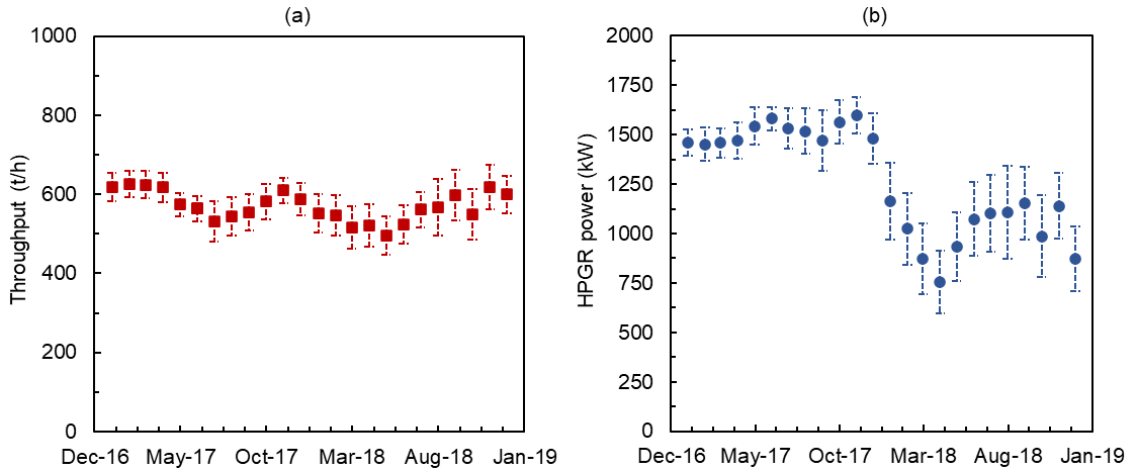


Figure 7.4. Monthly variation of throughput (a) and power consumption (b) over a period of 24-months. Markers represent the average value, whereas vertical lines are the standard deviations for each month.

On the other hand, Figure 7.4b presents both average values (from 710 to 1583 kW) and standard deviations (up to 279 kW) for HPGR power with important variations. Comparing results from Figure 7.4b and Figure 7.2b it is possible to argue that power consumption for this HPGR is mainly determined by changes in operating pressure.

From the ratio between power and throughput, Figure 7.5 allows assessing the specific energy consumption along the entire period, which demonstrates a significant drop in the process variable for the last few months of operation investigated, where average values varied from 2.9 kWh/t to 1.4 kWh/t. Since no significant changes in throughput were presented (Figure 7.4a), it is clear that specific energy consumption is mainly governed by HPGR power variations in the process (Figure 7.4b). Further investigations on how changes in specific energy will impact the product BSA are presented in Section 7.1.4.

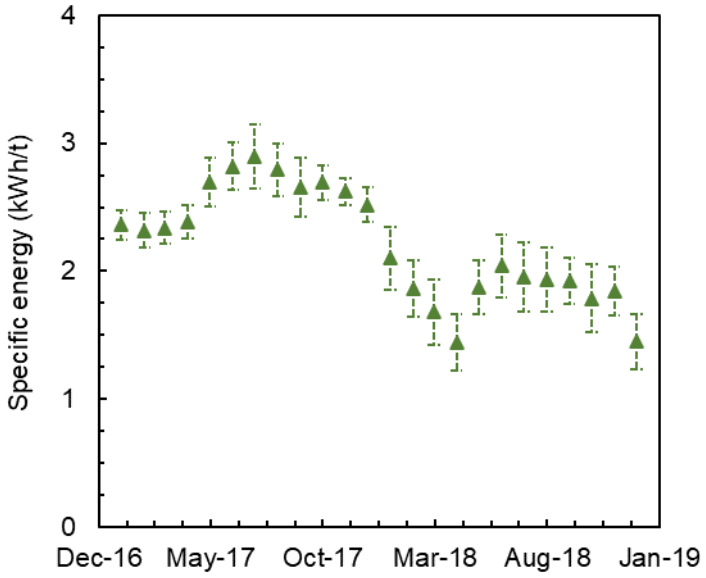


Figure 7.5. Monthly variation of specific energy consumption over a period of 24 months. Markers represent the average value, whereas vertical lines are the standard deviations for each month.

Data from the BSA of the pelletizing plant fresh feed, that is, feed to the ball milling circuit that is upstream, are presented in Figure 7.6a. Results presented minor differences in the BSA in the first fifteen months investigated with small standard

deviation up to 58.3 cm²/g and average values varying from 388 to 473 cm²/g. These results are likely related to small variability in the blend composition up to this point, as shown in Figure 7.6b. On the other hand, when dealing with data from the last nine months of operation, it is worth mentioning that a significant change in the feed blend to the plant occurred, with an associated increase in the proportion of both Carajás and Timbopeba in the feed. The result was a reduction in the BSA to average values around 378 cm²/g. Owing to the different responses of these different ores fed to the plant, which was already demonstrated in Section 5, it is worth mentioning that variations are probably substantial in terms of their response in ball milling and pressing. The larger proportion of Timbopeba and Carajás in the feed blend in the last eight months of 2018 can be explained by the operational strategy adopted in order to compensate the significant wear profile at the end of roll wear lifetime (Figure 7.1). Since these two concentrates are much more amenable for breakage (Section 5), their presence would be able to compensate the worn rolls and reductions in operating pressure at the same period.

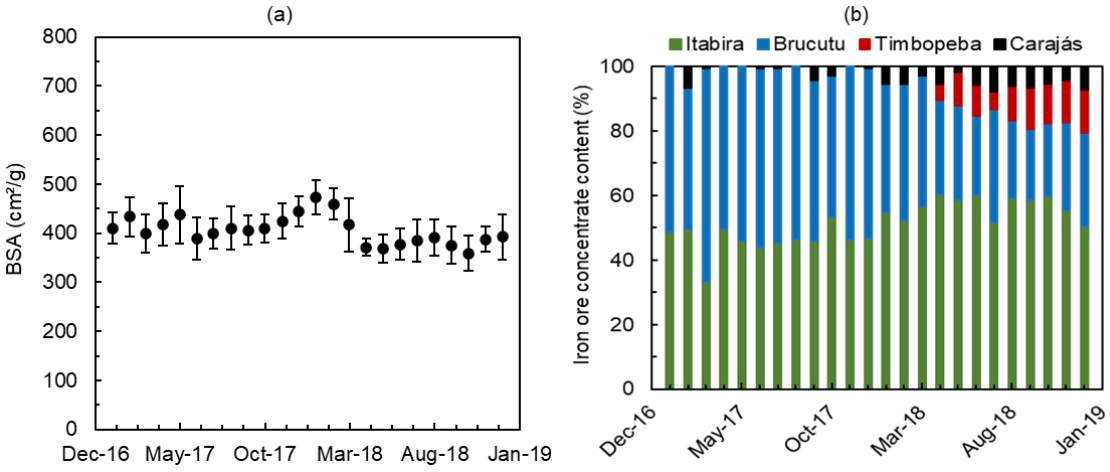


Figure 7.6. Monthly variation of the pelletizing plant BSA fresh feed (a) and iron ore concentrate content over a period of 24 months (b). Markers in Figure 7.6a represent the average value, whereas vertical lines are the standard deviations within each month.

Additional results can also be seen in Figure 7.7 with data from laboratory analyzes characterizing the HPGR feed and HPGR product are presented. Important month-to-month variations are evident, with the average value for each month varying

from 1550 to 1640 cm²/g in the HPGR feed and 1787 to 1916 cm²/g in the HPGR product. Important variations within each month, evident from the high standard deviations, also demonstrate the significant changes in both feed and product size. Moreover, results from Figure 7.7 show that the product BSA is highly influenced by the feed BSA and, beyond the improvement in the product surface area, it is almost ever following the trend imposed by the feed.

As suggested from previous analysis in Figure 7.6, the large proportion of Timbopeba and Carajás in the feed allowed to keep the quality of the HPGR product when the machine was facing the high surface wear (Figure 7.1), thus justifying the strategy adopted in that period.

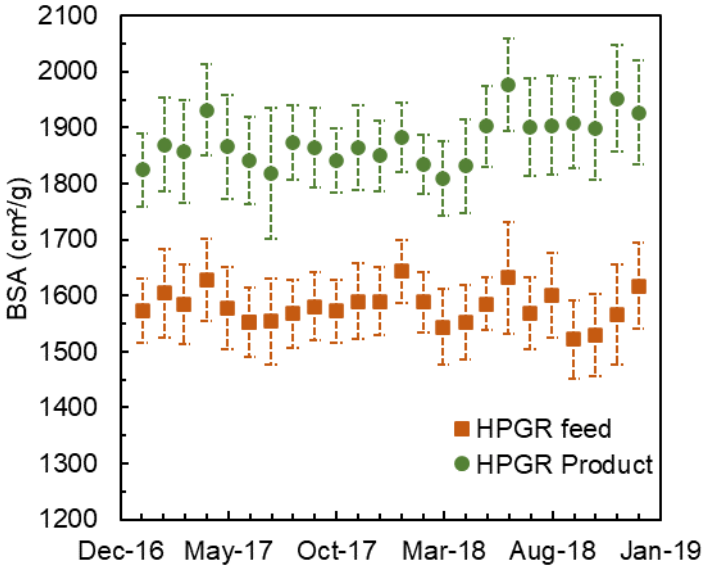


Figure 7.7. Monthly variation of Blaine specific surface areas of the feed and product of the HPGR over a period of 24 months. Markers represent the average value, whereas vertical lines are the standard deviations for each month.

Looking close to a short period, corresponding to one month of operation, Figure 7.8 shows a comparison between HPGR feed and product. Beyond the BSA improvement, it is worth mentioning the trend imposed by the HPGR feed and almost followed by the HPGR product. These results allow concluding that, at least partially, upstream operations are able to govern the HPGR operation imposing a trend in the product provided by the equipment.

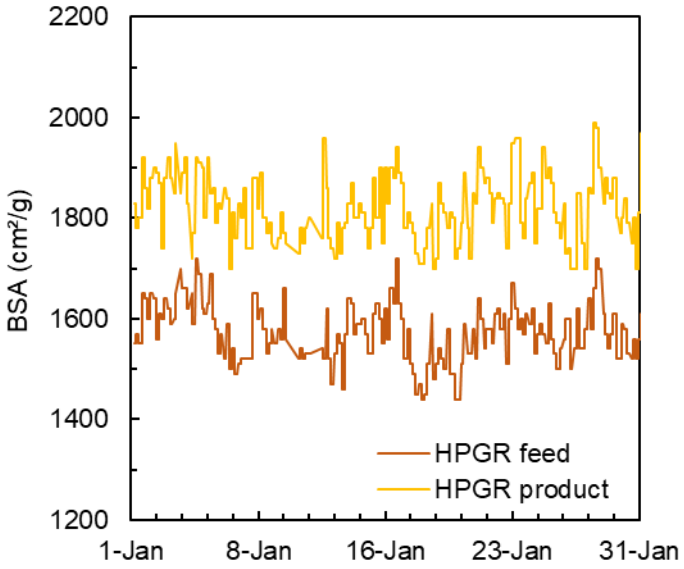


Figure 7.8. Comparison between specific surface area (BSA) of the HPGR feed and product along in the month of January 2017. Values measured every 4h.

As defined by RUMPF (1973), extensively used by the authors (CAMPOS *et al.*, 2019a) and applied to investigate the amenability for breakage of the different iron ore concentrates (Section 5.3), the energy utilization is a convenient way to assess the process efficiency of HPGRs pressing iron ore concentrates. Figure 7.9 presents the month-to-month variation of the energy utilization for the entire period assessed, which allows to state an average process efficiency around 110 cm²/g/kWh/t from December 2017 to March 2018. An average increment up to 63% in the process efficiency (average value up to 218 cm²/g/kWh/t) from Abril/2018 to December/2018 would suggest an optimal scenario from a preliminary analysis. Nevertheless, the high standard deviation up to 67 cm²/g/kWh/t in the last 8 months of operation limits the real application of this scenario, since worn rolls (Figure 7.1) are imposing several variabilities to the process in that period.

Analysis of results presented in Figure 7.9 with data from Figure 7.6b and toughs on breakage behavior of the different iron ore concentrates (Section 5), it is possible to establish a relationship between the increase in Carajás and Timbopeba samples in the blend (Figure 7.6b) with the increment in the average energy utilization of the HPGR operation.

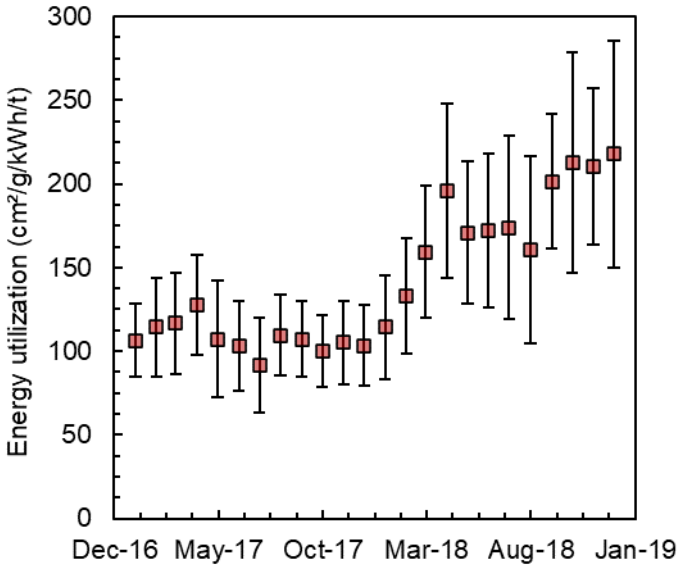


Figure 7.9. Month-to-months variation of energy utilization for the HPGR operation over a period of twenty-four months. Markers represent the average values, whereas vertical lines are the standard deviations within each month.

## 7.2. Online model

The online model is hereby investigated and proposed describing the HPGR for the entire dataset, which relies on the operation varying from the beginning-middle (4,320 hours of operation) to the end (22,000 hours of operation) of roll wear lifetime. Beyond the unusual range of operating conditions from January 2018 to December 2018 due to the significant wear on the rolls (Figure 7.1), changes in the blend composition (Figure 7.6b) also represent a key role in the description of the process. Model predictions will be made on the basis of a pseudo-dynamic approach.

### *7.2.1. Power and throughput*

Power and throughput models from the modified Torres and Casali model were calibrated on the basis of data from industrial survey performed under steady-state and controlled conditions (Section 6.1 and 6.2). Results from Figure 7.10 compare model predictions and experiments in a 10-day period for throughput (a) and power consumption (b), which allows highlighting the excellent description provided by the model. It is worth mentioning that up to this point HPGR was operating under good roll

wear conditions, with approximately 4,320 hours of operation. In addition, a distribution with relative absolute deviation from measurements is presented in Figure 7.11 for both power consumption and throughput predictions.

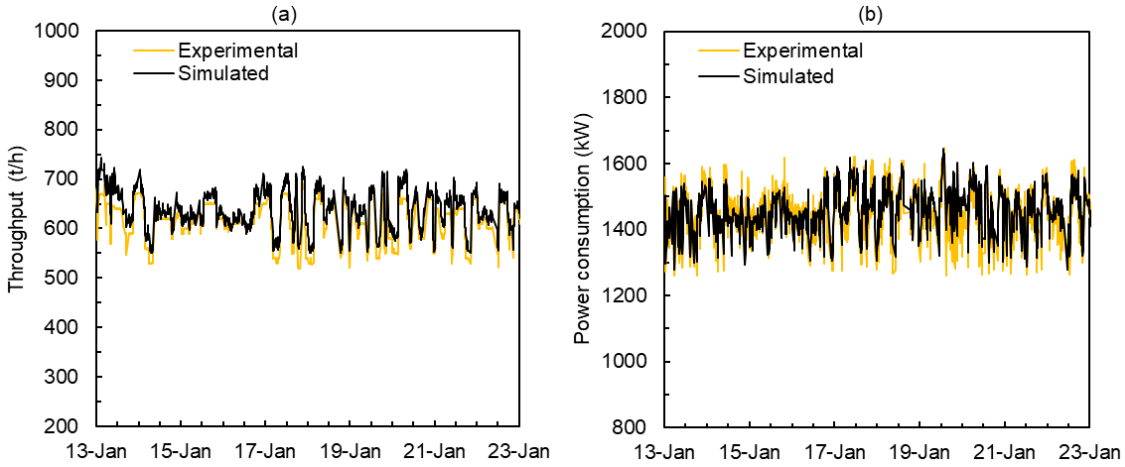


Figure 7.10. Comparison of experimental and predicted values for throughput (a) and power consumption (b) for a 10-day period investigated (January 2017). Data is presented for every 5 min of operation.

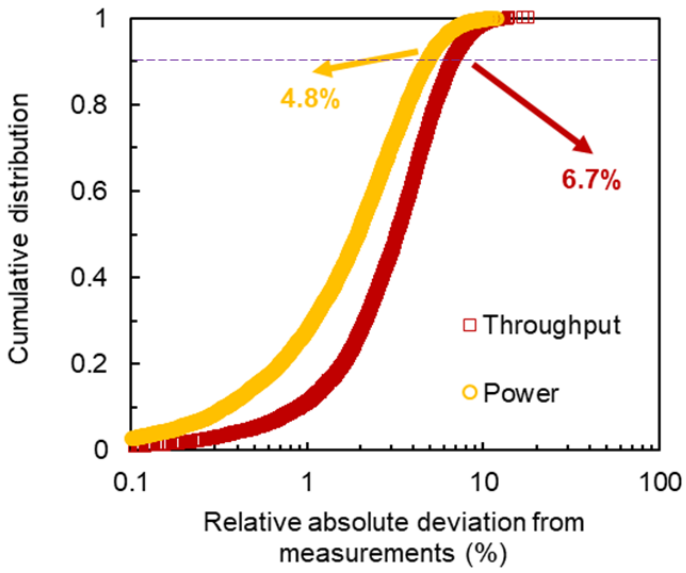


Figure 7.11. Cumulative distribution for the relative absolute deviations from measurements for throughput and power for the first month of operation in the dataset. Arrows show the 90$^{th}$ percentile for both distributions, whereas the purple dashed line shows a division between data with deviations higher and lower than the 90$^{th}$ percentile.

Results from Figures 7.10 and 7.11 demonstrate that predictions were very close to experimental values for the entire dataset analyzed in the first month of operation, with the 90$^{th}$ percentile equal to 4.8% for power consumption and 6.7% for throughput. Beyond that, it is worth mentioning the ability of the model on capturing variabilities in operating conditions to describe small nuances in both performance variables.

Now comparing model predictions to measurements during the entire (24-month) period assessed, Figure 7.12 shows results for throughput (a) and power consumption (b). Good agreement was reached for the first four months analyzed (close to 7,200 hours of operation) with average absolute relative deviation from measurements up to 7.8% for the throughput and 6.3% for the power consumption. This period corresponds to the same period when the HPGR was operating from the beginning of lifetime until a point when the roll wear patterns reached an initial bathtub profile (Figure 7.1). After April 2017, considering the severe wear reported in operation (Figure 7.1), results from Figure 7.12 demonstrate the poor prediction of the model for both power and throughput, with relative absolute deviation from measurements up to 51% for predicting both performance variables. Under these conditions, the nip angle parameter ($\kappa$ in Eq. 3.27) and all parameters from Eq. (3.16) in the throughput model were kept constant and equal to values calibrated based on an industrial survey conducted under steady-state conditions (Section 6.1 and 6.2).

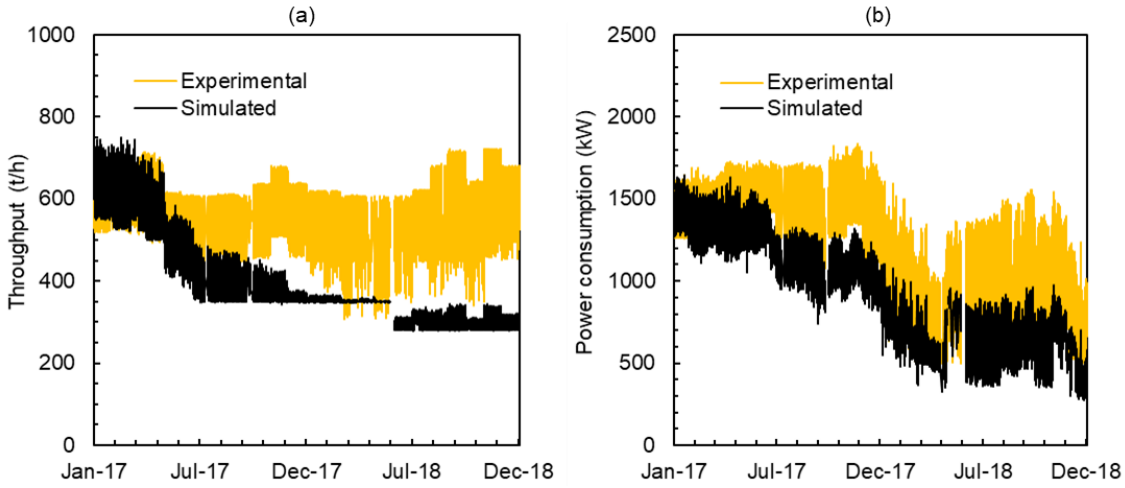


Figure 7.12. Comparison of experimental and predicted values for power consumption (a) and throughput (b) in the twenty-four months investigated. Data is presented for every 5 min of operation.

With the aim of improving the model prediction when dealing with different roll wear patterns (Figure 7.1), the present work proposes modifications to Eq. (3.19) and Eq. (3.27) as follows:

$$Q = f_1 U_g L \chi_g \rho_g \left(\frac{100}{100 - \delta}\right) \tag{7.1}$$

$$P = f_2 2 F_m \sin\left(\frac{\kappa \alpha_{ip}}{2}\right) U \tag{7.2}$$

where $f_1$ and $f_2$ are fitting parameters that should vary according to the roll surface wear and are given as 1 when the HPGR is operating with relatively new rolls. Based on these revised equations, the present work proposes an algorithm to recalibrate $f_1$ and $f_2$ parameters following the approach described in the diagram from Figure 7.13.

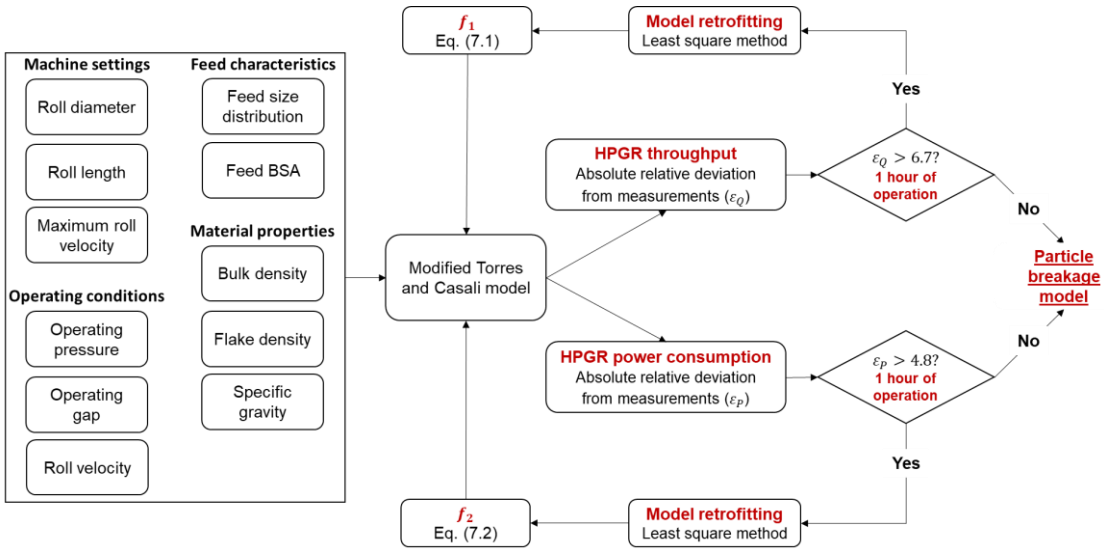


Figure 7.13. Approach used to recalibrate model parameters based on the deviations in model prediction owing to roll wear. $\varepsilon_Q$ and $\varepsilon_P$ are the absolute relative deviations from measurements for the throughput and power consumption, respectively.

The step-by-step approach consisted in a progressive analysis used to verify power consumption and throughput predictions, respectively. A value of absolute relative deviation from measurements equal to the 90$^{th}$ percentile for each error

distribution presented in Figure 7.11 is used as threshold for model accuracy. If the absolute relative deviation from measurements is higher than the respective threshold for more than one hour of operation, the approach allows the model to recalibrate $f_1$ or $f_2$ as discussed previously. Parameter optimization is performed from the difference between calculated and experimental values for a reference test selected in the previous hour of operation using the least squares method. Figure 7.14 finally presents how parameters $f_1$ from Eq. (7.1) (a) and $f_2$ from Eq. (7.2) (b) behave along the entire period assessed. An increment on the value for each parameter is presented, even though no clear trend can be seen. Noisy values can be related to changes in the feed size (Figure 7.7) and ore grindability (Figure 7.6b).

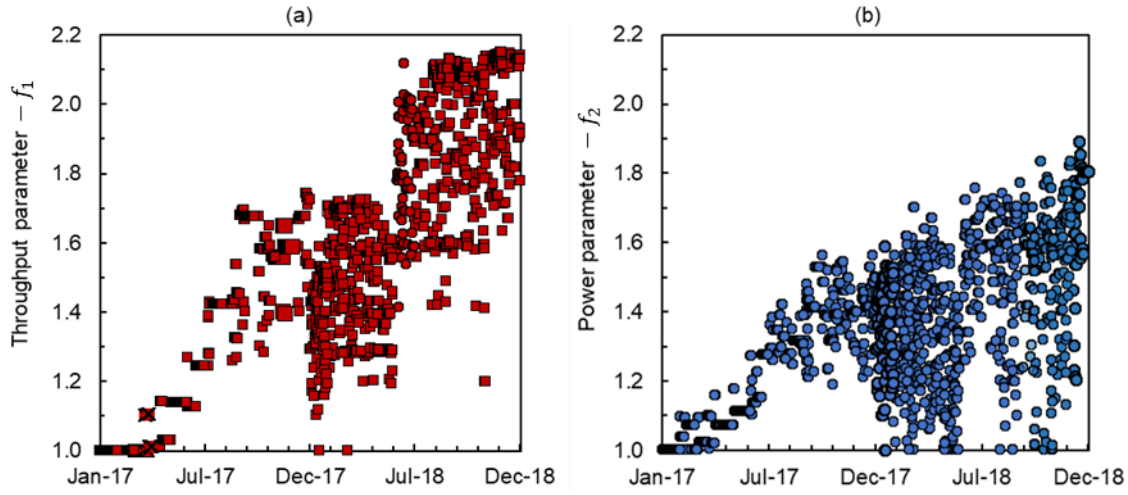


Figure 7.14. Evolution of $f_1$ parameter in Eq. (7.1) (a) and $f_2$ parameter in Eq. (7.2) (b) when applying the method proposed in Figure 7.13 for the entire 24-month period.

Figure 7.15 then presents the comparison between model and experiments when the approach presented in Figure 7.13 was applied. Results showed very good agreement over the entire period, with absolute relative deviations of simulations to measurements of up to 5.4% for power consumption and 9.5% for throughput. The approach adopted appears to be able to circumvent the bias in the model prediction when dealing with worn rolls, as well as important variations in feed competence (Figure 7.6b). Nevertheless, results from Figure 7.15a shows the model limited the ranges of predicted values for HPGR throughput after November 2017. These poor predictions may be explained, at least in part, by the simplified assumption of

recalibrating a single parameter to compensate the error of the operating gap measurement (Figure 7.3), which may be regarded as a limitation of the algorithm.

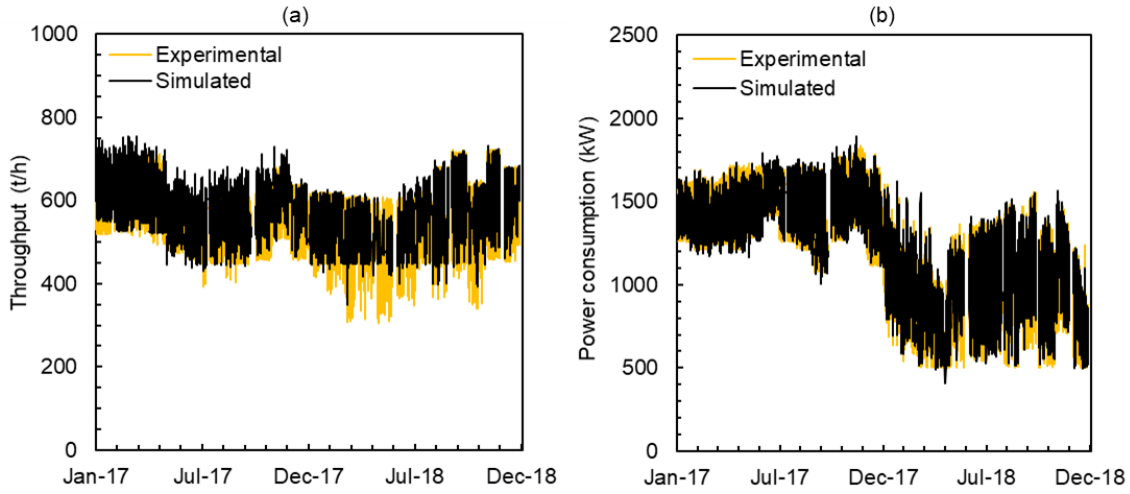


Figure 7.15. Comparison between experimental and predicted throughput (a) and power consumption (b) in a period of twenty-four months assessed after applying the calibration approach depicted in Figure 7.13. Data is presented for every 5 min.

Moreover, Figure 7.16 presents a comparison between experimental and predicted specific energy consumption for short (a) and long (b) periods.

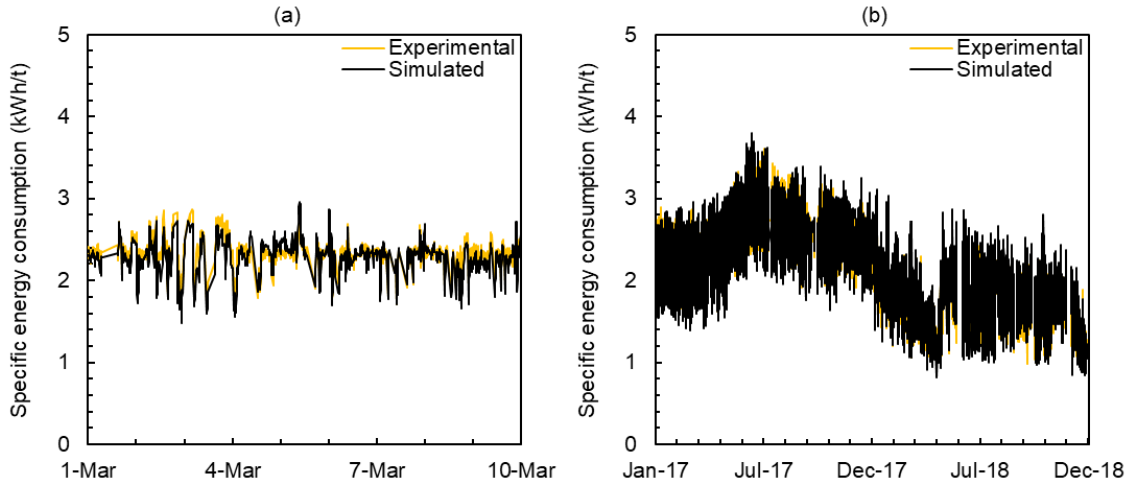


Figure 7.16. Comparison between experimental and predicted specific energy consumption in a 10-day period (a) and twenty-four-month period (b) assessed after applying the method from Figure 7.13. Data is presented for every 5 min of operation.

For comminution operations, it is useful to compare the specific energy consumption from the predicted on the basis of predicted power consumption and throughput. Those results demonstrated good agreement between model and experiments and an ability to capture variations on this process variable both in the short and the long term (Figure 16). Results from this Section give support to answer R#2 (Section 2).

*7.2.2. Size reduction*

In order to simulate the size reduction in the HPGR the breakage model was calibrated based on survey data. Parameters from breakage and selection function were considered constant as calibrations made using data under steady-state conditions as depicted in Section 6.3. As such, considering the model presented in Eqns. (4.3) and (4.4) and the previous calibration (Section 6.3), Figure 7.17 presents the comparison between experimental and predicted values for the HPGR product BSA when considering a constant and average feed size distribution with 1573 cm²/g in a period of 1-month.

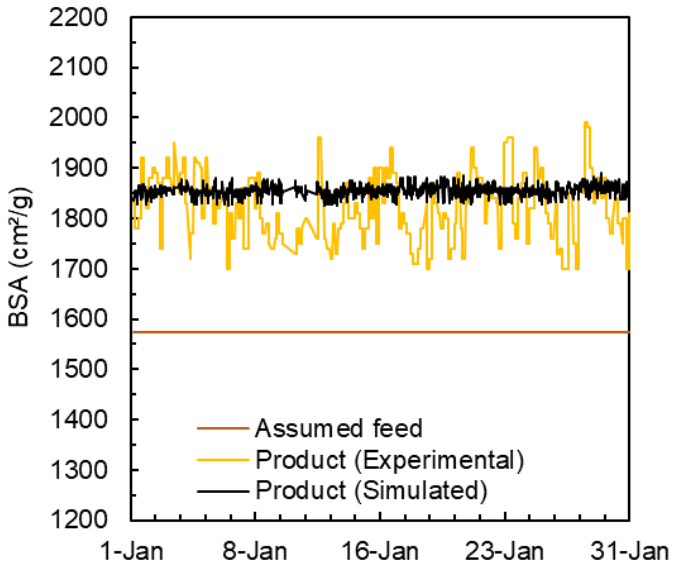


Figure 7.17. Comparison between experimental and predicted value for the HPGR product BSA considering a fixed feed size distribution with 1573 cm²/g. Fixed feed was estimated based on the average value for the entire month of operation.

This simplified assumption was adopted in order to check the real effect of the feed size distribution in the model prediction. Indeed, as discussed in Figures 7.7 and 7.8, there is a clear trend between both HPGR feed and product, being the second one strongly determined by the first. Analyzing both results together allows to explain the poor agreement between model and experiments presented in Figure 7.17.

Figure 7.18 then presents a more complete version of the model dealing with the measured feed size distribution in real time. First it is worth highlighting the variation of the HPGR product over the entire period assessed following the trend imposed by the HPGR feed. Nevertheless, results from Figure 7.18 show the very good agreement between experimental and predicted values for the HPGR product BSA with average absolute relative deviation from measurements equal to 2.7%. Results also allow to conclude that the model is able to capture key variations in the feed size distribution and accurately describe the HPGR product. The predicted HPGR product BSA was calculated on the basis of the predicted product size distribution using a method proposed elsewhere (ZHANG & NAPIER-MUNN, 1995) with calibration and validation presented in Appendix A.

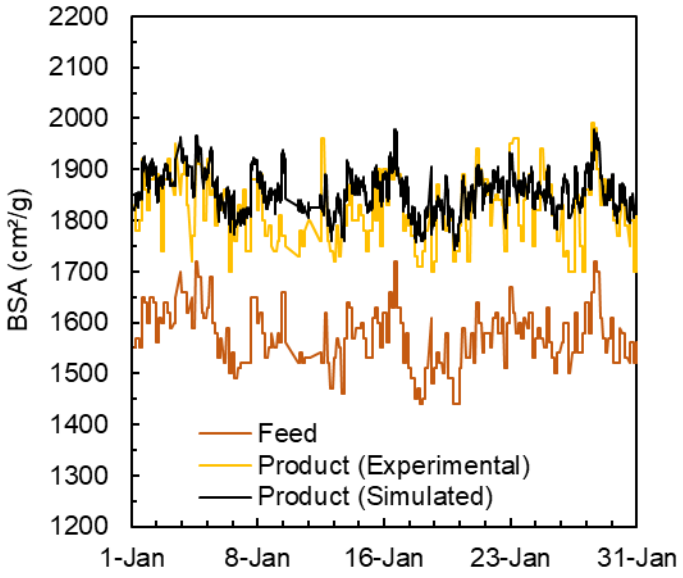


Figure 7.18. Comparison between experimental and predicted value for the HPGR product BSA on the basis of the feed BSA measured every 4 hours. Data presented refers to the month of January 2017.

Now examining the entire (24-month) period investigated in the present work, Figure 7.19a presents a comparison between experimental and predicted values for the HPGR product BSA. Results demonstrate a very good agreement between model and experiments from January 2017 to March 2018 with average absolute relative deviation from measurements up to 3.5%, whereas model predictions from Abril 2018 to December 2018 slightly underestimated the experimental product BSA with average absolute deviation from measurements going up to 5.6% (Figure 7.19a). Since very good predictions for specific energy consumption were presented in Figure 7.16, deviations in model predictions for the last nine months of operation in 2018 are likely related to changes in the blend composition, as already evidenced in Figure 7.6b.

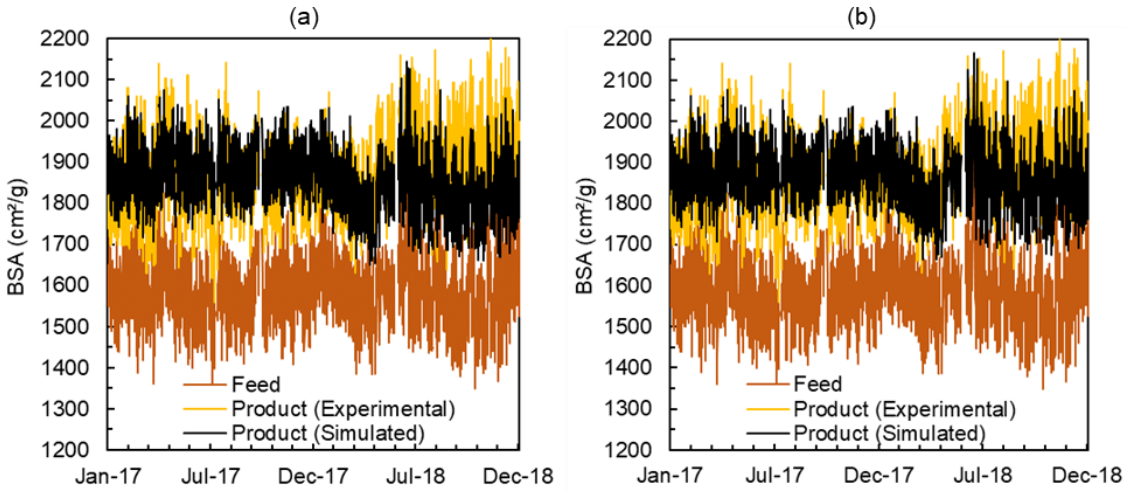


Figure 7.19. Comparison between experimental and predicted HPGR product BSA using the fitted breakage function from CAMPOS *et al.* (2019b) (a) and considering different average breakage functions determined from piston-and-die tests carried out with the different iron ore concentrates (Section 5.4) and an average blend composition from Figure 7.6b (b) in a period of twenty-four months assessed. Data is presented for every 5 min of operation.

As already discussed in Section 5, Carajás and Timbopeba concentrates are much more amenable for breakage than Brucutu and Itabira concentrates, with much higher energy utilization for Carajás and Timbopeba concentrates (Table 5.1). Evidence presented up to this point allows to conclude that differences in their amenability for breakage are highly associated to the energy-specific progeny size distribution for those

concentrates. Taking into account the energy specific progeny size distribution estimated for each concentrate in Section 5.4 (Figure 5.16), a comparison is then made between them and the fitted cumulative breakage function (CAMPOS *et al.*, 2019b) used in the present work is presented in Figure 7.20a. High similarity was observed between the energy specific progeny size distribution and the fitted breakage function (CAMPOS *et al.*, 2019b), with the exception of Carajás with a much more aggressive progeny size distribution and Timbopeba with a slightly finer progeny size distribution.

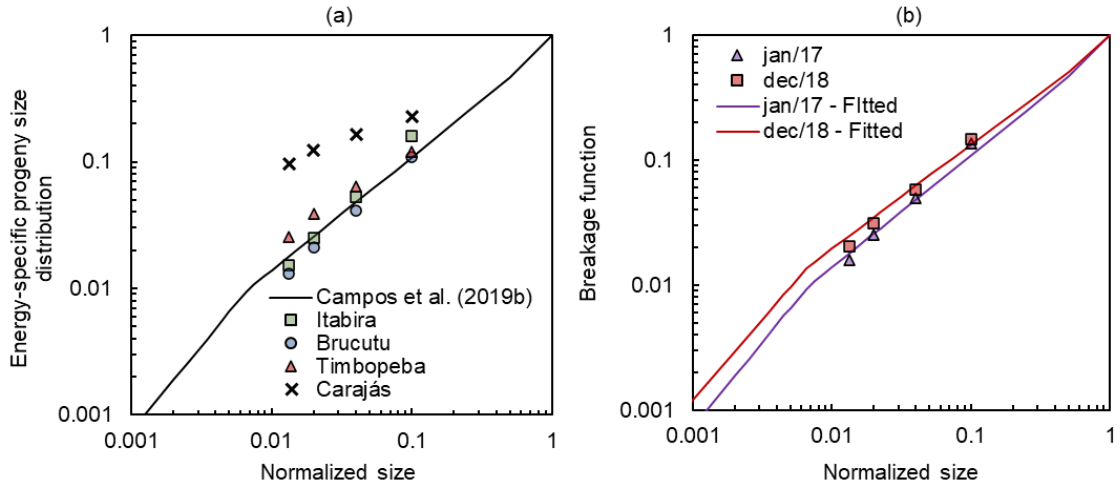


Figure 7.20. Comparison between fitted breakage function used in the present work (CAMPOS *et al.*, 2019b) and the energy-specific progeny size distribution for the different iron ore concentrates composing the blend feeding the pelletizing plant (a) and the energy-specific progeny size distribution estimated and fitted for the blend in two different periods (b). Fitted breakage function in (b) relies on fitting the parameter $\gamma$ (Eq. (3.46)) to 0.89 in January 2017 and to 0.82 in December 2018.

Assuming data from Figure 7.6b, a breakage function was then estimated for each month from a weighted average of the energy-specific progeny size distribution depicted in Section 5.4 and presented in Figure 5.16 and 7.20a. For this new approach, parameter $\gamma$ from Eq. (3.46) was fitted for each new energy-specific progeny size distribution estimated in the entire period in order to introduce it in the original modeling approach. The choice of parameter $\gamma$ to be refitted was made since no reliable information for the coarser part of the energy-specific progeny size distribution was presented to justify fitting any other parameter from Eq. (3.46). Beyond that one,

remaining parameters from both Eqns. (3.46) and (3.39) were kept constant. Figure 7.20b presents a comparison between the estimated energy-specific progeny size distribution and the respective fitted breakage function (Eq. (3.46)) for different periods along the twenty-four months investigated.

Using these new modeling approach to describe the different periods along the twenty-four months investigated, Figure 7.19b finally shows a comparison between model and experiments for the HPGR product BSA. Slight improvement in model prediction for the last nine months in 2018 was achieved with an average absolute relative deviation from measurements going down to 3.9%. An important ability of the model to capture material breakage behavior in real-time using information from bench-scale tests was successfully demonstrated. Minor improvements achieved, even though using detailed information from piston-and-die tests, would be explained, at least in parts, by several important effects in the particle bed still neglected by this modeling approach. Results from this Section allows giving support to answer the R#1c raised in Section 2.

### *7.2.3. HPGR online digital assistant application*

Simulation of case studies using the HPGR online model as a digital assistant are presented as follows according to their main purpose, being the first one aiming to reduce the variability of the final product and the second one with the objective of emulating a reduction in the work carried out by the ball milling stage (upstream operation) to check how the HPGR would absorb a coarser feed size distribution in the circuit.

- <u>Reducing the variability of the final product</u>

Results from Figure 7.21a show a comparison between the HPGR product BSA observed in January 2017 (Base case) and the prediction made by the HPGR online model as described in Section 4.4.4 for the same period. A clear reduction of the BSA variability can be seen when using the new scenario predicted, being the standard deviation equal to 66.1 $cm^2/g$ for the base case and 13.6 $cm^2/g$ when achieving the new desired setpoint.

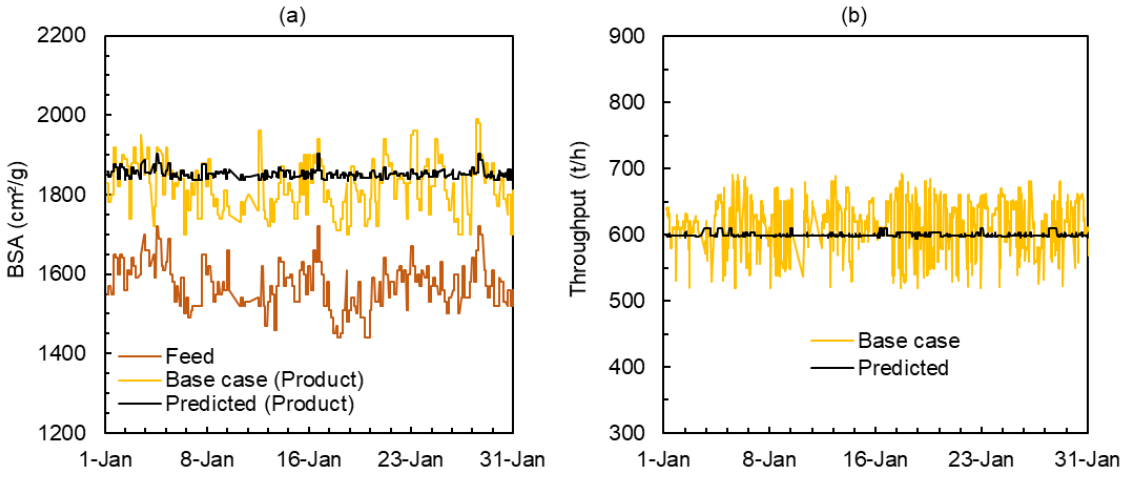


Figure 7.21 Comparison between HPGR product BSA (a) and throughput (b) observed during operation in January 2017 (Base case) and predicted by the HPGR online model when considering the desired setpoint in case study 1 as a new operational strategy. Data is presented for every 5 min of operation.

Beyond achieving the main objective, results from Figure 7.21a also demonstrated an ability of the new scenario to keep the quality of the final product in an acceptable level and the ability to absorb variabilities in the feed and provide a more constant product that is fed to the pelletizing circuit. Figure 7.21b also compares base case and HPGR online model predictions for the throughput, demonstrating an ability to reach the target value with an almost constant throughput of 600 t/h.

Besides the results in Figure 7.21, analysis on the manipulated variables is critical to understand how the new set of conditions defined by the model that would allow the machine to achieve this new desired setpoint. Figure 7.22 presents a comparison between the base case conditions and the new scenario predicted by the HPGR online model for the roll peripheral velocity (a) and operating pressure (b). Throughput results from the new scenario analyzed (Figure 7.21b) coupled to results from Figure 7.22a showed the feasibility of operating with roll peripheral velocities not higher than 1.1 m/s to achieve a more constant throughput. Those results are key to present feasibility of the new scenario since high roll velocities would not allow the feed hopper to keep a choke fed condition (Section 4.3.2). Values of operating pressure from Figure 7.22b in this new set of conditions (37.8 to 86.7 bar) reinforce the potential application of this scenario since it varied within the operational range allowed.

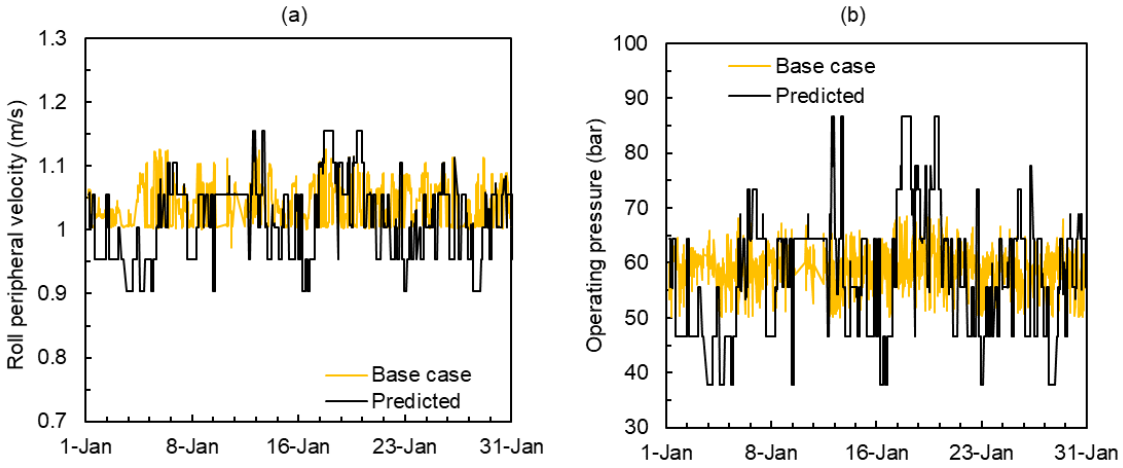


Figure 7.22. Comparison between roll peripheral velocity (a) and operating pressure (b) observed during operation in January 2017 (Base case) and predicted by the HPGR online model when considering the desired setpoint in case study 1 as a new operational strategy. Data is presented for every 5 min of operation.

Analysis on the process efficiency is also possible comparing specific energy consumption (Figure 7.23a) and energy utilization (Figure 7.23b) in this new scenario.

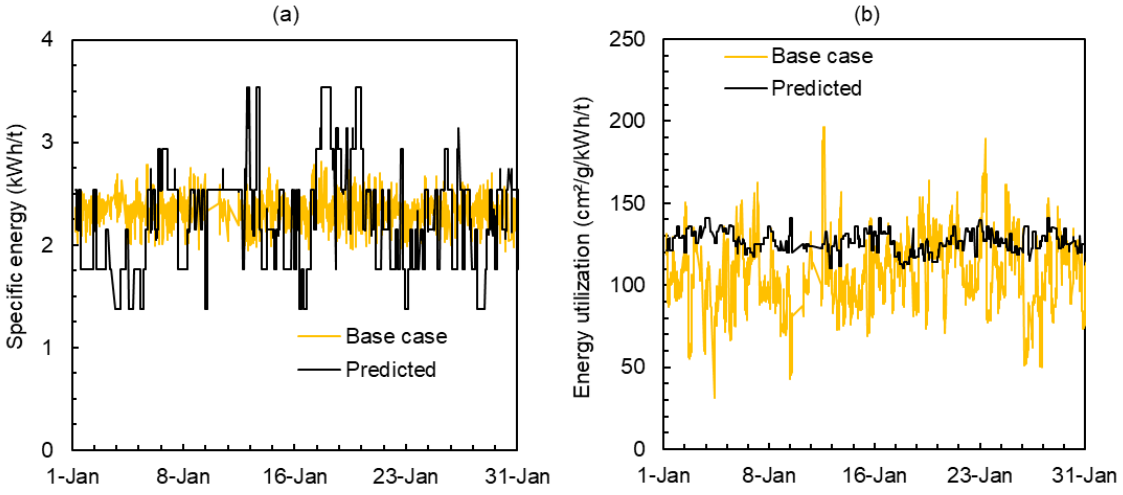


Figure 7.23. Comparison between specific energy consumption (a) and energy utilization (b) observed during operation in January 2017 (Base case) and predicted by the HPGR online model when considering the desired setpoint in case study 1 as a new operational strategy. Data is presented for every 5 min of operation.

Results showed an average reduction of 5.8% on the specific energy consumption for the new scenario predicted by the HPGR online model, being the base case equal to 2.36 kWh/t and the new scenario equal to 2.23 kWh/t (Figure 7.23a). A more complete analysis depicted in Figure 7.23b allows concluding that an average reduction in energy utilization of almost 19.2% would be possible with the new scenario, being the base case equal to 107 cm²/g/kWh/t and 127 cm²/g/kWh//t for the new scenario predicted. A summary of the main results is presented in Table 7.1.

- Coarser HPGR feed BSA

As presented in Figure 4.10 (Section 4.4.4), a reduction of 100 cm²/g in the HPGR feed would be provided by reducing the work carried out by the ball milling stage, which is well-known for its poor energy efficiency. As such, Figure 7.24a presents a comparison between the HPGR product BSA in the base case and when using the new proposed feed. Results by the model indicated an ability of the HPGR absorbing a coarser feed to provide a qualified product BSA with small variabilities (standard deviation of 7.2 cm²/g) and close to the original goal of 1850 cm²/g. As well as presented in Figure 7.21b, small variabilities in the throughput were also achieved when adapting the operating conditions.

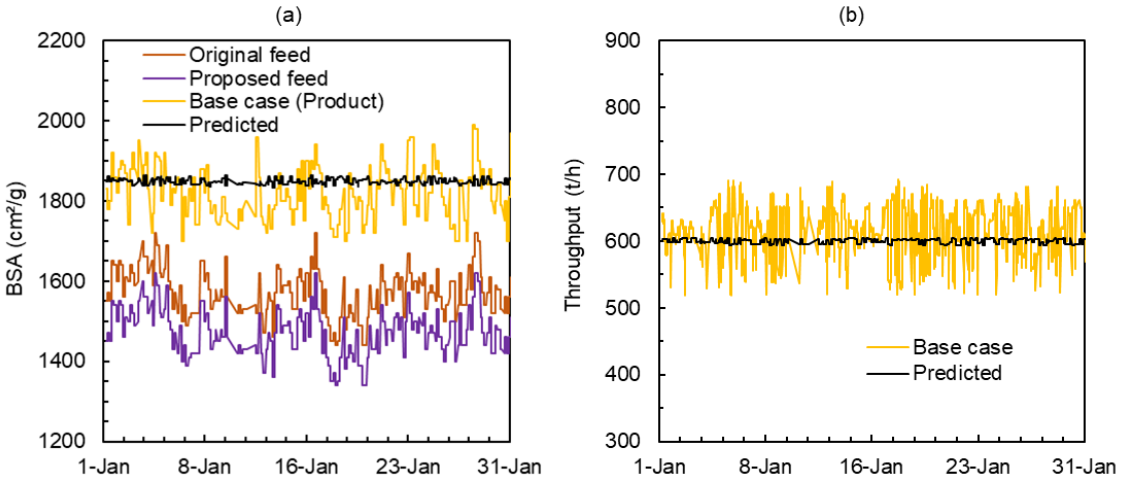


Figure 7.24. Comparison between HPGR product BSA (a) and throughput (b) observed during operation in January 2017 (Base case) and predicted by the HPGR online model when considering the desired setpoint in case study 2 as a new operational strategy and dealing with the new proposed feed. Data is presented for every 5 min of operation.

Differently from results in the previous case study, changes in roll peripheral velocity (Figure 7.25a) and operating pressure (Figure 7.25b) were much higher for this new scenario.

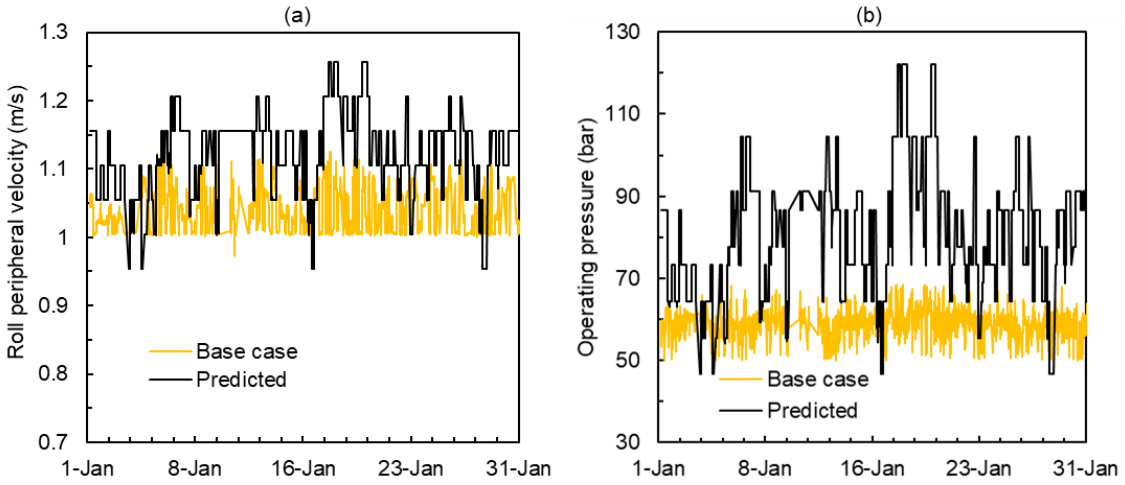


Figure 7.25. Comparison between roll peripheral velocity (a) and operating pressure (b) observed during operation in January 2017 (Base case) and predicted by the HPGR online model when considering the desired setpoint in case study 2 as a new operational strategy.

Indeed, to compensate the coarser feed an increment in operating pressure was required with values going from 47 to 122 bar. The consequent reduction of the operating gap induced an increment in roll peripheral velocity up to 1.3 m/s to keep the throughput target, which is still acceptable for this operational variable. Nevertheless, roll peripheral velocities beyond that would reflect in values out of the boundary recommended for keeping the choke fed condition (Section 4.3.2).

Additional results are also presented Figure 7.26 showing a comparison between base case and the current case study for the power consumption (a) and specific energy consumption (b) in the entire month assessed. As expected, high power (Figure 7.26a) was achieved following the high-pressure values presented in Figure 7.25b, thus proving, as peer-discussed (Section 7.1.2), that HPGR power consumption is mainly influenced by the operating pressure. Moreover, Figure 7.26b shows how specific energy consumption followed the trend imposed by the power consumption (Figure

7.26a) since an almost constant throughput was achieved. High values for power and specific energy are below the operational range limit presented in Table 4.3.

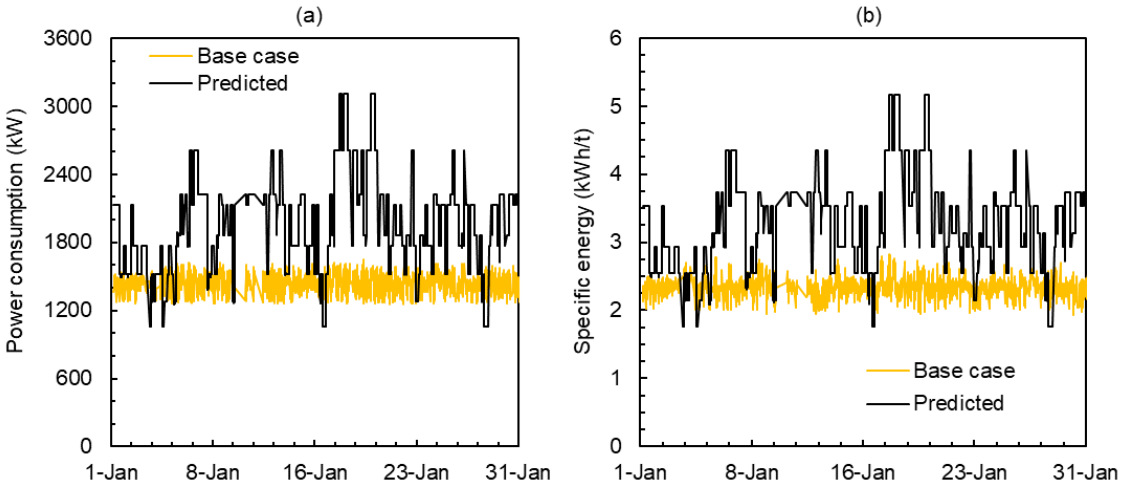


Figure 7.26. Comparison between consumption (a) and specific energy consumption (b) observed during operation in January 2017 (Base case) and predicted by the HPGR online model when considering the desired setpoint in case study 2 as a new operational strategy.

Comparison between the HPGR energy utilization in the current case study and the energy utilization in the ball milling stage is finally presented in Figure 7.27.

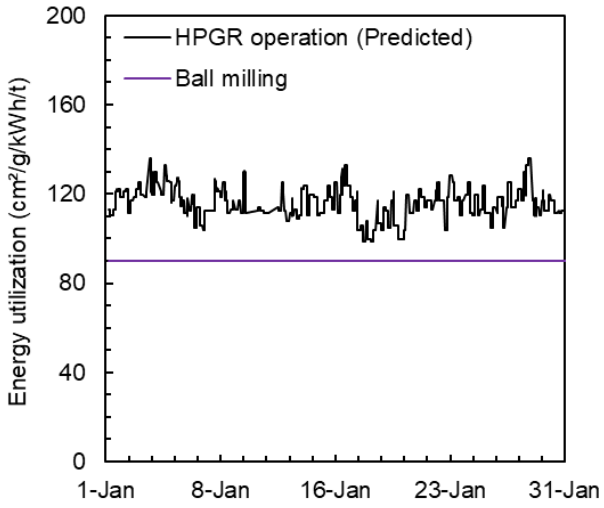


Figure 7.27. Comparison between the energy utilization for the HPGR online model prediction in the current case study and the ball milling stage.

A 29% higher energy utilization for the HPGR operation is demonstrated and shows the significant improvement associated with the new scenario proposed when looking to the average energy utilization in the entire month of operation investigated. Energy utilization for the ball milling and classification step was calculate from a historical mean from one of the pelletizing plants from Vale S.A. and is given as 90 cm²/g/kWh/t (VIANNA *et al.*, 2019).

A summary of the main results comparing the base case and case studies 1 and 2 are presented in Table 7.1. Results from this Section give support to answer R#3 raised in Section 2.

Table 7.1. Summary of the main results for the base case and two case studies investigated in the present work.

| | Base case | Case study 1 | Case study 2 |
|---|---|---|---|
| Average feed BSA (cm²/g) | 1573 | 1573 | 1473 |
| Average specific energy (kWh/t) | 2.36 | 2.23 | 3.29 |
| Coef. of variation of HPGR product BSA (%) | 3.6 | 0.7 | 0.4 |
| Coef. of variation of HPGR throughput (%) | 5.9 | 0.6 | 0.6 |
| Average energy utilization (cm²/g/kWh/t) | 106 | 127 | 116 |

### 7.3. Final discussions

An application of the online model was demonstrated with good agreement between model and experiments. An ability of the model to capture variabilities in real time was presented and the new method proposed allowed circumventing the model limitation dealing with worn rolls. Nevertheless, it is important to recognize that the main issue on the poor model prediction dealing with worn rolls e fully related to the unreliable estimation of the operating gap. Future works with a more realistic version of the HPGR online model would be able to incorporate this effect instead of using the proposed method to parametrize the model according to different roll surface wear conditions. Results from Sections 5 and 6 gave support for the online application with model being able to use information from bench-scale tests to characterize the particle

breakage behavior of the blend of iron ore concentrates used to feed the pelletizing plant. Research objectives raised in Section 2 (R#1c, R#2 and R#3) were finally met.

Results were presented when using the HPGR online model as a digital assistant aiming to find an alternative set of conditions to optimize the HPGR product BSA and throughput based on a desired setpoint of HPGR performance. Potential new operational strategies were presented and allowed a key reduction in the product BSA variability, beyond keeping constant the quality of final product and the HPGR throughput. New scenarios still presented a reduction in energy consumption and an increment in process efficiency. Despite the interesting operational strategies analyzed, it is worth to recognize that frequent changes in operating pressure as predicted by the HPGR online model in Figures 7.22 and 7.25 would provide damages to the bearing system, thus compromising a bit the application of this scenario for huge changes in operating pressure.

Considering potential applications of this HPGR online model structure as an engineering tool in the minerals industry, it is key to have a deep understanding about the HPGR operation under different conditions and feed characteristics, beyond looking to the whole circuit surrounding the HPGR to check for their main influence on the machine performance. The step-by-step to apply this HPGR online model is presented as follow:

- Calibrate and validate the HPGR phenomenological model describing the machine performance under steady-state conditions.

- Ensure that information like operating conditions will be recorded in real-time and used as an input to the model. HPGR feed size distribution, which is a key model input, should be estimated in real-time or, at least, measured and assumed as constant for a given period of time. Information used as a model input should be analyzed in advance to avoid “garbage in, garbage out”.

- Understand the main influence of the HPGR upstream and downstream process on the machine performance and use it to improve model prediction.

- Capture variabilities in the different grindability of the ore typologies feeding the HPGR. Since this information would be quite important for several industrial operations, it is important to have some evidence on their breakage behavior to improve particle breakage description.

## 8. SOFT SENSOR DESIGN AND ASSESSMENT

Considering the good description of the first module of the online modeling approach (Section 7), the second module will be discussed in this Section. As depicted in Section 4.4.2, this module relies on a more complete online model structure with the HPGR feed being predicted from a data driven soft sensor model modelled on the basis of operating conditions recorded from the ball milling and classification step. As such, Section 8.1 will present a detailed analysis of some of the operating conditions of the ball milling and classification step, beyond highlighting the poor estimation of the BSA from the PSI. Assuming that the HPGR feed BSA will be predicted based on ball milling and classification data, an important residence time should be considered between the hydrocyclone overflow and the HPGR feed (Figure 3.2). Section 8.2 will estimate the time delay between them. Section 8.3 will then provide the feature selection, whereas Section 8.4 will show the model training. Application of this second module of the online model will be discussed in Section 8.5. Figure 8.1 presents a schematic diagram with the main steps in the data driven soft sensor design.

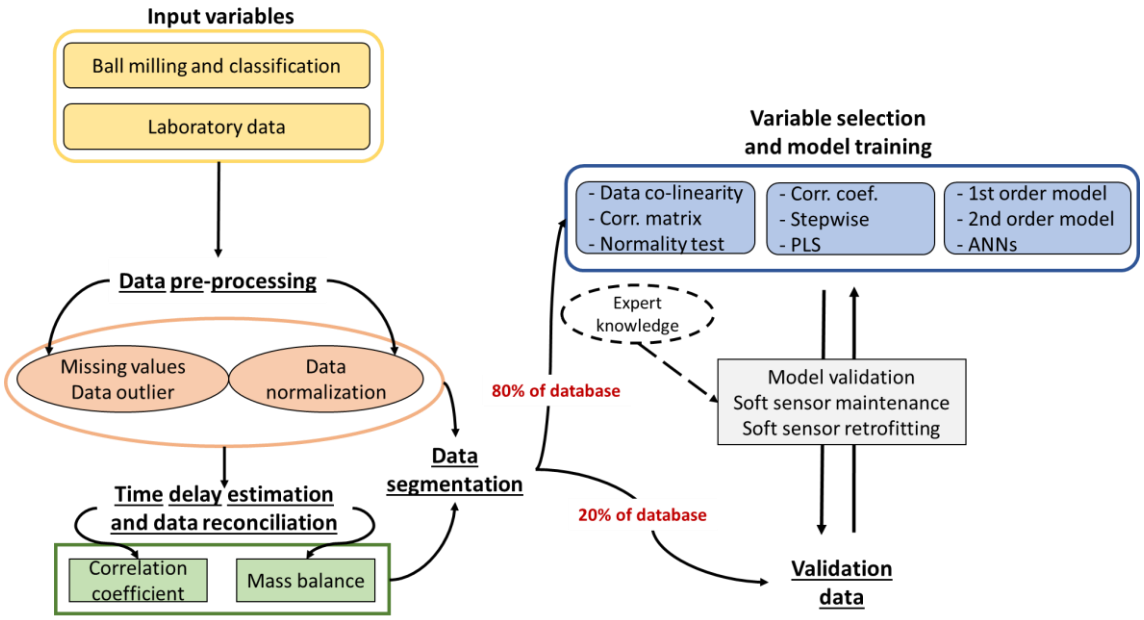


Figure 8.1. Schematic diagram with the main steps within the data-driven soft sensor design used to predict the Blaine specific surface area (BSA) of the HPGR feed.

## 8.1. Data quality assessment

### *8.1.1. Data pre-processing*

To use a more reliable dataset in the design of the data driven soft sensor model, the steps proposed in Section 4.3.3 for data pre-processing were adopted. Beyond avoiding missing values and removing data outliers using Eq. (4.1), expert knowledge was also used to filter data of the ball milling and classification steps, in which ranges are presented in Table 8.1.

Table 8.1. Limit ranges used for each variable within the circuit in order to remove outliers on the basis of expert knowledge.

| Variable | Minimum | Maximum |
|---|---|---|
| Fresh solids feed rate (t/h) | 100 | 500 |
| Mill power (MW) | 0.5 | 5 |
| Mill specific energy (kWh/t) | 10 | 15 |
| Hydrocyclone slurry feed rate ($m^3/h$) | 200 | 1500 |
| Inlet pressure ($kgf/cm^2$) | 0.2 | 2 |
| Water addition in the hydrocyclone feed ($m^3/h$) | 100 | 1400 |

### *8.1.2. PSI data analysis*

Aiming to check the reliability of the BSA feed estimated by the PSI, Figure 8.2 presents a comparison between the average values for the HPGR feed BSA estimated by the PSI in both ball mill lines and the BSA measured in laboratory in a period from January to December 2017. Significant global variation can be seen in the average BSA from PSI with values varying from 1467 $cm^2/g$ to 1981 $cm^2/g$, beyond high standard deviation for each month. On the other hand, BSA data from laboratory measurements, which presented average values from 1551 $cm^2/g$ to 1628 $cm^2/g$ and standard deviations up to 79 $cm^2/g$, were better behaved and more coherent to this variable range reported elsewhere (BUENO, 2019).

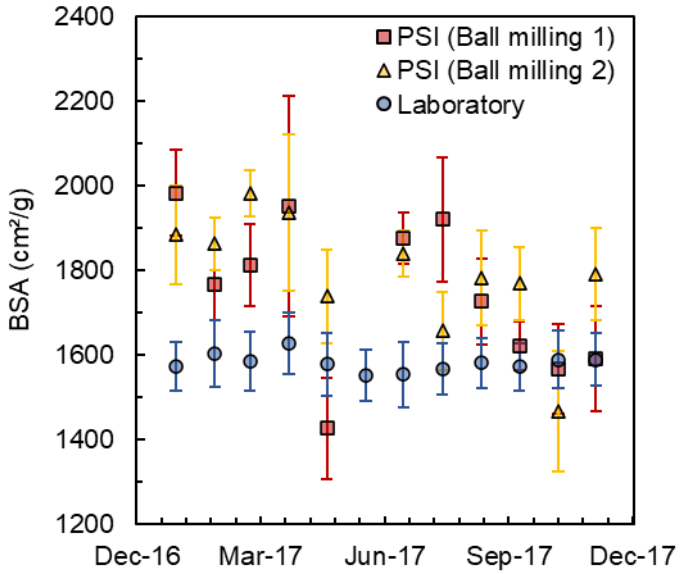


Figure 8.2. Variation in a period of twelve months of the average value for the HPGR feed BSA estimated in the PSI and measured in laboratory. Markers represent the average value for each month, whereas vertical lines represent the respective standard deviation.

To confirm the poor estimation made by the PSI, Figure 8.3 shows that no trend or correlation can be stated between the BSA from both PSI and laboratory measurements.

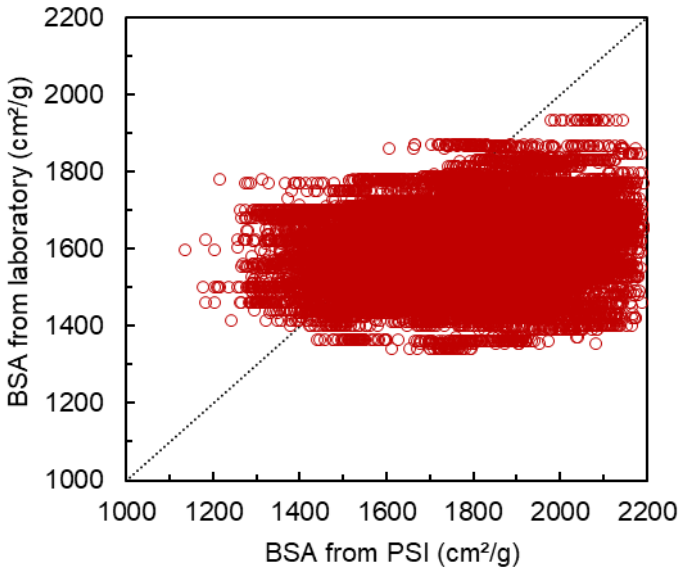


Figure 8.3. Relationship between HPGR feed BSA estimated by the PSI and measured in laboratory for data collected in a twelve-month period.

To ensure a fair comparison, PSI data presented in Figure 8.3 was calculated based on the mass balance with the overflow solids rate in each ball milling line and their respective PSI estimations. Results from Figures 8.2 and 8.3 when analyzed with some reports from the operational team (BUENO & OLYMPIO, 2021) already reported in Section (4.3.3) allows to conclude no reliability in the PSI estimation and, therefore, provides a technical justification to design a soft sensor model based on the HPGR feed BSA measured every 4-hours.

### *8.1.3. Ball milling and classification*

A set of six operational variables can be investigated in each ball milling-classification line (Figure 4.5). Figure 8.4 presents the average value for the mill power (a) and the solids feed rate (b) in the twenty-four months, where vertical lines represent the standard deviation for each month.

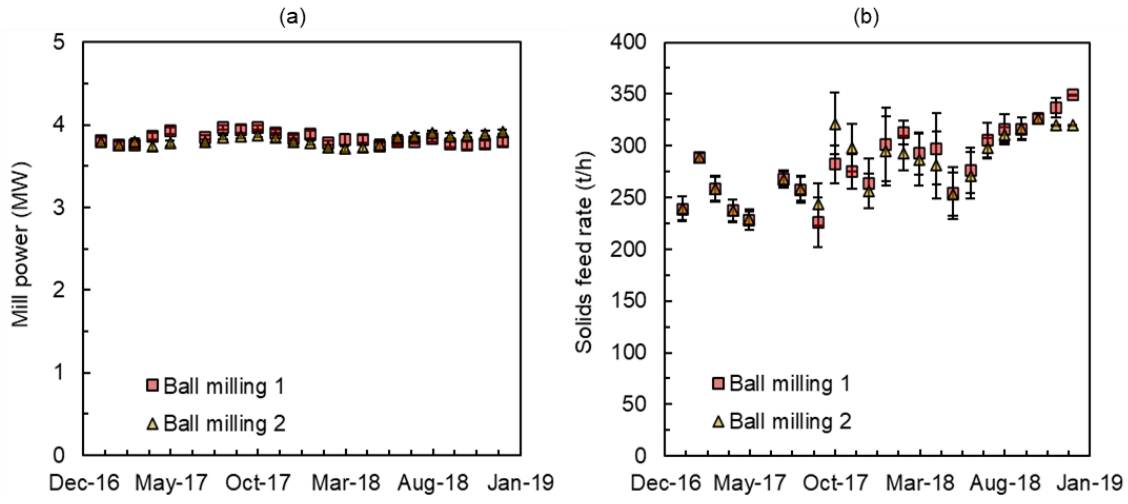


Figure 8.4. Monthly variation of the average mill power (a) and average solids feed rate (b) for the ball mill in Plant 3 in the entire period investigated. Markers represent the average value and vertical lines represent the standard deviation for each month.

Minor deviations from the average value can be seen in mill power along the entire period. Considering no variation in the mill filling (usually equal to 31%) and the mill velocity (usually equal to 68%), results from Figure 8.4a allows to find a value for mill power closer to 3.8 MW, which is very similar to other measurement made

elsewhere for the same operation (FARIA *et al*., 2019). On the other hand, Figure 8.4b showed significant changes in solids feed rate varying from 225 to 349 t/h in the average value and standard deviations up to 35 t/h.

In addition to Figure 8.4, the specific energy can also be estimated from the ratio between mill power and solids rate, which is presented in Figure 8.5 for the entire period assessed. Reduction of the specific energy consumption in the last months of 2018, which was around 12.1%, is fully related to the increment in solids rate presented in Figure 8.3b. A comparison between data from Figures 8.4 and 8.5 and Figure 7.6 allows to conclude that a reduction in the solids rate from April to December 2018 is related to the increment of Carajás and Timbopeba in the blend feeding the pelletizing plant. Indeed, the use of those concentrates to compensate the HPGR operating with worn rolls (Section 7.1.2) also allowed ball milling operation to increase solids rate, which reduces the mean residence time, but still kept constant the quality of the HPGR feed (Figure 7.7).

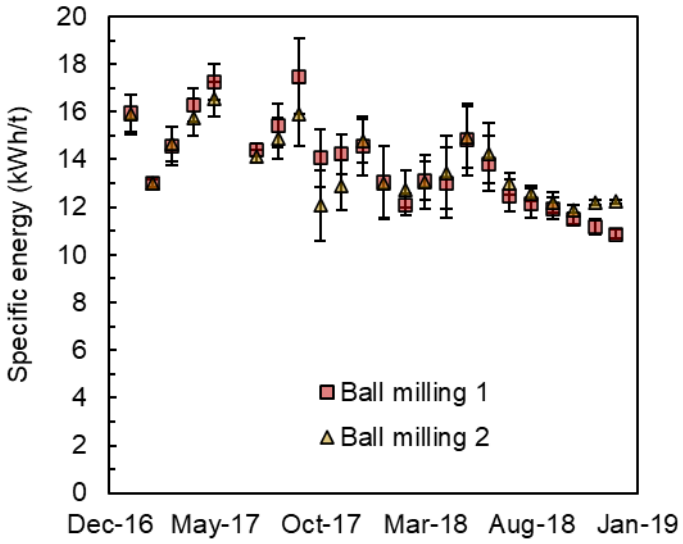


Figure 8.5. Monthly variation of the specific energy consumption of ball milling lines 1 and 2 for the entire period assessed. Markers represent the average value, whereas vertical lines represent the standard deviation for each month.

Analysis on the hydrocyclone operation, also possible from Figure 8.6, shows the monthly variation of the inlet pressure in the entire period investigated. Variations

from 0.78 to 1.25 kgf/cm² indicated minor variations, but very important to change the classification performance. Usually, changes in the inlet pressure are of almost importance given their impact on the volumetric slurry rate. However, it is important to bear in mind that the cluster often operates with just a part of the hydrocyclone working full time, being the control system responsible for turning on or turning off a new hydrocyclone depending on the increment or decline of inlet pressure. As such, the relatively small variation in this process variable (Figure 8.6) can be, at least in part, be explained by this feature in the operation.

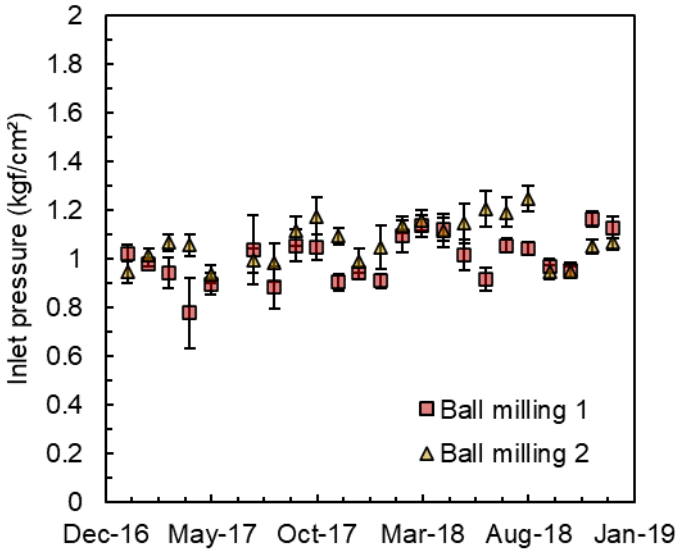


Figure 8.6. Monthly variation of the inlet pressure in the hydrocyclone cluster in the entire period assessed. Markers represent the average value, whereas vertical lines represent the standard deviation for each month.

Results presented in this Section stated the ball milling and classification variables with great potential to be used in the development of the soft sensor model, since important variations were observed. It is also important to bear in mind that up to this point the experimental evidence from the process indicated quite small variabilities in the blend feeding the pelletizing plant (Figure 7.6), whereas huge variabilities were presented in the HPGR feed (product from the ball milling and classification step) in Figure 7.7. Those results suggest, at least partially, that HPGR feed BSA has been mainly governed by the changes in ball milling and classification conditions, with the pelletizing plant feed BSA (Figure 7.6a) and feed blend (Figure 7.6b) filling a

secondary role. Those results give support to the development of a data driven soft sensor model based only on online data recorded from the supervisory system.

### 8.2. Time delay estimation and data reconciliation

Analyzing the schematic diagram from Figure 4.5, a potential requirement for properly modeling the HPGR feed should be raised about the time delay between the data collected in the hydrocyclone overflow (supervisory system) and the data collected and analyzed in HPGR feed (laboratory data). Estimations made by the Vale S.A. team were reported with an average time delay between 7 to 9 hours in the process (OLYMPIO & BUENO, 2021).

With the aim of confirming this value, the BSA estimated from PSI was compared against the BSA data measured every 4-hours when dealing with time delays between 0 to 10 hours. Very low correlations presented in Figure 8.7 were expected since poor prediction have been made by the PSIs (Section 8.1.2). Nevertheless, results are able to show a higher correlation for time delays closer to 7.5 h, which is lined up with other estimations made by the Vale S.A. team (OLYMPIO & BUENO, 2021). Results then allow to conclude that predictions made by the soft sensor model will be able to predict 7.5 h in advance the HPGR feed BSA. This achievement can provide heads up to the operator on how to change operating conditions in advance in order to absorb important variabilities in the HPGR feed BSA, which is one of the research objectives raised in Section 2 (R#4a).

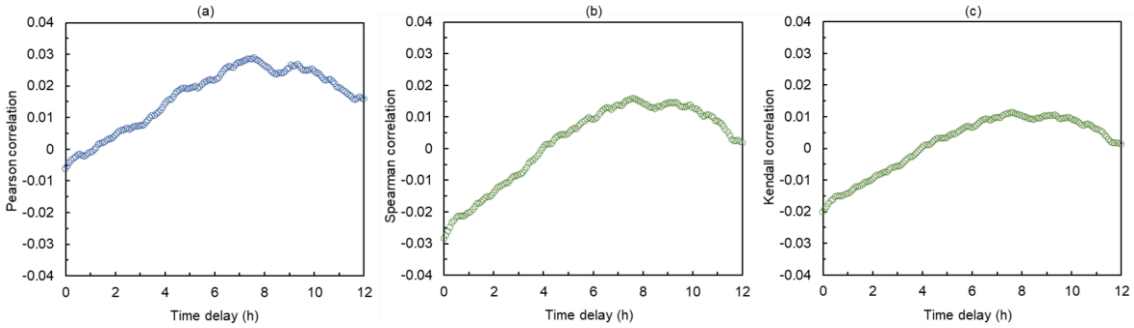


Figure 8.7. Pearson, Spearman and Kendall correlations for the BSA using different time delays from 0 to 10 hours. Correlations were gathered from laboratory data and PSI data for both ball milling-classification lines.

The simplified assumption of an average residence time distribution from the hydrocyclone overflow to the HPGR feed BSA is recognized as limitation of the present work. Nevertheless, the approach seems to be valid at this point for a preliminary investigation, even though is well-known that material will be mixed in the thickener, homogenization tanks and disk filters (HPGR upstream processes – Figure 3.2). Poor reliability on the process data gathered from all unit operations between hydrocyclone overflow and HPGR feed did not allow to use it in a more accurate estimation of the time delay. Results analyzing all those process variable were omitted for brevity.

## 8.3. Feature selection

Feature selection is a key step on data analytics and will be used in the present work to select the best process variable to be used in model training. Normality test and data normalization are presented in Section 8.4.1. New variables from the original process variables are created in Section 8.4.2, besides a method being proposed to account for the two ball milling lines in the HPGR feed BSA every 4-hours and used for model training. Statistical methods and expert knowledge are then used to select the main process variables to be used in the model development (Section 8.4.3).

### *8.3.1. Normality assessment and data normalization*

Andersen-Darling tests following the null-hypothesis of dataset following the normal distribution (5% of significant level) were carried out with data for each operational variable within the ball-milling and classification circuit. Results indicated no dataset following the normal distribution. Additional verifications were also performed from graphic analyzes and selected results are presented in Figure 8.8, thus indicating mostly a bimodal distribution. Remaining figures analyzing the entire dataset are presented in the Appendix C. In general, no dataset followed the normal distribution according to the Andersen-Darling tests, besides some of them presenting a bimodal behavior (Appendix C).

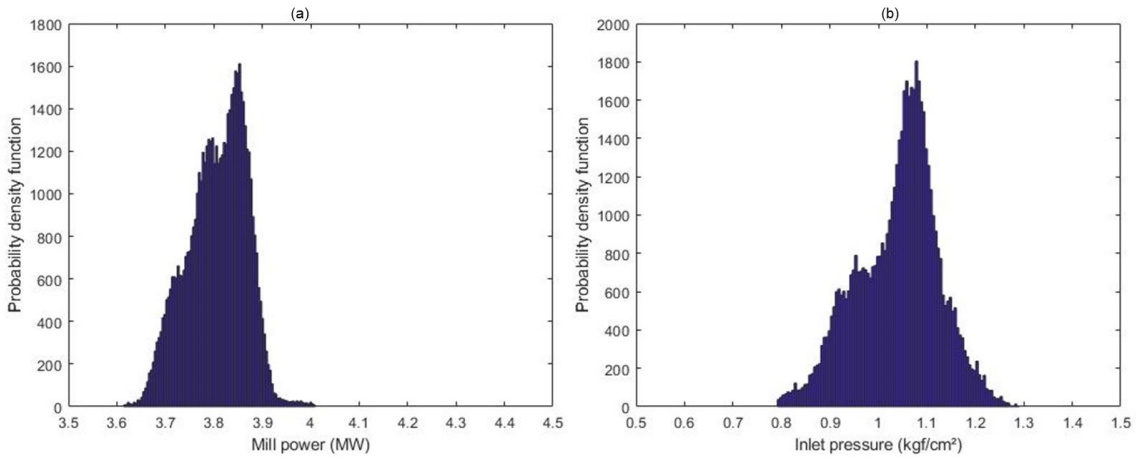


Figure 8.8. Probability distribution function for the mill power (a) and inlet pressure (b) in the ball milling line 1. Data used to plot the graphs was recorded every 5-min.

Following the key steps within the data pre-processing, data normalization was also performed. This approach is usually required when dealing with a large number of process variables, otherwise important elements with small magnitudes can be overshadowed by other elements with higher magnitudes, which provides a bias in the model training. Therefore, the present work normalizes the data from the ratio between each variable ($var_i$) and its historical mean value in the entire period ($\overline{var}$) as:

$$var_{norm} = \frac{var_i}{\overline{var}} \tag{8.1}$$

where $var_{norm}$ is the normalized variable.

### *8.3.2. Model training variables*

Beyond the original variable gathered from the process, additional ones were also created using the central difference derivation with the truncation error of $O(h^4)$ as:

$$var_i' = \frac{var_{i-2} - 8var_{i-1} + 8var_{i+1} - var_{i+2}}{12h} \tag{8.2}$$

To avoid overfitting data in the model presented, correlation between variables and the model output, as well as data collinearity are analyzed. Figure 8.9 presents the Pearson (a) and Kendall (b) correlations between each process variables and HPGR feed BSA. Results indicated the mill power and specific energy for each ball milling line as the higher positive correlation, whereas slurry rate and inlet pressure the ones with relatively negative correlations. The unexpected negative correlation between inlet pressure and HPGR feed BSA should be explained, at least in part, by some effects provided by the hydrocyclone cluster operational control when changing the cyclone performance according to variations in the mill product.

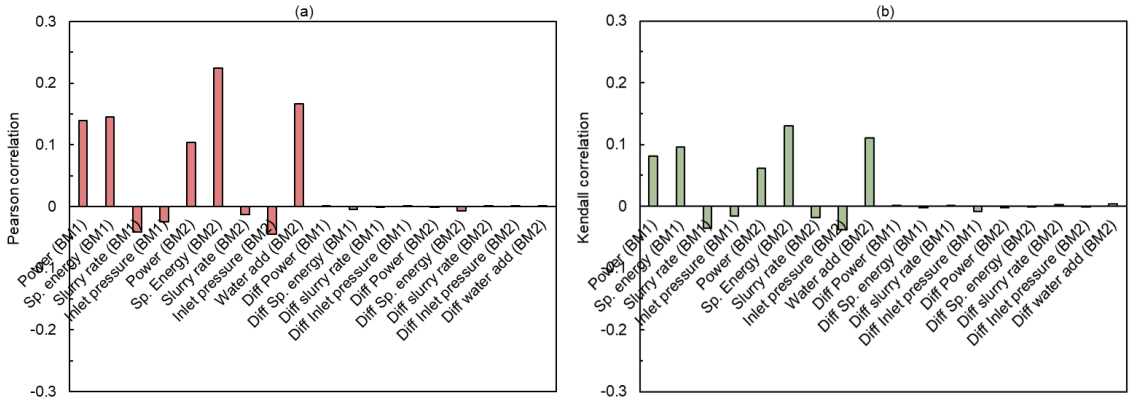


Figure 8.9. Pearson (a) and Kendall (b) correlations between each process variable and the HPGR feed BSA.

Data collinearity was also analyzed to avoid overfitting in the model prediction and the results can be found in the Appendix D. As such, the present work uses three process variables and their respective derivatives (Eq. (8.2)) for both ball mill lines, which were: specific energy consumption, inlet pressure and water addition to the hydrocyclone feed.

To account for both ball milling lines, a method is hereby proposed with a mass balance between them. The fresh feed solids rate will be used to perform a weighted average between both lines and then predict the HPGR feed BSA.

### 8.4. Model training

For model training and validation, the present work selected data from the first twelve months, whereas dataset from the last twelve months were used for model testing. The approach first relied on data segmentation with 80% of the original dataset being randomly selected for model calibration, whereas the remaining 20% was used for model validation, which is well-accepted as a good data segmentation technique.

On the basis of the new dataset, a stepwise method was used to fit the model and a comparison between predictions and experiments is presented in Figure 8.10 for both linear (a) and quadratic (b) models.

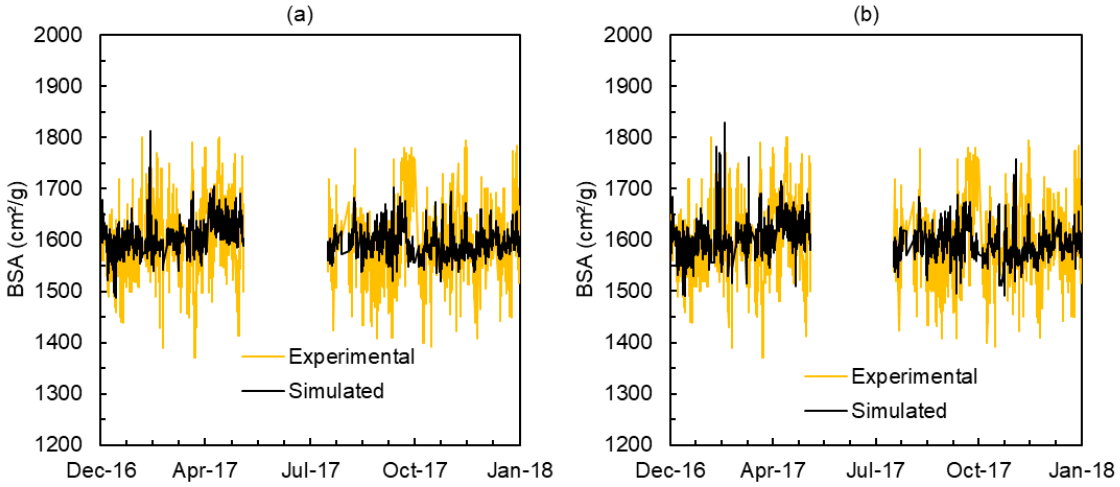


Figure 8.10. Comparison between measure and predicted HPGR feed BSA using a soft sensor model built with stepwise linear regression (a) and stepwise quadratic regression (b). Data is presented every 5-min.

Relatively good predictions can be seen in the entire period assessed with average absolute relative deviation from measurements equal to 3.6% and 3.5% for both linear and quadratic models, respectively. Distributions of the absolute relative deviation from measurements is presented in Figure 8.12. The models showed potential to barely capture variations in the feed according to changes in the grinding and classification conditions and small improvements were noticed when moving from a linear to a quadratic model. Nevertheless, it is worth mentioning that both models were able to just describe the HPGR feed close to the historical mean value, being unable to

capture important variabilities along the period assessed, thus limiting its application as predictor of the HPGR feed BSA. Missing data from May to August 2017 is related to the poor sensor measurements in that period.

Aiming to circumvent the bias provided in model prediction from Figure 8.10, an Artificial Neural Network (ANN), previously discussed in Section 3.7.4, is then proposed in order to describe the HPGR feed on the basis of the grinding and classification data. An optimal ANN was found and built with three nodes composing the hidden layer and 46 artificial neurons in each node. The tangent function was used as an activation function, whereas resilient backpropagation was used as a training function. Figure 8.11 then presents a comparison between measured and predict HPGR feed BSA in the 12-month period assessed (a) and in a 10-day period (b), which highlights the model ability on capturing variabilities in the process in both long period (Figure 8.11a) and short period (Figure 8.11b). Improvements in model prediction when comparing Figure 8.11 with results from Figure 8.10 are noticeable, being the average absolute relative deviation from measurements equal to 2.3 for the ANN prediction. Peaks of HPGR feed BSA higher than 2000 cm²/g and lower than 1200 cm²/g should be related to overfitting in the modeling approach.

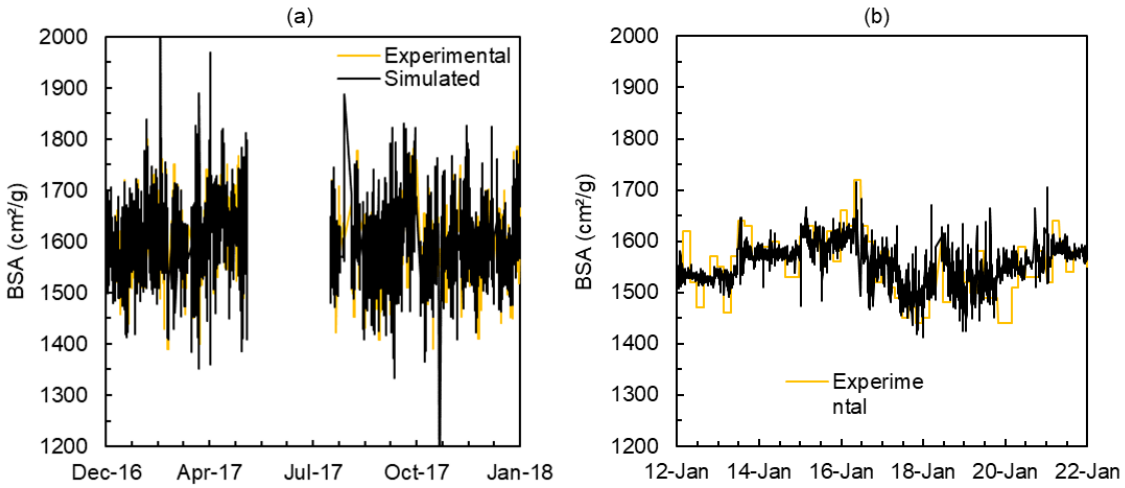


Figure 8.11. Comparison between measure and predicted HPGR feed BSA in a 12-month period (a) and 10-day period (b) using a soft sensor model built an Artificial Neural Network (ANN). Data is presented every 5-min frequency.

In addition to Figures 8.11 and 8.10, a comparison between the full distribution of the complete absolute relative deviation from measurements is presented in Figure 8.12. Results allow to support the statement of a better prediction achieved by the soft sensor designed with the ANN.

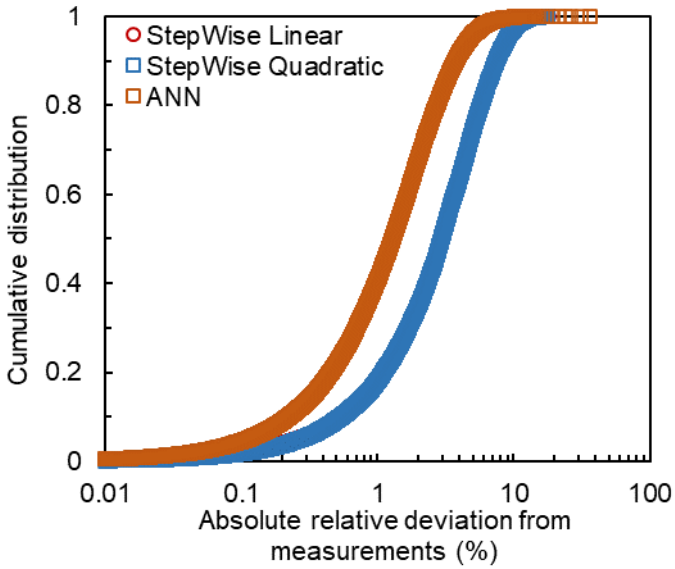


Figure 8.12. Comparison between cumulative distributions for the absolute relative deviation from measurements using the three models presented with data from the entire 12-month assessed.

Figure 8.13 finally presents a comparison between measured and predicted values for the HPGR feed BSA in a period of 12-monts for the year of 2018, which was just selected as model testing dataset. Unlike presented in Figure 8.11, poor agreement was found between model and experiments up to this point, which highly limits the application of the soft sensor model as predictive tool. Indeed, prediction from Figure 8.13 highlights a well-known limitation of ANNs for describing a separated dataset than the one used for model training and validation. In general, the ANN captured the trend in the entire dataset presented in 2017 and allowed to provide a good prediction for that period. Nevertheless, changes in the grinding and classification conditions (Figure 8.4 to 8.6) coupled to important changes in the pelletizing plant feed BSA and blend composition (Figure 7.6), were key to compromise model description. As previously discussed in Section 3.7.4, it has been proven that fully empirical models relying only in online data would not be able to properly describe variabilities in the process.

Improvements in the model would be able to achieve using a hybrid approach with online data and physical description of the process, but the approach is not within the scope of the present work.

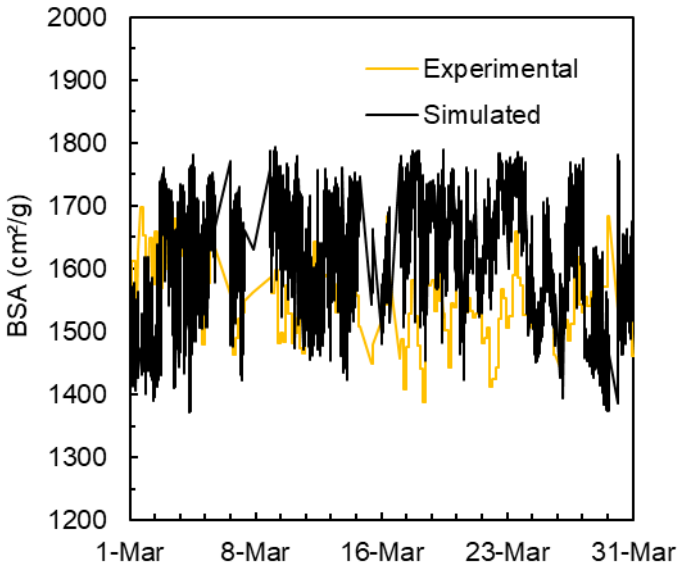


Figure 8.13. Comparison between measure and predicted HPGR feed BSA in 1-month period for the year of 2018 using the soft sensor model built an Artificial Neural Network (ANN) and validated in Figure 8.12. Data is presented for every 5-min.

## 8.5. Soft sensor model application

Considering the ANN soft sensor model proposed in Section 8.4 and partially validated for operational data from 2017, Figure 8.14 presents a comparison between measured and predicted values for the HPGR product BSA using the novel online modeling approach when accounting for the HPGR feed BSA predicted with the soft sensor as a model input. Results showed a very good agreement between model and experiments and highlighted the potential application of this new approach as a more complete online model. Looking to the distribution of absolute relative deviation from measurements, the third quartile was equal to 4.4%, which shows the ability of the model on capturing the process variabilities and accurate describing the HPGR product BSA. Nevertheless, it is important to mention that no reliability on the ANN soft sensor model prediction for the last 12 months of 2018 limited the application of this new approach as proper predictive alternative tool.

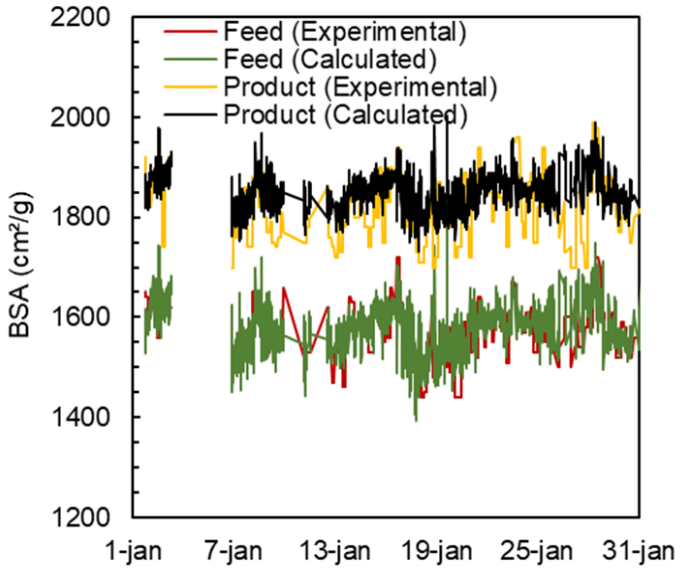


Figure 8.14. Comparison between experimental and predicted values for the HPGR product BSA using the novel online HPGR modeling and accounting for the HPGR feed BSA predicted by the ANN soft sensor model as a model input. Data is presented for every 5-min.

In general, this preliminary analysis on the soft sensor shows a potential application of this simulation tool to predict the HPGR feed up to 7.5 hours in advance, thus giving heads up to the operator in real-time on how operating conditions should be fitted in order to achieve the desired objective in the process.

Since this Section relies on exploratory analyzes of the soft sensor model, it is worth mentioning that several other machine learning tools can be used to improve model development, calibration and validation. These features are, however, scope of future works.

### 8.6. Final discussions

Application of a data drive soft sensor model demonstrated potential use describing the HPGR feed in real time being used as an input to the HPGR model. Results presented up to this point were critical to demonstrate the main challenges and capabilities of applying a phenomenological model coupled with a data driven soft sensor model. Even though several authors have argued about using this approach to predict operational performance using different techniques as previously discussed

(Section 3.7.4), it is worth mentioning that the poor prediction of this approach dealing with comminution operations should be mainly related to variations on ore grindability, wear, ore rheology, etc. A model relying solely on backfitted equations with no clear description of the physics of the process would be limited to describe a process with very constant performance, which is not the case in the present work.

Nevertheless, results presented in this section allowed to answer the R#4 raised in Section 2 as one of the research objectives.

## 9. SUMMARY AND CONCLUSIONS

The present work demonstrated that, despite the high complexity involved in the HPGR operation, it was possible to propose and validate a novel HPGR online modeling approach responding to real-time variabilities in an industrial-scale process. A pelletizing plant was selected as a case study and analyzes were carried out covering from improvements in understanding and mathematical description of size reduction under confined conditions to application of a phenomenological model giving accurate responses according to real-time information.

Piston-and-die tests were performed with all iron ore concentrates used to feed the pelletizing plant. The three narrow size ranges investigated and the wide range of compressive forces applied allowed a detailed investigation on the compaction behavior in the particle bed, surface area generation and energy utilization. In general, Carajás sample presented a highest amenability for breakage in the particle bed, which was lined-up with its softer response in the particle bed. The remaining concentrates were quite similar from the point of view of size reduction, with Timbopeba sample presenting a slightly higher amenability for breakage. Values of energy utilization were calculated and relatively similar values were found when comparing piston-and-die tests performed in the present work and lab-scale HPGR tests (BEUNO, 2019) for the same sample. Additional analysis on the bench-scale tests also allowed to estimate the energy-specific progeny size distribution for all iron ore concentrates on the basis of the appearance function method. As demonstrated assessing the surface area generation, Carajás sample presented the most aggressive progeny size distribution, whereas the other concentrates were relatively similar.

A phenomenological model proposed by the authors, which is called Modified Torres and Casali model, was applied to describe the industrial-scale HPGR pressing iron ore concentrates. Data from selected tests carried out in industrial surveys under steady state conditions were used to calibrate and validate the model. Throughput and power consumption models showed very good agreement describing the industrial HPGR for a wider range of operating conditions. Product size distribution was also well described by the model for regular operating conditions, whereas an overestimation of the product BSA was found when the machine was operating with high compressive forces ($F_{sp}$ > 2.1 N/mm²). To improve model prediction dealing with high compressive forces, a modification was proposed to the breakage model aiming to incorporate the

breakage saturation effect. The equation was depicted and calibrated based on piston-and-die tests carried out with all samples investigated, with the model providing good agreement and a key improvement on model prediction.

An additional modification was proposed in order to describe the different shapes of the pressure profile along the roll length. Since the original model accounts only for a parabolic shape profile, the present work proposes an equation based on the Fourier Transform with an ability to describe from a parabolic profile to a trapezoidal profile just with a single fitting parameter. Modification on this provided an improvement in model prediction.

The application of the online model finally relied on data collected from the process in a period of 24-month. Data collected in the that period corresponded to the HPGR operating with roll wear lifetime from 4,320 hours to 22,000 hours, being the wear profile recorded in three different periods. A significant parabolic wear profile was presented when the HPGR was operating close to 15,000 hours, which is the usual roll lifetime for the machine pressing iron ore concentrates. Operation going up to 22,000 hours should be explained by external unexpected factors in the plant. Looking close to operating conditions it was easy to state the HPGR roll peripheral velocity almost constant and equal to 1 m/s in the entire period, since the machine cannot operate with high roll velocities. Significant reduction of the measured operating gap was showed when the equipment operated with worn rolls. Since those measurements were made by the edge of the rolls, no reliability on this should be considered as a process variable since a parabolic profile with more intense wear in the middle of the rolls was presented. Reduction in the operating pressure was applied when the equipment was operating with worn rolls, which should be explained as operational strategy aiming to avoid rolls touching each other during grinding.

Throughput in the entire period followed an almost constant value around 600 t/h, whereas power consumption and specific energy reduced significantly with decrease in pressure for the last months of 2018. Investigation on the HPGR feed and product BSA showed that HPGR product is mostly predefined by the trend imposed by the HPGR feed, which comes from the upstream process (ball milling and classification step). An almost constant pelletizing plant feed BSA and blend of iron ore concentrates was presented from January 2017 to March 2018. After that, an important increment on Carajás and Timbopeba concentrates in the blend was noticeable, which also reduced a

bit the feed BSA of the plant. Changes up to this point should be explained by the necessity on increasing the efficiency of HPGR size reduction with softer concentrates that allowed to keep the quality of the final product when the machine was operating with worn rolls.

Application of the phenomenological model as pseudo-dynamic approach coupled with real-time information was first demonstrated for power and throughput predictions. Results showed the model ability on capturing variabilities in the process and providing a good prediction of both performance variables when the HPGR was operating up to 7,200 hours of roll wear lifetime. Considering the poor prediction of the model after that, which was related to the worn rolls, a method was hereby proposed and validated to improve model prediction in this new scenario. Considering both throughput and power models validated, the model as also able to capture variabilities in the HPGR feed and operating conditions to provide a good description of the HPGR product BSA in real-time. Breakage function fitted for each month on the basis of blend composition and bench-scale data was used and demonstrated fair prediction of size reduction.

HPGR online model was applied as part of structure composing a digital assistant able to find the best set of operating conditions based on a given HPGR performance variable target. Application of this tool highlighted potential scenarios to reduce the variability of the HPGR product when dealing with very large changes in the HPGR feed, besides absorbing a coarser feed size distribution provided by a reduction in the ball milling work.

Application of a soft sensor model to predict the HPGR feed based on grinding and classification conditions was presented with relatively good prediction in a selected time window. Nevertheless, limitation when dealing with variabilities in the process related to offline parameters compromised the model application.

Results presented up to this point would allow implementing this HPGR online model as an engineering tool to support operation in one of the pelletizing plants from Vale S.A. (Brazil). The HPGR online system will work as digital assistant describing the process in real-time, beyond providing the operator new set of conditions that will allow the machine to improve quality of the final product, reduce energy consumption

or increase throughput on the basis of variabilities in the HPGR feed BSA, roll surface wear and any type of operational demand from the downstream process.

## APPENDICES

### A: Blaine specific surface area (BSA) model

Given that the model equations provide as output the size distribution in the HPGR discharge, an equation must be available to estimate the BSA from it. Zhang and Napier-Munn (1995) proposed an expression to predict the BSA according to the size distribution, given by:

$$SS_A = \frac{6}{\rho_{sp}} \sum_{i=1}^{N} \frac{w_i}{\bar{x}_i} \tag{A1}$$

where $SS_A$ is the equivalent spherical specific surface area, $\rho_{sp}$ is the specific gravity, $w_i$ is the fraction retained in each size class and $\hat{x}_i$ is the harmonic mean of each size class, given by:

$$\hat{x}_i = \left[ \frac{(x_i^2 + x_{i-1}^2)(x_i + x_{i-1})}{4} \right]^{\frac{1}{3}} \tag{A2}$$

where $x_i$ and $x_{i-1}$ are, respectively the lower and the upper sizes of the interval.

The authors then proposed an empirical expression to calculate Blaine specific surface area (BSA) (ZHANG & NAPIER-MUNN, 1995):

$$BSA = GSS_A + J \tag{A3}$$

where G and J are constants that must be fitted to data. On the basis of data from pressing iron ore concentrates in a pilot-scale campaign, CAMPOS *et al.* (2019a) estimated the optimal values of G = 0.996 and J = 18.0. However, given the differences in material characteristics between that study and the feed to the various HPGRs in the present work, given by a blend of different ore type feeding the pelletizing plants

(Section 4.3), a need for re-estimating the parameters became evident. This resulted in the constants G equal to 1.39 and J equal to 27.97. The constants G and J were calibrated based in the equivalent spherical specific surface area ($SS_A$) given in m²/kg and, therefore, the BSA (Eq. (A3)) will be calculated in m²/kg. Transformation of this value to cm²/g requires multiplying the values achieved in Eq. (A3) by 10. A comparison between experimental data and the model fit is given in Fig. A1, which shows that the average difference between measured and fitted results was 100 cm²/g.

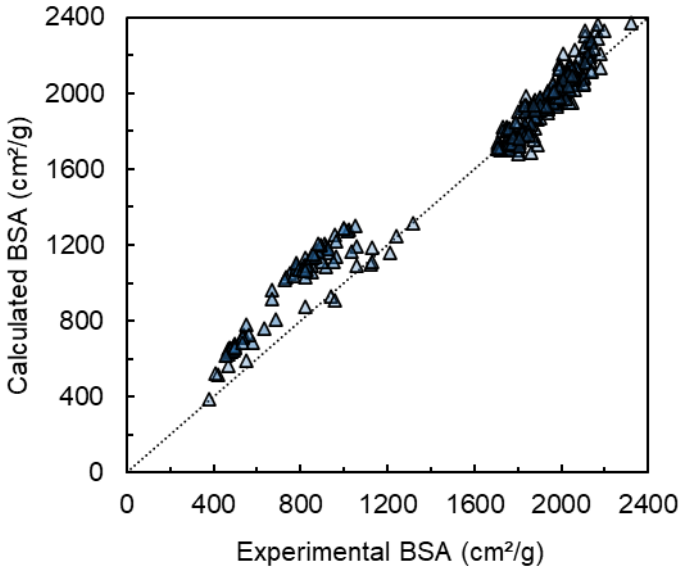


Figure A1. Comparison between experimental and calculated values for the Blaine specific surface area (BSA) using Eqns. (A1) to (A3).

**B: Experimental results**

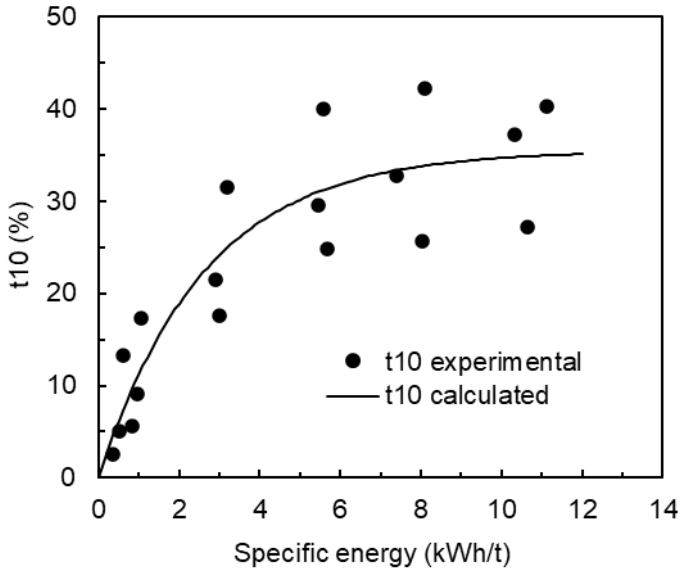


Figure B1. Relationship between the $t_{10}$ parameter and the specific input energy for particles tested in different narrow size ranges in the piston-and-die apparatus with Brucutu sample. Optimal parameters for Eq. (5.4) were A as 35.5 and $b_{PD}$ as 0.38.

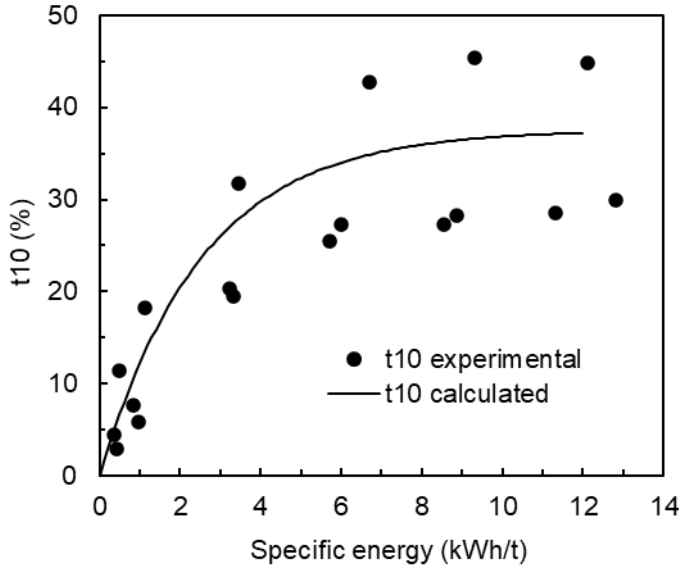


Figure B2. Relationship between the $t_{10}$ parameter and the specific input energy for particles tested in different narrow size ranges in the piston-and-die apparatus with Timbopeba sample. Optimal parameters for Eq. (5.4) were A as 37.6 and $b_{PD}$ as 0.39.

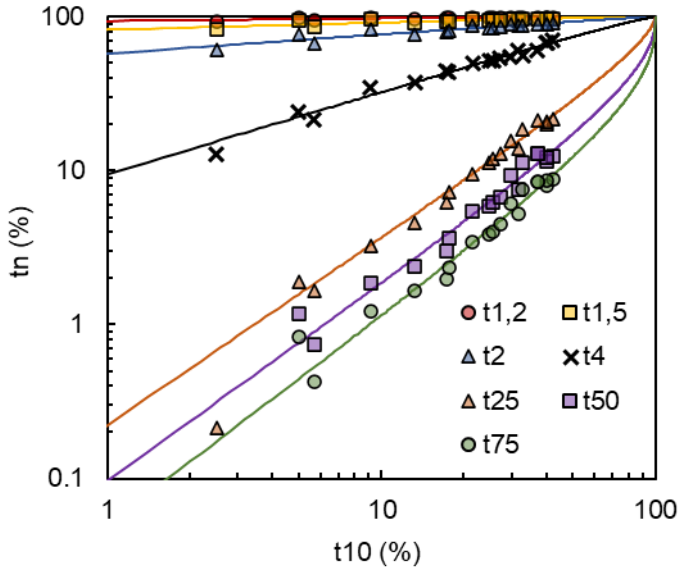


Figure B3. $t_n$-$t_{10}$ relationship considering all narrow size ranges tested in the piston-and-die apparatus with Brucutu sample.

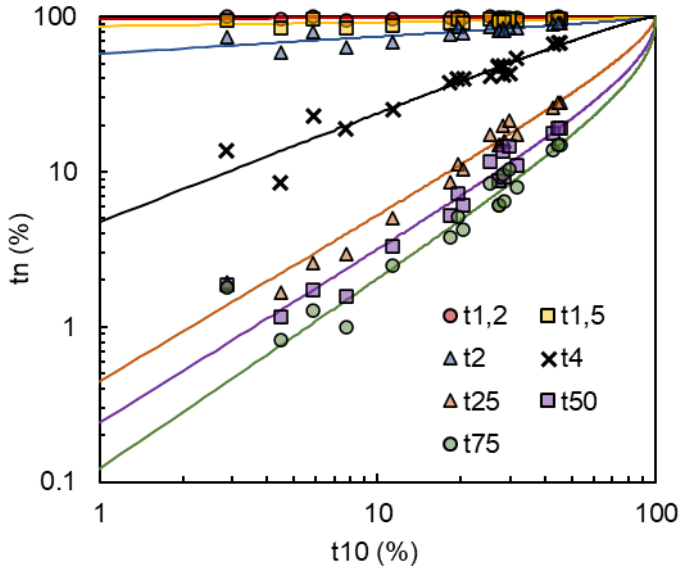


Figure B4. $t_n$-$t_{10}$ relationship considering all narrow size ranges tested in the piston-and-die apparatus with Timbopeba sample.

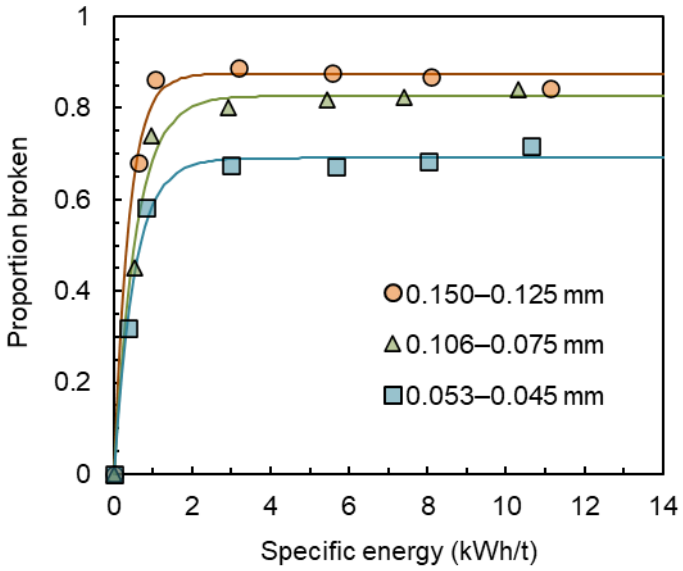


Figure B5. Proportion broken out of the original size Brucutu sample for different specific energies and feed particle sizes.

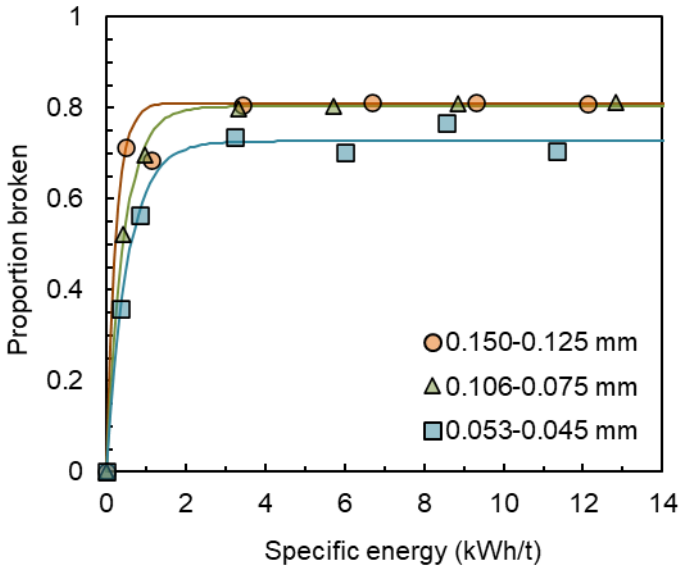


Figure B6. Proportion broken out of the original size Timbopeba sample for different specific energies and feed particle sizes.

## C: Normality tests

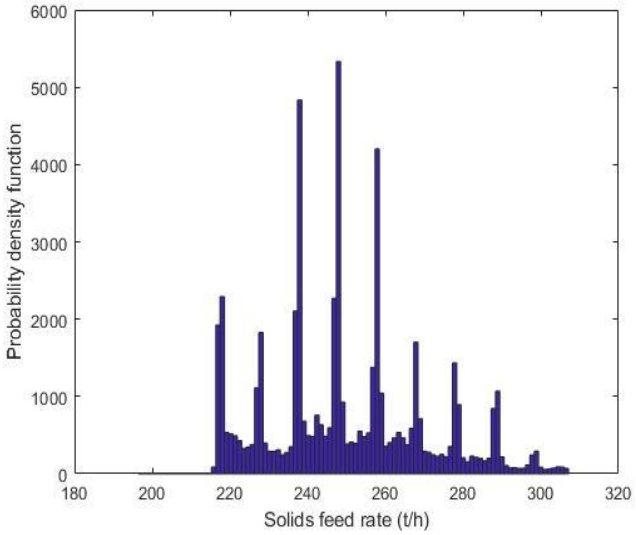


Figure C1. Probability distribution function for the fresh feed solids rate in the pelletizing circuit. Data used to plot the graphs was recorded every 5-min frequency.

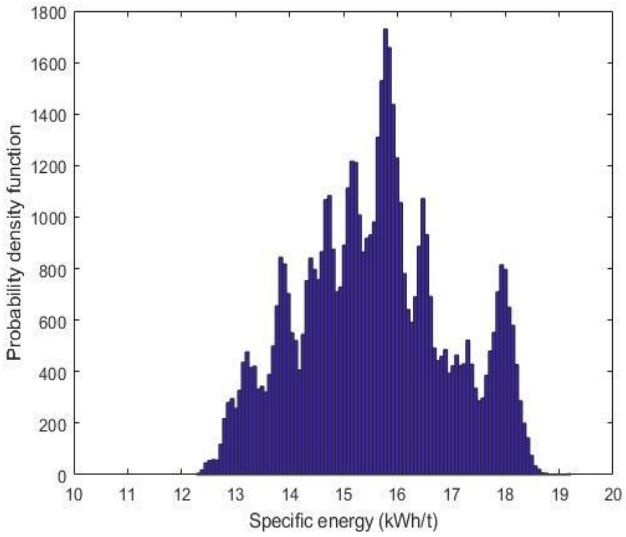


Figure C2. Probability distribution function for the ball mill specific energy. Data used to plot the graphs was recorded every 5-min frequency.

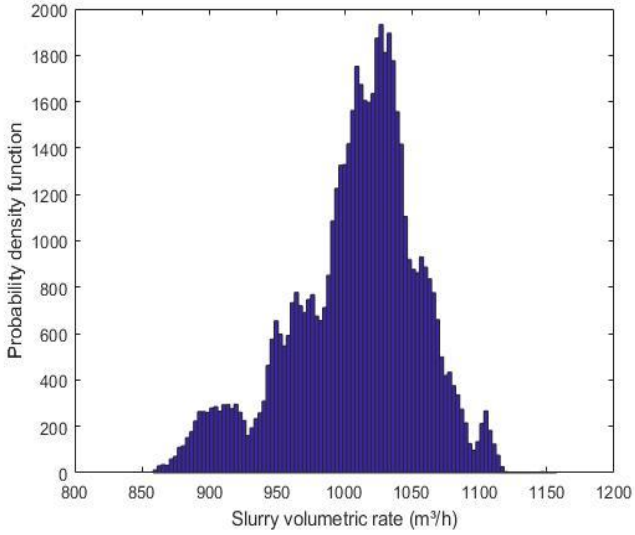


Figure C3. Probability distribution function for the slurry volumetric rate used to feed the hydrocyclone cluster. Data used to plot the graphs was recorded every 5-min frequency.

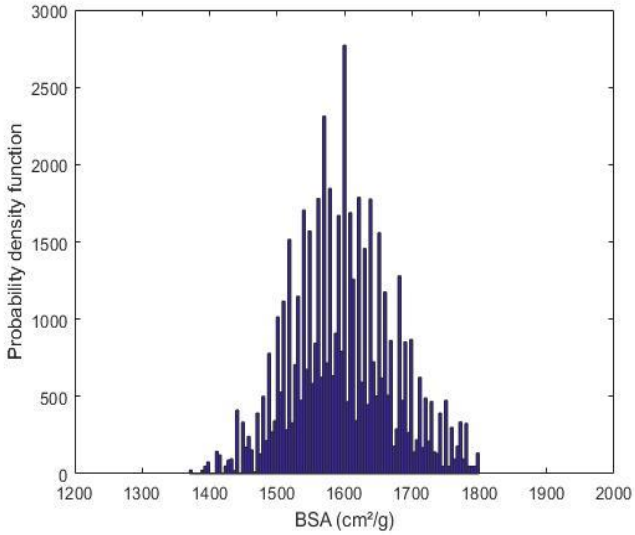


Figure C4. Probability distribution function for the HPGR feed BSA measured every 4-hours frequency. Data used to plot the graphs consists of the reconciled dataset discussed in Section (4.3.3).

**D: Collinearity matrix**

Table D1. Collinearity matrix for all process variables in the ball milling and classification steps considered for the design of the data driven soft sensor model (Section 8). Matrix condition number was 27.

| | Mill power (BM1) | Specific energy (BM1) | Slurry rate (BM1) | Inlet pressure (BM1) | Slurry volumetric rate (BM1) | Specific energy (BM1) | Mill Power (BM2) | Inlet pressure (BM1) | Slurry rate (BM2) | Specific energy (BM2) | Mill Power (BM2) | Slurry rate (BM2) | Inlet pressure (BM2) |
|---|---|---|---|---|---|---|---|---|---|---|---|---|---|
| Mill power (BM1) | 1.000 | 0.499 | 0.293 | 0.113 | 0.293 | 0.499 | 0.558 | 0.113 | 0.407 | 0.269 | 0.558 | 0.407 | 0.330 |
| Specific energy (BM1) | 0.499 | 1.000 | 0.004 | -0.042 | 0.004 | 1.000 | 0.322 | -0.042 | 0.179 | 0.736 | 0.322 | 0.179 | 0.050 |
| Slurry rate (BM1) | 0.293 | 0.004 | 1.000 | 0.589 | 1.000 | 0.004 | 0.342 | 0.589 | 0.259 | -0.068 | 0.342 | 0.259 | 0.239 |
| Inlet pressure (BM1) | 0.113 | -0.042 | 0.589 | 1.000 | 0.589 | -0.042 | 0.202 | 1.000 | 0.161 | 0.041 | 0.202 | 0.161 | 0.121 |
| Slurry volumetric rate (BM1) | 0.293 | 0.004 | 1.000 | 0.589 | 1.000 | 0.004 | 0.342 | 0.589 | 0.259 | -0.068 | 0.342 | 0.259 | 0.239 |
| Specific energy (BM1) | 0.499 | 1.000 | 0.004 | -0.042 | 0.004 | 1.000 | 0.322 | -0.042 | 0.179 | 0.736 | 0.322 | 0.179 | 0.050 |
| Mill Power (BM2) | 0.558 | 0.322 | 0.342 | 0.202 | 0.342 | 0.322 | 1.000 | 0.202 | 0.129 | 0.320 | 1.000 | 0.129 | 0.041 |
| Inlet pressure (BM1) | 0.113 | -0.042 | 0.589 | 1.000 | 0.589 | -0.042 | 0.202 | 1.000 | 0.161 | 0.041 | 0.202 | 0.161 | 0.121 |
| Slurry rate (BM2) | 0.407 | 0.179 | 0.259 | 0.161 | 0.259 | 0.179 | 0.129 | 0.161 | 1.000 | -0.129 | 0.129 | 1.000 | 0.875 |
| Specific energy (BM2) | 0.269 | 0.736 | -0.068 | 0.041 | -0.068 | 0.736 | 0.320 | 0.041 | -0.129 | 1.000 | 0.320 | -0.129 | -0.227 |
| Mill Power (BM2) | 0.558 | 0.322 | 0.342 | 0.202 | 0.342 | 0.322 | 1.000 | 0.202 | 0.129 | 0.320 | 1.000 | 0.129 | 0.041 |
| Slurry rate (BM2) | 0.407 | 0.179 | 0.259 | 0.161 | 0.259 | 0.179 | 0.129 | 0.161 | 1.000 | -0.129 | 0.129 | 1.000 | 0.875 |
| Inlet pressure (BM2) | 0.330 | 0.050 | 0.239 | 0.121 | 0.239 | 0.050 | 0.041 | 0.121 | 0.875 | -0.227 | 0.041 | 0.875 | 1.000 |

## E. List of publications

### *E.1. International journals*

Campos, T. M., Bueno, G., Barrios, G. K.P., Tavares, L. M., 2019. Pressing iron ore concentrate in a pilot-scale HPGR. Part 1: Experimental results. Miner. Eng., v. 140, p. 105875.

Campos, T. M., Bueno, G., Barrios, G. K. P., Tavares, L. M., 2019. Pressing iron ore concentrate in a pilot-scale HPGR. Part 2: Modeling and simulation. Miner. Eng., v. 140, p. 105876.

Campos, T. M., Bueno, G., Tavares, L. M., 2020 Confined Bed Breakage of Fine Iron Ore Concentrates. Minerals, v. 10, p. 666, 2020.

Campos, T M., Bueno, G., Tavares, L. M., 2021. Modeling comminution of iron ore concentrates in industrial-scale HPGR. Powder Tech., v. 338, p. 244-255.

Campos, T. M., Bueno, G., Rodriguez, V. A., Bottcher, A-C., Kwade, A., Mayerhofer, F., Tavares, L. M., 2021. Relationships between particle breakage characteristics and comminution response of fine iron ore concentrates. Miner. Eng., v. 164, p. 106818.

Carvalho, R. M., Campos, T. M., Faria, P. M., Tavares, L. M., 2021. Mechanistic modeling and simulation of grinding iron ore pellet feed in pilot and industrial-scale ball mills. Powder Tech., v. 392, p. 489-502.

Rodriguez, V. A., Campos, T. M., Barrios, G. K. P., Bueno, G., Tavares, L. M., 2022. A Hybrid PBM-DEM Model of High-Pressure Grinding Rolls Applied to Iron Ore Pellet Feed Pressing. KONA Powder and Particle Journal, v. 40, p. 2023011.

Campos, T. M., Petit, H. A., Olympio, R., Tavares, L. M., 2023. Online prediction of pressing of iron ore concentrates in an industrial HPGR. Part 1: Modeling approach. Miner. Eng., *Submitted for publication*.

Campos, T. M., Petit, H. A., Olympio, R., Tavares, L. M., 2023. Online prediction of pressing of iron ore concentrates in an industrial HPGR. Part 2: Simulation and process control. Miner. Eng., *Submitted for publication*.

*E.2. Complete papers in conference proceedings*

Campos, T M., Barrios, G. P., Salazar, J. S., Mazzinghy, D. B., Russo, J. F. C., Tavares, L. M., 2016. Comparison of mathematicals models in high pressure grinding rolls of an itabirite iron ore. Proc. 17th Min. Symp., p. 737, Rio de Janeiro, Brazil.

Cavalcanti, P. P. S., Campos, T. M., Rodrigues, M. B., Bailon, A. M. G., Tavares, L. M., 2016. Relationships between composition and microstructure and susceptibility to mechanical degradation of burned direct reduction iron ore pellets Proc. 17th Min. Symp., p. 548, Rio de Janeiro, Brazil.

Campos, T. M., Barrios, G. K. P., Bueno, G., Tavares, L. M., 2017. Desafios na modelagem da capacidade e potência consumida da prensa de rolos. Proc. XXVII Braz. Meet. of Ore Proc. and Extract. Metal., p. 1743-1753, Belém, Brazil.

Campos, T. M., Barrios, G. K. P., Bueno, G., Tavares, L. M. 2018. Comparison of circuits for roller pressing of pellet feed prior to milling. In: Proc. 6th Braz. Ore Agglom. Symp, p. 57-68, São Paulo, Brazil.

Campos, T. M., Bueno, G., Tavares, L. M., 2019. Comparison of scenarios of industrial-scale pellet feed pressing through simulation. Proc. 7th Braz. Ore Agglom. Symp, p. 13-25, São Paulo, Brazil.

Campos, T. M., Bueno, G., Tavares, L. M., 2019. Investigation of HPGR product edged recycle for pressing iron ore concentrates in industrial-scale through simulation. Proc. XXVIII Braz. Meet. of Ore Proc. and Extract. Metal., Belo Horizonte, Brazil.

Campos, T. M., Bueno, G., Tavares, L. M., 2020 Scale-up of HPGR in size reduction of iron ore pellet feed. Proc. XXX Int. Miner. Proc. Cong., p. 569-579, Cape Town, South Africa.

Carvalho, R. M., Faria, P., Campos, T. M., Tavares, L. M., 2020. Mechanistic modeling of continuous fine grinding in a ball mill. Proc. XXX Int. Miner. Proc. Cong., p. 612-622, Cape Town, South Africa.

Rocha, B. K. N., Campos, T. M., Franca, J. R., Franca, Turrer, H. D. G., Tavares, L. M., 2022. Multicomponent particle breakage behavior in pressing itabirite iron ore. Proc. 21st Min. Symp., p. 212-225, São Paulo, Brazil.

Campos, T. M., Petit, H. A., Olympio, R., Tavares, L. M. 2022. A HPGR pseudo-dynamic model approach integrated with real-time information for pressing iron ore concentrates in industrial-scale. Proc. IMPC Asia Pacific 2022, p. 100-113, Melbourne, Australia.

Rocha, B. K. N., Campos, T. M., Alvez, L. P., Silva, J., Turrer, H. D. G., Lichter, J., Tavares, L. M., 2022. Multicomponent modeling and simulation of the Minas Rio iron ore grinding circuit. Proc. IMPC Asia Pacific 2022, p. 313-324, Melbourne, Australia.

Campos, T. M., Petit, H. A., Bueno, G., Olympio, R., Tavares, L. M., 2022. Pseudo-dynamic simulation integrated with real-time information for pressing iron ore concentrates in industrial-scale. Proc. XXIX Braz. Meet. of Ore Proc. and Extract. Metal., Armação do Buzios, Brazil.

Rocha, B. K. N., Campos, T. M., Silva, J., Turrer, H. D. G., Tavares, L. M., 2022. Modeling and simulation of ball milling and classification circuit grinding itabirite iron ore. Proc. XXIX Braz. Meet. of Ore Proc. and Extract. Metal., Brazil.

*E.3. Extended abstract in conference proceedings*

Campos, T. M., Bueno, G., Tavares, L. M., 2019. HPGR modeling of iron ore pellet feed. Proc. 16th Europ. Symp. on Comm. and Classif., p. 56-58, Leeds, United Kingdom.

Campos, T. M., Petit, H. A., Olympio, R., Bueno, G., Tavares, L. M., 2022. A novel online modeling and simulation approach for pressing iron ore concentrates in industrial-scale HPGR. Proc. 17th Europ. Symp. on Comm. and Classif p. 47-48, Toulouse, France.

Rocha, B. K. N. Campos, T. M. Carvalho, R. M. Tavares, L. M., 2022. Mechanistic modeling and simulation of multi-component batch ball milling of iron ore. Proc. 17th Europ. Symp. on Comm. and Classif, p. 45-46, Toulouse, France.

Rodriguez, V. A., Campos, T. M., Barrios, G. K. P., Bueno, G., Tavares, L. M. 2022. Investigation of effect of roller wear in HPGR operation using a hybrid DEM-PBM approach. Proc. 17th Europ. Symp. on Comm. and Classif p. 41-42, Toulouse, France.

**REFERENCES**


ABAZARPOOR, A., HALALI, M., HEJAZI, R., et al., 2017, “HPGR effect on the particle size and shape of iron ore pellet feed using response surface methodology”, *Physicochemical Problems of Mineral Processing*. 53(2), pp. 1-9.

ALSMANN, L., 1996, KHD Humboldt Wedag.

ALTUN, O., BENZER, H., DUNDAR, H., et al., 2011, “Comparison of open and closed circuit HPGR application on dry grinding circuit performance”, *Minerals Engineering*, 24(3-4), pp. 267-275.

AMINALROAYA, A., POURGHAHRAMANI, P., 2022, “The Effect of Feed Characteristics on Particles Breakage and Weakening Behavior in High Pressure Grinding Rolls (HPGR)”, *Mineral Processing and Extractive Metallurgy Review*, 43(5), pp. 610-621.

ANDRÉ, F. P., 2019, "Validation and application of breakage model in the discrete element method through the simulation of comminution systems", M.Sc. dissertation, Federal University of Rio de Janeiro, Rio de Janeiro, Brazil.

ARGO IPS, 2020, www.argo-ips.com, *Accessed on 18th May 2020*.

ARMSTRONG, N. A., HAINES-NUTT, R. F., 1974, “Elastic recovery and surface area changes in compacted powder systems”, *Powder Technology*. 9(5-6), pp. 287-290.

AUSTIN, L. G., 1997, “Mill power for high-pressure grinding rolls in coal grinding”, *Minerals and Metallurgical Processing*, 14, pp. 18-26

AUSTIN, L. G., KLIMPEL, R. R., LUCKIE, P. T., 1984, “Process engineering of size reduction: ball milling”, In: *Proceedings of Society of Mining Engineers of the AIME*, New York, USA, pp. 112-113.

AUSTIN, L. G., LUCKIE, P. T., 1972, “The estimation of non-normalized breakage distribution parameters from batch grinding tests”, *Powder Technology*, 5(5), pp. 267–271.

AUSTIN, L. G., TRUBELJA, M. P., 1994, “The capacity and product size distribution of high-pressure grinding rolls”, In: *Proceedings of IV Meeting of the Southern Hemisphere on Mineral Technology*, Concepcion, Chile. pp. 4-67.

AUSTIN, L. G., TRUBELJA, M. P., VON SEEBACH, H. M., 1995, “Capacity of high-pressure grinding rolls”, *Mining, Metallurgy & Exploration*, v. 12, n. 2, pp. 65-73.

AUSTIN, L. G., VAN ORDEN, D. R., PEREZ, J. W., 1980, “A preliminary analysis of smooth roll crushers”, *International Journal of Minerals Processing*, 6(4), pp. 321-336.

AUSTIN, L. G., VAN ORDEN, D., MCWILLIAMS, B., et al., 1981, “Breakage parameters of some materials in smooth roll crushers”. *Powder Technology*, 28(2), pp. 245-251.

AUSTIN, L. G., WELLER, R., LIM, I., 1993, “Phenomenological modeling of the High-Pressure Grinding Rolls”, In: *Proceedings XVIII International Minerals Processing Congress, AUSIMM*, Sydney, pp. 87–96.

AYDOGAN, N. A., ERGUN, L., BENZER, H., 2006, “High pressure grinding rolls (HPGR) applications in the cement industry”, *Minerals Engineering*. 19, pp. 130–139.

BANINI, G., VILLANUEVA, A., HOLLOW, J., et al., 2011, “Evaluation of Scale up Effect on High Pressure Grinding Roll (HPGR) Implementation at Pt Freeport Indonesia”, In: *Proceedings of SAG Conference 2011*, Vancouver, Canada.

BARBOSA, V. D. S. B., DA SILVA, G. R., CAMPOS, P. H. A., et al., 2019, “Analysis of Mobile Communication Coverage and Capacity for Automation in Open-Pit Mines”, In: *Proceedings of International Symposium on Mine Planning and Equipment Selection*, Springer, Nature, pp. 262-270.

BARRICELLI, B. R., CASIRAGHI, E., FOGLI, D., 2019, “A Survey on Digital Twin: Definitions, Characteristics, Applications, and Design Implications”, *IEEE Acces*s, 7, pp. 167653-167671.

BARRIOS, G. K. P., DE CARVALHO, R. M., TAVARES, L. M., 2011, “Extending breakage characterization to fine sizes by impact on particle beds”, *Mineral Processing and Extractive Metallurgy*., 120(1), pp. 37-44.

BARRIOS, G. K. P., TAVARES, L.M., 2016, “A preliminary model of high pressure roll grinding using the discrete element method and multi-body dynamics coupling”, *International Journal of Minerals Processing*, 156, pp. 32-42.

BARRIOS, G. K., DE CARVALHO, R. M., TAVARES, L. M., 2011, “Modeling breakage of monodispersed particles in unconfined beds”, *Minerals Engineering*, 24(3-4), pp. 308-318.

BARRIOS, G.K.P., 2015, “Modelagem da Prensa de Rolos Usando o Método dos Elementos Discretos com Acoplamento Dinâmico e o Modelo de Substituição de Partículas”, Ph.D. thesis, Federal University of Rio de Janeiro, Brazil.

BARRIOS, G. K. P., NARCÉS, J-H., TAVARES, L. M., 2020, "Simulation of particle bed breakage by slow compression and impact using a DEM particle replacement model", *Advanced Powder Technology*, 31, pp. 2749-2758.

BAUER, W., 2011, *Hydro-pneumatic suspension systems*, 1st ed. Berlin, Springer.

BENZER, H., DÜNDAR, H., ALTUN, O., et al., 2017, “HPGR simulation from piston-die tests with an itabirite ore”, *REM-International Engineering Journal*, 70(1), pp. 99-107.

BENZER, H., ERGUN, L., LYNCH, A.J., et al., 2001, “Modeling cement grinding circuits”, *Minerals Engineering*. 14 (11), pp. 1469–1482.

BUENO & OLYMPIO, 2021, “Personal communication”, 6th September 2021.

BUENO, G., 2019. “Desvendando a prensagem de pellet feed de minério de ferro”, M.Sc. dissertation, Federal University of Rio de Janeiro, Brazil.

BUENO, G., TAVARES, L. M., BARRIOS, G. K. P., et al., 2017, “Comparação de vedações laterais em prensas de rolos via simulação pelo método dos elementos discretos”, In: *Proceedings of 5th Brazilian Ore Agglomeration Symposium*, São Paulo, Brazil.

BURCHARDT, E., MACKERT, T. 2019, “HPGR’s in minerals: What do more than 50 hard rock HPGRs tell us for the future? (Part 2 – 2019)”, In: *Proceedings of SAG Conference 2019*, Vancouver, Canada, pp. 1-28.

CABISCOL, R., SHI, H., WÜNSCH, I., MAGNANIMO, V., et al., 2020, "Effect of particle size on powder compaction and tablet strength using limestone", *Advanced Powder Technology*, *31*(3), pp. 1280-1289.

CAMPOS, T. M., BUENO, G., BARRIOS, G. K., et al., 2019a, "Pressing iron ore concentrate in a pilot-scale HPGR. Part 1: Experimental results", *Minerals Engineering*, 140, pp. 105875.

CAMPOS, T. M**.,** BUENO, G., TAVARES, L. M., 2019c, "Comparação de cenários industriais de prensagem de pellet feed via simulação", In: *Proceedings of 7th Brazilian ore Agglomeration Symposium*, São Paulo, Brazil, pp. 13-25

CAMPOS, T. M., BUENO, G., TAVARES, L. M., 2019d, "Avaliação do reciclo de bordas do produto da prensa de rolos em prensagens industriais de pellet feed via simulação computacional", In: *Proceedings of XXVIII Brazilian Meeting of Minerals Processing and Extractive Metall*urgy, Belo Horizonte, Brazil.

CAMPOS, T.M., 2018, "Modelagem matemática da prensa de rolos aplicada à cominuição de minério de ferro", B.E thesis, Federal University of Rio de Janeiro, Rio de Janeiro, Brazil.

CAMPOS, T.M., BARRIOS, G.K.P., BUENO, G., et al., 2017, "Desafios na modelagem da capacidade e potência consumida da prensa de rolos", In: *Proceedings of XXVII Brazilian Meeting of Minerals Processing and Extractive Metall*urgy, Belém, Brazil, pp. 1743-1753.

CAMPOS, T.M., BARRIOS, G.K.P., BUENO, G., et al., 2018, "Comparação de circuitos de prensagem de pellet feed previamente à moagem", In: *Proceedings of 6th Brazilian Ore Agglomeration Symposium*, São Paulo, Brazil, pp. 57-68.

CAMPOS, T.M., BARRIOS, G.K.P., SALAZAR, J.S., et al., 2016, "Comparação de modelos matemáticos na prensagem de rolos de minério de ferro itabirítico", In: *Proceedings of 17th Iron Ore Seminar*, Rio de Janeiro, Brazil, pp. 737.

CAMPOS, T.M., BUENO, G., BARRIOS, G.K., et al., 2019b, "Pressing iron ore concentrate in a pilot-scale HPGR. Part 2: Modeling and simulation", *Minerals Engineering*, 140, pp. 105876.

CAMPOS, T.M., BUENO, G., TAVARES, L.M., 2020, “Scale-up of HPGR in size reduction of iron ore pellet feed”, In: *Proceedings of XXX International Minerals Processing Congress*, Cape Town, South Africa.

CANEDO, A., 2016, “Industrial IoT lifecycle via digital twins,” In: *Proceedings of 11th IEEE/ACM/IFIP*, Pittsburgh, PA, USA, 2016, Art. no. 29.

CHELGANI, S. C., NASIRI, H., TOHRY, A., 2021, “Modeling of particle sizes for industrial HPGR products by a unique explainable AI tool-A “Conscious Lab” development”, *Advanced Powder Technology*, 32(11), pp. 4141-4148.

CLEARY, P. W., SINNOTT, M. D., 2021, “Axial pressure distribution, flow behavior and breakage within a HPGR investigation using DEM”, *Minerals Engineering*, 163, pp. 106769.

COOPER JR, A. R., La E. EATON, 1962, "Compaction behavior of several ceramic powders." *Journal of the American Ceramic Society*, 45.3, pp. 97-101.

DANIEL, M.J., 2002, “HPGR Model Verification and Scale-up”, M.Sc. dissertation, Julius Kruttschnitt Mineral Research Center, University of Queensland, Brisbane.

DANIEL, M.J., MORRELL, S., 2004, “HPGR model verification and scale-up”, *Minerals Engineering* 17, pp. 1149 1161

DAVAANYAM, Z., 2015, “Piston press test procedures for predicting energy-size reduction of high-pressure grinding rolls”, D.Sc. thesis, University of British Columbia, Canada.

DAVID, S.T., AUGSBURGER, L.L., 1977, “Plastic flow during compression of directly compressible fillers and its effect on tablet strength”, *Journal of pharmaceutical sciences*, 66(2), pp. 155-159.

DAVIS, J., EDGAR, T., PORTER, J., et al., 2012, “Smart manufacturing, manufacturing intelligence and demand-dynamic performance”, *Computational Chemical Engineering*, 47, pp. 145–156

DIETER, G. E., BACON, D., 1986, *Mechanical metallurgy*, (Vol. 3). New York, McGraw-hill.

DUNDAR, H., BENZER, H., AYDOGAN, N. A., et al., 2011, “Importance of the feed size distribution and recycle on the HPGR performance”, In: *Proceedings of SAG Conference 2011*, Vancouver, Canada.

DUNDAR, H., BENZER, H., AYDOGAN, N., 2013, “Application of population balance model to HPGR crushing”, *Minerals Engineering*, 50, pp. 114-120.

DUNNE, R., 2006, “HPGR–the Journey from Soft to Competent and Abrasive” In: *Proceedings of SAG Conference 2006*, Vancouver, Canada, pp. 190-205.

EHRENRAUT, G., RAO, R., 2001. “Experience with Roller Press in the Pellet Plant Kudremukh Iron Ore Company Ltd”, *Aufbereit Technik* 10, pp. 469–476.

FARAHMAND, A, EHRENTRAUT, G, 1997, “Erzmetall”, pp. 201-210.

FARIA, P.M., RAJAMANI, R.K., TAVARES, L.M., 2019. “Optimization of solids concentration in iron ore ball milling through modeling and simulation”, *Minerals* 9(6), pp. 366.

FERNANDEZ DE CANETE, J., DEL SAZ-OROZCO, P., BARATTI, R., et al., 2016. “Soft-sensing estimation of plant effluent concentrations in a biological wastewater treatment plant using an optimal neural network”, *Expert Systems with Application*, 63, pp. 8–19.

FETTKE, P., 2013. “Big Data, Industrie 4.0 and Wirtschaftsinformatik”, *Vortrag vom*, 25.

FLEET, K. H., 2019. “Vale’s Carajás Mine Adopts”.

FORTUNA, L., GRAZIANI, S., XIBILIA, M.G., 2005. “Soft sensors for product quality monitoring in debutanizer distillation columns”. *Control Engineering Practice*, 13, pp. 499–508.

FUERSTENAU D.W., GUTSCHE, O., KAPUR, P.C., 1996. “Confined particle bed comminution under compressive loads”, *International Journal of Minerals Processing*, 44-45, pp. 521–537.

FUERSTENAU, D.W., ABOUZEID, A.Z.M., 1998, “The Performance of the High-Pressure Roll Mill: Effect of feed moisture”, *Fizykochemiczne Problemy Mineralugii*, 32, pp. 227–241.

FUERSTENAU, D.W., SHUKLA, A., KAPUR, P.C., 1991, “Energy consumption and product size distributions in choke-fed, high-compression roll mills”, *International Journal of Minerals Processing*. 32, pp. 59–79.

GABOR, T., BELZNER, M., KIERMEIER, M., et al., 2016, “A simulation-based architecture for smart cyber-physical systems,” In: *Proceedings of IEEE International Conference of Autonomic Computing*, Wurzburg, Germany, pp. 374– 379.

GARDULA, A., DAS, D., DITRENTO, M., et al., 2015, “First year of operation of HPGR at Tropicana Gold Mine–Case Study”, In: *Proceedings of SAG Conference 2015,* Vancouver, Canada, pp. 15-36.

GARNER, S., STRONG, J, ZAVALIANGOS, A., 2018, “Study of the die compaction of powders to high relative densities using the discrete element method”, *Powder Technology,* 330, pp. 357-370.

GATZKE, E. P., DOYLE III, F. J., 2001, “Model predictive control of a granulation system using soft output constraints and prioritized control objectives”, *Powder Technology,* 121(2-3), pp. 149-158.

GE, 2017, “Transform Your Mine into a Digital Industrial Company”, *GE company brochure.*

GLAESSGEN, E., STARGEL, D., 2012, “The digital twin paradigm for future NASA and US Air Force vehicles”. In: *Proceedings of 53rd AIAA/ASME/ASCE/AHS/ASC structures, structural dynamics and materials conference 20th AIAA/ASME/AHS adaptive structures conference 14th AIAA,* pp. 1818.

GRIEVES, M., 2014, “Digital twin: Manufacturing excellence through virtual factory replication,” *White paper*.

GUEVARA, F., MENACHO, J., 1993, “Mechanical and metallurgical modeling of the high pressure roll mill Modelacióon mecáanica y metalúurgica del molino de rodillos de alta presióon”, *Centro de lnvestigación Minera y Metalúrgica*, Santiago de Chile, pp. 547-563.

GUTSCHE, O., KAPUR, P. C., FUERSTENAU, D. W., 1993, “Comminution of single particles in a rigidly-mounted roll mill Part 2: Product size distribution and energy utilization”, *Powder technology*, 76(3), pp. 263-270.

HAWKINS, R., 2007, “A Piston and Die Test to Predict Laboratory-Scale HPGR Performance”, M.Sc. dissertation, Julius Kruttschinitt Mineral Research Center, University of Queensland, Brisbane, Australia.

HECKEL, R.W., 1961, “Density–pressure relationships in powder compaction”, *Trans. Metall. Soc. AIME*, 221, pp. 671–675.

HERBST, J. A., MULAR, M. A., PATE, W. T., 2011, “Detailed modeling of an HPGR/HRC for prediction of plant scale unit performance”, In: *Proceedings of SAG Conference 2011*, Vancouver, Canada.

HERBST, J.A., FUERSTENAU, D.W., 1980. “Scale-up procedure for continuous grinding mill design using population balance model”, *International Journal of Minerals Processing*, 7, pp. 1–31.

HERMAN, V., KNORR, B., WHALEN, D., 2013, “HRC: Taking HPGR efficiency to the next level by reducing edge effect”. In: *Proceedings of 10th International Minerals Processing Conference*, Santiago, Chile, pp. 195–202

HILDEN, M., REYES, F., YE, Z., et al., 2022, “Soft Sensors for Advanced Process Monitoring and Control of Comminution Circuits”, In: *Proceedings of IMPC 2022 Asia-Pacific*, Melbourne, Australia.

HILDEN, M., SUTHERS, S., 2010, “Comparing energy efficiency of multi-pass high pressure grinding roll (HPGR) circuits”, In: *Proceedings of AUSIMM Conference*, Australia.

HULTHÉN, E., & EVERTSSON, C. M., 2011, “Real-time algorithm for cone crusher control with two variables”, *Minerals Engineering*, 24(9), pp. 987-994.

IBRAHIM, O., 2019, “Digital twin technology: A study of differences from simulation modeling and applicability in improving risk analysis”, M.Sc. dissertation, University of Stavanger, Norway.

JANKOVIC, A., VALERY, W., SÖNMEZ, B., et al., 2014, “Effect of circulating load and classification efficiency on HPGR and ball mill capacity”. In: *Proceedings of XXVII International Minerals Processing Congress*, Santiago, Chile.

JOHANSSON, M., EVERTSSON, C. M., 2018, “Applying linear model predictive control to crushing circuit simulations”. In: *Proceeding of XXIX International Minerals Processing Congress,* Moscow, Russia.

JOHANSSON, M., EVERTSSON, M., 2019, “A time dynamic model of a high-pressure grinding rolls crusher”, *Minerals Engineering,* 132, pp. 27-38.

JONES, B., 2012, “VFD control methodologies in High-pressure Grinding drive systems”, In: *Proceedings of 54th Cement Industry Technical Conference*, Texas, USA, pp. 1-7.

KADLEC, P., GABRYS, B., STRANDT, S., 2009, “Data-driven soft sensors in the process industry”, *Computational Chemical Engineering*, 33(4), pp. 795-814.

KALALA, J.T., DONG, H, HINDE, A.L., 2011, “Using piston die tests to predict the breakage behavior of HPGR”, In: *Proceedings of SAG Conference 2011*, Vancouver, Canada.

KAWAKITA, K., LÜDDE, K. H., 1971. “Some considerations on powder compression equations”, *Powder Technology,* 4(2), pp. 61-68.

KELLERWESSEL, H., 1990, “High pressure material bed comminution in practice”, *ZKG International,* 43(B), pp. 71–75.

KING, R.P., 2001. “Modeling and simulation of mineral processing systems”, *Butterworth Heinemann*.

KLYMOWSKY, I.B., LIU, J., 1997, “Modeling of the comminution in a roller press”, In: *XX International Mineral Processing Congress*, Aachen, Germany, pp. 141-154.

KLYMOWSKY, R., 2003, “High pressure grinding rolls for minerals”. *Polysius publication.*

KLYMOWSKY, R., PATZELT, N., KNECHT, J., et al., 2002, “Selection and sizing of high-pressure grinding rolls”, In: *Proceedings of Minerals Processing Plant Design., Practice. and Control,* 1, pp. 636-668.

KLYMOWSKY, R., PATZELT, N., KNECHT, J., et al., 2006, “An overview of HPGR technology”, In: *Proceedings of SAG Conference 2006*, Vancouver, Canada, pp. 11-26.

KNAPP, H., HANNOT, S., VAN DER MEER, F., 2019, HPGR: "Why skewing is a requirement for operational applications". In: *Proceedings of SAG Conference 2019,* Vancouver, Canada.

KNORR, B., HERMAN, V., WHALEN, D., 2013, "HRC™: Taking HPGR efficiency to the next level by reducing edge effect", In: *Proceedings of 10th International Minerals Processing Conference,* Santiago, Chile.

KÖPPERN, 2009. "High-pressure grinding", *Köppern brochure*.

KRITZINGER, W., KARNER, M., TRAAR, G., et al., 2018, Digital Twin in manufacturing: A categorical literature review and classification", *IFAC Papers Online*, 51(11), pp. 1016–1022.

LAGARIAS, J. C., REEDS, J. A., WRIGHT, M. H., et al., 1998, "Convergence properties of the Nelder-Mead simplex method in low dimensions", *SIAM Journal on optimization*, 9(1), pp. 112-47.

LASI, H., FETTKE, P., KEMPER, H.-G., et al., 2014, "Industry 4.0", *Business & information systems engineering*, 6(4), pp. 239–242.

LEONIDA, C. 2018, "The Intelligent guide to: digital twins in mining", *https://theintelligentminer.com/2018/12/29/digital-twins-in-mining*.

LIM, C., KIM, K.-H., KIM, M.-J., et al., 2018, "From data to value: A nine-factor framework for data-based value creation in information-intensive services", *International Journal of Information Management*, 39, pp. 121–135.

LIM, K. Y. H., ZHENG, P., CHEN, C. H., 2019, "A state-of-the-art survey of Digital Twin: techniques, engineering product lifecycle management and business innovation perspectives", *Journal of Intelligent Manufacturing*, 31(6), pp. 1-25.

LIM, W., CAMPBELL, J., TONDO, L., 1997, "The effect of rolls speed and rolls surface pattern on high pressure grinding rolls performance", *Minerals Engineering*, 10(4), pp. 401–419.

LIM, W., VOIGT, W., WELLER, K.R., 1996, "Product size distribution and energy expenditure in grinding minerals and ores in high pressure rolls", *International Journal of Minerals Processing*, 44-45, pp. 539-559.

LIM, W., WELLER, K., 1999, “Some benefits of using studded surfaces in high pressure grinding rolls”, *Minerals Engineering*, 12(2), pp. 187–203.

LIU, J., JANG, S. S., WONG, D. S. H., 2016, “Developing a Soft Sensor with Online Variable Selection for Industrial Multi-mode Processes”, *Computer Aided Chemical Engineering, 38,* pp. 398-403.

LIU, J., SCHÖNERT, K., 1996. “Modeling of interparticle breakage”, *International Journal of Minerals Processing*, 44, pp. 101-115.

LU, Y., LIU, C., KEVIN, I., et al., 2020. “Digital Twin-driven smart manufacturing: Connotation, reference model, applications and research issues”, *Robotics and Computer-Integrated Manufacturing*, 61, pp. 101837.

LUBJUHN, U., 1992. “Axiale Druckverteilung”.

LUBJUHN, U., SANDER, U., SCHONERT, K., 1994. “Pressure profile in the compression zone of the high-pressure roller mill”, *ZKG International*, 47(4), pp. 192-9.

LUBJUHN, U., SCHÖNERT, K., 1993, “Material flow in the acceleration zone and throughput of High-Pressure Roller Mills”, In: *Proceedings of XVIII International Minerals Processing Congress*, Australia, pp. 161–168.

MAURER, T., 2017, “What is a digital twin?”

MAZZINGHY, D. B., RUSSO, J. F. C., MAIA, F., et al., 2017, “Avaliação do início de operação das prensas de rolos do projeto minas-rio”, In: *Proceedings of 17$^{th}$ Iron Ore Seminar*, São Paulo, Brazil.

MCIVOR, R. E., 1997, “High Pressure Grinding Rolls- A review”, *Comminution Practices*, pp. 95–98.

MENEZES, R. L., MENDES, P. H. C., VIANA, G. F., et al., 2015, “Implantação do controle automático de gap de trabalho no roller press para maximização da qualidade do pellet feed”. In: *Proceedings of 3$^{rd}$ Brazilian Ore Agglomeration Symposium*, Rio de Janeiro, Brazil.

MEYER, K., 1980, “Pelletizing of iron ores”, Springer-Verlag.

MICHAELIS, H.V.O.N., 2009, “How energy efficient is HPGR?”, In: *Proceedings of World Gold Conference*, Johannesburg, South Africa, pp. 7–18.

MORLEY, C., 2006, *High-Pressure Grinding Rolls – A Technology Review'*, Kawatra, S.K. (Ed.), Advanced Comminution, 1st ed., Littleton, USA, SME, pp. 15–40.

MORRELL, S., LIM, W., SHI, F., et al., 1997, *Modeling of the HPGR crusher*, Comminution Practices, Kawatra, S.K., p. 117–126.

MÜTZE, T. 2016. "Modeling the stress behavior in particle bed comminution", *International Journal of Minerals Processing*, 156, pp. 14–23.

MÜTZE, T., 2015 "Energy dissipation in particle bed comminution", *International Journal of Minerals Processing*, 136, pp. 15–19.

MÜTZE, T., HUSEMANN, K., 2007, "Compressive stress: effect of stress velocity on confined particle bed comminution", *Chemical Engineering Research and Design*, 86(4), pp. 379–383.

NAGATA, Y., TSUNAZAWA, Y., TSUKADA, K., et al., 2020, "Effect of the roll stud diameter on the capacity of a high-pressure grinding roll using the discrete element method", *Minerals Engineering*., 154, pp. 106412.

NARAYANAN, S.S., WHITEN, W.J., 1988, "Determination of comminution characteristics from single particle breakage tests and its application to ball mill scale-up", *Transactions of the Institution of Mining and Metalurgy*, C 97, pp. 115–124.

NATIS, Y., JACOBSON, S., REYNOLDS, M., et al., 2017, "Innovation Insight for Digital Twins — Driving Better IoT-Fueled Decisions".

NAZARI, S., CRISTONFFANINI, C., 2019, "Digital twin in mineral processing", In: *Proceedings of 51st Annual Canadian Mineral Processors Operators Conference*, Ottawa, Ontario, Canada.

NEJAD, R.K., SAM, A., 2017, "The wear pattern in high pressure grinding rolls", *Mineral Processing and Extractive Metallurgy*, 126, pp. 238–244.

NUMBI, B. P., XIA, X. 2015. "Systems optimization model for energy management of a parallel HPGR crushing process", *Applied Energy*, 149, pp. 133-147.

OCS PLANT 3, 2019, "Manual of advanced HPGR control system – Optimizing Control System (OCS) operation manual", *HPGR operational team from Complexto de Tubarão*, Vale S.A., Brazil.

OLIVER, S.J., TOOHER, R., 2018, “Optimizing flotation plant operation by using a digital twin in the control room”, In: *Proceedings of Mill Operators’ Conference*, Brisbane, Australia.

OTTE, O., 1988, “Polycom high pressure grinding principles and industrial application”, In: *Proceedings of 30rd of Mill Operators’ Conference*, Australia, pp. 131–136.

OZCAN, O., AYDOGAN, N. A., BENZER, H., 2015, “Effect of operational parameters and recycling load on the high-pressure grinding rolls (HPGR) performance”. *International Journal of Minerals Processing*, 136, pp. 20-25.

PAMPARANA, G., KLEIN, B., BERGERMAN, M. G., 2022, “Methodology and Model to Predict HPGR Throughput Based on Piston Press Testing”, *Minerals*, 12(11), pp. 1377.

PANI, A. K., MOHANTA, H. K., 2011, “A survey of data treatment techniques for soft sensor design”, *Chemical Product and Process Modeling*, 6(1).

PATEL, S., KAUSHAL, A. M., BANSAL, A. K., 2007, “Effect of particle size and compression force on compaction behavior and derived mathematical parameters of compressibility”, *Pharmaceutical Research*, 24(1), pp. 111-124.

PODCZECK, F., SHARMA, M., 1996. “The influence of particle size and shape of components of binary powder mixtures on the maximum volume reduction due to packing”, *International Journal of Pharmaceutics*, 137(1), pp. 41-47.

POWELL, M. S, HILDEN, M. M, EVERTSSON, C. M., et al., 2012, “Optimization Opportunities for High Pressure Grinding Rolls Circuits”, In: *Proceedings of AUSIMM Conference*, Australia, 1, pp. 483-498.

POWELL, M. S., HILDEN, M. M., EVERTSSON, C. M., et al., 2017, “Optimization opportunities for high pressure grinding rolls circuits”. In: *Proceedings of AUSIMM Conference*, Australia, 1, pp. 483–498.

QIN, Y., ZHANG, S., ZHU, X., et al., 2007, “Semi-parametric optimization for missing data imputation”, *Applied Intelligence*, 27(1), pp. 79-88.

QUIST, J., EVERTSSON, C. M., 2012, “Simulating Pressure Distribution in High Pressure Grinding Rolls Using the Discrete Element Method”, In: *Comminution’12*, Cape Town, South Africa.

RAMASAMY, M., NARAYANAN, S. S., RAO, C. D., 2005, “Control of ball mill grinding circuit using model predictive control scheme”, *Journal of Process Control*, 15(3), pp. 273-283.

RASHIDI, S., RAJAMANI, R. K., 2020, “HPGR Rolls Surface Wear: In-line Scanning of a Laboratory-Scale HPGR”, *Mining, Metallurgy & Exploration*, 37(1), pp. 239-249.

RASHIDI, S., RAJAMANI, R., DUNNE, R., 2014, “A comparison of open multiple-pass and closed-circuit tests in a laboratory scale HPGR”, In: *XXVII International Mineral Processing Congress (IMPC)*, Santiago, Chile, pp. 12.

RASHIDI, S., RAJAMANI, R.K., FUERSTENAU, D.W., 2017, “A review of the modeling of high-pressure grinding rolls”, *KONA Powder and Particle Journal*, 34, pp. 125–140.

REID, K. J., 1965, “A solution to the batch grinding equation”, *Chemical Engineering Science*, 20(11), pp. 953-963.

RICKS, T.M, LACY, T.E., PINEDA, E.J., et al., 2015, “Computationally efficient solution of the high-fidelity generalized method of cells micromechanics relations”, In: *Proceedings of 30th Technical Conference of American Society of Composites*, USA.

ROCHA, B. K. N., CAMPOS, T. M., ALVEZ, L. P., et al., 2022b, “Multicomponent modeling and simulation of the Minas Rio iron ore grinding circuit”, In: *Proceedings of IMPC Asia Pacific 2022*, Melbourne, Australia, pp. 313-324.

ROCHA, B. K. N., CAMPOS, T. M., FRANCA, J. R., et al., 2022a, “Multicomponent particle breakage behavior in pressing itabirite iron ore”, In: *Proceedings of 21st Mining Symposium*, São Paulo, Brazil, pp. 212-225.

RODRIGUEZ, V. A., BARRIOS, G. K., BUENO, G., et al., 2021, “Investigation of Lateral Confinement, Roller Aspect Ratio and Wear Condition on HPGR Performance Using DEM-MBD-PRM Simulations”, *Minerals*, 11(8), 801.

RODRIGUEZ, V. A., BARRIOS, G. K., BUENO, G., et al., 2022a, “Coupled DEM-MBD-PRM simulations of high-pressure grinding rolls. Part 1: Calibration and validation in pilot-scale”, *Minerals Engineering*, 177, pp. 107389.

RODRIGUEZ, V. A., BARRIOS, G. K., TAVARES, L. M., 2022b, “Coupled DEM-MBD-PRM simulations of high-pressure grinding rolls. Part 2: Investigation of roll skewing”, *Minerals Engineering*, 178, pp. 107428.

RODRIGUEZ, V. A., CAMPOS, T. M., BARRIOS, G. K., et al., 2023, “A Hybrid PBM-DEM Model of High-Pressure Grinding Rolls Applied to Iron Ore Pellet Feed Pressing”, *KONA Powder and Particle Journal*, pp. 2023011.

ROUSSEEUW, P. J., CROUX, C., 1993. “Alternatives to the median absolute deviation”, *Journal of the American Statistical association*, 88(424), pp. 1273-1283.

RUMPF, H., 1973. “Physical aspects of comminution and new formulation of a law of comminution”, *Powder Technology*, 7(3), pp. 145-159.

RÜBMANN, M., LORENZ, M., GERBERT, P., et al., 2015, “Industry 4.0: The future of productivity and growth in MANUFACTURING industries”, *Boston Consulting Group*, 9(1), pp. 54-89.

SARAMAK, D., KLEIV, R. A., 2013, “The effect of feed moisture on the comminution efficiency of HPGR circuits”, *Minerals Engineering*, 43, pp. 105-111.

SARAMAK, D., NAZIEMIEC, Z., 2013, “Determination of the nip zone angle in high-pressure grinding rolls”, *Physicochemical Problems of Mineral Processing*, 49(1), pp. 243-253.

SCHNEIDER, C. L., ALVES, V. K., AUSTIN, L.G., 2009, “Modeling the contribution of specific grinding pressure for the calculation of HPGR product size distribution”, *Minerals Engineering*, pp. 643-649

SCHONERT, K., 1979, “Aspects of the physics of breakage relevant to comminution”, In: *Proceedings of 4$^{th}$ Tewkesbury Symposium*, Australia, 3.1–3.30.

SCHÖNERT, K., 1985, “Sizing of high-pressure twin-roller mills”, ZKG, Zement-Kalk-Gips, Edition A, 38(12), pp. 728-30.

SCHÖNERT, K., 1988, “A first survey of grinding with high-compression roller mills”, *International Journal Minerals Processing*, 22, pp. 401–412.

SCHÖNERT, K., 1990, “Physical and technical aspects of very and micro fine grinding”, In: *Proceedings of 2nd World Congress on Particle Technology*, Kyoto, Japan: Society of Technology, pp. 557-71.

SCHÖNERT, K., 1996, “The influence of particle bed configurations and confinements on particle breakage”, *International Journal Minerals Processing,* 44–45, pp. 1–16.

SCHÖNERT, K., FLÜGEL, F., 1980, “Zerkleinerung spröder Minerale im hochkomprimierten Gutbett, Prepr”, In: *Proceedings of European Symposium of Particle Technology*, Dechema, Frankfurt, pp. 82– 95.

SCHÖNERT, K., LUBJUHN, U., 1990, “Throughput of high compression roller mills with plane and corrugated rollers”, In: *Proceedings of 7th European Symposium on Comminution and Classification*, pp. 213-217.

SCHÖNERT, K., Sander, U., 2002. “Shear stresses and material slip in high pressure roller mills”, *Powder Technology*., 122, pp. 136-144.

SCHROEDER, G., STEINMETZ, C., PEREIRA, C. E., et al., 2016, “Visualising the digital twin using web services and augmented reality”, In: *Proceedings of 14th International Conference on Industrial Informatics*, pp. 522-527.

SCHUBERT, H., 1967, “Zu einigen Fragen der Kollektivzerkleinerung”, *Chem. Technol*. 19, pp. 595–598.

SCHUG, B., ANDERSON, C., NAZARI, S., et al., 2019, “Real world improvement through virtual instrumentation at OceanaGold Haile”, *Mining Engineering*, 1, pp. 20-25.

SEGURA-SALAZAR, J., 2014, “Comparação de rotas de cominuição de minérios de ferro itabiríticos usando conceitos de sustentabilidade e eficiência energética”, M.Sc. dissertation, Federal University of Rio de Janeiro, Rio de Janeiro, Brazil.

SHANG, C., GAO, X., YANG, F., et al., 2015. “A comparative study on improved DPLS soft sensor models applied to a crude distillation unit”, *IFAC-PapersOnLine*, 48(8), pp. 234-9.

SÖNMEZ, B., OLIVEIRA, R., JANKOVIC, A., 2015, “Metso HRC-Energy efficient comminution technology basic principles”, In: *Proceedings of Balk. Proc. Min. Process. Congr,* 1, pp. 131–138.

STARK, R., KIND, S., NEUMEYER, S., 2017, “Innovations in digital modeling for next generation manufacturing system design”, *CIRP Annals - Manufacturing Technology*, 66(1), pp. 169–172

SUICHIES, M., LEROUX, D., DECHERT, C., 2000, “An implementation of generalized predictive control in a flotation plant”, *Control Engineering Practice*, 8(3), pp. 319-325.

TAGGART, A. F., 1945, *Handbook of mineral dressing*, (Vol. 1), Wiley.

TAO, F., ZHANG, H., LIU, A., et al., 2018. “Digital twin in industry: State-of-the-art”, *IEEE Transactions on Industrial Informatics*, 15(4), pp. 2405-2415.

TAVARES, L. M., 1999, “Energy absorbed in breakage of single particles in drop weight testing”, *Minerals Engineering*, 12(1), pp. 43-50.

TAVARES, L. M., das NEVES, P. B., 2008, “Microstructure of quarry rocks and relationships to particle breakage and crushing”, *International Journal of Minerals Processing*, 87(1-2), pp. 28-41.

TAVARES, L.M., 2000, “Role of particle microstructure in comminution”, *Development in Minerals Processing*, 13, pp. C4-99.

TAVARES, L.M., 2005, “Particle weakening in high-pressure roll grinding”, *Minerals Engineering*, 18, pp. 651-657.

TAVARES, L.M., 2007, “Breakage of particles: Quasi-static”, *Powder Technology*, Elsevier B.V., 12, pp. 3-68.

THIVIERGE, A., BOUCHARD, J., DESBIENS, A., 2021, “An off-line state observer of the slip, shear stress, and pressure profiles in the high-pressure grinding rolls crusher working gap”, *Advanced Powder Technol*ogy, 32(10), pp. 3484-3498.

THIVIERGE, A., BOUCHARD, J., DESBIENS, A., 2022, “Unifying high-pressure grinding rolls models”, *Minerals Engineering*, 178, pp. 107427.

THOMAZINI, A. D., TRÉS, E. P., MACEDO, F., et al., 2020, “Development of a Novel Grinding Process to Iron Ore Pelletizing through HPGR Milling in Closed Circuit”, *Mining, Metallurgy & Exploration*, 37(3), pp. 933-941.

TOHRY, A., CHELGANI, S. C., MATIN, S. S., et al., 2020, “Power-draw prediction by random forest based on operating parameters for an industrial ball mill”, *Advanced Powder Technology*, 31(3), pp. 967-972.

TORRES, M., CASALI, A., 2009, “A novel approach for the modeling of high-pressure grinding rolls”, *Minerals Engineering*, 22(13), pp. 1137–1146.

TRAIN, D., 1956. “An investigation into the compaction of powders”, *Journal of Pharmacy and Pharmacology*, 8(1), pp. 745-761.

TYE, C.K., SUN, C.C., AMIDON, G.E., 2005, “Evaluation of the effects of tableting speed on the relationships between compaction pressure, tablet tensile strength, and tablet solid fraction”, *Journal of Pharmaceutical Science*, 94(3), pp. 465-472.

VACHON, M.G., CHULIA, D., 1999, “The use of energy indices in estimating powder compaction functionality of mixtures in pharmaceutical tableting”, *International Journal of Pharmaceutics*, 177(2), pp. 183-200.

VAN DER ENDE, R., KANAPP, H, VAN DER MEER, F., 2019, “Reducing edge effect and material bypass using spring-loaded cheek plates in HPGR grinding”, In: *Proceedings of SAG Conference 2019*, Vancouver, Canada.

VAN DER MEER, F. P., 2010, “HPGR Scale-Up and Experiences”, In: *Proceedings of XXV International Minerals Processing Congress*, Brisbane, Australia, pp. 6-10.

VAN DER MEER, F. P., DICKE, R., 2008, “High Pressure Grinding: How high can you go”, In: *Proceedings of 5$^{th}$ International Minerals Processing Conference*, Santiago, Chile, pp. 22-24.

VAN DER MEER, F.P., 1997, “Roller Press Grinding of Pellet Feed. Experiences of KHD in the Iron Ore Industry”, In: *Proceedings of AUSIMM* Conference, Australia, pp. 1–15.

VAN DER MEER, F.P., 2015, “Pellet feed grinding by HPGR”, *Minerals Engineering*, 73, pp. 21–30.

VAN DER MEER, P.F., LEITE, I.A., 2018, “Aspects of HPGR in iron ore pellet feed preparation”, In: *Proceedings of 6$^{th}$ Brazilian Ore Agglomeration Symposium*, São Paulo, Brazil, pp. 102-115.

VIANNA, I.Q., FREITAS, M.L., COSTA, L.S., et al., 2019, “Utilização do fino comum anfibolítico de brucutu na matriz de minério na pelotização”, *Proceedings of 7th Brazilian Ore Agglomeration Symposium*., Brazil, pp. 52-63.

VYHMEISTER, E., REYES-BOZO, L., RODRIGUEZ-MAECKER, R., et al., 2019, “Modeling and energy-based model predictive control of high-pressure grinding roll”, *Minerals Engineering*, 134, pp. 7-15.

WATSON, S., BROOKS, M., 1994, “KCGM evaluation of high-pressure grinding roll technology”, In: *Proceedings of 50th MillOps Conference*, pp. 69-83.

WHITEN, W. J., 1972, “The simulation of crushing plants with models developed using multiple spline regression”, *Journal of the Southern African Institute of Mining and Metallurgy*, 72(10), pp. 257-264.

WÜNSCH, I., FINKE, J. H., JOHN, E., et al., 2019, “A mathematical approach to consider solid compressibility in the compression of pharmaceutical powders”, *Pharmaceutics,* 11(3), pp. 121.

XIANG, F., ZHI, Z., JIANG, G., 2018, “Digital Twins technology and its data fusion in iron and steel product life cycle”, In: *Proceedings of 15th International Conference on Networking, Sensing and Control*, pp. 1-5.

XU, Y., SUN, Y., LIU, X., 2019, “A digital-twin-assisted fault diagnosis using deep transfer learning”, *IEEE Access*, 7.

YAHYAEI, M, et al., 2020, “Amira Global Project P9Q Final Report”, In: Amira P9Q project, Brisbane, Australia.

YAHYAEI, M., HILDEN, M., REYES, F., et al., 2021, “Soft sensors and their application in advanced process control of mineral processing plants”, In: *Proceedings of International Minerals Processing Conference*, Santiago, Chile.

ZERVAS, G., 2019, “The Metcalf concentrator HRC™3000: Performance at variable specific force”, In: *Proceedings of SAG Conference 2019*, Vancouver, Canada.

ZHANG, C., ZOU, Y., GOU, D., 2022, “Experimental and numerical investigation of particle size and particle strength reduction in high pressure grinding rolls”, *Powder Technology*, 410, pp. 117892.

ZHANG, Y. M., NAPIER-MUNN, T. J., 1995, “Effects of particle size distribution, surface area and chemical composition on Portland cement strength”, *Powder Technology*, 83(3), pp. 245-252.

ZHOU, W., WANG, D., MA, G., CAO, X., et al., 2020, “Discrete element modeling of particle breakage considering different fragment replacement modes”, *Powder Technology*, 360, pp. 312-323.

ZHUANG, C., LIU, J., XIONG, H., 2018, “Digital twin-based Smart production management and control framework for the complex product assembly shop-floor”, *International Journal of Advanced Manufacturing Technology*, 96(1–4), pp. 1149–1163.